THE EROSION OF TITANIUM ALUMINIDE INTERMETALLIC ALLOYS

by

Robert Llewellyn Howard

A thesis submitted to the Faculty of Engineering, University of Cape Town in fulfilment of the degree of Doctor of Philosophy

Department of Materials Engineering

University of Cape Town

May 1995

ABSTRACT

The erosion behaviour of titanium aluminide intermetallic alloys has not been widely reported in the scientific literature and is part of the current international research effort aimed at exploiting these materials for turbine engine and automotive applications. In the present study titanium aluminides have been subjected to both solid particle erosion and cavitation erosion.

The erosion rates have been measured and the damage mechanisms have been identified and discussed in terms of the microstructures and mechanical properties of the titanium aluminide alloys. This has been achieved with a variety of investigative techniques, including electron microscopy, mechanical testing and microstructural examination; and, where necessary, the erosion performance of other materials have been evaluated for comparison.

In particle erosion, conducted with air blast rigs at room temperature and at elevated temperature, the titanium aluminide alloys exhibit a ductile mode of material removal, and their limited strain to fracture results in higher particle erosion rates than those for 304 stainless steel. Heat treatment to produce changes in microstructure and hardness does not significantly affect particle erosion performance, and elevated temperature tests reveal an increase in particle erosion rate with increasing temperature.

In cavitation erosion, the titanium aluminide alloys exhibit a ductile mode of damage accumulation and material loss, and the rates of material loss are lower than those for other engineering materials such as 304 stainless steel and some hardmetal grades which are currently used in erosive environments.

The mechanism of cavitation erosion of the Ti_3Al-based alloy involves the accumulation of strain in phase boundary regions and the preferential removal of the more brittle component of the microstructure. For the Ti_3Al-based alloy, cavitation erosion resistance increases with an increase in hardness produced by heat treatment. The TiAl-based alloys exhibit twinning during the initial stages of cavitation, which is characteristic of the high strain rate deformation of TiAl-based alloys, followed by substantial work hardening and preferential material loss from phase interfaces and twinned regions.

ACKNOWLEDGEMENTS

I wish to express my sincere appreciation to all those who assisted me during the course of this project, in particular:

Professor A Ball and Dr C Lang, my supervisors, for their advice and encouragement.

Messrs B Greeves and J Petersen for photography, messrs G Newins and N Dreze for technical support, Mrs M Topic for laboratory assistance, Mr K Howard for assistance with computer graphics and Mrs E Milewski for assistance with line drawings.

The staff of the Electron Microscope Unit, for their technical assistance.

Professor M Loretto and Dr Z Chen of the I.R.C. in Materials, University of Birmingham, for supplying materials and for useful discussions.

Mrs J Sharland and Mrs A Ball for their administrative support.

The staff and students in the Department of Materials Engineering for their support and encouragement.

Finally, the South African Foundation for Research Development and the University of Cape Town for the provision of financial support.

Dedicated to my wife Ruth.

Table of Contents

1. INTRODUCTION

Ordered intermetallic alloys have received attention over the past thirty years because of their good high temperature mechanical properties, low density, and hence their potential as materials for turbine blades and discs, airframes[1], and more recently as automotive components such as valves and connecting rods[2]. Three stoichiometric intermetallic compounds exist in the titanium-aluminium binary system[3], namely Ti_3Al (α_2), TiAl (γ) and $TiAl_3$ (δ); $TiAl_3$-based titanium aluminides have received much less attention than the first two because of their extremely low room temperature ductility. The α_2 and γ titanium aluminide alloys which are of engineering importance consist of at least two phases, namely (α_2+B2) and ($\gamma+\alpha_2$) respectively.

Ti_3Al-based (α_2) alloys of current engineering significance include Ti-24Al-11Nb (at.%) and Ti-25Al-10Nb-3V-1Mo (at.%). Ti-25Al-10Nb-3V-1Mo (at.%) is a second generation α_2 alloy known as super α_2 and is available commercially as rolled plate. The maximum service temperature of Ti_3Al-based alloys is approximately 600°C[4], which is between that of conventional near-α titanium alloys and the higher temperature nickel base superalloys. Ti_3Al-based alloys, with lower density (4.1-4.7 $g.cm^{-3}$) than superalloys (approximately 8.3 $g.cm^{-3}$)[1] are candidate materials for the lower temperature sections of aircraft turbine engines.

TiAl-based (γ) alloys are capable of operating at higher temperatures (approximately 750°C) than the Ti_3Al-based alloys and have lower density (3.7-3.9 $g.cm^{-3}$) than Ti_3Al-based alloys[5]; however the room temperature ductility of TiAl-based alloys is lower than that of Ti_3Al-based alloys[38].

Several turbine engine components have been fabricated from α_2 and γ alloys and have been engine tested[6,7]. An automotive turbocharger rotor has been fabricated from a γ alloy and may be produced commercially[1]. Processing is an important aspect of the development of α_2 and γ titanium aluminides for engineering applications and thermomechanical processing is widely used to refine the microstructure and improve ductility. Interstitial oxygen and hydrogen have a detrimental effect on strength and ductility and production processes such as plasma arc melting are used to produce high purity ingots.

The particle erosion of α_2 and γ titanium aluminides is an aspect of their mechanical performance which is relevant to their performance as turbine engine components, but has not been widely reported. In particular, the ingestion of erodent particles during take-off into low slung engine inlets erodes the components in the front compressor section of the engine[8].

Cavitation erosion can be a problem in any fluid system in which there is a cyclic pressure variation and it is an important aspect of the mechanical performance of the titanium aluminides as they begin to find applications other than for jet engine components[2].

1.1. Research Approach

This thesis focuses on the particle erosion and cavitation erosion of a Ti_3Al-based alloy and two TiAl-based alloys. The thesis initially deals with the microstructure of each material. Uniaxial tensile tests were conducted on the Ti_3Al-based alloy and 304 stainless steel for comparative purposes and compression tests were conducted on the Ti_3Al-based alloy. The results of the microstructural examination and the tensile properties and deformation characteristics of the Ti_3Al-based alloy are used to facilitate interpretation of the erosion results.

Particle erosion and cavitation erosion tests were performed on the titanium aluminide alloys and comparative materials, 304 stainless steel, WC-15Co (wt.%) hardmetal, glass and annealed 6261 aluminium. A limited amount of high temperature particle erosion testing was conducted to assess the effect of temperature on the particle erosion performance of the titanium aluminide alloys.

The surface topographies associated with the onset and steady state conditions of room temperature particle erosion and cavitation erosion were examined primarily with optical and scanning electron microscopy techniques. An attempt is made to identify the origin of the deformation markings on the cavitation eroded surfaces of TiAl-based alloys with transmission electron microscopy.

The erosion test results are discussed in terms of the mechanical properties and microstructures of the titanium aluminide alloys and the erosion damage characteristics of the titanium aluminides are compared with those of the comparative materials.

2. LITERATURE REVIEW

2.1. Introduction

Review papers have dealt with the nature of intermetallic compounds and their potential as engineering materials[4], ways of improving ductility and toughness[9], mechanical properties[10,11] and alloy development[12].

Intermetallic compounds consist of well-defined (stoichiometric) proportions of two or more metals in an ordered atomic configuration, with a predominance of unlike nearest neighbours and stronger bonds between atoms than usually exist in disordered materials[4]. The strong bonds promote stiffness and strength retention at elevated temperature[4]. The low symmetry of the ordered structure means that only a limited number of slip systems is available for dislocation movement, and usually less than the five required to satisfy the condition for arbitrary changes in shape[4]. A consequence of the limited number of slip systems is ineffective transmission of strain between neighbouring grains, which can lead to strain accumulation at grain boundaries and consequent cracking.

Intermetallic compounds are generally more brittle and have higher work hardening rates than disordered materials. If the ordering energy of an intermetallic compound is low enough, slip occurs by the movement of coupled pairs of dislocations known as super-dislocations, as shown in Figure 1. The passage of a super-dislocation creates an anti-phase boundary (A.P.B.), the spacing of which is controlled by the competing effects of A.P.B. energy and the repulsive force between the two super-partials that make up the super-dislocation[13]. Work hardening rates are high in these materials because the super-partials must associate before cross-slip can occur[14]. In intermetallic compounds with a high ordering energy, the A.P.B. associated with a super-dislocation cannot be tolerated because of its high energy, and dislocations with Burgers vectors equal to the unit lattice vector operate to produce slip[13]. Slip in the strongly ordered NiAl intermetallic compound occurs in this way with {110} <001> slip providing only three independent slip systems[15]. Strain incompatibility at grain boundaries due to an insufficient number of independent slip systems results in grain boundary fracture in polycrystalline NiAl[16].

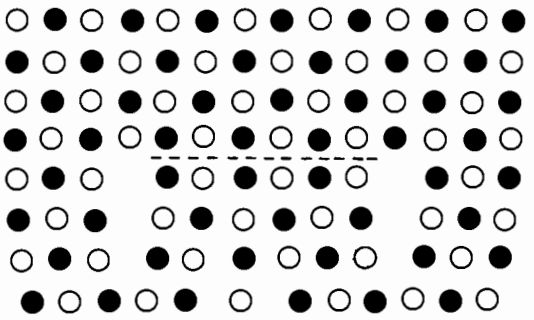

Figure 1. Schematic diagram of a super-dislocation in an intermetallic compound consisting of two super-partials separated by a stacking fault. The passage of a super-dislocation results in the formation of an anti-phase boundary (after Smallman[13]).

The development of intermetallic alloys for engineering applications has shown that grain refinement is even more effective in imparting increased strength in an intermetallic compound than in a disordered material[17]. Multiphase microstructures, in which a second more ductile phase is stabilised by alloying are sought for improved ductility and toughness. Although stoichiometry is inherent in the definition of an intermetallic compound, deviations from stoichiometry can be accommodated. Intermetallics for engineering applications are alloyed to optimise properties and are therefore usually off-stoichiometric.

The purpose of this review is to examine those aspects germane to an understanding of the particle erosion and cavitation erosion performance of Ti_3Al-based and TiAl-based titanium aluminide alloys. A brief outline of some of the major works on the mechanical behaviour of Ti_3Al-based and TiAl-based titanium aluminides and the relationship between microstructure and mechanical properties is given in sections 2.2.1. and 2.3.1. The mechanical properties of the titanium aluminide alloys at high strain rates are briefly reviewed since high strain rates prevail during particle erosion and cavitation erosion.

2.2. Ti_3Al-Based Titanium Aluminide Alloys

2.2.1. Microstructure/ Property Relationships

The equilibrium phases in the titanium-aluminium binary system are shown in the phase diagram in Figure 2. Two main equilibrium phases exist in the Ti_3Al-based alloys, namely α_2 (with stoichiometric composition, Ti_3Al) with an ordered DO_{19} crystal structure and β with a disordered body-centred cubic crystal structure[18]. The B2 phase, with an ordered body-centred cubic (CsCl-type) crystal structure, is a metastable phase in Ti-Al binary alloys and is stabilized by the addition of niobium[17]. There are only four independent slip systems in the α_2 phase, an insufficient number to satisfy the five-shear condition for producing arbitrary changes of shape. Court et al.[19] showed that Ti_3Al-based alloys undergo plastic deformation by the movement of super-partial pairs of dislocations. The dominant slip system at room temperature in Ti-25Al (at.%) was identified as <110> {100} and dislocations move as super-partial pairs with the Burgers vector **b**=1/6 [110]. Samples of Ti-25Al-4Nb (at.%) exhibited slip along the <110> direction on {100}, {001} and {101} planes and high densities of dislocations were observed in bands with b = 1/6 <116> on {111} planes at room temperature.

B2 has a higher yield strength than α_2 and strengthens the Ti_3Al-based alloys. The high temperature B2 phase is stabilised by niobium, vanadium and molybdenum[17]. Deformation in the B2 phase is inhomogenous and localised into non-planar slip bands, but this phase has five independent slip systems. Dislocations glide as coupled a/2 <111> super-partials[20]. B2 grain refinement is essential to overcoming the inhomogeneity of slip in this phase.

Ternary ordering of niobium on the titanium sublattice of the α_2 (DO_{19}) structure[21] and the distortion of the α_2 (DO_{19}) structure produce the ordered orthorhombic (O) phase based on the Ti_2AlNb composition which was first identified by Banerjee and co-workers[22]. The similarity between the structures of the α_2 phase and O phase is shown schematically in Figure 3. Because of its crystallographic relationship with the α_2 phase, the O phase exhibits very similar slip behaviour. The response of the O and α_2 phases to thermomechanical treatment is very similar and the distinction between them is not as critical from a practical point of view as the control of grain size and phase morphology[17]. In a review of deformation twinning in intermetallics, Gray[23] noted that twinning was observed by Morris and Morris[24] in the α_2 phase of Ti-24Al-11Nb (at.%), but numerous other microscopy studies showed that twinning did not occur in α_2 titanium aluminides.

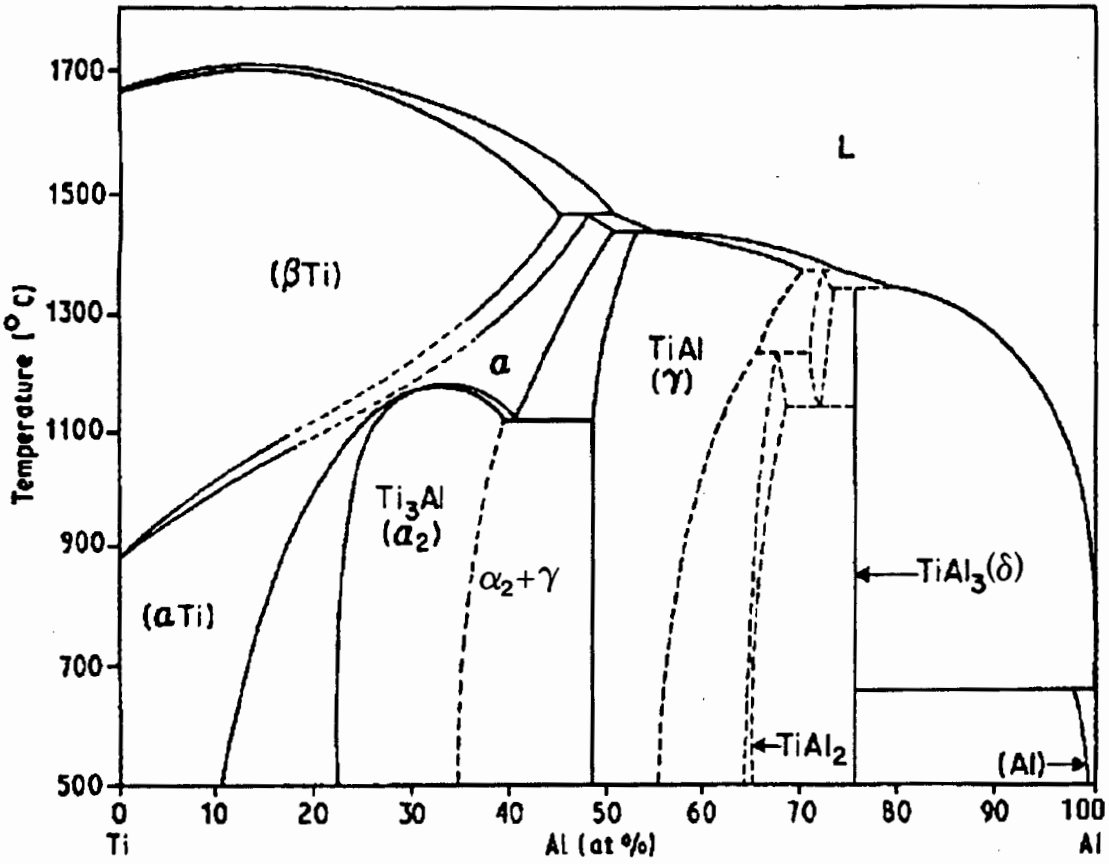

Figure 2 Ti-Al binary phase diagram (after Rowe and Huang[25]).

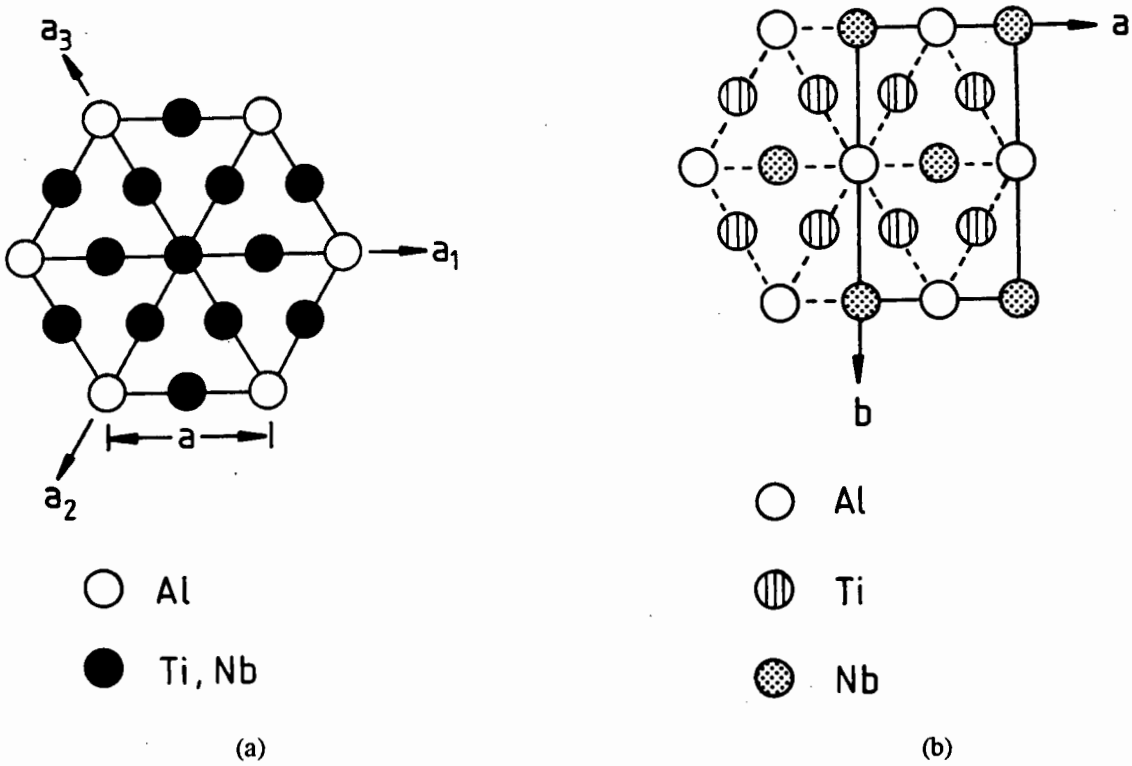

Figure 3. Schematic diagrams of the (001) planes of (a) the ordered hexagonal (DO_{19}) structure of the α_2 phase and (b) the ordered orthorhombic phase (after Ward[17]).

Cleavage fracture is initiated at α_2/α_2 grain boundaries due to strain incompatibilities between the grains, along slip bands in the α_2 phase and within the B2 phase[26]. In a dual-phase (α_2+B2) microstructure the B2 phase (with its larger number of available slip modes) improves ductility by delaying cleavage fracture of the α_2 phase to larger strains by its ability to plastically accommodate incompatibility stresses at α_2/B2 grain boundaries as shown schematically in Figure 4. B2 grain distributions that avoid α_2/α_2 contact are more effective in imparting toughness and ductility because they avoid the strain incompatibility at α_2/α_2 grain boundaries[18].

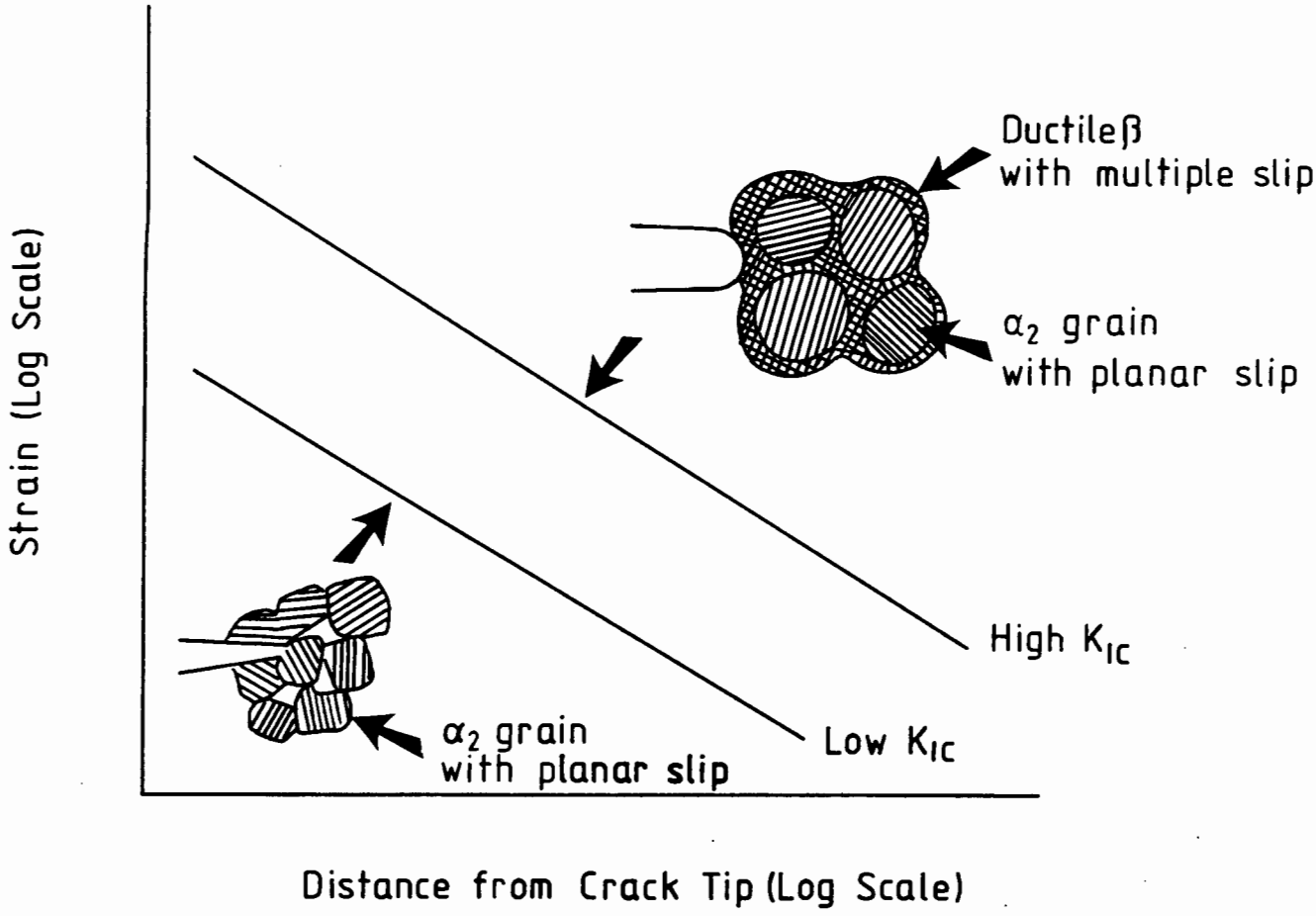

Figure 4. Schematic diagrams showing that the near-tip strain distribution and the fracture toughness of the brittle intermetallic phase, α_2, which is susceptible to grain boundary cracking due to planar slip, may be increased by the presence of a continuous ductile phase that blunts the crack tip and accommodates strain incompatibility at the α_2 grain boundaries (after Chan[27]).

Haddad, Zevin and Eliezer[28] studied the phase relations in Ti-25Al-10Nb-3V-1Mo (at.%) using X-ray diffraction. The lattice parameters of the α_2 and β (B2) phases are shown in Table 1 with the results of similar studies. The detection of the superlattice lines, (101) for the α_2 phase and (100) for the β (B2) phase, indicated ordering of both phases. Dickson's[29] multi-peak method for averaging the intensities of a number of peaks of each phase in a two-phase system with preferred orientation was used to calculate the volume fractions of α_2 and B2 phases. R values relative to corundum were determined for both phases. Calculated intensities for each hkl plane were used in the calculation of phase proportions to effectively produce a unique R value for each set of hkl

planes. These relative R values were used in a modified form of the multi-peak equation[29] to calculate the proportions of α_2 and B2 phases.

Table 1. Summary of lattice parameters (measured in nanometres) for Ti_3Al-based alloys.

Alloy (at. %)	α_2 phase		B2 phase	O phase		
	a	b	a	a	b	c
Ti-24Al-11Nb[24]	0.595	0.467	0.322 (β)	0.595	0.985	0.450
Ti-25Al-12.5Nb[22]	-	-	-	0.588	0.960	0.450
Ti-25Al-10Nb-3V-1Mo[28]	0.578	0.463	0.323	-	-	-

Morris and Morris[24] studied the deformation of Ti-24Al-11Nb (at.%). Different microstructures were produced by annealing for 24 hours at temperatures between 700°C and 1000°C followed by water quenching. Annealing at 700°C and 800°C produced fine needles of the O phase within the B2 matrix. In compression tests conducted to 2.5% strain, the α_2 grains were deformed in specimens annealed at 700°C and 900°C, while they remained undeformed in specimens annealed at 800°C. Matrix areas (B2) contained dislocations in all specimens. Deformation twins were observed within primary α_2 grains in the specimens annealed at 950°C and 1000°C, although no selected area electron diffraction pattern evidence was provided to support this observation. Work hardening behaviour of the different annealed materials differed significantly. The fine lath structures within the B2 matrix and smaller primary α_2 grains of the specimens annealed at 700°C and 800°C provide many strong obstacles to dislocation movement and hence higher values of work hardening than the microstructures with featureless matrixes. Work hardening rates between 25 GPa and 5 GPa were recorded at slow strain rate between strains of 0.2% and 2% respectively.

Chen, Simca and Cope[30] conducted ageing heat treatments at 650°C, 750°C, 850°C and 950°C for 2 hours on Ti-25Al-10Nb-3V-1Mo (at.%) after solution treatment at 1060°C for 1 hour in the α_2 + β (disordered B2) phase field. The B2 phase transformed to α_2 or O depending on the ageing temperature as shown in Figure 5. The solution treatment temperature affected the stability of the B2 phase and hence the rate of transformation of this phase during ageing. The B2 matrix transformed to fine orthorhombic laths after ageing at 650°C and at 850°C. The O laths were resolvable with the transmission electron microscope after ageing at 650°C. At 850°C these laths were resolvable with the optical microscope because of their increased size. Ageing at 950°C produced a microstructure consisting of primary α_2, secondary α_2 laths and retained B2 matrix. The strength of the alloy was a maximum and ductility was a minimum after ageing at 650°C (Table 2). The larger volume fraction of retained B2 matrix after ageing at higher temperatures provided greater ductility. Zones surrounding the α_2 phase that were denuded of fine laths were susceptible to fracture.

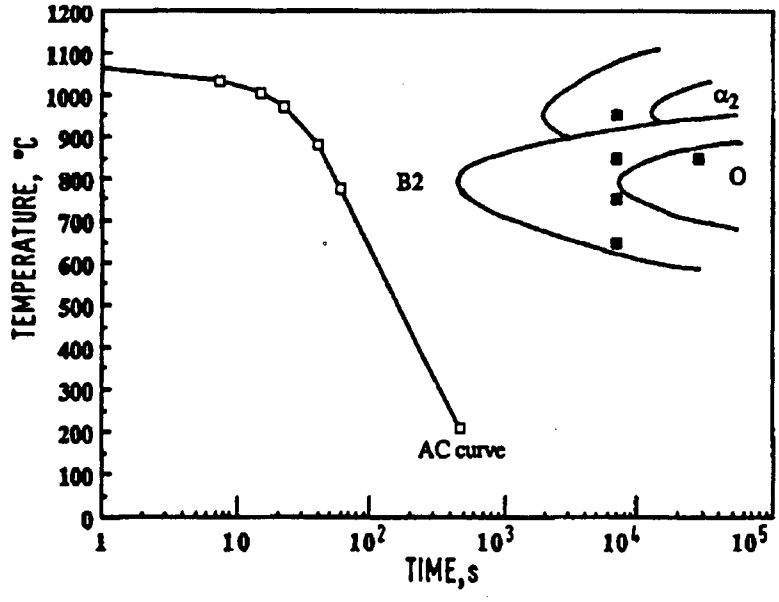

Figure 5. TTT curves of super α_2 solution treated at 1060°C for 1 hour estimated from analytical electron microscopy and microanalysis data (shown as solid squares); the air cooling (AC) curve is shown with open squares (after Chen et al.[30]).

Table 2. 0.1% Proof stress and tensile elongation results for Ti-25Al-10Nb-3V-1Mo (at.%) after ageing heat treatment[30].

Ageing temperature (°C)	0.1% Proof stress (MPa)	Elongation (%)
650	1293	0.1
850	940	1.55
950	817	1.2

Proske, Lutjering, Albrecht, Helm and Daenbler [31] modified the microstructure of Ti-25Al-10Nb-3V-1Mo (at.%) by thermomechanical processing to produce lamellar, equiaxed and bimodal microstructures. The lamellar microstructures consisted of aligned α_2 and β plates with colony sizes corresponding to the prior β grain size of approximately 1 mm. The two equiaxed microstructures consisted of equiaxed α_2 grains, with the matrix consisting of fine α_2/β lamellae in one condition and including no transformation product in the other. The bimodal microstructures

consisted of sparse primary α_2 grains and varying amounts of fine α_2/β lamellae. The higher yield strength of the equiaxed material over the lamellar microstructure was ascribed to the shorter slip length in the equiaxed grains. The lamellar grains were larger in one direction than the equiaxed grains and the alignment of neighbouring grains along the same crystallographic orientation formed a colony and facilitated slip transfer between many grains, over a large effective slip length. This lead to intense shear, crack nucleation at smaller strains and reduced ductility of the lamellar microstructure.

Kim and Froes[32] reviewed the relationship between mechanical properties and microstructure obtained by thermomechanical processing. A fine Widmanstatten microstructure in super α_2 with a small amount of primary α_2 offers the best boundary strengthening and better ductility than coarse Widmanstatten α_2 or aligned secondary α_2 needles. Aligned plates provide a longer effective slip length because the colony acts as a single grain in providing continuous slip across the colony. Greater strain incompatibility at the colony boundaries leads to a loss of ductility. In order to promote ductility, a random arrangement of α_2 plates, limited primary α_2/α_2 grain boundary contact and the absence of large amounts of primary α_2 are desirable, while fine α_2 plates surrounded by B2 matrix promote strength and toughness.

Ward reviewed the effect of microstructure on the tensile and fracture behaviour of (α_2+B2) titanium aluminides[17]. Figure 6 shows that for super α_2 a two-phase microstructure consisting of α_2 and β phases was stable over the temperature regime indicated and that the volume fraction of the α_2 phase increased below 1020°C. In this diagram no distinction was made between O and α_2 phases since there is an orientation relationship between them, their slip systems are similar and they consequently exhibit very similar mechanical behaviour and responses to thermomechanical treatment.

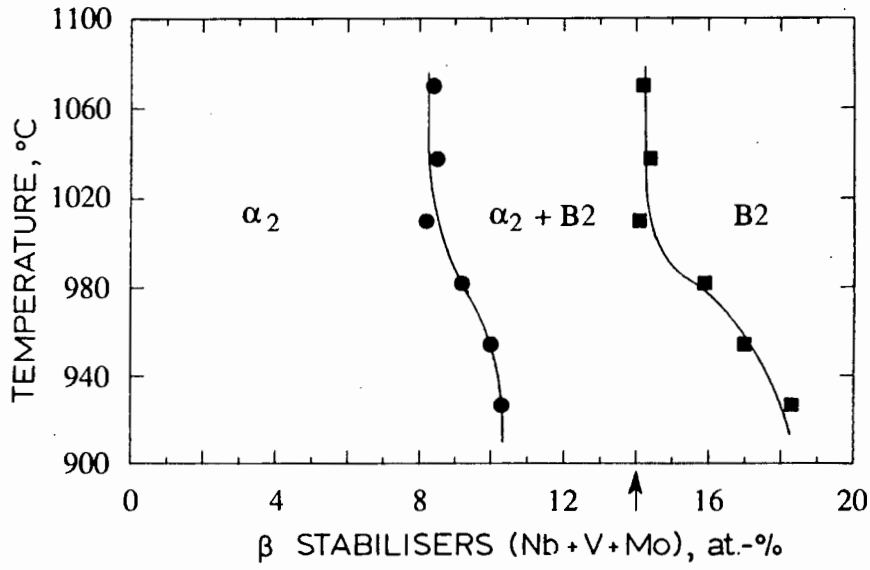

Figure 6. Temperature-composition diagram for β-stabilised Ti_3Al-based titanium aluminides; samples were isothermally aged for 168 h after 2 h β solution treatment: the arrow indicates nominal alloy composition (Ti-25Al-10Nb-3V-1Mo (at.%) (after Ward[17]).

In quasi-static compression tests (strain rate = $10^{-3}s^{-1}$)[33], Ti-24Al-11Nb (at.%) and Ti-24.5Al-10.5Nb-1.5Mo (at.%) showed gradually decreasing hardening rates with increasing strain to final strains of 20% and 55% respectively, although both alloys reached an absolute flow stress of approximately 1500 MPa.

2.2.2. High Strain Rate Behaviour

Gray, Hong and Marquardt[34] investigated the influence of strain rate on the damage substructure and compressive stress-strain response of Ti-24.5Al-10.5Nb-1.5Mo (at.%). Dislocations were observed and the slip systems were identified for the range of strain rates and no twinning was observed. Yield strength increased from approximately 1000 MPa at $10^{-3}s^{-1}$ to 1250 MPa at $6x10^{3}$ s^{-1}. The work hardening rate increased from 3300 MPa per unit strain to 4200 MPa per unit strain with an increase in strain rate from $10^{-3}s^{-1}$ to $6x10^{3}$ s^{-1}. A true strain of 18% was achieved at a strain rate of $10^{-3}s^{-1}$ and 11% at a strain rate of $3x10^{3}s^{-1}$.

2.2.3. The Effect of Temperature on Mechanical Properties

Ward, Thompson and Williams[35] investigated the elevated temperature tensile properties of Ti-25Al-10Nb-3V-1Mo (at.%) in vacuum and a strain rate of $10^{-3}s^{-1}$. Yield strength decreased from approximately 750 MPa at 25°C to approximately 500 MPa at 500°C and the percentage elongation increased from 5 percent at 25°C to 30 per cent at 500°C.

Ward and Balsone[36] investigated the effect of primary α_2 volume fraction, the scale and morphology of the secondary α_2/B2 transformed matrix and test temperature on the tensile and creep behaviour of Ti-25Al-10Nb-3V-1Mo (at.%). Tensile tests were conducted in air and vacuum at temperatures between room temperature and 700°C. Thermomechanical processing routes were used to produce four different microstructures, namely microstructure 1 with 20 v/o (volume percent) primary α_2 and fine α_2/B2 transformed martix; microstructure 2 with 25 v/o primary α_2 and coarser and more aligned α_2/B2; microstructure 3 similar to microstructure 2, but with more refined primary and secondary α_2; microstructure 4 with 5 v/o primary α_2, coarse secondary α_2/B2 transformed matrix and aligned secondary α_2 laths. The strength of microstructure 1 was significantly higher than that of the other three microstructures for all the testing temperatures. Microstructure 1 exhibited superior strength because of the shorter slip length of the fine non-aligned secondary α_2 laths. As the test temperature was increased tensile ductility increased. Testing in vacuum raised the temperature of the elongation maxima to 540°C from 427°C in air, which suggested that the air environment caused embrittlement; however, the exact reason for the embrittlement was not identified. Examination of longitudinal sections of the gauge lengths of tensile specimens of microstructure 1 after failure showed that the room temperature specimen underwent brittle failure of the primary α_2 grains and the primary α_2/transformed matrix interfaces. At 427°C, the cracks that initiated within the primary α_2 grains were blunted by the matrix and at 540°C, the primary α_2 grains no longer failed in a brittle manner; voids were observed at the primary α_2/matrix interfaces and primary α_2 grains exhibited

some plasticity. At 650°C, failure occurred by ductile rupture, with void nucleation at the primary α_2/B2 interfaces.

At a strain rate of $3x10^3s^{-1}$, Gray and co-workers[34] found that the compressive yield stress of Ti-24.5Al-10.5Nb-1.5Mo (at.%) decreased from approximately 900 MPa to 650 MPa with an increase in temperature from 200°C to 700°C. The true strain increased from approximately 11% at 200°C to 12.5% at 700°C.

2.3. TiAl-Based Titanium Aluminide Alloys

2.3.1. Microstructure/ Property Relationships

Two review papers by Kim[37,38] provide an overview of TiAl-based (γ) titanium aluminide alloys, including alloy development, processing, phase relations, microstructure and mechanical properties. Room temperature ductility of the γ alloys is limited to approximately 1% and tensile strength is 400 MPa - 700 MPa.

The γ phase has the stoichiometric composition TiAl with an $L1_0$ ordered face-centred cubic tetragonal crystal structure. The Ti-52Al (at.%) composition lies within the single phase γ region of the Ti-Al binary equilibrium diagram, while alloying elements niobium and molybdenum stabilise the α_2 phase, which places Ti-48Al-2Mn-2Nb (at.%) diagramatically within the $\alpha_2+\gamma$ two-phase region at ambient temperature as shown in Figure 2. Small additions of vanadium, chromium and manganese to Ti-48Al (at.%) increase the ductility of two-phase γ alloys, while niobium, molybdenum and tantalum are effective substitutional solid solution strengtheners[38].

Various microstructures can be produced by static heat treatment (i.e. not thermomechanical heat treatment). The lamellar α_2/γ morphology arises from the eutectoid transformation ($\alpha \rightarrow \alpha_2 + \gamma$) during slow cooling from the α phase field ($T \geq 1370°C$). The α phase orders on cooling to form α_2 and the γ phase precipitates from the α phase. The orientation relationship between α_2 and γ phases is as follows: $\{001\}\alpha_2 // (111)\gamma$, $<110>\alpha_2 // <110>\gamma$[39].

Four different microstructures, namely subduplex, duplex, nearly-γ and Widmanstatten were produced in a study by Takeyama[40] of the microstructural evolution and tensile properties of a titanium-rich Ti-48Al (at.%) alloy. All four heat treatments were performed in the $\alpha+\gamma$ two-phase field followed by cooling at 3.7° C/s (222 °C/min.). The $\alpha/(\alpha+\gamma)$ solvus temperature was determined as approximately 1383° C. The as cast microstructure (nearly lamellar) consisted mainly of lamellar α_2/γ in a dendritic morphology, with a small amount of single phase γ in the interdendritic regions. Heat treatment in the $\alpha+\gamma$ phase field at 1350° C for 1 hour produced the subduplex microstructure consisting of lamellar α_2/γ with a network of single phase γ which emerged preferentially at the interdendritic regions. The duplex microstructure of samples heat treated at 1350° C for 15 minutes followed by 1200° C for 1 hour consisted of approximately equal amounts and sizes of lamellar and single phase γ grains. A nearly γ microstructure was produced by heat treatment at 1200° C for 24 hours. It consisted of nearly all single phase γ grains, with some α_2/γ lamellar structures at or near the grain boundaries. A Widmanstatten-type microstructure was produced by heat treating the two samples previously heat treated at 1200° at

1350° C for 1 hour. This microstructure consisted of plate-like precipitates of α_2 on four different orientations within each γ grain.

Zhang and Chaturverdi[41] investigated the effect of Widmanstatten-type (W-type) α_2 precipitates on the room temperature deformation and fracture behaviour of Ti-50Al-2Mn-2Nb (at.%). A nearly-γ microstructure consisting of mainly equiaxed γ grains and a small fraction of α_2/γ lamellar colonies was produced by heat treatment at 1100°C for 48 hours followed by air cooling. A W-type microstructure consisting of equiaxed γ grains and α_2 laths along γ grain boundaries and within γ grains was produced by the following heat treatment: 1000°C/ 48 hours + 1280°C/ 4 hours and air cooled. The α phase precipitates from grain boundaries on four {111} habit planes during heat treatment at 1280°C in the ($\alpha + \gamma$) phase field.

Compression tests were performed on samples with nearly-γ and W-type microstructures at a strain rate of 10^{-4} s^{-1} [41]. Analysis of diffraction patterns from the W-type microstructure showed that the orientation relationship, i.e. $\{001\}\alpha_2$// $\{111\}\gamma$, $<110>\alpha_2$// $<110>\gamma$ was retained. Fine γ laths were detected within many of the α_2 laths. Grain boundary α_2 laths retained the orientation relationship with one of the neighbouring γ grains, but were oriented at random with the other grain. Compressive true stress - true strain curves revealed the slightly lower yield strength, but greater work hardening rate of the W-type material.

The nearly-γ microstructure exhibited intergranular and transgranular fracture[41]. Some grains were more heavily deformed than others. This incompatibility could have contributed to intergranular fracture by promoting the accumulation of strain at the γ grain boundaries. Transgranular fracture seemed to occur along the deformation planes in the deformed grains. In the W-type material, fracture along the α_2/γ interfaces was the dominant mode and led to a more faceted appearance than the nearly-γ fracture surface. Both cleavage and separation of the α_2/γ interfaces were observed.

Transmission electron microscopy (T.E.M.) was used to study the substructures produced by compression[41]. The deformation substructure of the nearly-γ material consisted predominantly of dislocations in some grains, while deformation twins were the dominant features in others, depending on the orientation of each grain to the applied stress. Twins intersected each other by mechanisms which were identified by T.E.M. W-type material also exhibited twinning and slip and the α_2 plates inhibited the passage of twinning dislocations and caused ordinary dislocations to pile up around the plates. Some twins crossed the α_2 plates, while others were stopped by them. Although T.E.M. showed that the W-type α_2 precipitates impeded deformation twins and dislocations, the yield strength of this microstructure was slightly lower than that of the nearly-γ microstructure. Explanations were offered to explain this apparent anomaly and included the enhanced mobility of 1/2 <110] ordinary dislocations and the nucleation of dislocations at α_2/γ

interfaces in the W-type microstructure (where <hkl] denotes all distinct permutations of ±h and ± k as the first two indices[42]). The study concluded that the W-type precipitates have no significant effect on the room temperature mechanical properties of the TiAl alloy. Deformation twins and ordinary dislocations can cross α_2 precipitates with a larger stress input than is required for the nearly-γ material without these precipitates, which may account for the higher work hardening rate of the W-type microstructure.

Prasad Rao and Tangri[43] studied the room temperature deformation behaviour of single phase Ti-32Al (at.%) and Ti-52Al (at.%) consisting of equiaxed grains of the α_2 and γ phases respectively and two-phase alloys, Ti-44Al (at.%), Ti-48Al (at.%) and Ti-50Al (at.%), consisting of equiaxed γ grains and α_2/γ lamellae in different proportions. Compression tests were conducted at room temperature and a strain rate of $10^{-4}s^{-1}$. The work hardening rates of the two-phase alloys increased with increasing amount of lamellar constituent, which was attributed to increased slip activity in these alloys compared to the single phase alloys. Work hardening rates were of the order of 5 GPa-25 GPa. Single phase γ Ti-52Al (at.%) had a lower work hardening rate than the two-phase alloys. The yield strength of the single phase α_2 alloy, Ti-32Al, was the highest, but it exhibited the lowest work hardening rate of all the alloys. Yield strength was increased by larger volume fractions of lamellar α_2/γ phase in the two-phase alloys. Twinning within γ grains was observed in Ti-48Al (at.%) and Ti-50Al (at.%) after approximately 3 % plastic strain. Ti-52Al (at.%) (single phase γ) did not exhibit twinning. After approximately 9% strain, heavy deformation bands in the form of wavy slip in Ti-48Al (at.%) and straight slip in Ti-50Al (at.%) were observed. Ti-48Al (at.%) contained 50% primary γ and 50% lamellar α_2/γ grains and Ti-50Al (at.%) contained 90% γ and 10% lamellar $\alpha_2+\gamma$. The wavy slip in Ti-48Al (at.%) was ascribed to the increased slip activity, including cross slip caused, by the larger volume fraction of α_2/γ lamellar grains.

Rogers and Bowen[44] studied the fracture toughness of Ti-49.1Al-2Nb-1.9Mn (at.%). Material was tested in the as cast (consisting mainly of lamellar grains with small γ precipitates at the grain boundaries) and heat treated (1200°C for 1.7 hours to give 24% lamellar / 76% allotriomorphic (equiaxed) γ grains) conditions, at temperatures from ambient to 800° C. At room temperature the fracture surface of the as cast material exhibited two different fracture modes: the lamellar structure failed in a stepping manner to produce a lamellar-like fracture surface and the γ phase failed by transgranular cleavage. The material with a mainly lamellar microstructure showed superior toughness at test temperatures from room temperature to 800°C. The fracture toughness of the two phases was different; 20 MPa$\sqrt{m}$-30 MPa$\sqrt{m}$ for lamellar regions and 8 MPa$\sqrt{m}$-14 MPa$\sqrt{m}$ for equiaxed γ regions. A variety of different failure mechanisms were observed across the temperature range for the heat treated material. At ambient temperature the equiaxed γ in the heat treated material failed by transgranular cleavage, with the lamellar structure clearly visible on

the fracture surfaces. Large equiaxed γ grains which precipitated during heat treatment were deleterious to the fracture toughness of the heat treated material.

Chan reviewed the toughening mechanisms in γ alloys[45]. The insufficient number of slip systems in TiAl (and Ti_3Al) leads to plastic incompatibility and slip-induced fracture by either grain boundary decohesion or cracking along planar slip bands. The presence of a ductile phase at the site of incompatibility, i.e., at a grain or phase boundary, can alleviate strain and allow the accumulation of greater amounts of strain prior to crack nucleation. Chan and Kim[46] investigated the effect of microstructure on the crack tip micro-mechanics and fracture behaviour of two-phase Ti-47Al-2.6Nb-2(Cr+V) (at.%). The lamellar microstructure consisting of α_2/γ lamellae and a small amount of equiaxed γ at colony boundaries exhibited better toughness than the duplex microstructure consisting of equiaxed γ and a small amount of α_2 particles and plates. Fracture surface examination *in situ* in the scanning electron microscope and after tensile testing revealed translamellar cleavage fracture and delamination of the lamellar interfaces. The thin grain boundary α_2 plates in the duplex microstructure exhibited slip-induced γ grain boundary decohesion and the maximum strain measured near the crack tip prior to the onset of crack growth was close to the yield strain. In the lamellar microstructure, greater strain was measured near the crack tip and the α_2/γ lamellae interfaces were better able to accommodate the incompatibility strains as shown in Figure 7. The higher near-tip strains lead to a higher fracture toughness for the lamellar material.

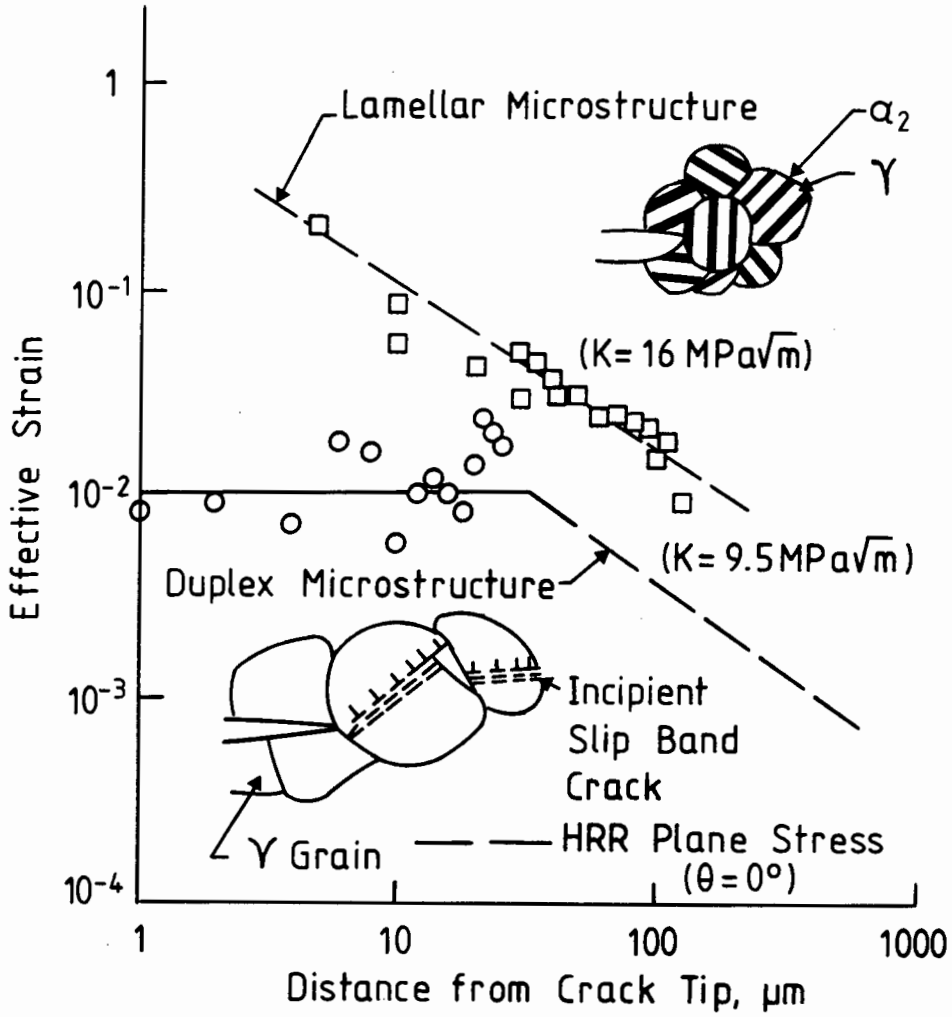

Figure 7. Comparison of the near-tip fracture process and strain distribution in the duplex and lamellar microstructures of TiAl-based alloys at 25°C (after Chan and Kim[46]).

2.3.2. High Strain Rate Behaviour

The effect of strain rate (varied between 10^{-5} s^{-1} and 10^{-1} s^{-1}) on the room temperature tensile properties of Ti-47Al-1.5Cr-1V-2.3Nb (at.%) in duplex and fully lamellar microstructural conditions was investigated by Kim and Dimiduk[47]. No differences in deformation and fracture behaviour were observed between different strain rates for a given microstructure. The fracture strength and plastic strain to fracture of the duplex microstructure increased as the strain rate was increased from 10^{-5} to 10^{-2} s^{-1}, while the yield stress showed only a small increase with increase in strain rate. Above a strain rate of 10^{-2} s^{-1}, fracture stress and plastic strain to failure decreased and yield stress increased slightly. Similar variations in tensile properties were observed for the fully lamellar material, but with fracture stress and plastic strain maxima at 10^{-3} s^{-1}. The fracture surfaces of duplex specimens were brittle after testing at $5x10^{-5}$ s^{-1} and $2x10^{-2}$ s^{-1} and consisted mainly of cleavage-like fracture and some intergranular cracking. Higher magnification

examination revealed significant plasticity which gave the duplex grains a layered structure. Fracture stress and plastic strain were lower for the fully lamellar specimens than the duplex specimens. The fracture surfaces of the fully lamellar specimens, after tensile tests to 0.36% plastic strain at a strain rate of 1.4×10^{-3} s^{-1}, revealed translamellar, interlamellar and mixed mode fracture. Interlamellar fracture surfaces revealed less evidence of deformation than the translamellar fracture surfaces which usually revealed slip/twin activity. The fine translamellar slip/twins were observed within a narrow zone below the fracture surface and deformation bands or slip steps parallel to the laths with 10μm-20μm spacing were observed in abundance on the electro-polished surfaces.

Gray[48] examined the effect of strain rate and temperature on the substructure evolution and mechanical response of Ti-48Al-1V (at.%) in compression. Quasi-static tests were conducted on a screw-driven load frame at strain rates between $10^{-3}s^{-1}$ and $10^{-1}s^{-1}$. Dynamic tests were performed using Split-Hopkinson Bar apparatus at strain rates between $1000s^{-1}$ and $8000s^{-1}$. Strain hardening increased slightly from 3790 MPa per unit strain at a strain rate of $10^{-3}s^{-1}$ to 4640 MPa per unit strain at $4500s^{-1}$. The microstructure of annealed Ti-48Al-1V (at.%) consisted of equiaxed γ grains and lamella α_2/γ (α_2 volume fraction = ± 10%). The flow stress and rate of hardening increased with increasing strain rate. In contrast, Ti-6Al-4V (wt.%) shows a drastic decrease in strain hardening at increasing strain rate due to adiabatic heating. Substructure evolution depended on applied strain rate and temperature. Room temperature compression to a strain of 20% at a strain rate of $10^{-3}s^{-1}$ produced random dislocation debris. Isolated twins, especially at grain boundaries were also observed, but no super-dislocations were observed. At a strain rate of 7500 s^{-1}, the density of deformation twins increased and so did the overall random dislocation debris density. It was argued that the relative constancy of strain hardening rate with increased strain rate, despite the greater twinning, suggests that twinning does not significantly influence the strain hardening behaviour of Ti-48Al-1V (at.%).

In a further study of the compressive work hardening behaviour of titanium and nickel-based aluminides at strain rates between $10^{-3}s^{-1}$ and $8000s^{-1}$, Gray and Embury[33] showed that all of the alloys exhibited extended work hardening to stress levels of 1.5 GPa to 2 GPa. Compression suppressed fracture processes, leading to higher stress and strain levels being attained than in tension. In the γ titanium aluminide, Ti-48Al-1V (at.%), compressed quasi-statically to a true strain of 25%, twins and dislocations were observed in the γ phase but twins were not observed in the α_2 phase. Ni_3Al, Ti-48Al-1V (at.%) and Ti-48Al-2Cr-2Nb (at.%) showed increasing work hardening with increasing strain.

2.3.3. The Effect of Temperature on Mechanical Properties

Kim[37], in a review of γ titanium aluminides, showed that yield strength decreases and elongation increases as temperature increases for single-phase and two-phase γ alloys. The elastic moduli of TiAl and Ti-48Al-1V-0.1C (at.%) decreased from between 160 GPa and 176 GPa at room temperature to approximately 155 GPa at 500°C and approximately 140 GPa at 850°C. The fracture toughness, K_{IC}, of Ti-48Al-1V-0.1C (at.%) increased from 12.3 MPa$\sqrt{m}$ at room temperature to 25 MPa$\sqrt{m}$ at 440°C.

The impact fracture energy of Ti-51Al (at.%) was measured at temperatures between 0°C and 1000°C[49]. Miniature U-notch specimens were impacted by a punch moving at 1 $m.s^{-1}$. The load was measured by a load cell and the punch displacement was measured by a laser-sensor. The fracture impact energy was calculated as the area below the load displacement curves. The impact energy increased with increasing temperature from $2x10^7$ J/m^3 at room temperature to $9x10^7$ J/m^3 at 1000°C. Fracture surface examination revealed mainly cleavage fracture and some intergranular fracture at room temperature, and mainly intergranular fracture at elevated temperature.

2.4. Particle Erosion

Particle erosion is a complex phenomenon which has received attention from numerous workers[50,51]. The conditions during solid particle erosion are very different to those in a conventional slow strain rate tensile test, which leads to poor correlations between particle erosion performance and conventional mechanical properties. Solid particle erosion involves a multi-axial stress distribution. The material immediately below the impacting particle is plastically constrained by the surrounding material and strain rates between 10^5 s^{-1} and 10^7 s^{-1} are experienced for particle diameters between 20 μm and 200 μm and velocities between 10 $m.s^{-1}$ and 100 $m.s^{-1}$ [52] and fracture is inhibited by the constraint of the surrounding material. In contrast, a tensile test involves uni-axial tension, unconstrained deformation, strain rates of approximately 10^{-3} s^{-1} and no inhibition of fracture.

2.4.1. Modes of material removal

2.4.1.1. *Brittle Erosion*

Glass and other brittle materials erode predominantly by the formation and intersection of subsurface cracks and involve very little plastic deformation. The particle erosion rate is a maximum at 90° impact where fracture processes are most efficient[53]. The two major crack systems are Hertzian cone cracking under elastic conditions for blunt erodent particles at low velocities and radial/median cracking and lateral cracking under elastic/plastic conditions for sharp particles at high velocities.

Finnie[54] analysed the formation of ring cracks by a steel sphere striking the surface of a glass specimen in terms of the Hertzian stresses that are developed. The Hertzian stresses have a maximum value in the radial direction around the periphery of the contact area and produce a ring crack which grows downwards and outwards as shown schematically in Figure 8. He suggests that in the early stages of particle erosion, each impact produces a ring crack which flares out beneath the surface. With further impacts the cracks interact and fragments of material are removed.

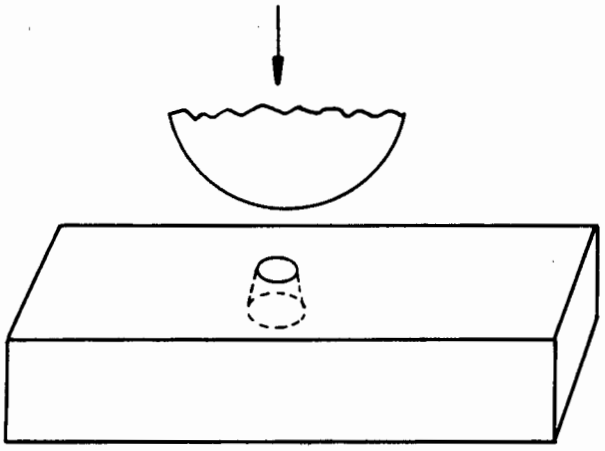

Figure 8. A schematic diagram of a Hertzian cone crack formed by the impact of a steel sphere against a glass specimen (after Finnie[54]).

The indentation loading cycle of a sharp indenter is described by Lawn[55] and is shown schematically in Figure 9. During the loading cycle the sharp indenter produces plastic deformation until the contact area is large enough to support the load. Subsurface radial or median cracks are produced by tensile stresses on median planes and propagate radially from the centre of the impact site as shown schematically in Figure 9. On unloading, the radial cracks close up and further unloading produces lateral cracks which propagate parallel to the surface of the target material. The intersection of lateral cracks with the surface produces saucer-shaped flakes of material which are subsequently removed and account for the major loss of material by erosion.

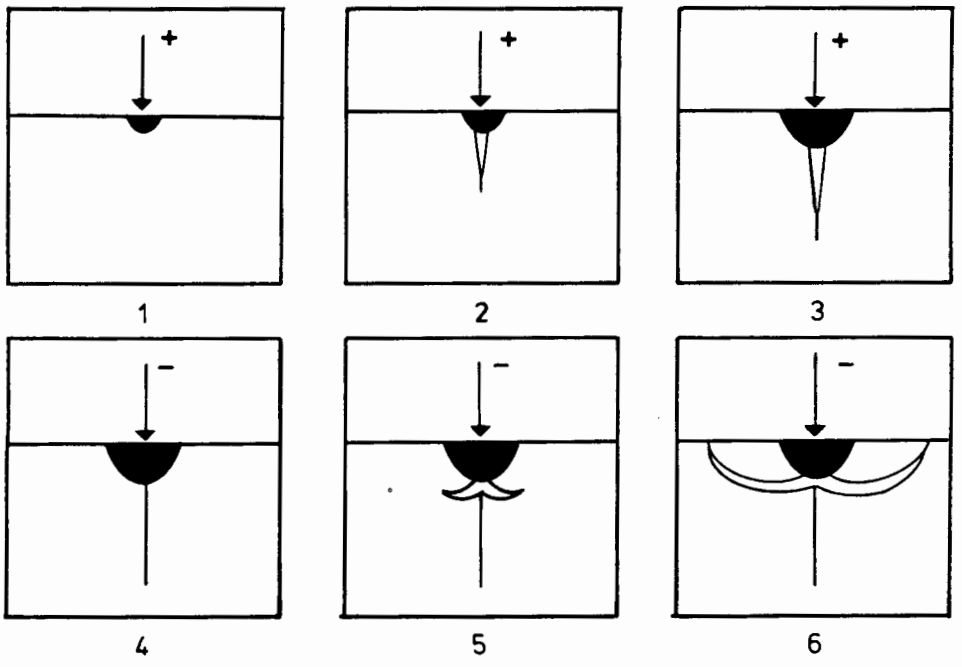

Figure 9. Sequence of schematic diagrams of the radial/median and lateral crack systems. Cross-sectional view of the formation of a radial crack during the loading cycle (+) and of the formation of lateral cracks during the unloading cycle (-). The dark region represents the zone of plastic deformation (after Lawn[55]).

2.4.1.2. *Ductile Erosion*

Ductile particle erosion is characterised by plastic deformation, maximum erosion rates at impact angles between 20° and 30° and material removal by ductile surface rupture. Ductile particle erosion involves substantial plastic deformation and strain accumulation which is localised around the impact site. Ives and Ruff[56] used selected area electron channelling to measure the compressive strains at single impact sites on copper and 310 austenitic stainless steel produced by angular Al_2O_3 and spherical glass particles approximately 50 μm in diameter travelling at a velocity of approximately 60 $m.s^{-1}$. Selected area electron channelling patterns were obtained from areas in and around the single impact craters and were used to measure the average compressive strain in these areas. A compressive strain of approximately 15 % was measured at single impact sites on copper by averaging the strain over a volume of approximately $10\mu m^3$ while the maximum strain was 37 % nearest the impact crater. Transmission electron microscopy observations of the impact craters on 310 stainless steel revealed a region of high dislocation density extending a few microns in each direction from the crater with a clear boundary between deformed and undeformed regions and deformation twins indicative of a high strain rate in some cases.

The platelet mechanism of particle erosion of ductile metals was proposed by Levy[57] based on numerous experimental observations. The mechanism involves erosion by the extrusion and forging of thin platelets in the form of lips or mounds of material on the edges of the impact craters. The platelets are knocked off the surface by ductile fracture after the accumulation of

substantial strain. It was observed that for several steels and aluminium alloys, greater ductility led to greater erosion resistance, because the ability to deform plastically and to absorb the kinetic energy of the impacting particle delayed the attainment of the fracture stress and limited material loss. There is a limit to the beneficial effect of increasing ductility; when ductility is increased at the expense of strength the material fractures under very small loads. An increase in hardness by prior work hardening results in an increase in erosion rate, although this correlation is in general not as reliable as that with ductility. A higher strain hardening exponent resulted in the earlier formation of the subsurface anvil against which material is forged and this leads to the earlier onset of steady state erosion.

Sundararajan[58] developed the model proposed by Sundararajan and Shewmon[59] for the solid particle erosion of ductile materials. The assumptions on which the model is based include that material loss is by extrusion and subsequent fracture of lip material, that the erosion rate is controlled by lip formation and that deformation is adiabatic. According to the model, work hardening below an impact site proceeds up to a critical strain after which strain softening occurs due to the temperature rise produced by the high strain rate deformation. Plastic flow is localised at strains higher than the critical strain and leads to lip formation, which controls the rate of material removal.

The possibility of local heating during particle impact at room temperature was considered by Hutchings and Levy[60]. Their model assumes a spherical impacting particle, a perfectly plastic target material which resists indentation with a constant indentation pressure and that all the kinetic energy of the impacting particle is imparted to the volume of the target material which is plastically deformed. The extent of local heating depends on the ability of the material to dissipate the energy imparted by the impacting particle. Adiabatic conditions prevail if the depth of the plastic zone (assumed to be equal to x_c, the depth of the indentation) is greater than the distance through which the heat produced by the impacting particle can diffuse during the course of the impact (i.e. the root mean square (r.m.s.) diffusion distance).

This is expressed by the ratio x_p / x_d where x_p is the depth of the plastic zone and x_d is the r. m. s. diffusion distance as shown in Figure 10(a). The r. m. s. diffusion distance depends on the thermal diffusivity of the material and the impact time[60]:

$x_d = \sqrt{(6kt_p)^{1/2}}$

where t_p is the impact time and k is the thermal diffusivity, given by the following equation:

$k = \lambda / (C_p\rho)$

where λ is the thermal conductivity ($W.m^{-1}.K^{-1}$), C_p the specific heat ($J.kg^{-1}.K^{-1}$) and ρ the density of the target material. The impact time, t_p, and the depth of the plastic zone, x_p, are given by the following expressions[61]:

$t_p = r\pi/2 \sqrt{(2\rho_e / 3P)^{1/2}}$

$x_p \approx rv \sqrt{(2\rho_e / 3P)^{1/2}}$

where r is the radius of the impacting particle, v is the particle velocity and P is the indentation pressure (Vickers hardness number x 10^{-2}). These derivations combine to give the following expression for the ratio of the depth of the plastic zone to the depth of the r. m. s. diffusion distance[60]:

$x_p / x_d = v(r/3\pi k)^{1/2} (2\rho_e / 3P)^{1/4}$.

The analysis of heating during single particle impact was extended to address the question of whether significant thermal reinforcement of the temperature rise caused by an impact can result from residual heat from earlier impacts[60]. This was evaluated by comparing the distance through which heat diffuses in the time between impacts on the same impact site with the dimensions of the impact site or depth of the plastic zone. During erosion, impact sites are produced at random over the exposed surface and give rise to an almost steady energy input into the surface. On this basis heat flow was assumed to be one dimensional (perpendicular to the eroded surface) as shown schematically in Figure 10(b). The following expression was derived for the ratio of the r.m.s. diffusion distance, x_i, to the radius of the impact site radius, a:

$x_i / a = (\pi k d^2 P / 8mrv^2)$;

where k is the thermal diffusivity of the target material, d is the diameter of the exposed surface, P is the indentation hardness of the target material, m is the particle feed rate, r is the particle radius and v is the particle velocity.

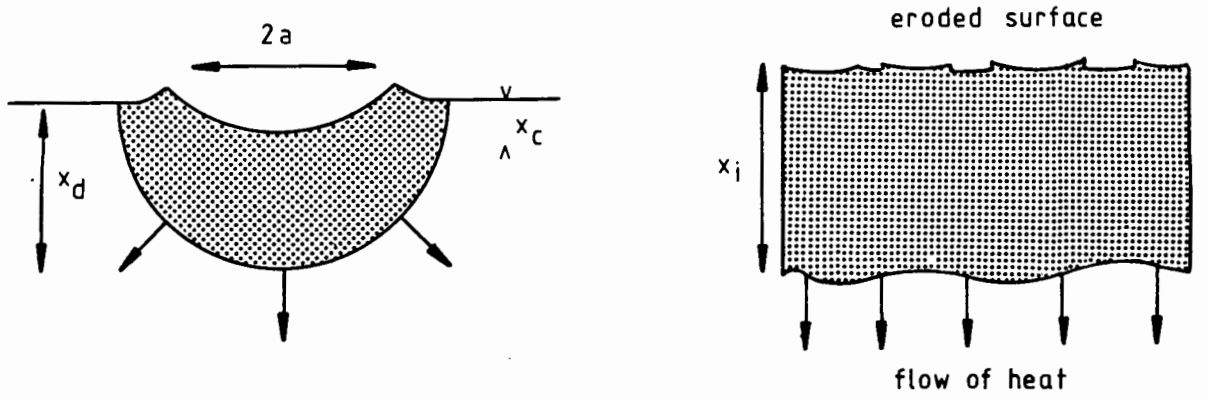

(a) (b)

Figure 10. (a) Schematic diagram of a single impact site of a spherical particle defining the root mean square diffusion distance, x_d the depth of the indentation, x_c, and the chordal radius, a. (b) Schematic diagram showing linear heat flow into the bulk from an eroded surface and defining the root mean square diffusion distance, x_i.

Doyle and Ball[62] applied the analysis of Hutchings and Levy[60] to the erosion of alumina, steel and ultrahigh molecular weight polyethylene by 100 μm SiC erodent particles at a feed rate of $0.1 g.s^{-1}$ travelling at 40 ms^{-1}. Figure 11 shows a plot of the isothermal-adiabatic boundary for various conditions of indentation hardness and target thermal diffusivity (after Doyle and Ball[62]) for their experimental conditions. A small indentation hardness and small thermal diffusivity, as for ultra high molecular weight polyethylene, are required for adiabatic conditions to prevail, as shown on Figure 11.

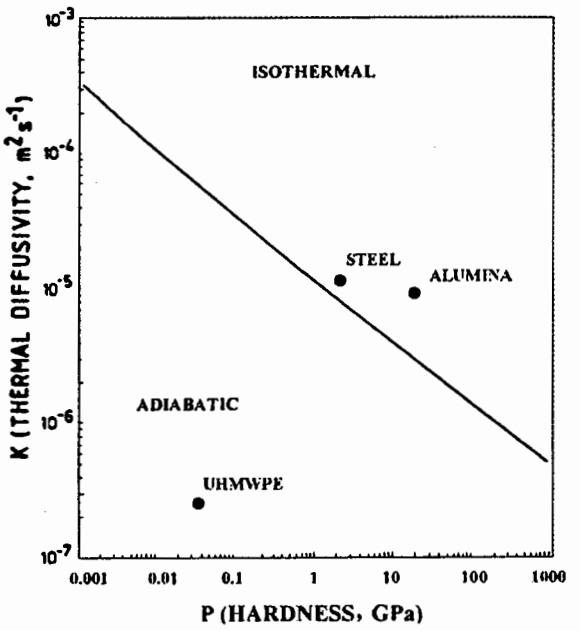

Figure 11. The isothermal-adiabatic boundary appropriate for the experimental conditions used for the various values of thermal diffusivity and hardness. The values for various materials are plotted on the diagram (after Doyle and Ball[62]).

Material removal during mainly single impact events was considered in a review by Field and Hutchings[52]. The mechanism of erosion depends strongly on the velocity of impact and a useful description of the velocity regime is the damage number, D, where $D = \rho V^2/Y$ (ρ= density, V = impact velocity and Y = yield stress for the target material). The regime of interest in most industrial environments is the "sub-ordnance" regime. The mean strain rate was modelled by Hutchings[63], assuming a constant plastic indentation pressure for spherical particles. For a typical erosion environment where particles are between 20 μm and 200 μm in size, and impact velocities lie between 10 $m.s^{-1}$ and 100 $m.s^{-1}$, the mean strain rates are in the range $10^5\ s^{-1}$ to $10^7\ s^{-1}$.

2.4.2. Particle Erosion of Intermetallic Alloys

Intermetallic materials behave like metals in particle erosion and exhibit greater deformation and higher erosion rates at oblique impact than at normal impact. Marquardt, Baker and Wert[64] studied the particle erosive wear of two long-range ordered (L.R.O.) alloys of the $(Fe, Co, Ni)_3V$ system (with $L1_2$ crystal structures), Ni-37.6Fe-22.4V-0.4Ti (wt.%) and Co-16.3Fe-22.2V-0.4Ti (wt.%), at room temperature and a particle velocity of 65 $m.s^{-1}$. 304L and 316 austenitic stainless steels and AISI 52100 steel were included for comparison.

The L.R.O. alloys[64] exhibited erosion rates at 90° and 30° impact which were similar to those for the 304L and 316 austenitic stainless steels. The 90° particle erosion rates were an order of magnitude less than those at 30° impact and the single impact sites were smaller at 90° impact than at 30° impact for all the experimental materials. The effect of hardness on particle erosion rate was observed at 30° impact, but not as clearly at 90° impact. At 30° impact, 52100 steel with the highest hardness, exhibited a slightly higher particle erosion rate than the other materials and 316 stainless steel, with the lowest hardness, exhibited the lowest particle erosion rate. The particle eroded surface of 52100 steel contained only a small amount of deformation at 30° impact; in contrast the eroded surface of 304 stainless steel exhibited extensive ploughing deformation at 30° impact. The greater ploughing deformation on the softer surfaces absorbed more particle impact energy and resulted in lower erosion rates than those for the harder materials.

The Knoop microhardness of the materials was measured before and after particle erosion[64] and one of the L.R.O. alloys, Ni-37.6Fe-22.4V-0.4Ti (wt.%), showed greater work hardening than the other materials, while Co-16.3Fe-22.2V-0.4Ti (wt.%) exhibited similar hardening to the austenitic stainless steels.

2.4.3. High Temperature Particle Erosion

Gat and Tabakoff[65] investigated the influence of temperature (25°C < T < 200°C) on the particle erosion performance of Ti-6Al-4V (wt.%), 2024 aluminium and 410 ferritic stainless steel using a quartz sand erodent (138 μm -164 μm), impact velocities of 116 $m.s^{-1}$ - 125 $m.s^{-1}$ and impact angles of 20°, 60° and 90°. At 20° impact, the erosion rates of all three materials decreased between room temperature and 200°C, with 410 stainless steel exhibiting a much smaller difference compared to the other materials. A second set of tests was performed with lead at an homologous temperature (HT) > 0.5, ductile tantalum with HT < 0.1 (DBTT = -195 °C) and brittle tungsten with HT < 0.1 (DBTT = 427°C). At 20° impact, the erosion rate of lead increased dramatically with increasing temperature; tantalum showed a slight increase and tungsten showed a dramatic decrease with increased temperature. The factors involved in the temperature dependence of erosion were divided into Type I, i.e. those which cause a decrease in the energy required to remove material as temperature increases and Type II which have the opposite effect. Type I factors include a decrease in mechanical strength, Young's modulus and work hardening. Type II factors include an increase in ductility. Erosion rate (cm^3/g) was plotted against the homologous temperature for the six materials at 20°, 60° and 90° impact. For lead, with 0.5 < H.T. < 0.7, no cold work was observed and the erosion rate increased with increasing temperature at all impact angles. For tungsten (H.T. < 0.1, D.B.T.T. = 427°C), tested at 60° and 90° impact, the erosion rate decreased with increasing temperature due to the decrease in ductility. Tantalum (H.T. < 0.15, D.B.T.T. = -195°C) exhibited a weak temperature dependence at all impact angles

because of the competing effects of Type I and Type II factors. The homologous temperature scale was recommended for investigating the influence of temperature on erosion rate. It was found that erosion decreases as temperature increases at a range of H.T. < 0.2 and increases for H.T. > 0.5.

Zhou and Bahadur[66] studied the erosion-corrosion behaviour of annealed Ti-6Al-4V (wt.%) in an air-blast type rig at eight different temperatures between 25°C and 800°C. Specimens were eroded at velocities between 55 $m.s^{-1}$ and 110 $m.s^{-1}$ and impingement angles between 10° and 90° using 120 grit SiC particles. Specimens were tested in the annealed and precipitation hardened conditions. At 30° impact and 65 $m.s^{-1}$, three distinct ranges of behaviour were identified between room temperature and 800°C. The erosion rates were not significantly different between room temperature and 200°C. This was ascribed to the competing effects of a decrease of strength and an increase in ductility over this temperature range. Between 200°C and 650°C, the erosion rate increased moderately with increasing temperature and strength and ductility both decreased in this range. Ti-6Al-4V (wt.%) was also tested in the aged condition (at temperatures below 550°C) and exhibited similar erosion rates and variation in erosion rates with temperature as the annealed material. Above 650°C, oxide formation led to rapid erosion and a dramatic increase in erosion rate. Furthermore, the annealed material was tested at normal impact and showed a similar variation in erosion rate with temperature up to 650°C and a much larger increase above 650°C because of the more efficient removal by spallation of the oxide than by cutting at oblique impact. Oxide growth experiments showed that significant oxidation occurred above 650°C. Below this temperature nucleation and growth rates were very slow and oxides were small and sparse and unlikely to affect erosion.

2.5. Cavitation Erosion

2.5.1. Introduction

Cavitation can occur in any fluid system in which there is a cyclic pressure fluctuation. During cavitation erosion, high stresses varying from 100 MPa-1000 MPa are produced by the implosion of cavities against surfaces[67]. These high stresses can cause severe plastic deformation, strain accumulation, crack propagation and subsequent material loss. Since the cavitation erosion conditions involve large stresses and high strain rates, no simple correlation exists between mechanical properties measured in conventional low strain rate tests and cavitation erosion performance.

Twins, microtwins and martensite formation in metallic materials are favoured in the high strain rate conditions of shock loading (strain rate : 10^5s^{-1}-$10^{10}s^{-1}$) and cavitation erosion (strain rate : 10^{-4}-10^6s^{-1})[67]. These planar defects are more favoured in low stacking fault energy (S.F.E.) materials and these materials generally exhibit superior cavitation erosion performance. Low S.F.E. aids martensite formation and twinning and leads to a higher work hardening rate because of the difficulty of cross slip and the resulting dislocation pile up which increases the stress required for further strain.

Woodford[68] investigated cavitation erosion performance of Stellite 6B and several transformation-induced plasticity (T.R.I.P.) steels and the effect of ageing on the performance of Stellite 6B. He failed to find a simple correlation between the percentage transformation in Stellite 6B and cavitation erosion resistance, however the transformable alloys generally showed better cavitation erosion resistance than the non-transformable materials and it was concluded that lower S.F.E. contributes to cavitation erosion resistance.

Heathcock, Protheroe and Ball[69] investigated the cavitation erosion performance of a large number of engineering materials using standard vibratory equipment. The materials included polymers, metals, hardmetals and a NiTi shape-memory intermetallic compound, Ni-51Ti (at.%). Ductile and brittle failure and preferential removal of the hard reinforcement in the hardmetals were identified as modes of material removal. Stellites, 304 stainless steel, lightly tempered carbon steel and Ni-51Ti (at.%) intermetallic showed superior resistance. Their superior performance was explained in terms of their ability to accommodate fatigue-like strain and to limit dislocation build-up by undergoing a stress-induced phase transformation. The fine lath-like transformation product also improved the fracture toughness and cavitation erosion resistance by inhibiting the propagation of microcracks which lead to material loss. The brittle failure of body-centred cubic (b.c.c.)-structure metals, 409 and 430 ferritic stainless steels, was attributed to the increase in yield stress and brittle behaviour of b.c.c. materials at high strain rates.

Factors which promote resistance to cavitation erosion were identified as follows[69]: (i) a high work hardening rate, (ii) a high starting hardness or yield strength and (iii) a stress-induced phase transformation which accommodates the imposed strain and delays fracture to higher stress levels.

The importance of a high work-hardening in providing wear resistance was postulated by Ball[70] as follows. Material removal during erosive and abrasive wear occurs once a critical strain for fracture is attained, consequently a material which delays the attainment of the critical strain for fracture will exhibit superior wear resistance. The response of three types of materials to a mean applied stress of erosive or abrasive wear were considered. Firstly, in materials with a large strain to fracture but low strength, a small amount of wear will stress the material beyond its yield strength and result in a strain greater than the critical strain for fracture. Secondly, high strength materials that exhibit only elastic deformation are susceptible to sudden fracture at stress raising inhomogeneities within the material. Thirdly, a material of intermediate strength and ductility, but possessing a high work hardening rate requires increasing amounts of stress to cause a given amount of strain as wear proceeds, thereby delaying the attainment of the critical strain for fracture to a higher stress and imparting superior wear resistance.

Richman and McNaughton[71] compared the fatigue performance and stacking fault energy of a range of metals and alloys with their cavitation erosion performance. The best correlation was found between cavitation resistance and the product of the fatigue strength coefficient, σ_f ', and the cyclic strain hardening exponent, n'. Further, a good correlation was found between stacking fault energy and the product, σ_f 'n', with low stacking fault energy promoting fatigue resistance and cavitation erosion resistance.

2.5.2. Damage Initiation

Karimi and Avellan[72] observed the initiation of vibratory cavitation erosion damage at the grain boundaries of an $\alpha + \beta$ brass. The initial damage was followed by more homogenous deformation of the exposed surface and the preferential removal of the β phase. Their study involved the comparison of flow cavitation, using a Francis turbine, a water tunnel and a vortex cavitation generator and vibratory cavitation using an ultrasonic generator fitted with a magnetostrictive exponential horn. They found that the vibratory cavitation device was unique in its ability to produce damage which was initially spread over the exposed surface, compared to the isolated damage which was produced by flow cavitation.

Richman and Rao[73] investigated the early stages of cavitation damage of cast and wrought structural alloys and weldments using vibratory apparatus and related these to microstructural features. Grains and pearlite colonies were delineated on AISI steel (0.2 % C, 1.0 % Mn) after 5 minutes of cavitation and small pits were formed, especially at grain boundaries. The cast

disordered material which favoured crack nucleation. Johnson, Nikkola,

tested the abrasion and cavitation erosion resistance of alloys based on Ni_3Al (alloyed with boron to promote room temperature ductility) and Fe_3Al. Volume loss rates of nickel aluminides were appreciably less than for 304 stainless steel, while fine-grained powder metallurgy material had lower volume loss rates than cast nickel aluminides. The nickel aluminides exhibited lower erosion rates than the Stellite 21 weld overlay tested in the same conditions.

Okada and Hattori[81] investigated the cavitation erosion performance of cast Ti-50Al (at.%) and Ti-48Al (at.%) and of hot isostatically pressed (H.I.P.) specimens of the same compositions. Pure titanium and austenitic stainless steels, 304 and 316, were tested for comparison with the titanium aluminides. The cavitation erosion rate of each material was expressed as the mean depth of penetration rate (M.D.P.R.), i. e. volume loss/ (time x exposed surface area). The steady state erosion rates of the titanium aluminides were 20 to 30 times lower than those for pure titanium and the austenitic stainless steels.

Surface profiles were obtained from the polished specimens of cast and H.I.P. titanium aluminides and from pure titanium before and after cavitation erosion[81]. The heights of the five highest surface asperities were averaged for each surface profile and the average values were plotted as a function of time of cavitation erosion for each material. These graphs and micrographs of the surfaces after erosion showed that pure titanium developed larger asperities than the titanium aluminides after the same amount of cavitation erosion and the sintered materials developed smaller asperities than the cast materials after the same amount of erosion. Material was removed preferentially from these asperities.

The Vickers (200 gf) hardness of each specimen increased after exposure to cavitation erosion[81]. Pure titanium showed only a small (approximately 20%) increase in hardness after the completion of the steady state test. Cast Ti-48Al (at.%) increased in hardness from 310 VHN before cavitation erosion to 450 VHN (approximately 45%) after one hour and remained at this value with increasing time until the completion of the test. The hardness of cast Ti-50Al (at.%) increased from a starting value of 327 VHN to between 700 VHN and 750 VHN after 4 hours and remained at this level until the completion of the test. The hardness of the H.I.P. Ti-50Al (at.%) and Ti-48Al (at.%) specimens increased from 327 VHN and 367 VHN respectively to values between 700 VHN and 750 VHN.

The cavitation erosion resistance (1 / M.D.P.R.) of each material was plotted as a function of VHN^2/E, where VHN = Vickers (200 gf) hardness after cavitation and E = Young's modulus[81]. The cavitation erosion resistance was directly proportional to VHN^2/E and the superior performance of the titanium aluminides was ascribed to their work hardening ability.

2.6. Overview

Ti_3Al-based and TiAl-based titanium aluminides have received considerable attention over the last 30 years. Consequently, their microstructural characteristics and mechanical behaviour are relatively well understood. For Ti_3Al-based alloys, superior strength, toughness and ductility are promoted by a fine transformed matrix which is distributed so as to avoid α_2/α_2 grain contact. Ti_3Al-based alloys generally exhibit greater ductility and toughness than TiAl-based alloys.

In particle erosion, Marquardt et al.[64] found that $(Fe, Co, Ni)_3V$ intermetallics behave like ductile metals during particle erosion. In cavitation erosion, the outstanding performance of NiTi and TiAl-based titanium aluminides intermetallic alloys have been ascribed to their high work hardening rates.

3. MATERIALS AND EXPERIMENTAL METHODS

3.1. Materials

The titanium aluminide alloys investigated consisted of the Ti_3Al-based alloy, Ti-25Al-10Nb-3V-1Mo (at.%) and the TiAl-based alloys with nominal compositions Ti-52Al (at. %) and Ti-48Al-2Mn-2Nb (at.%).

Ti-25Al-10Nb-3V-1Mo (at.%) was supplied by *R. M. I. Titanium* in the hot rolled and annealed (980°C for 1 hour and air cooled) condition, termed the "as received" condition in this thesis. The mechanical properties supplied by the producer are shown in Table 3 and the composition of the experimental material in weight percent was given nominally as Ti-14Al-20Nb-3V-2Mo.

Table 3. Mechanical property data supplied by the producer of Ti-25Al-10Nb-3V-1Mo (at.%), *R. M. I. Titanium.* A range of values is shown for each property.

Test Temperature		25°C	650°C
Mechanical Properties	Longitudinal/ Transverse		
Ultimate tensile strength (MPa)	L	1016-1036	888-943
	T	1150-1151	929-1025
0.2% proof strength (MPa)	L	898-927	713-734
	T	1094-1101	776-954
% Elongation	L	4	6-7
	T	1	6
% Area reduction	L	4-8	7-21
	T	2	7-10
Young's modulus (GPa)	L	104-108	99-107
	T	112	97-99

Ti-52Al (at.%) and Ti-48Al-2Mn-2Nb (at.%) were plasma-arc-melted at the *Interdisciplinary Research Centre in Materials for High Performance Applications*, University of Birmingham and were received in the as cast condition. The bottom end of an ingot of Ti-52Al (at.%) and a disc of Ti-48Al-2Mn-2Nb (at.%) cut from an ingot, both 95 mm in diameter, were received.

Values obtained from the scientific literature[37] for selected room temperature mechanical properties of TiAl-based alloys are shown in Table 4.

Table 4. Mechanical properties of TiAl-based titanium aluminide alloys[37]. A range of values is shown for each property.

Property	Value
Density (g/cm^3)	3.7 - 3.9
Elongation (%)	1 - 3
Yield strength (MPa)	400 - 630
Tensile strength (MPa)	450 - 700
E modulus (MPa)	160 - 176

The following materials were selected for comparative testing: 304 stainless steel, a WC-15Co (wt.%) hardmetal, an extruded aluminium alloy 6261 and soda-lime-silica glass. The 304 stainless steel was received as 16mm extruded rod and the WC-15Co (wt.%) hardmetal was supplied by *Boart Hardmetals* in the hot-isostatically-pressed and sintered condition. The aluminium alloy was received as 12.7 mm diameter extruded bar and was annealed in a laboratory air chamber furnace to remove the effects of working. Glass specimens were cut from 1 mm thick soda-lime-silica glass mounting slides which are free of macroscopic flaws.

3.2. Specimen orientation

3.2.1. Ti-25Al-10Nb-3V-1Mo (at.%)

The orientation and position relative to the orientation of the plate of the Ti-25Al-10Nb-3V-1Mo (at.%) specimens for particle erosion and cavitation erosion are shown in Figure 12.

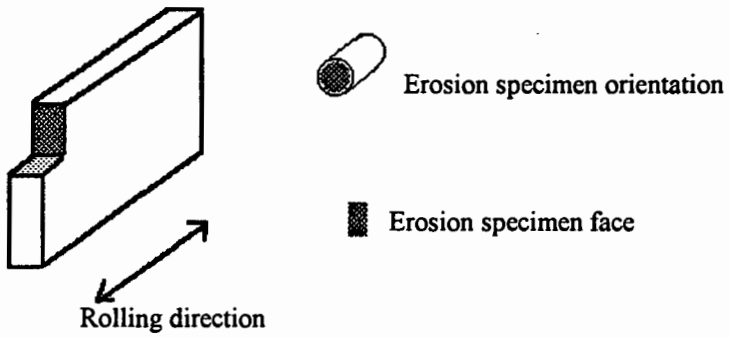

Figure 12. Rolling direction, specimen orientation and position on the hot rolled Ti-25Al-10Nb-3V-1Mo (at.%) plate. Tensile specimens were oriented parallel to the rolling direction.

3.2.2. Ti-52Al (at.%) and Ti-48Al-2Mn-2Nb (at.%)

Specimens of Ti-52Al (at.%) and Ti-48Al-2Mn-2Nb (at.%) for erosion testing were electro-discharge machined from the discs of plasma-arc-melted material using a withdrawable wire electrode. The faces of the coupon specimens were in the orientation transverse to the length of the ingot as shown in Figure 13. In addition to the coupon specimens, a rectangular specimen was cut from the edge of the Ti-48Al-2Mn-2Nb (at.%) disc using a water fed abrasive cut-off wheel, such that the face was oriented parallel to the length of the ingot as shown in Figure 13.

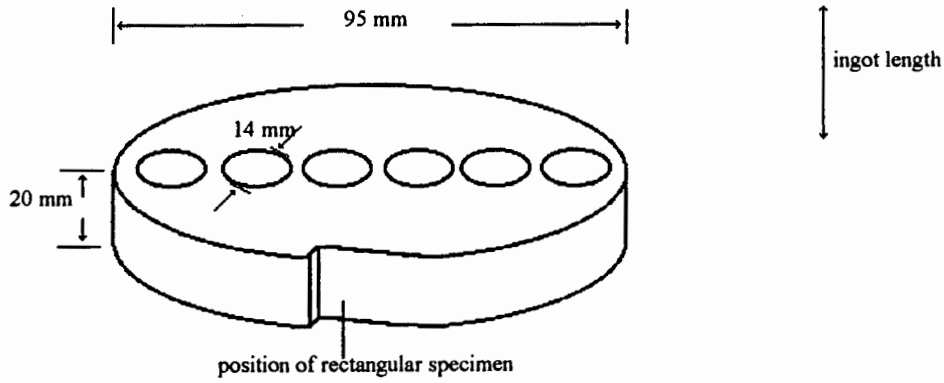

Figure 13. A disc machined from an ingot of plasma-arc-melted Ti-48Al-2Mn-2Nb (at.%) showing the disc-shaped coupon specimens and the position of the rectangular specimen which was machined from the side of the ingot.

3.3. Heat treatment

3.3.1. Ti-25Al-10Nb-3V-1Mo (at.%)

Specimens of as received Ti-25Al-10Nb-3V-1Mo (at.%) were annealed at 700°C, 800°C, 900°C, 950°C and 1000°C for twenty four hours followed by quenching into water. In addition, specimens were solution treated at 1060°C for one hour and air cooled and subsequently aged at 650°C, 850°C and 950° C for two hours followed by air cooling.

3.3.2. Ti-52Al (at.%) and Ti-48Al-2Mn-2Nb (at.%)

Ti-52Al (at.%) and Ti-48Al-2Mn-2Nb (at.%) were homogenized at 1380°C within the single phase α field for one hour followed by furnace cooling at 200°C/hour. The furnace took 5 hours to reach 1380°C. Ti-48Al-2Mn-2Nb (at.%) was heat treated at 1200°C for 4 hours followed by air cooling.

3.4. Microscopy

Optical microscopy was performed using a *Reichert MeF3A* metallurgical microscope.

A *Cambridge S200* scanning electron microscope with a *Tracor Northern TN5400* energy dispersive x-ray microanalysis system and back scattered electron detector was used for microstructural examination, standardless semi-quantitative (S.S.Q.) energy dispersive x-ray spectroscopy (E.D.S.) analysis and the examination of particle eroded and cavitation eroded surfaces.

Transmission electron microscopy was carried out on a *Jeol 200CX* at an accelerating voltage of 200 keV using a double tilt specimen holder, to determine whether or not the β phase in as received Ti-25Al-10Nb-3V-1Mo (at.%) was ordered B2 or disordered. Bright and dark field images and selected area electron diffraction patterns were obtained from the α_2 phase and the β phase.

Three millimetre discs for T.E.M. were punched from a slice of material machined to a thickness of approximately 1 mm. The discs were then mechanically ground on 1200 grit SiC paper in order to obtain a disc thickness of approximately 100μm. The discs were jet polished with a *Struers Tenupol 3* with a polishing solution consisting of 2% perchloric acid, 36% n-butyl alcohol and 62% methanol[82] at an applied potential of 35 V and a current of 50 mA. The solution was cooled to -30°C using a mixture of alcohol and dry ice.

A homogenized Ti-52Al (at.%) specimen was cavitation eroded for 10 minutes and then machined to a thickness of approximately 1 mm. Three millimetre discs were punched from the specimen and the uneroded surfaces were mechanically ground to reduce the thickness of the discs to approximately 100 μm. The uneroded surface of each disc was jet polished and the eroded surface was protected with a plastic covering.

3.4.1. Microstructure examination

Optical and scanning electron microscopy were used to examine the microstructures of the titanium aluminides. Dip etching was performed with Keller's reagent, i. e. 2.5 ml nitric acid, 1.5 ml 36% hydrochloric acid, 1 ml (40%) hydroflouric acid and 95 ml distilled water for approximately 15 seconds. Other etchants were used to etch Ti-52Al (at.%) and Ti-48Al-2Mn-2Nb (at.%) since hydroflouric acid can produce groove-like artefacts[83] on γ alloys, but the use of these etchants met with very limited success.

Where compositional differences between phases were substantial, the detection of back-scattered electrons and/or a mixed signal of secondary electrons and back-scattered electrons produced atomic number contrast on a polished (unetched) surface.

The parameters shown in Table 5 were used for all the S.S.Q. analyses. The detector distance is defined as the straight line distance between the detector window and the incident electron beam.

Table 5. Standardless semi-quantitative energy dispersive x-ray analysis parameters.

Parameter	Value
Accelerating voltage (kV)	20
Specimen tilt (degrees)	20°
Working distance (mm)	25
Detector distance (mm)	82
Compensated take off angle (degrees)	51.2°

3.4.2. Erosion specimen examination

Extensive use was made of the scanning electron microscope (S.E.M.) to examine specimens after single impact particle erosion, light cavitation erosion and steady state particle erosion and cavitation erosion. Most often, a secondary electron signal was detected to produce images of the eroded surfaces; however, a mixed secondary electron and back-scattered electron signal was occasionally used to reduce topographical contrast and to simultaneously examine erosion damage and microstructural features on lightly eroded surfaces.

3.5. Tensile testing

The tensile stress-strain behaviour of as received Ti-25Al-10Nb-3V-1Mo and 304 stainless steel were determined by conducting uni-axial tensile tests to failure on a *Zwick 1484 Universal Testing Machine* at a strain rate of 10^{-4} s^{-1} and using three specimens of each material. Standard round Hounsfield test pieces were used as shown in Figure 14.

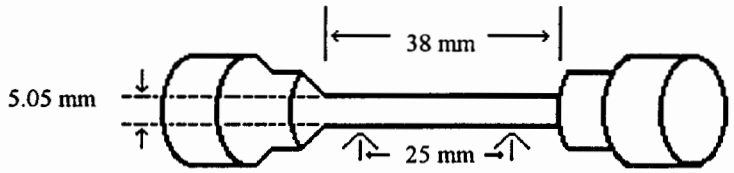

Figure 14. Drawing of the Hounsfield round tensile specimens used for uni-axial tensile tests on Ti-25Al-10Nb-3V-1Mo (at.%) and 304 stainless steel. The gauge length was 25 mm and the length of the total reduced section was 38 mm. The specimen diameter was 5.05 mm.

The reduced section was extended from the standard 28.2 mm to 38 mm to allow adequate space for the extensometer arms which were separated by 25 mm, i.e. the gauge length at the start of each test. The tensile specimens were machined so that the gauge length was parallel to the rolling direction for Ti-25Al-10Nb-3V-1Mo (at.%) and parallel to the length of the extruded 304 stainless steel rod. The gauge length of the specimens was mechanically polished before testing to a 0.25 μ m finish to remove grinding marks. Scanning electron microscopy was employed to establish the tensile fracture mode of the Ti-25Al-10Nb-3V-1Mo (at.%) specimen.

23.5.1. Work hardening rate calculations

The true stress-true strain curves were derived with the aid of a computer spreadsheet package using the equations:

$$\varepsilon_t = \ln(1+\varepsilon_n); \qquad \sigma_t = \sigma_n(1+\varepsilon_n)$$

where ε_t and σ_t are the true strain and true stress and ε_n and σ_n are engineering strain and engineering stress respectively.

The work hardening rate, $d\sigma_t / d\varepsilon_t$, was calculated using every 17th data point (ε_t; σ_t) for Ti-25Al-10Nb-3V-1Mo (at.%) and every 47th data point (ε_t; σ_t) for 304 stainless steel in order to reduce the scatter which was produced by using every data point.

The following equation was used to calculate the work hardening rate[84]:

$$d\sigma_t / d\varepsilon_t = \sum \varepsilon_t.\sigma_t - n\varepsilon_t'.\sigma_t' \; / \; \sum \varepsilon_t^2 - n\varepsilon_t'^2$$

where ε_t' and σ_t' are average values for ε_t and σ_t respectively and n is the number of data points (ε_t; σ_t) over which the averages are taken.

Each value of $d\sigma_t / d\varepsilon_t$ was plotted against the value of ε_t lying in the middle of the group of 17 data points used in the calculation of the particular $d\sigma_t / d\varepsilon_t$ value, i. e. the 9th value.

3.6. Compression testing

Uni-axial compression tests were conducted with the *Zwick 1484 Universal Testing Machine* at a strain rate of 10^{-4}/s on cylindrical and near-cylindrical specimens of as received Ti-25Al-10Nb-3V-1Mo (at.%) in order to compare deformation markings with those produced by cavitation and particle erosion. The gauge length of the cylindrical specimen and the flat side of the near-cylindrical specimen were polished to a 0.25 μm finish prior to testing to facilitate examination of the deformation markings produced by compression. The dimensions of the compression specimens are shown in Figure 15.

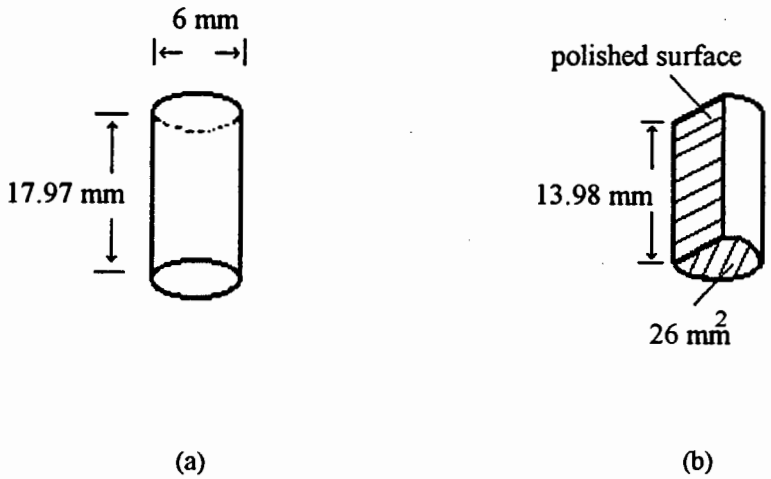

Figure 15. Drawings of the cylindrical and near-cylindrical compression specimens of as received Ti-25Al-10Nb-3V-1Mo (at.%). The specimens were machined so that their lengths were parallel to the rolling direction.

The cylindrical specimen was compressed to approximately 0.8 % strain and the polished gauge length was inspected for macroscopic deformation markings. The near-cylindrical specimen was compressed to approximately 3 % strain and the flat polished surface was examined with the

S.E.M. for evidence of microscopic deformation markings. Thereafter the specimen was etched with Kellers reagent and the microscopic deformation markings were examined in relation to the microstructure. The near-cylindrical specimen was further compressed to failure and the gauge length and fracture surface were examined with the S.E.M.

3.7. Solid particle erosion

3.7.1. Room temperature particle erosion apparatus

Solid particle erosion tests were performed using a conventional air blast rig. Before each test the specimen was polished to a 0.25 μm finish, ultrasonically cleaned and weighed. The angular SiC erodent particles (120 grit) had an average diameter of 100 μm. The particles travelled at 40 m/s and eroded the polished (0.25 μm finish) specimens at a 90° or 30° angle of impact. The test parameters are summarised in Table 6. The erodent particles are angular and typically possess the features shown in Figure 18. The pressure of the incoming air stream to achieve an average particle velocity of 40 $m.s^{-1}$ was measured as 270 kPa using the double rotating disc method[85]. The erosion rate, measured as mass loss per mass of erodent particles, was obtained by repeatedly measuring the mass loss of the target after erosion by a fixed mass of erodent. The erosion rate of each material was expressed as a volume loss per mass of erodent (cm^3/g) to facilitate comparison of materials with different densities.

Table 6. Summary of test parameters for the room temperature particle erosion apparatus.

Parameters	Values
Acceleration tube length	3 m
Acceleration tube diameter	10 mm
Compressed air pressure	270 kPa
Impact angles	90°, 30°
Particle velocity	40 $m.s^{-1}$
Erodent particle type	120 grit SiC
Specimen stand-off distance	30 mm
Exposed target area	50.3 mm^2
Feed rate	0.17 $g.s^{-1}$

A specimen holder which exposed a circular area of 8 mm diameter was used. This necessitated the normalisation of the erosion rates since some of the erodent particles strike the holder rather than the specimen and the number of particles striking the surface decreases as the angle of erosion decreases. In order to calculate a true erosion rate as the ratio of volume of material lost to mass

of erodent used, the amount of erodent striking the surface must be known for each erosion angle. The correction factor was determined from the ratio of erosion rate of the completely exposed specimen to the erosion rate of the partially covered specimen (in a holder). Each measured erosion rate was multiplied by the correction factor to give a normalised rate.

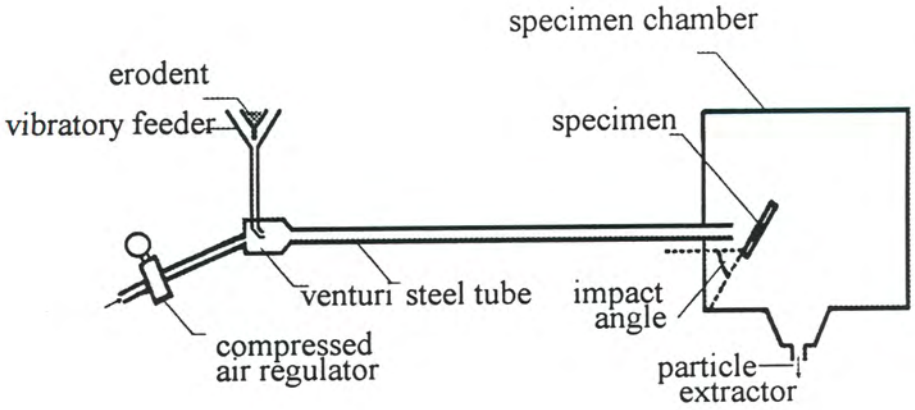

Figure 16. Drawing of the room temperature solid particle erosion apparatus.

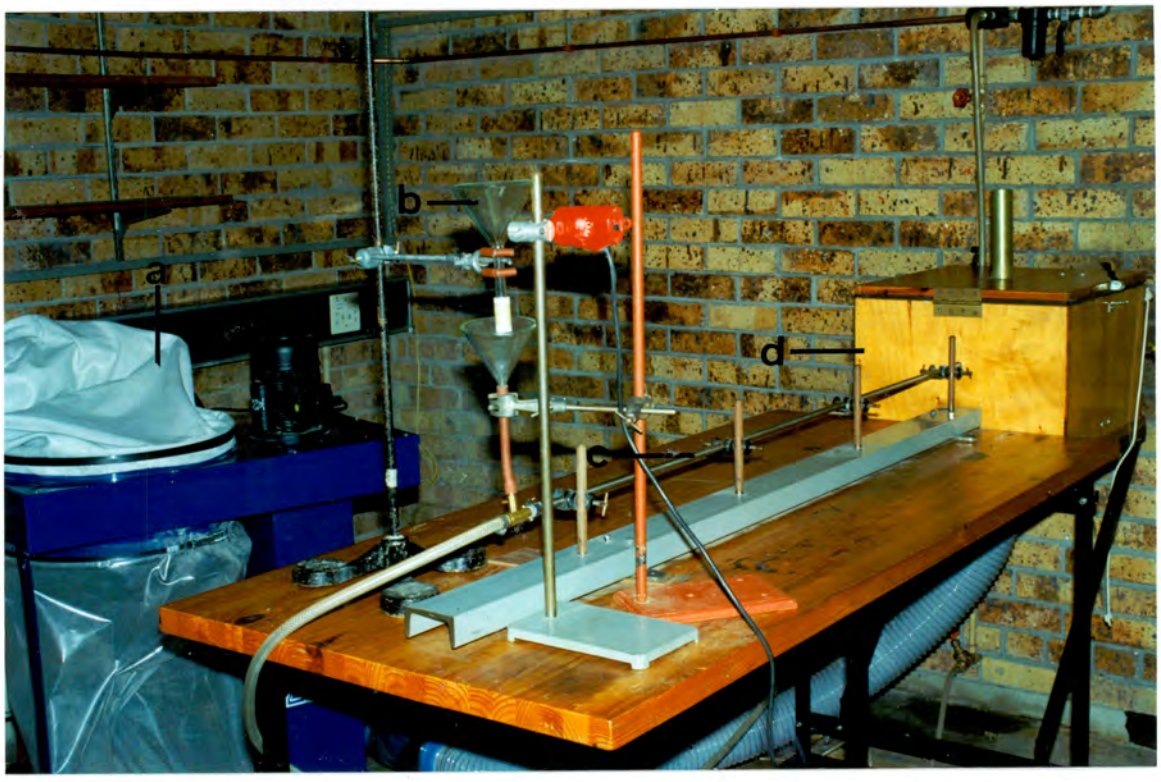

Figure 17. Photograph of the room temperature solid particle erosion apparatus showing the particle extractor (a), the vibratory feeder (b), the acceleration tube (c) and the specimen chamber (d).

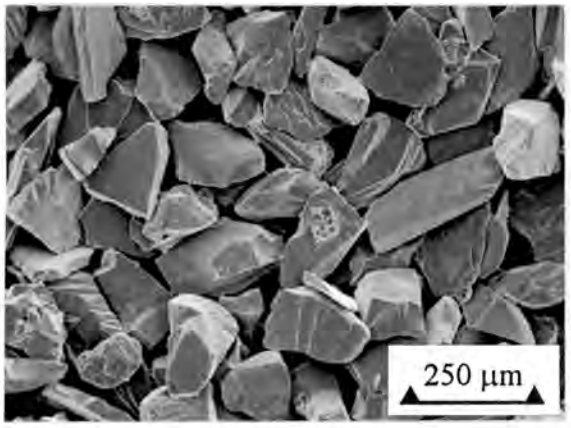

(a)

(b)

Figure 18. Micrograph showing 120 grit SiC erodent particles. (a) The erodent particles are angular and are approximately 100 μm in width. (b) The surfaces of the particles exhibit fracture steps.

3.7.2. High temperature particle erosion apparatus

Particle erosion tests were performed at room temperature, 300°C and 500°C using a high temperature apparatus for testing boiler tube materials[86] as shown in Figure 19.

The operation of the equipment was as follows. Compressed air was fed into a preheating chamber to heat the air to approximately 90°C. A venturi immediately below the chamber allowed particles from a hopper to be introduced into the air stream. The air/erodent mixture was directed through a vertical acceleration tube surrounded by ducting. A liquid petroleum gas (L.P.G.) flame was aimed into the duct to maintain the temperature of the acceleration tube at the desired temperature and to heat the air/erodent mixture. The specimen was held 30 mm from the end of the acceleration tube in a specimen holder attached to the specimen chamber cover. After striking the specimen, the air/ erodent mixture passed through a heat exchanger where it was cooled to 105°C. The erodent particles were recovered by a cyclone separator and the air passed through an exhaust duct of large surface area so as to reduce the temperature further before exit. Thermocouples were mounted at strategic locations on the apparatus, including on the side of the specimen and the temperature was monitored throughout each test.

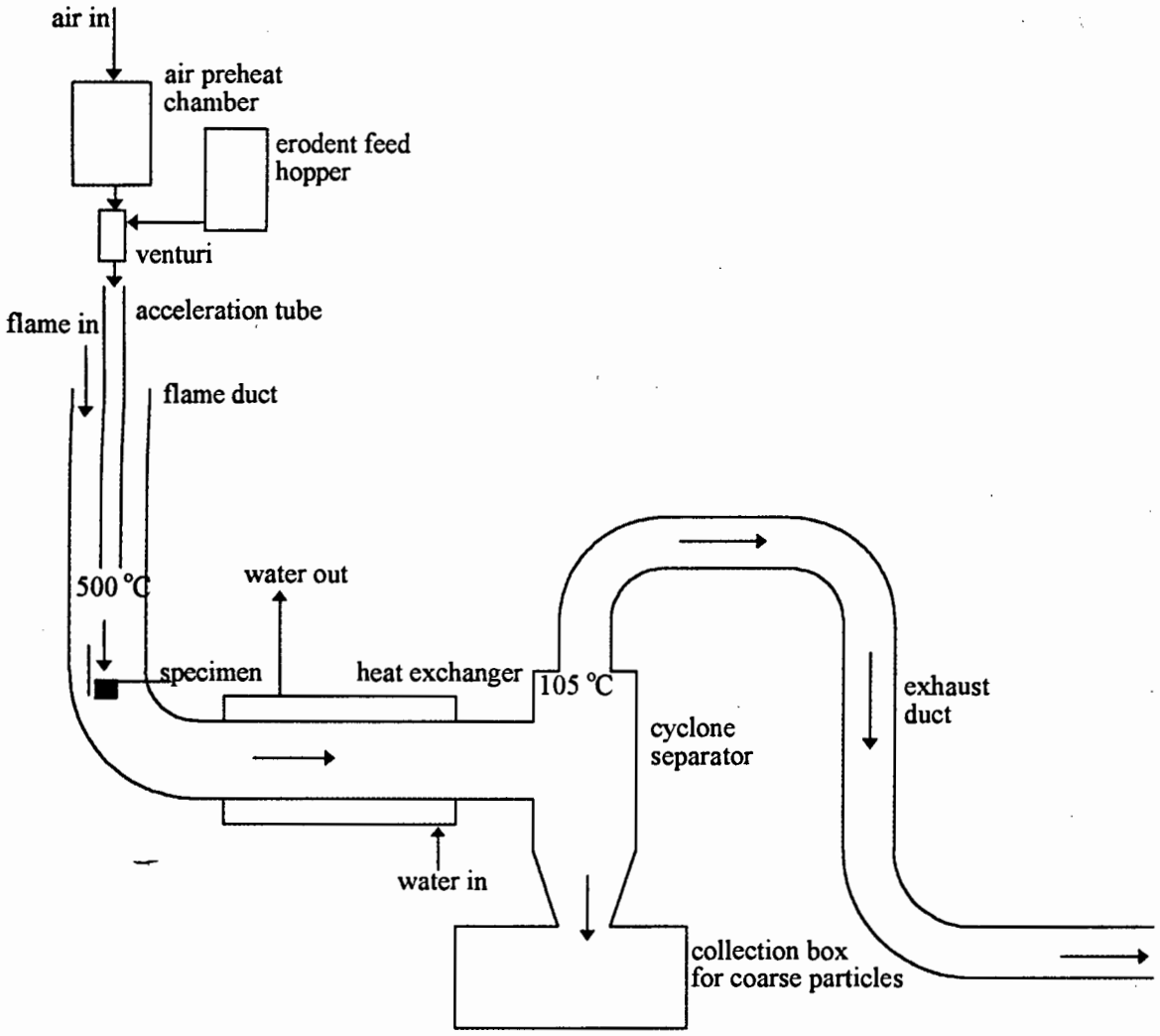

Figure 19. Particle erosion apparatus designed for testing boiler tube materials at temperatures up to 600°C[86].

The test procedure was as follows. A specimen was polished to a 0.25 μm finish, ultrasonically cleaned and weighed. It was loaded into the holder and the holder was mounted in the specimen chamber. The compressed air pressure was set to 140 kPa. For tests at 300°C and 500°C, the L.P.G. supply pressure was maintained at approximately 75 kPa and 170 kPa for temperatures of 300 ± 10°C and 500 ± 10°C respectively. Once the temperature, monitored with a thermocouple against the rear of the specimen, had stabilised (i.e. after 10 minutes) 30 g of erodent was fed into the acceleration tube through the hopper at a feed rate of 0.17 g/s. The feed rate was monitored by recording the time taken for each 30g erodent dosage. After each test the compressed air pressure was decreased to 80 kPa and the L.P.G. supply valve was closed. The elevated temperature specimens were allowed to cool to 140°C before removal from the specimen chamber. Further cooling to room temperature outside the holder was followed by ultrasonic cleaning in ethanol, drying and weighing. The test parameters for particle erosion tests with the high temperature rig are summarised in Table 7. Particle erosion rates were normalised to account for the particles which strike the holder rather than the target.

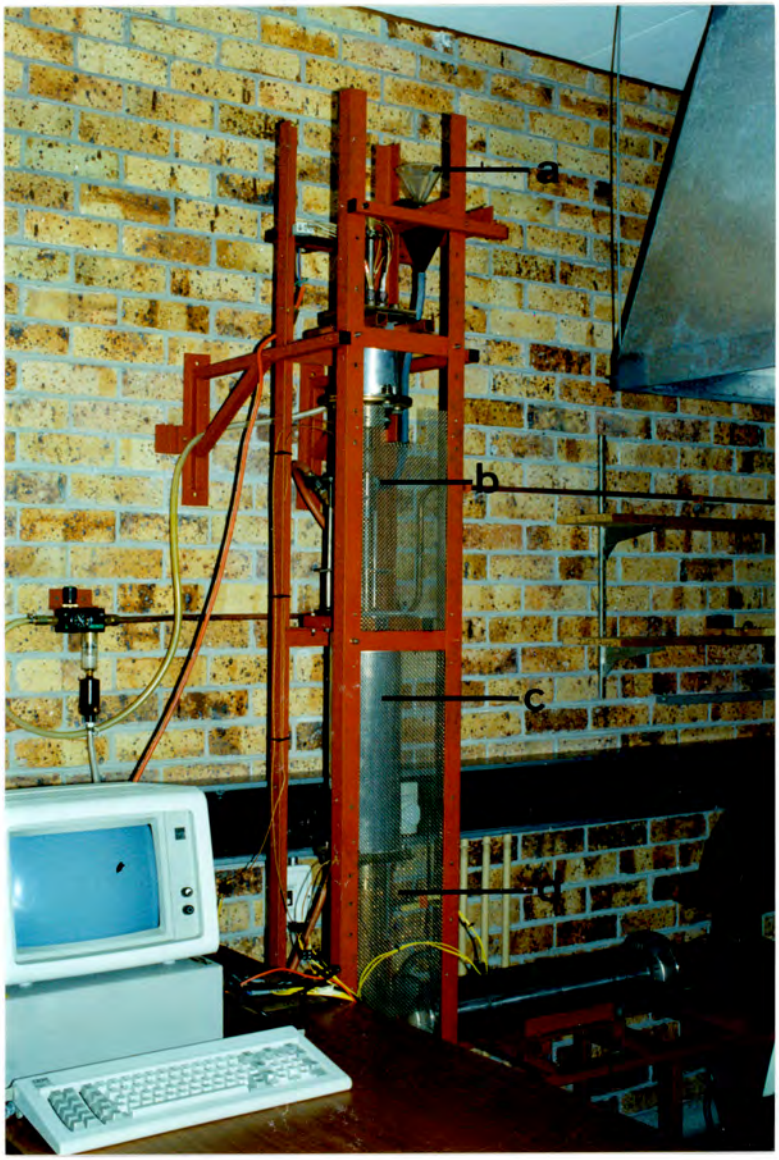

Figure 20. Photograph of the high temperature particle erosion apparatus showing the erodent feed hopper (a), the position of the venturi (b), the flame duct (c) and the position of the specimen (d).

Table 7. Test parameters for solid particle erosion tests with the high temperature particle erosion rig.

Parameter	Value
Test temperatures (°C)	25°C, 300°C, 500°C
Erodent particle type	120 grit SiC
Compressed air pressure	140 kPa
Mass of erodent per test	30 g
Exposed target area	50.3 mm^2
Specimen stand-off distance	30 mm
Particle velocity	20 $m.s^{-1}$
Feed rate ($g.s^{-1}$)	0.17 $g.s^{-1}$

3.8. Cavitation erosion

Vibratory cavitation equipment was used to generate controlled cavitation damage as shown in Figure 22 and Figure 23. A separation distance of 0.35 mm was maintained between the tip and the specimen. The ultrasonic drill vibrated at a frequency of approximately 20 kHz and an amplitude of between 75 μm and 120 μm. The apparatus was warmed up prior to testing to allow the change in the separation distance due to expansion of the tip to occur. The temperature of testing was maintained at less than 30°C throughout each test. Coupon specimens of each of the materials were prepared. Before each test the specimens were polished to a 0.25 μm finish, ultrasonically cleaned in ethanol and weighed. Erosion was monitored by weighing the specimen at regular intervals during each test. The steady state cavitation erosion rate was measured as the volume of material loss per hour of erosion. The duration of tests was either 20 hours or 40 hours. The Ti-6Al-4V (wt.%) tip on the end of the ultrasonic drill horn was replaced every eight hours because it eroded during testing. The incubation period i.e. the period before the onset of steady state erosion, was defined according to the A.S.T.M. standard[87] as the intercept on the time axis of a straight line extension of the steady state line. The definition of the steady state erosion rate and the incubation period used in the present study are shown in Figure 21. Changes in surface topography of the eroded specimens were monitored using scanning electron microscopy. The transition region, i. e. the region between the steady state erosion and the polished edge of the specimen provided evidence concerning damage initiation and the relationship of damage to the starting microstructure. Subsurface damage was investigated by making 5° taper sections of some of the cavitation eroded specimens.

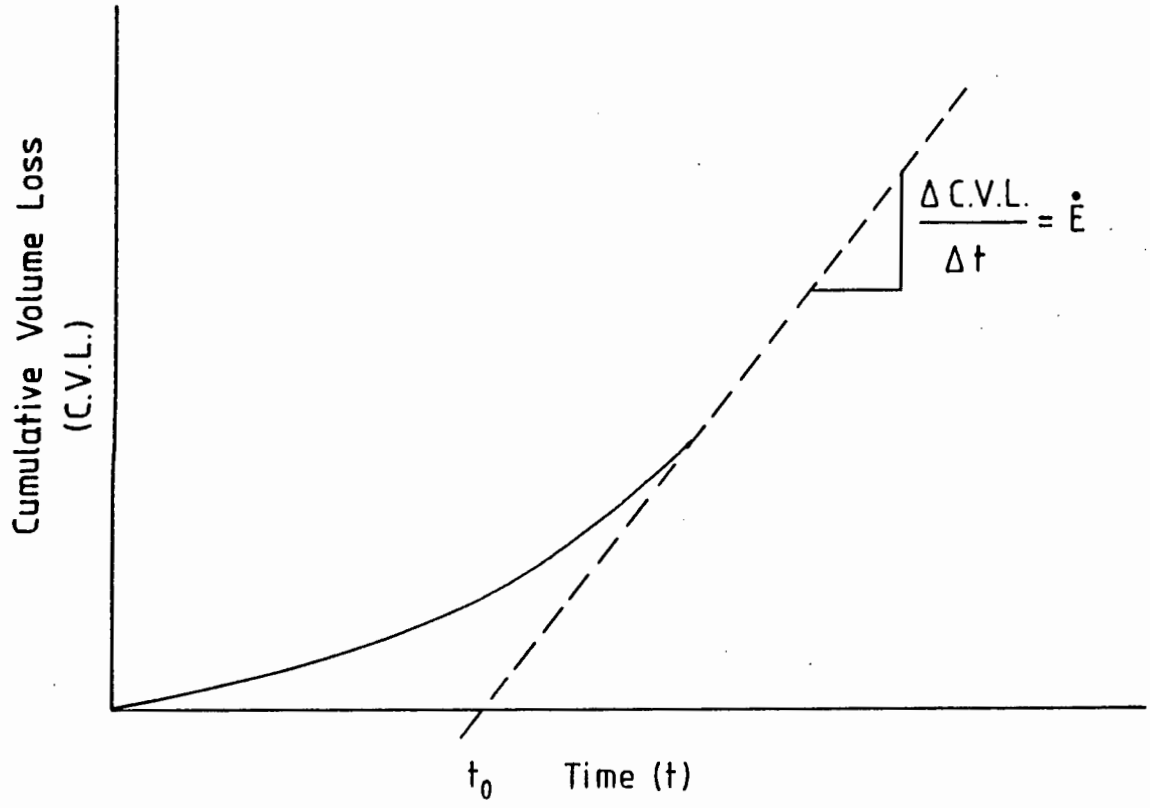

Figure 21. Definitions of the incubation period and steady state erosion rate used in this study. t_0 = incubation period; E = steady state cavitation erosion rate.

The development of cavitation erosion damage was monitored within an identified region on the surface of near-γ Ti-48Al-2Mn-2Nb (at.%). The region was adjacent to a flaw in the surface, which provided a reference point after each period of erosion. The starting microstructure was revealed by etching with Keller's reagent. The specimen was re-polished before the first fifteen minute exposure to cavitation in order to remove the effects of etching. Observation with the S.E.M. confirmed that the surface was polished and without features that could later be confused with erosion features. The surface features produced by cavitation erosion were observed with the S.E.M. after exposure to cavitation erosion for 15, 30, 45, 135 and 195 minutes and were correlated to the starting microstructure.

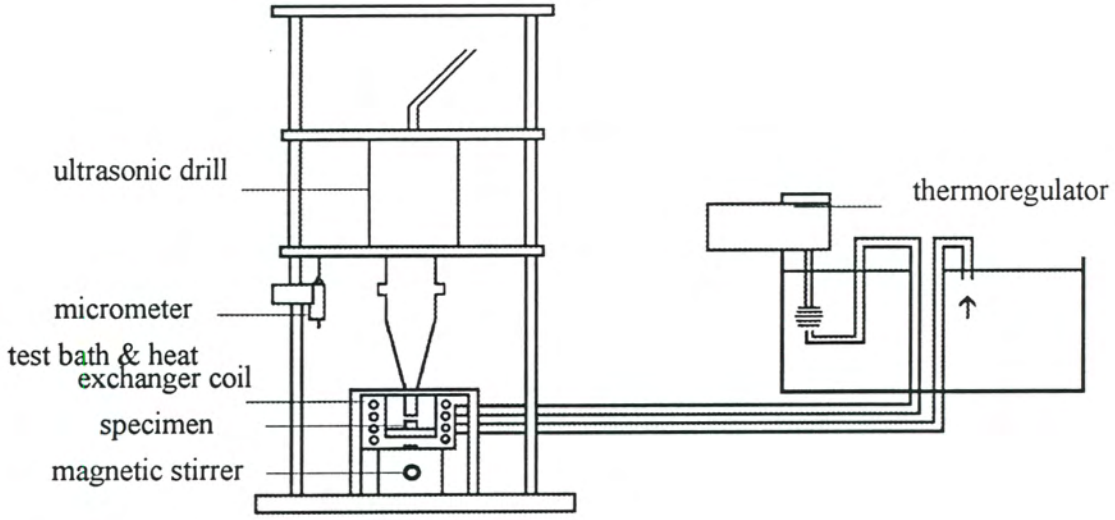

Figure 22. Drawing of the vibratory cavitation erosion apparatus.

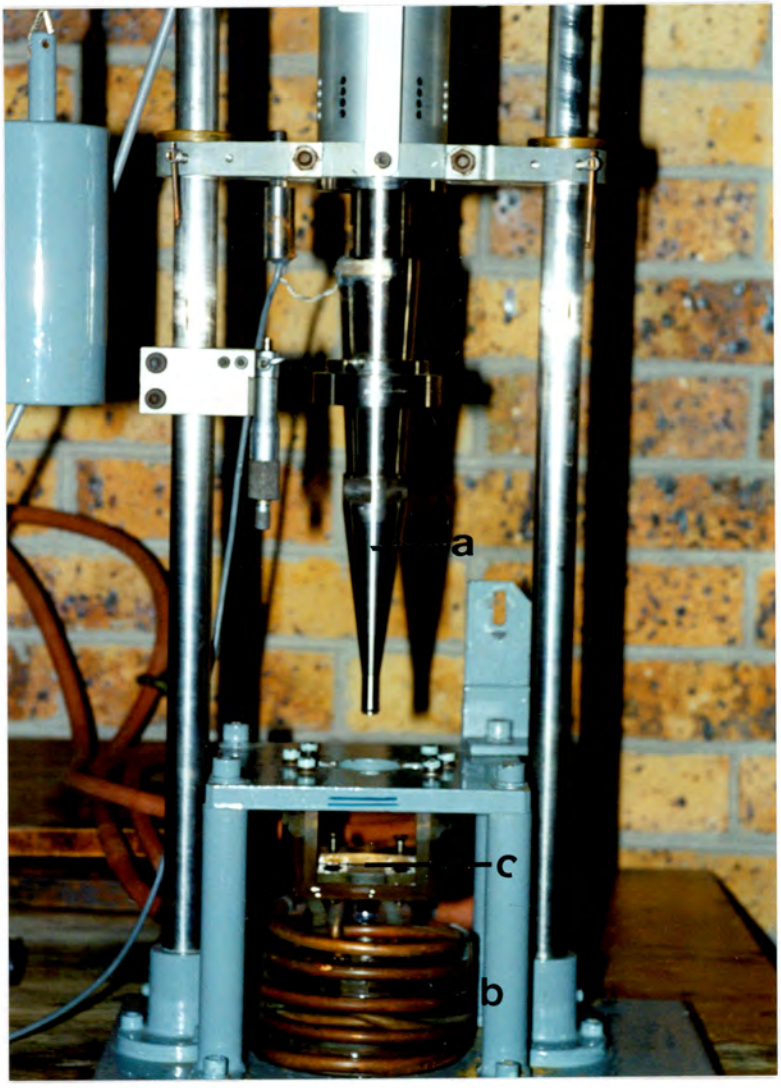

Figure 23. Photograph of the vibratory cavitation erosion apparatus showing the ultrasonic drill horn (a), the test bath and cooling coils (b) and the position of the specimen (c).

3.9. Selective electropolishing

A groove was produced in the cavitation eroded surface of a specimen of as received Ti-25Al-10Nb-3V-1Mo (at.%) according to the method employed by Shechtman[88] as shown in Figure 24. The entire specimen was coated with a proprietary lacquer (*Lacomit*) except for a narrow groove across the cavitation eroded surface. The specimen was electropolished for 3 minutes using an applied potential of 18 volts in an electrolyte consisting of 3 g succinic acid, 3 ml concentrated sulphuric acid and 1 litre methanol. After thorough rinsing, the specimen was etched in Keller's reagent to produce phase contrast. The top edges of the groove were examined with the S.E.M. in order to correlate the microstructural and cavitation erosion features.

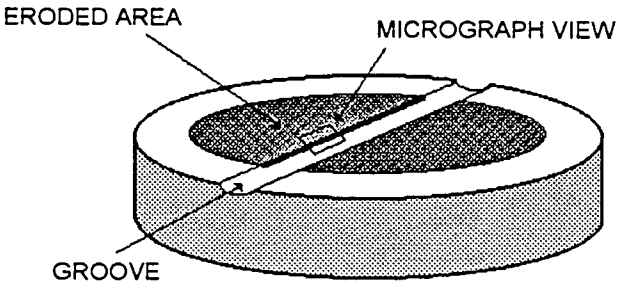

Figure 24. Cavitation erosion specimen of Ti-25Al-10Nb-3V-1Mo (at.%) with a groove electropolished across the cavitation eroded surface. The dark hatching indicates the cavitation eroded area. The lightly eroded edge of the eroded area is termed the "transition region" in this thesis.

3.10. X-Ray diffraction

X-ray diffraction (X.R.D.) was performed on polished (0.1 μm) specimens in order to identify the phases present in the titanium aluminide alloys. Spectra were also obtained from titanium aluminide specimens before and after cavitation erosion. A Philips diffractometer fitted with a monochromator and using Cu K_α radiation was used for all the X.R.D. investigations and the settings that were used are summarised in Table 8.

Table 8. X-ray diffractometer settings.

Parameter	Value
Radiation	CuK_α
Start angle (2θ)	10 °
End angle (2θ)	80 °
Step interval (2θ)	0.1 °
Count time (seconds)	1
Current (mA)	30
Voltage (kV)	40

The intensity of diffracted x-rays decreases exponentially from the surface so that the diffraction information originates from a thin surface layer a few microns deep[89]. The exact depth depends on the material and the type of plane from which the x-rays are diffracted and the intensity of the incident radiation.

3.10.1. Phase identification

The x-ray diffraction (X.R.D.) spectrum of a crystalline material is determined by the crystal structure of all the phases within the material according to Bragg's law[90]:

$$n\lambda = 2d\sin\theta$$

where n = 1, 2, 3, ...
λ = x-ray wavelength
d = interplanar spacing
θ = angle between incident x-ray and the set of atomic planes.

The peaks produced by the ordered hexagonal (DO_{19}) α_2 phase were indexed by analytical manipulations of the formula for disordered hexagonal crystal structures[91]:

$$\sin^2\theta = A(h^2 + hk + k^2) + Cl^2$$

where $A = \lambda^2/3a^2$, $C = \lambda^2/4c$, a and c are the lattice parameters for the disordered hexagonal structure and λ = wavelength of the incident radiation. The a lattice parameter of the DO_{19} structure is twice that of the disordered hexagonal structure[92].

The peaks produced by body-centred cubic (b.c.c.) B2 phase were indexed by analytical manipulations of the following formula for disordered b.c.c. crystal structures[93]:

$$\sin^2\theta / (h^2 + hk + k^2) = \lambda^2/4a^2$$

where a is the lattice parameter for the disordered b.c.c. crystal structure.

Indexing of the γ phase was performed by analytical manipulations of the formula for disordered tetragonal crystal structures[94]:

$$\sin^2\theta = A(h^2 + k^2) + Cl^2$$

where $A = \lambda^2/4a^2$ and $C = \lambda^2/4c^2$

Powder Diffraction File index card number 5-0678 containing the lattice parameters for the ordered tetragonal γ phase, TiAl, was also used to identify the diffraction peaks for the α_2 phase and is included in Appendix D.

3.10.2. Integrated intensity calculations

Each spectrum was plotted using a computer spreadsheet package. The start (θ_3) and end (θ_4) angles for the calculation of the area enclosed by each peak and the angles for the calculation of the left (θ_1 and θ_2) and right (θ_5 and θ_6) backgrounds were determined as shown in Figure 25.

A computer program was used to calculate the area enclosed by each peak and to subtract the background from each peak. The background for each peak was calculated in two ways; firstly by fitting a straight line and secondly by fitting a polynomial to the left and right backgrounds. Two integrated peak areas were thus obtained; one corresponding to the total area minus the background fitted with the straight line, and the other corresponding to the total area minus the background fitted with the polynomial. Angles for the background calculation were chosen so that the two integrated areas did not differ by more than 10 %. These two areas were averaged to produce an integrated intensity for each peak corrected for the background.

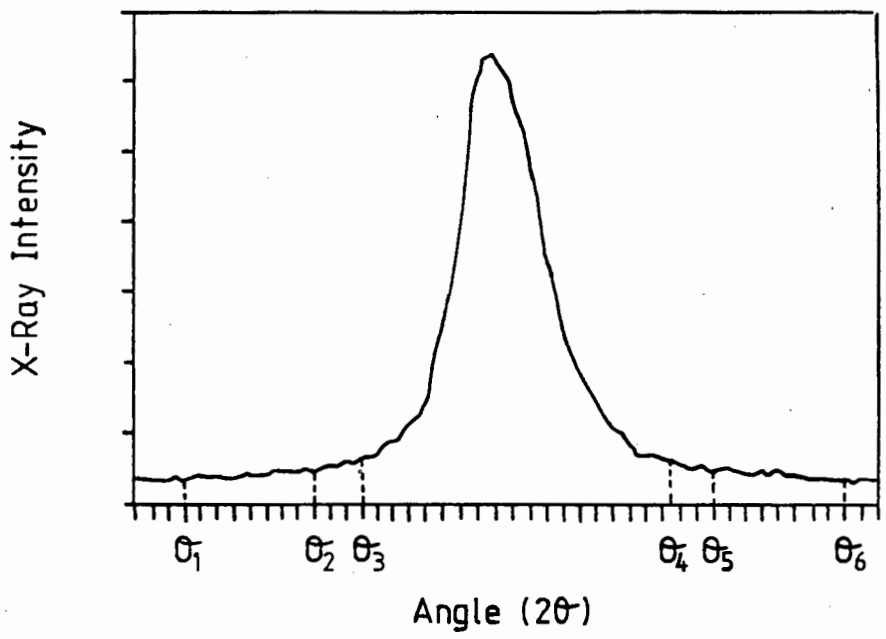

Figure 25. Schematic diagram showing an x-ray diffraction peak and the angles used to calculate the peak background.

3.11. Microhardness tests

A *Shimadzu* microhardness tester was used for all the microhardness tests. A Knoop indenter with the minimum load available, i.e. 15 gf was used to produce indents on 5° tapered sections of eroded specimens. The indents were staggered in order to maximise the number of indents within the near-surface region while keeping the minimum distance between the indents at approximately 2.5 times the length of the shorter diagonal to avoid interaction between adjacent indents. The distance from the eroded surface and the length of each indent was measured with a calibrated eyepiece graticule fitted to a *Reichert MeF3A* metallurgical microscope. Values of Knoop microhardness were obtained from the indent lengths and were plotted as a function of depth below the eroded surface. The depth which is presented with the microhardness test results was measured on the 5° tapered sections. The depth perpendicular to the surface is given by dsin5° where d is the distance from the eroded surface measured on the 5° tapered section.

3.12. Image analysis

A *Joyce-Loebl Genias 25* image analysis system was used to measure the volume fraction of the α_2 phase of Ti-25Al-10Nb-3V-1Mo (at.%) in the as received condition and after annealing heat treatments using 20 fields of view at two thousand times magnification for each microstructural condition.

4. RESULTS

4.1. Materials Characterisation

4.1.1. Introduction

The results of microstructural examination and mechanical tests on Ti-25Al-10Nb-3V-1Mo (at.%), Ti-52Al (at.%) and Ti-48Al-2Mn-2Nb (at.%) are presented in this section and provide background to the particle erosion and cavitation erosion results which are presented in later sections.

4.1.2. Ti-25Al-10Nb-3V-1Mo (at.%)

4.1.2.1. *X-ray diffraction*

An x-ray diffraction (X.R.D.) spectrum from Ti-25Al-10Nb-3V-1Mo (at.%) in the as received condition, i.e. hot rolled and annealed at 980°C for 1 hour followed by air cooling, is shown in Figure 26.

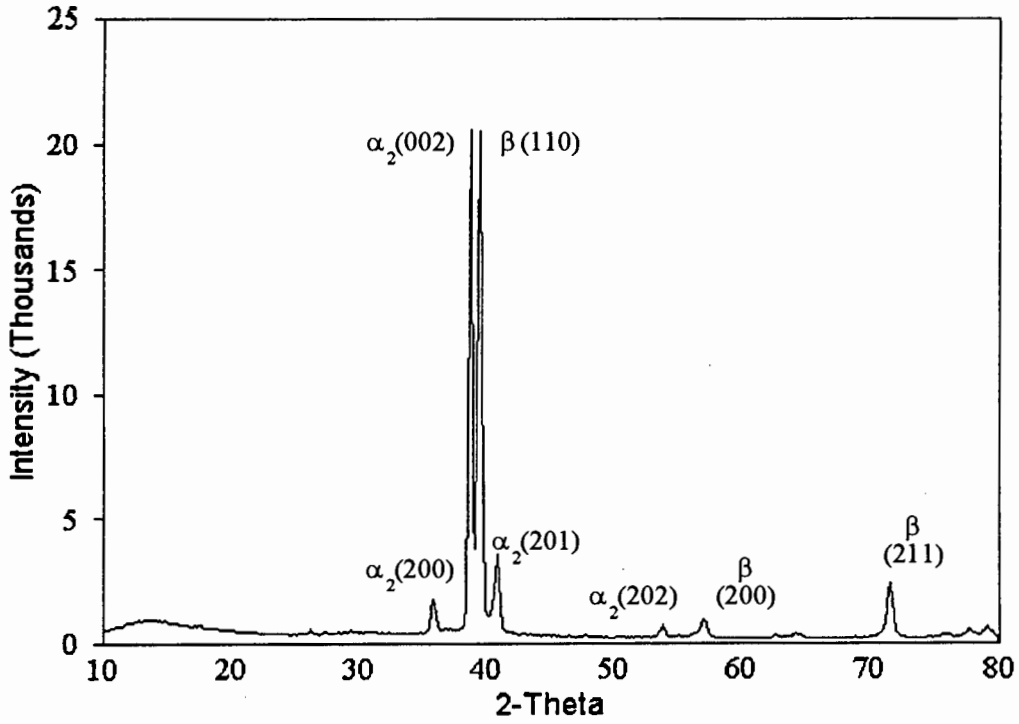

Figure 26. X-ray diffraction spectrum for as received Ti-25Al-10Nb-3V-1Mo (at.%). The peaks are indexed for the α_2 and β phases.

The integrated intensity of each peak, expressed as a percentage of the integrated intensity of the $\alpha_2(002)$ peak, is shown in summary in Table 9. The lattice parameters for the α_2 phase and β phase are shown in Table 10 and are in good agreement with those determined by Haddad et al.[28].

Table 9. Summary of indexed peaks for the x-ray diffraction spectrum for as received Ti-25Al-10Nb-3V-1Mo (at.%).

2-Theta	phase and hkl plane	I x 100 / I (α_2(002))
36.0	α_2 (200)	10
39.0	α_2 (002)	100
39.5	β (110)	117
41.0	α_2 (201)	23
54.0	α_2 (202)	3
57.0	β (200)	5
71.5	β (211)	24

Table 10. Lattice parameters (measured in nanometres) for the α_2 phase and β phase in as received Ti-25Al-10Nb-3V-1Mo (at.%).

α_2 phase		β phase
a	c	a
0.578	0.463	0.323

4.1.2.2. Transmission Electron Microscopy

The microstructure of as received Ti-25Al-10Nb-3V-1Mo (at.%) is shown in Figure 27. Transmission electron microscopy was undertaken in order to establish whether the β phase of as received Ti-25Al-10Nb-3V-1Mo (at.%) has a disordered b.c.c. crystal structure or an ordered B2 crystal structure.

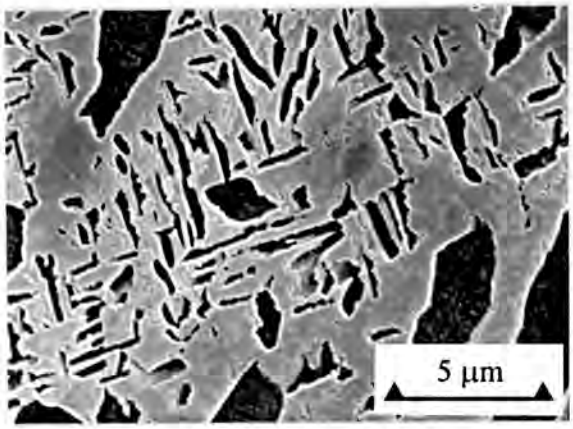

Figure 27. S.E.M. image showing the microstructure of as received Ti-25Al-10Nb-3V-1Mo (at.%). The areas in dark contrast were identified as the α_2 phase and those in light contrast as the ordered B2 phase using electron diffraction in the transmission electron microscope.

Bright field and dark field T.E.M. images and the accompanying [001] zone axis S.A.D.P. for the α_2 phase of as received Ti-25Al-10Nb-3V-1Mo (at.%) are shown in Figure 28. Both fundamental and superlattice reflections are detected for the ordered hexagonal crystal structure of the α_2 phase. The planar defects around the rim of the primary α_2 grains could be either the orthorhombic (O) phase[95] or twinning[96]. The [011] zone axis S.A.D.P. and the bright field and dark field images of the B2 phase are shown in Figure 29. The S.A.D.P. shown in Figure 29(a) is produced by the B2 matrix and the needle-like precipitates which are either α_2 phase or orthorhombic (O) phase. The dark field image is produced with the superlattice reflection indicated in Figure 29(a), which is either $\alpha_2(\bar{2}01)$ or the equivalent reflection from the O phase, O(111).

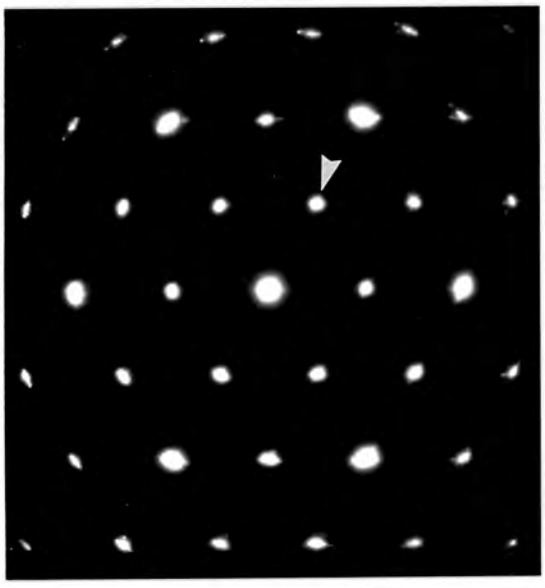

(a)

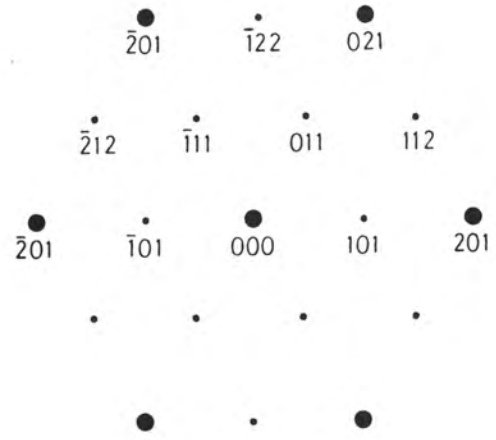

(b)

(c)

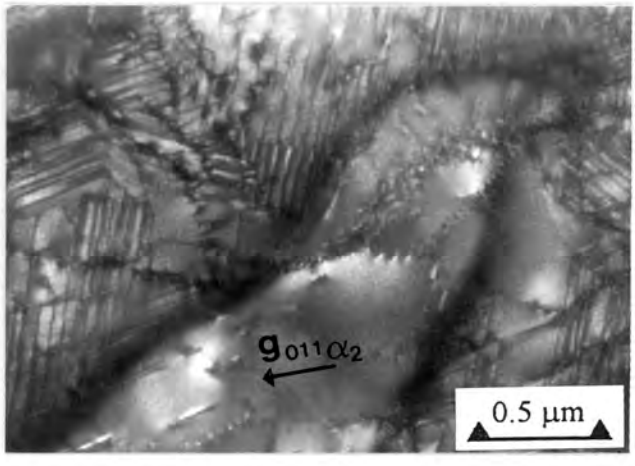

(d)

Figure 28. As received Ti-25Al-10Nb-3V-1Mo (at.%). (a) α_2 [001] zone axis S.A.D.P. (b) Schematic representation of the [001] zone axis diffraction pattern for the ordered hexagonal (DO_{19}) crystal structure. (c) Bright field image and (d) dark field image produced with the 011 superlattice reflection arrowed in (a), showing a primary α_2 grain containing substructures.

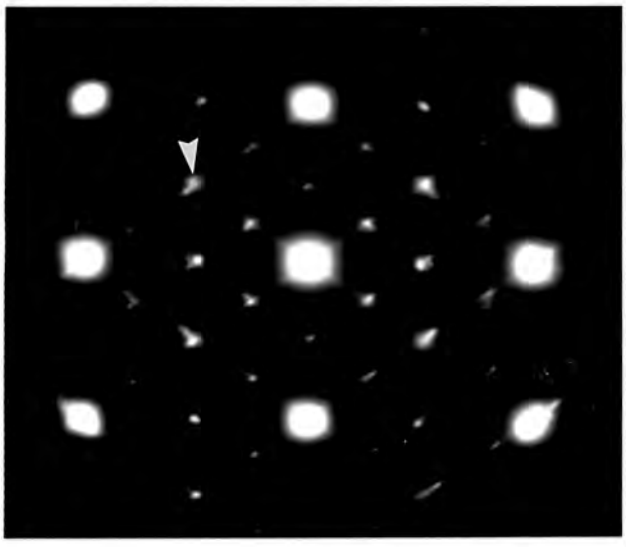

(a)

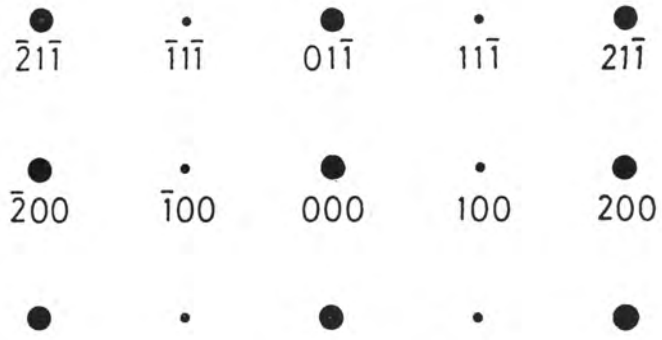

(b)

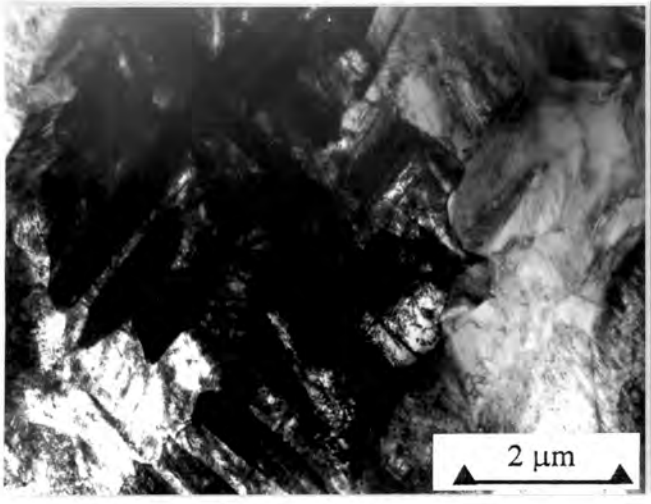

(c)

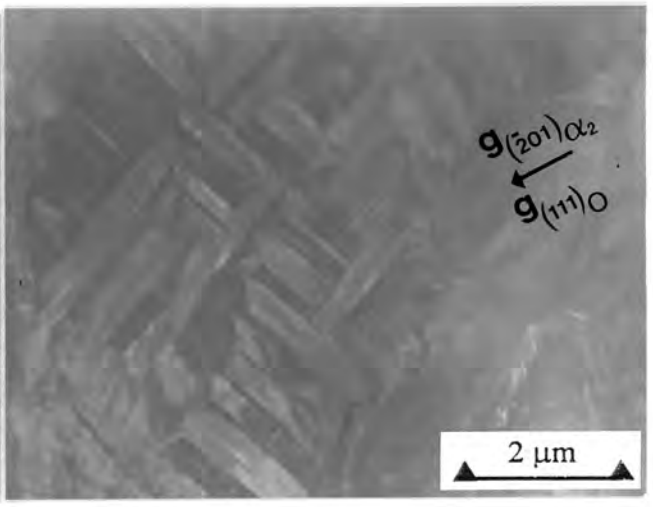

(d)

Figure 29. As received Ti-25Al-10Nb-3V-1Mo (at.%). (a) S.A.D.P. produced by the B2 matrix and α_2/O laths. (b) Schematic representation of the [011] zone axis electron diffraction pattern for the ordered B2 crystal structure. (c) Bright field T.E.M. image showing the B2 matrix region with lath-like precipitates. (d) Dark field image produced with the reflection indicated in (a) which is either $\alpha_2(\bar{2}01)$ or O(111).

4.1.2.3. *Annealing heat treatment*

The microstructures of as received and annealed Ti-25Al-10Nb-3V-1Mo (at.%) are shown in Figure 30. The lath-like morphology of the α_2 phase changes with heat treatment to a more equiaxed microstructure of two interconnected phases. No additional peaks were identified in the X.R.D. spectra after annealing heat treatments. The size of the primary α_2 grains increases with increasing annealing temperature. The volume fraction of the α_2 phase is between 50% and 60% in the as received condition and after annealing at temperatures up to 950°C, however after annealing at 1000°C the volume fraction of the α_2 phase increases to 71±3% as shown in summary in Table 11. The preferred orientation of the α_2 phase is dramatically reduced after annealing at 1000°C as shown in Figure 30(f). These microstructural changes produced by heat treatment have an effect on the bulk hardness of the alloy as shown in Figure 31.

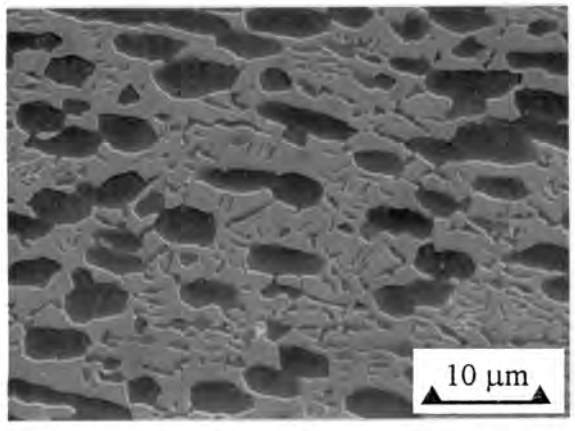

(a)

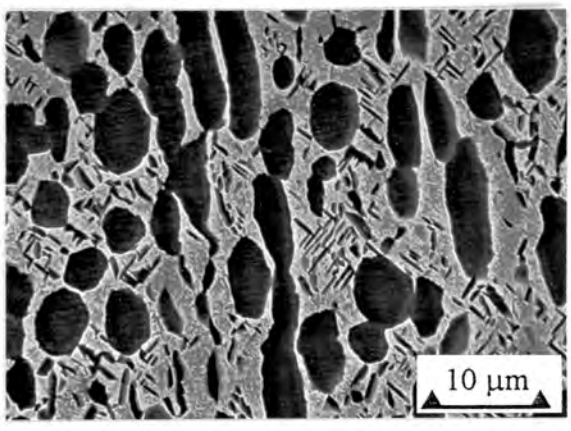

(b)

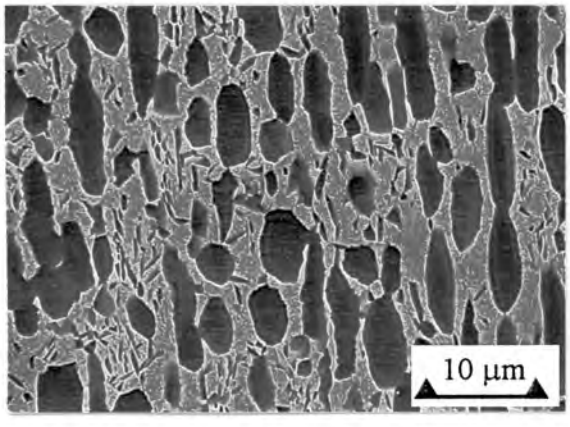

(c)

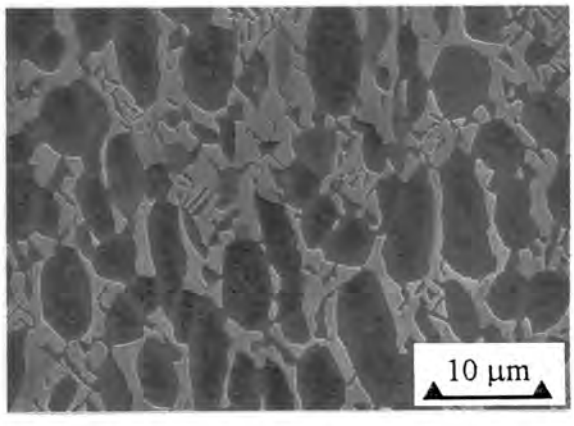

(d)

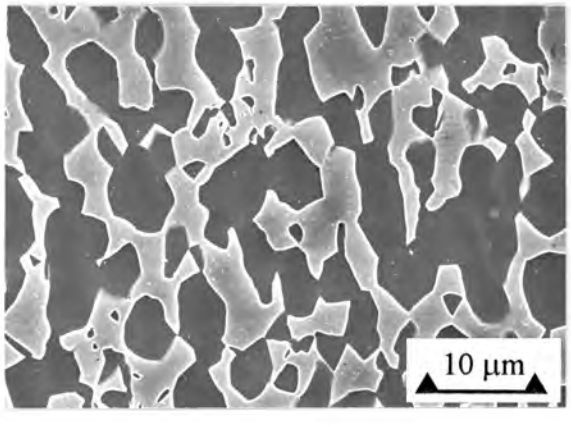

(e)

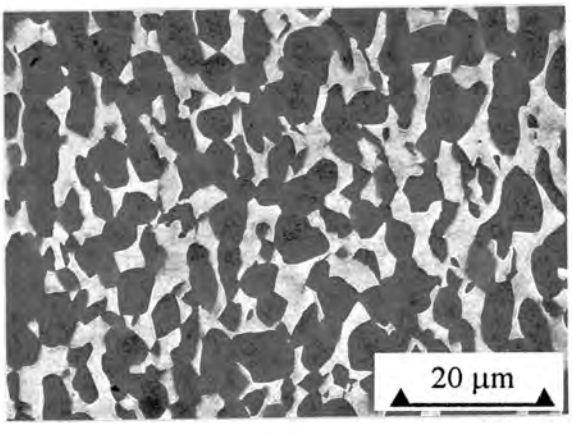

(f)

Figure 30. Scanning electron micrographs of as received and annealed microstructures of Ti-25Al-10Nb-3V-1Mo (at.%). (a) As received, (b) annealed at 700°C, (c) 800°C, (d) 900°C, (e) 950°C, (f) 1000°C. The α_2 phase is in dark contrast and the B2 phase is in light contrast.

Table 11. Bulk hardness and volume percent α_2 for Ti-25Al-10Nb-3V-1Mo (at.%) after annealing heat treatments for 24 hours at the temperatures shown, followed by water quenching.

Heat treatment	Hardness (HV30)	% α_2
As received	420	48±4
Annealed for 24 hours		
700 °C	370	54±3
800 ° C	342	52±4
900°C	350	62±4
950°C	350	54±3
1000°C	382	71±3

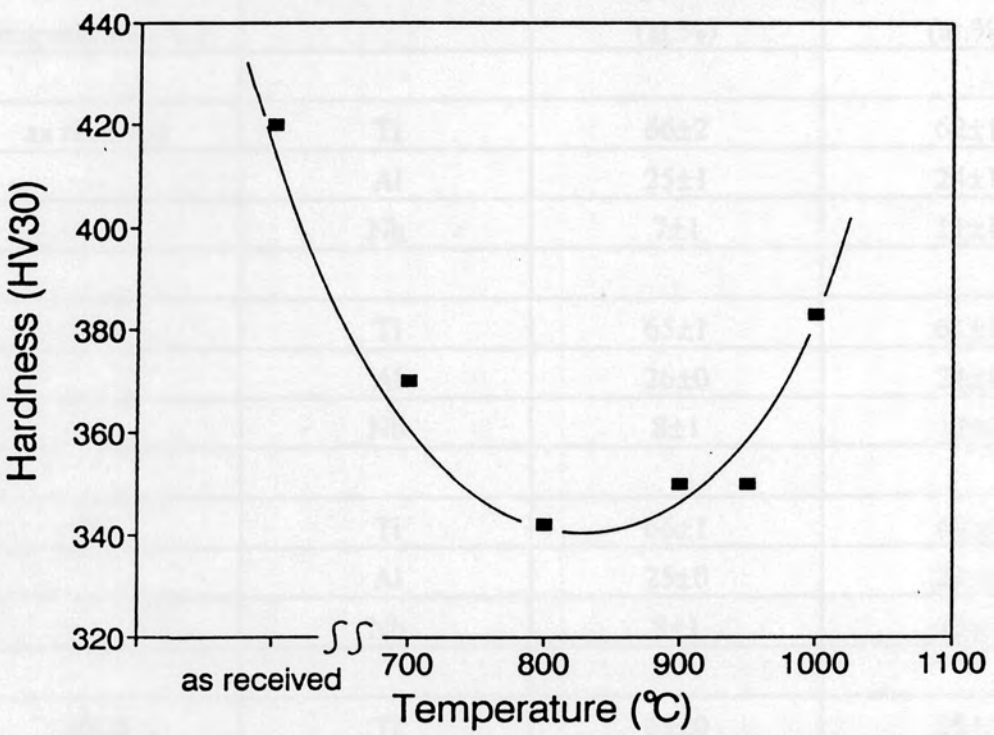

Figure 31. Bulk hardness of Ti-25Al-10Nb-3V-1Mo (at.%) as a function of annealing temperature.

The results of energy dispersive x-ray spectroscopy (E.D.S.) analysis shown in Table 12 reveal that the concentration of aluminium is higher in the α_2 phase than the B2 phase and that the niobium concentration is higher in the B2 phase and increases after annealing at 1000°C.

Table 12. E.D.S. (20 kV) analysis of Ti-25Al-10Nb-3V-1Mo (at.%) in the as received condition and after annealing at 800°C, 950°C and 1000°C.

Annealing temperature (°C)	Element	α_2 phase (at.%)	B2 phase (at.%)
as received	Ti	66±2	62±1
	Al	25±1	24±1
	Nb	7±1	11±1
800	Ti	65±1	61±1
	Al	26±0	24±1
	Nb	8±1	13±0
950	Ti	66±1	60±1
	Al	25±0	23±0
	Nb	8±1	13±0
1000	Ti	65±0	58±3
	Al	26±0	23±1
	Nb	8±1	15±2

4.1.2.4. *Ageing heat treatment*

Specimens of Ti-25Al-10Nb-3V-1Mo (at.%) were solution treated at 1060°C in the (α_2+B2) phase field to homogenize the α_2 phase distribution, and were subsequently aged for 2 hours at 650°C or 850°C or 950°C as shown in Figures 32 and 33. Ageing at 650°C does not produce changes in the matrix which are visible with the light microscope, but this microstructure has a greater microhardness than the other aged specimens as shown in Figure 32 and Table 13. This is presumably due to fine α_2 or O phase precipitates in the B2 matrix[30]. The Vickers (30 kg) hardness of the aged (650°C) material is 505 VHN, which makes it the hardest of the Ti-25Al-10Nb-3V-1Mo (at.%) specimens, including the as received material. Ageing at 850°C produces a change in the matrix which is visible with the light microscope as shown in Figure 33(a). Ageing at 950°C produces a microstructure consisting of primary and needle-like α_2 grains and a B2 matrix in light contrast as shown in Figure 33(b).

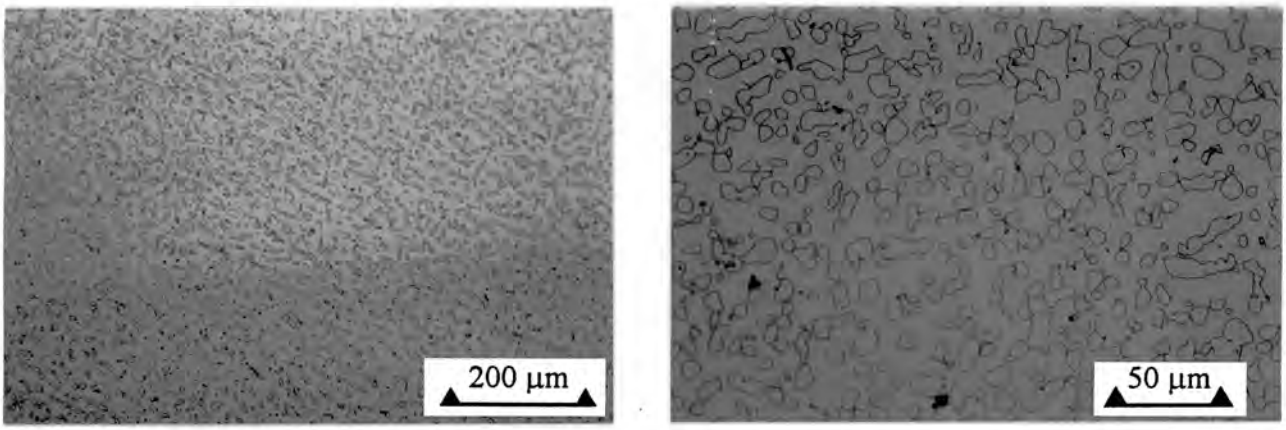

(a) (b)

Figure 32. Light micrographs of Ti-25Al-10Nb-3V-1Mo (at.%). (a) Microstructure after solution treatment at 1060°C for 1 hour followed by air cooling. (b) Microstructure after ageing at 650 °C. The B2 matrix appears featureless.

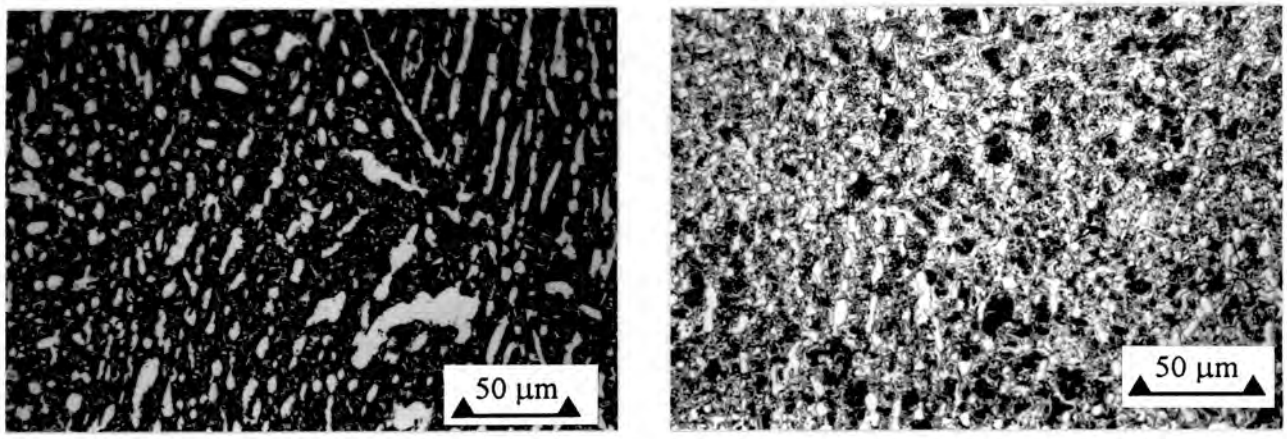

(a) (b)

Figure 33. Light micrographs of Ti-25Al-10Nb-3V-1Mo (at.%). The transformed B2 matrix region consists of fine substructure after ageing at (a) 850°C and (b) 950°C.

Table 13. Microhardness of Ti-25Al-10Nb-3V-1Mo (at.%) after solution treatment (1060 °C for 1 hour) and ageing for 2 hours at the temperatures shown.

Ageing temperature (°C)	Microhardness HK (500 gf)
650	500
850	300
950	335

4.1.2.5. *Compression tests*

The polished gauge length of the cylindrical as received Ti-25Al-10Nb-3V-1Mo (at.%) compression specimen exhibits macroscopic deformation marks parallel to the compressive axis after 0.8% strain and slip lines are observed within the α_2 phase after compression of the near cylindrical specimen to approximately 3% strain as shown in Figure 34(a). Re-loading the semi-cylindrical specimen and compressing to fracture results in an increase in the amount of strain observed in the B2 matrix and in the amount of slip in the α_2 phase, but the slip lines are still mainly confined to the α_2 phase. Fracture occurs at 45° to the compression axis and the fracture surface exhibits ductile shear dimples and smeared areas as shown in Figure 34(b).

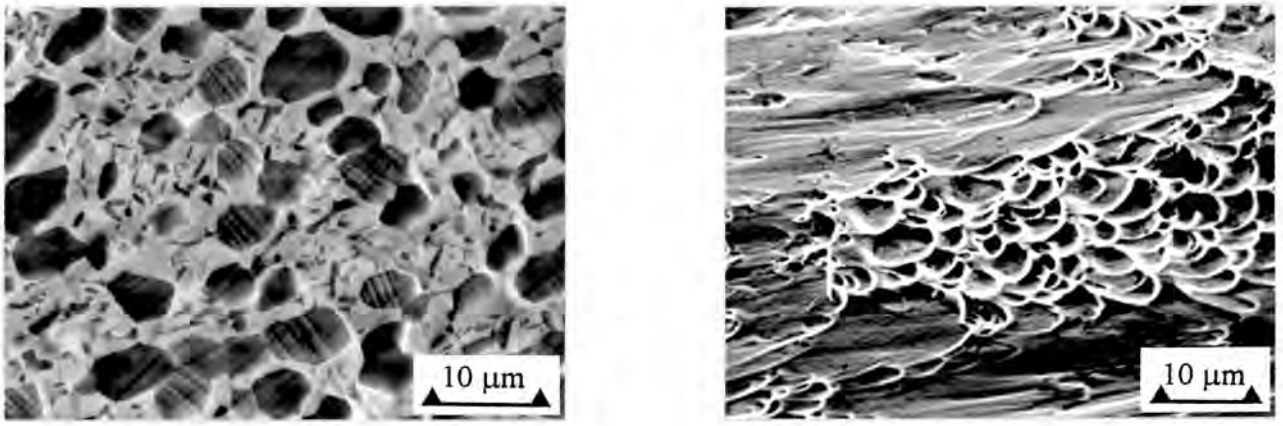

(a) (b)

Figure 34. S.E.M. image of as received Ti-25Al-10Nb-3V-1Mo (at.%). (a) After compression to approximately 8% strain slip lines are observed mainly within primary α_2 grains on the polished and etched gauge length. (b) The fracture surface exhibits shear dimples and smearing.

4.1.2.6. *Tensile tests*

Typical tensile stress/strain curves for as received Ti-25Al-10Nb-3V-1Mo (at.%) and 304 stainless steel are shown in Figures 35 and 37 and the test results are summarised in Table 14. The tensile properties of Ti-25Al-10Nb-3V-1Mo (at.%) are in agreement with those supplied by the producer, *R. M. I. Titanium* as shown in section 3.1. Graphs of work hardening rate versus true strain are shown in Figures 36 and 38. The work hardening rate of as received Ti-25Al-10Nb-3V-2Mo (at.%) is considerably higher than that of 304 stainless steel, which has a higher work hardening rate than many other metallic materials.

The fracture surface of Ti-25Al-10Nb-3V-1Mo (at.%) is perpendicular to the tensile axis and no necking is observed, but both brittle cleavage and ductile tensile dimpling are observed on the fracture surface on a microscopic scale as shown in Figure 39. Each set of cleavage markings is confined to an elongated area of approximately 30 μm^2 which is similar to the shape and area of the primary α_2 grains.

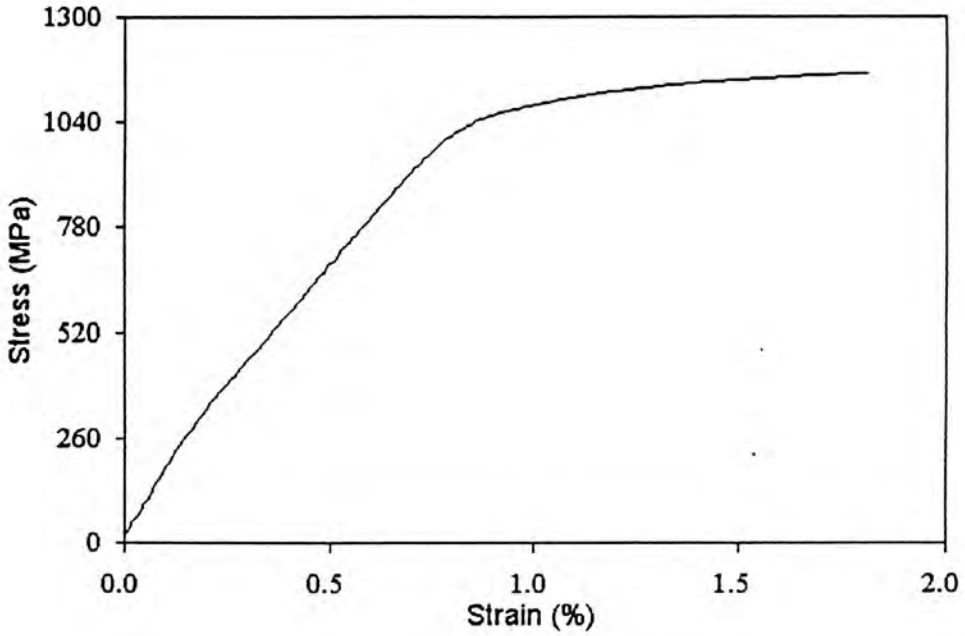

Figure 35. Tensile stress versus strain curve for as received Ti-25Al-10Nb-3V-1Mo (at.%).

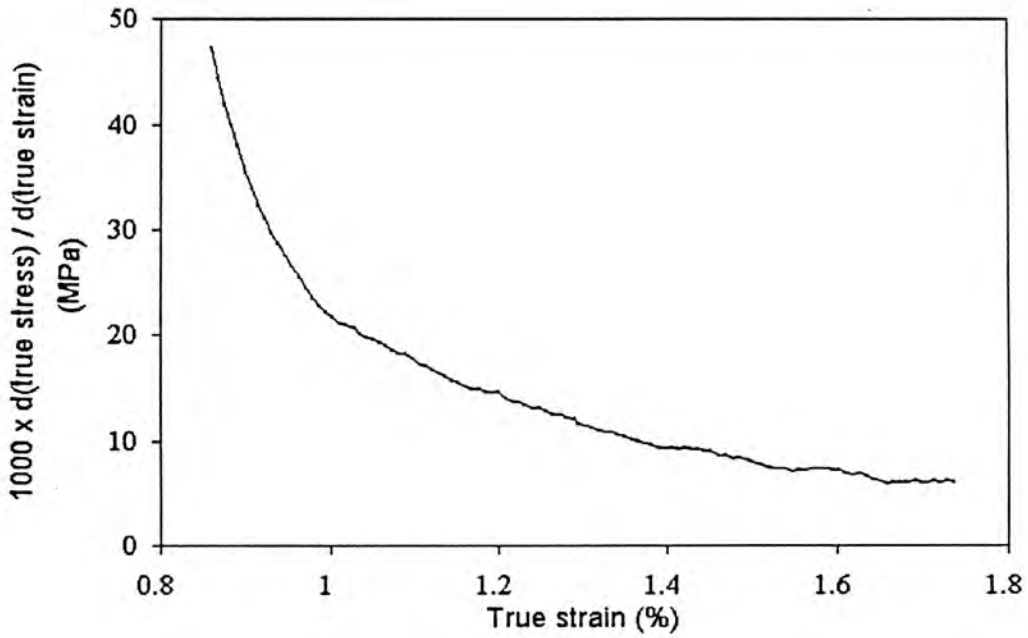

Figure 36. Graph of work hardening rate, $d\sigma/d\varepsilon$, versus true strain for as received Ti-25Al-10Nb-3V-1Mo (at.%).

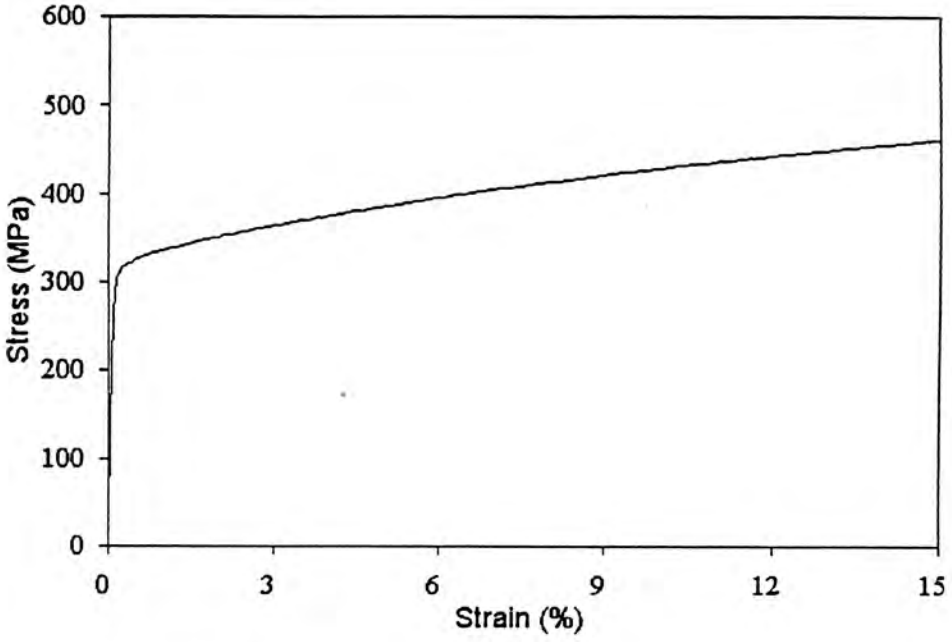

Figure 37. Tensile stress versus strain curve for 304 stainless steel.

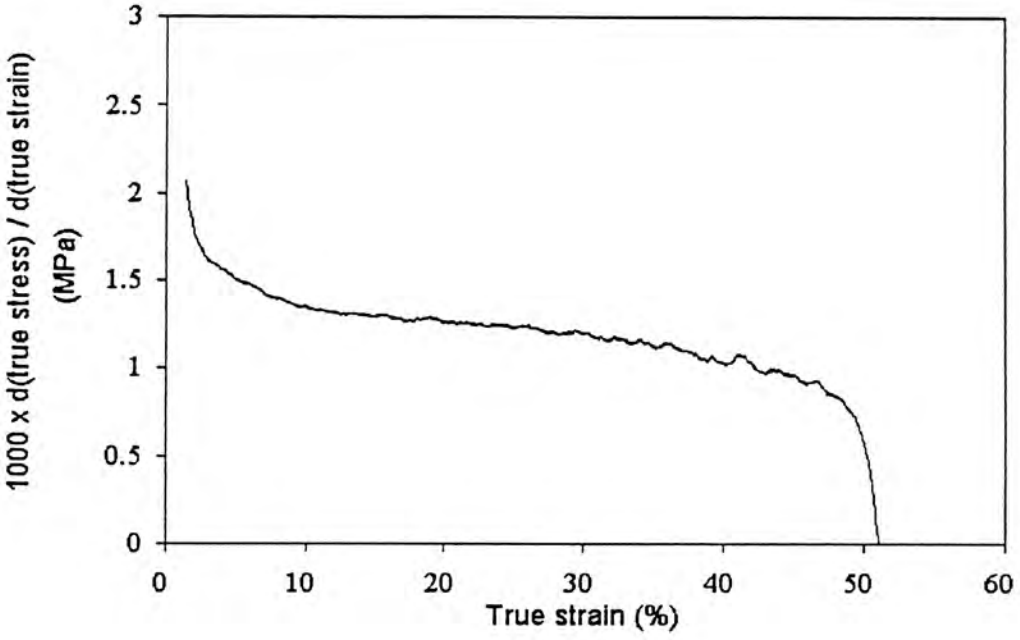

Figure 38. Graph of dσ/dε (work hardening rate) versus ε for 304 stainless steel.

Table 14. Tensile test results for as received Ti-25Al-10Nb-3V-1Mo (at.%) and 304 stainless steel.

Material	σ uts (MPa)	ε (%)	Work to break (J)	Yield strength (MPa)	E modulus (GPa)
Ti-25Al-10Nb-3V-1Mo (at.%)	1161	1.8	7.9	1000	122
	1180	2.1	9.5	1000	124
304 Stainless steel	572	57	191.4	265	238
	571	58	186.9	260	184

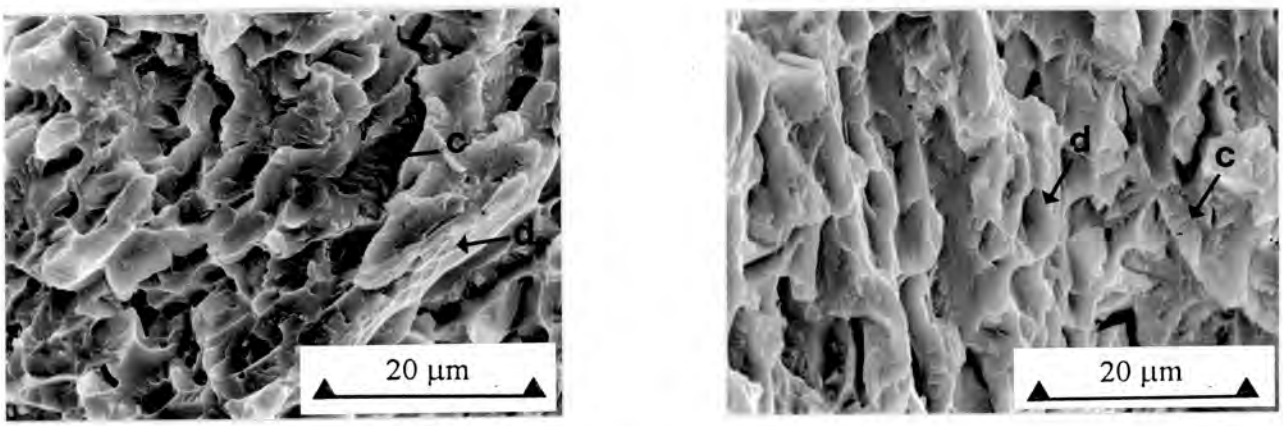

(a) (b)

Figure 39. S.E.M. images of the tensile fracture surface of as received Ti-25Al-10Nb-3V-1Mo (at.%). (a) Cleavage markings and fine dimples are shown in this micrograph. (b) Dimples created by ductile tearing and cleavage markings are shown in this micrograph.

4.1.3. Ti-52Al (at.%)

4.1.3.1. *X-Ray Diffraction*

An x-ray diffraction spectrum from Ti-52Al (at.%) in the homogenized condition, i.e. heat treated at 1380°C for 1 hour followed by furnace cooling is shown in Figure 40 and the integrated intensities and lattice parameters are summarised with those of Ti-48Al-2Mn-2Nb (at.%) in Tables 15 and 16 respectively.

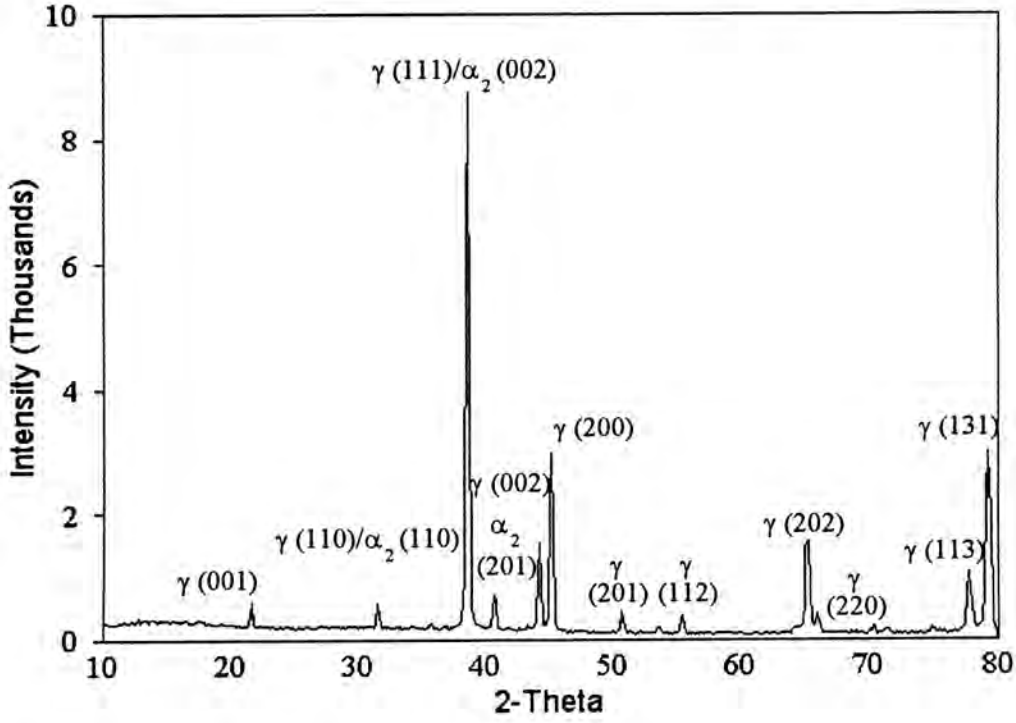

Figure 40. X-ray diffraction spectrum for homogenized Ti-52Al (at.%).

4.1.3.2. *Cast structure*

The macrostructure of the ingot in the transverse orientation (on the top surface) consists of a rim of columnar grains and a central region consisting of equiaxed grains as shown in Figure 41(a). The microstructure in the central region is dendritic as shown in Figure 41(b).

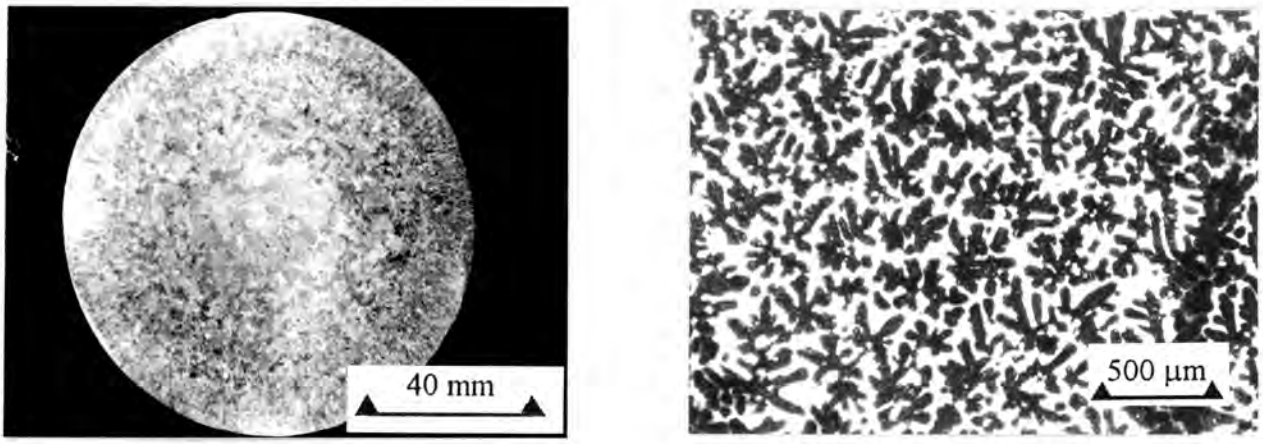

(a) (b)

Figure 41. Light micrographs of as cast Ti-52Al (at.%). (a) Macrostructure transverse to the length of the ingot. A region approximately 0.5 cm wide around the perimeter of the ingot contains columnar grains. (b) The microstructure in the central region consists of dendrites.

4.1.3.3. *Homogenized microstructure*

The homogenized microstructure of Ti-52Al (at.%) consists mainly of equiaxed γ grains as shown in Figure 42. The bulk hardness of the homogenized material is the same as the as cast material as shown in Table 17.

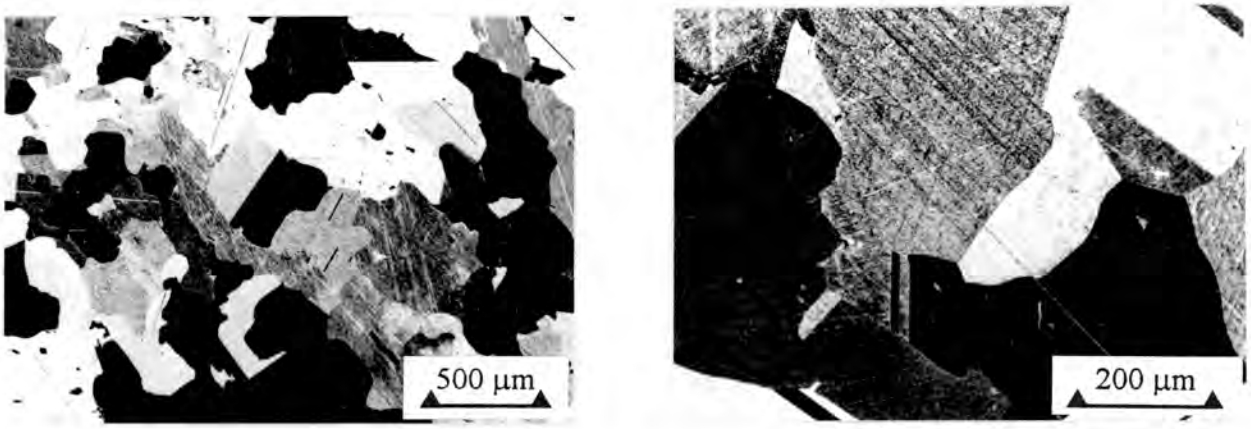

(a) (b)

Figure 42. Light micrographs of the homogenized microstructure of Ti-52Al (at.%). (a) The microstructure consists mainly of equiaxed γ grains. (b) At higher magnification annealing twins are visible in some of the γ grains.

4.1.4. Ti-48Al-2Mn-2Nb (at.%)

4.1.4.1. *X-Ray Diffraction*

X-ray diffraction spectra from Ti-48Al-2Mn-2Nb (at.%) in the homogenized condition, i.e. heat treated at 1380°C for 1 hour followed by furnace cooling and near-γ Ti-48Al-2Mn-2Nb (at.%) are shown in Figure 43. Peaks are indexed for the α_2 and γ phases and the integrated intensities and lattice parameters are shown in Tables 15 and 16 respectively. The peak at 32° is produced by either the α_2 (110) planes or the γ (110) planes and the peak at 39° is produced by either the α_2 (002) planes or the γ(111) planes since the Bragg condition is satisfied for both sets of planes at each angle.

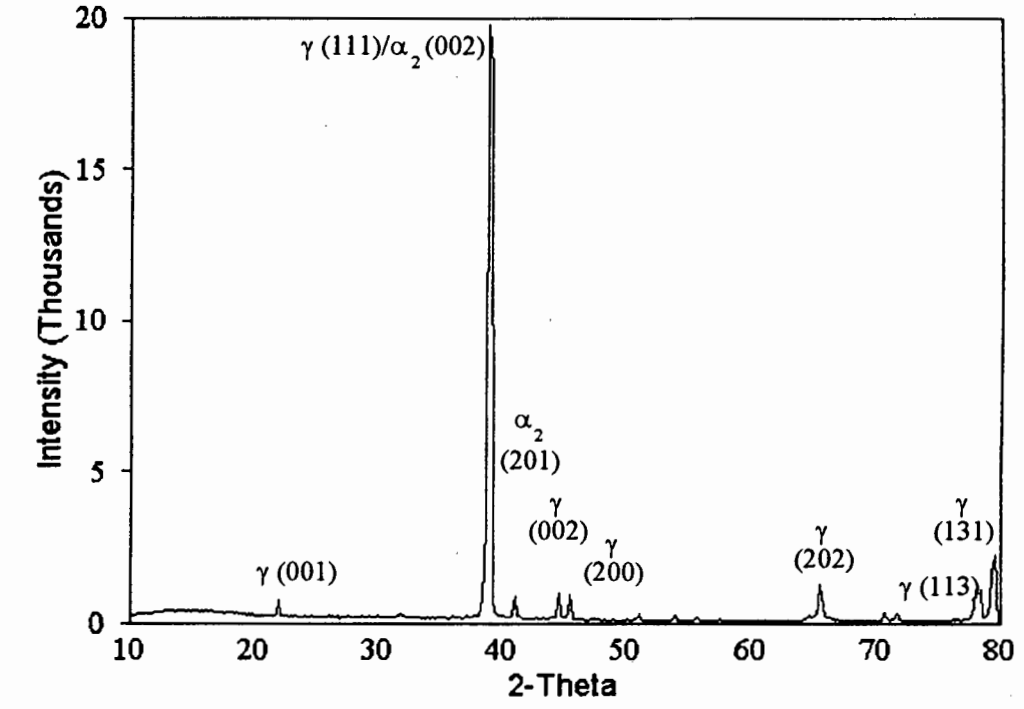

(a)

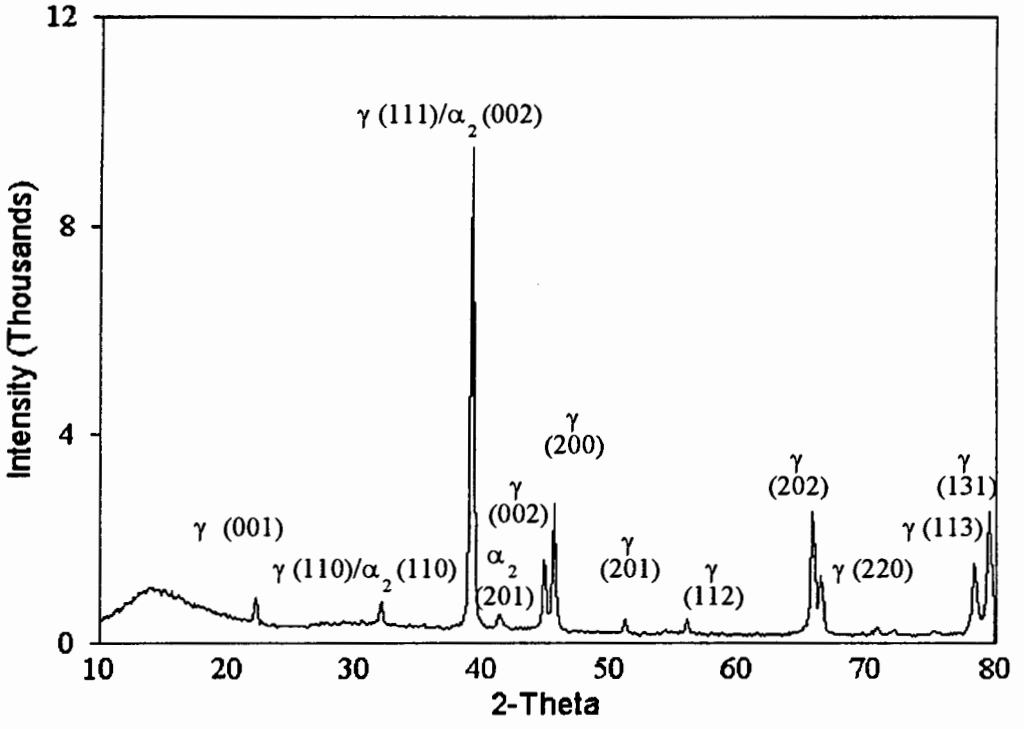

(b)

Figure 43. X-ray diffraction spectra for Ti-48Al-2Mn-2Nb (at.%) in the (a) homogenized and (b) near-γ heat treated conditions. The spectra are indexed for the α_2 and γ peaks.

Table 15. Summary of indexed peaks for the x-ray diffraction spectra for Ti-52Al (at.%) and Ti-48Al-2Mn-2Nb (at.%).

2-Theta	phase and hkl plane	I x 100 / I (γ(111)/ α_2(002))		
		homogenized Ti-52Al (at.%)	homogenized Ti-48Al-2Mn-2Nb (at.%)	near-γ Ti-48Al-2Mn-2Nb (at.%)
22.0	γ (001)	3.2	1.3	2.6
32.0	γ (110)/ α_2 (110)	4.7	-	2
39.0	γ (111)/ α_2(002)	100	100	100
41.0	α_2 (201)	6.6	3.1	1.8
45.0	γ (002)	14.7	3.7	9.0
45.5	γ (200)	34.5	4.1	16.6
51.0	γ (201)	4.4	0.9	2.0
55.5	γ (112)	3.7	0.7	2.2
65.5	γ (202)	20.7	6.7	14.3
66.0	γ (220)	3.3	-	5.8
78.0	γ (113)	12.7	10.3	8.1
79.5	γ (131)	63.1	10.4	20.7

Table 16. Lattice parameters (measured in nanometres) for the α_2 and γ phases in homogenized Ti-52Al (at.%) and homogenized Ti-48Al-2Mn-2Nb (at.%).

Material	α_2 phase		γ phase	
	a	c	a	c
Ti-52Al (at.%)	0.567	0.466	0.400	0.410
Ti-48Al-2Mn-2Nb (at.%)	0.562	0.462	0.400	0.406

4.1.4.2. *Cast structure*

The macrostructure of as cast Ti-48Al-2Mn-2Nb (at.%) in the transverse orientation consists of a rim of columnar grains approximately 2 cm wide around the perimeter of the disc and a central region of lamellar colonies and equiaxed γ grains as shown in Figure 44.

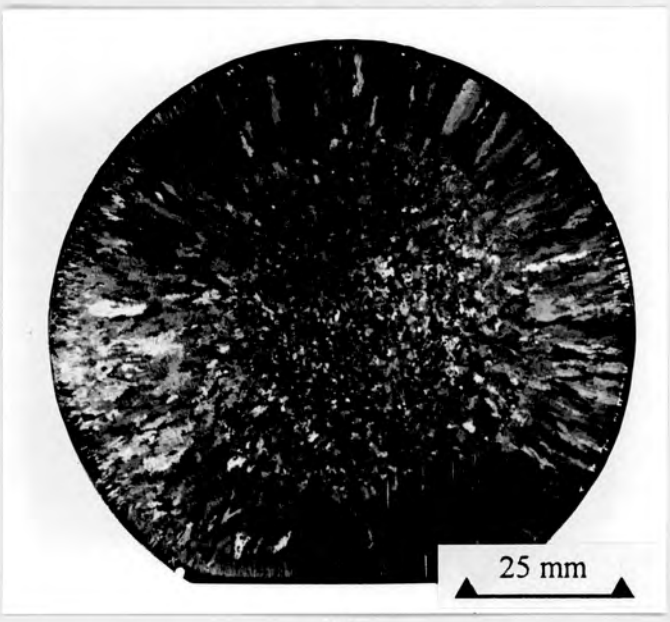

(a)

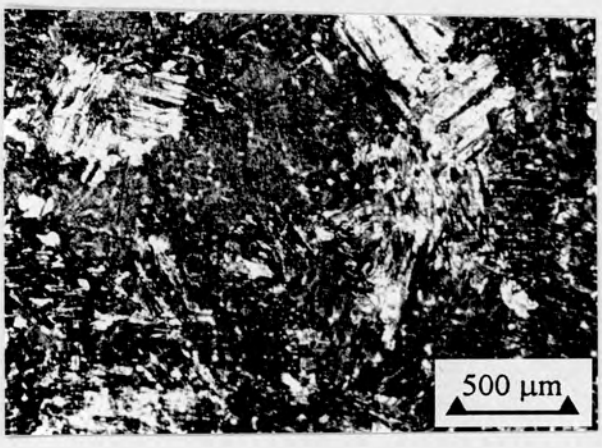

(b)

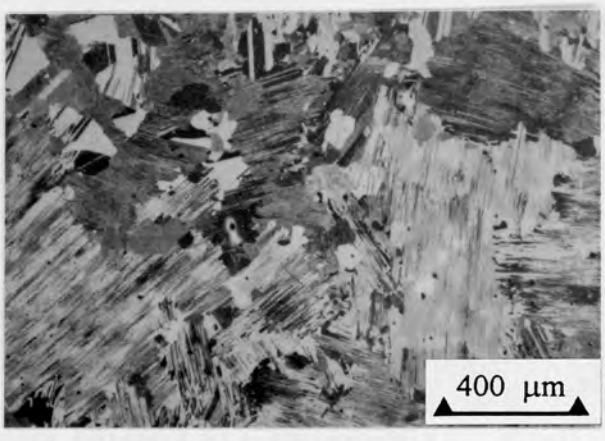

(c)

Figure 44. Light micrographs of as cast Ti-48Al-2Mn-2Nb (at.%) showing the macrostructure and microstructure in the transverse orientation. (a) The macrostructure of the cast ingot consists of an outside rim of columnar grains and equiaxed grains in the central region. (b) This higher magnification image reveals that the columnar grains consist of lamellae. (c) The microstructure of the central region consists of lamellar colonies and equiaxed γ grains.

The microstructure of as cast Ti-48Al-2Mn-2Nb (at.%) in the longitudinal orientation consists of columnar grains containing lamellae near the ingot edge and equiaxed γ grains nearer the centre as shown in Figure 45.

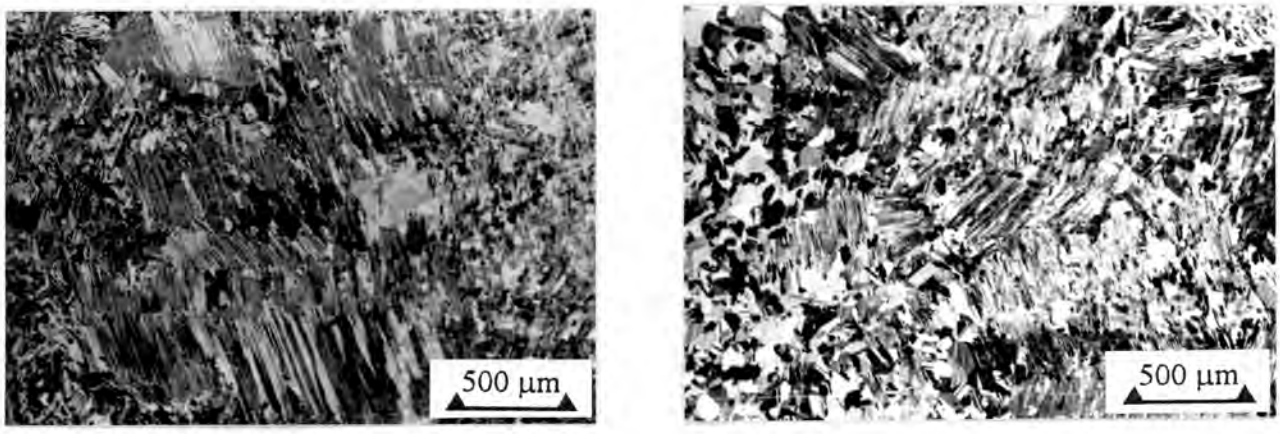

(a) (b)

Figure 45. Light micrographs of the microstructure of as cast Ti-48Al-2Mn-2Nb (at.%) in the longitudinal orientation. (a) The microstructure consists mainly of lamellae colonies and a small volume fraction of equiaxed γ grains. (b) In the radial plane, the microstructure consists of columnar grains containing lamellae near the ingot edge and equiaxed γ grains nearer the centre.

4.1.4.3. *Homogenized microstructure*

The microstructure of homogenized Ti-48Al-2Mn-2Nb (at.%) consists of equiaxed γ grains and needle-like α_2 precipitates and some of the γ grains are twinned as shown in Figure 46. Etching produces fine grooves in the γ grains similar to those observed by Baeslack and co-workers[83] as shown in Figure 46. The bulk hardness of Ti-48Al-2Mn-2Nb (at.%) is retained after homogenization as shown in Table 17. The results of standardless semi-quantitative (S.S.Q.) analysis of homogenized Ti-48Al-2Mn-2Nb (at.%) using a specimen in the transverse orientation near the ingot centre are shown in Table 18.

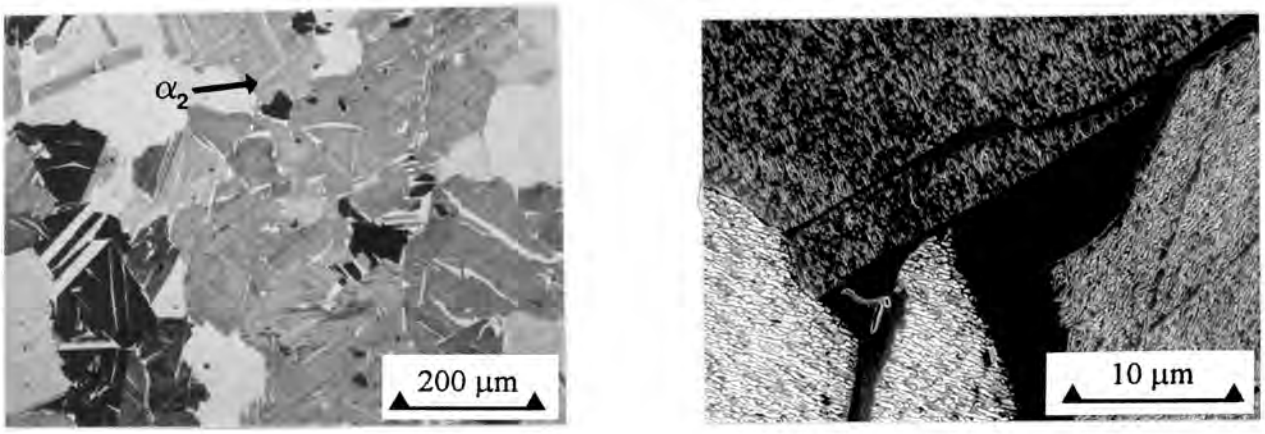

(a) (b)

Figure 46. Light micrographs of the microstructure of homogenized Ti-48Al-2Mn-2Nb (at.%) in the transverse orientation. (a) The microstructure consists of equiaxed γ grains. Some of the γ grains contain annealing twins. Most of the γ grains contain needle-like α_2 precipitates. (b) The higher magnification S.E.M. image shows equiaxed γ grains containing fine etched grooves which are aligned differently from one γ grain to another and the α_2 precipitates indicated in the micrograph are ungrooved.

Table 17. Bulk hardness (HV30) of as cast and homogenised Ti-52Al (at.%) and Ti-48Al-2Mn-2Nb (at.%).

Condition	Ti-52Al (at.%)	Ti-48Al-2Mn-2Nb (at.%)
As cast	182	230
Homogenized	182	230

Table 18. E.D.S. (20 kV) results for homogenized Ti-48Al-2Mn-2Nb (at.%).

Phase	Al (at.%)	Ti (at.%)
Needle-like α_2 precipitates	37±1	60±1
Equiaxed γ grain interior	49±1	47±1

4.1.4.4. *Near-γ heat treatment*

A specimen of as cast Ti-48Al-2Mn-2Nb (at.%) from the side of the ingot disc was heat treated at 1200°C for 4 hours and air cooled. The microstructure, termed "near-γ" in this thesis, consists mainly of equiaxed γ grains and small proportions of α_2 precipitates as shown in Figure 47.

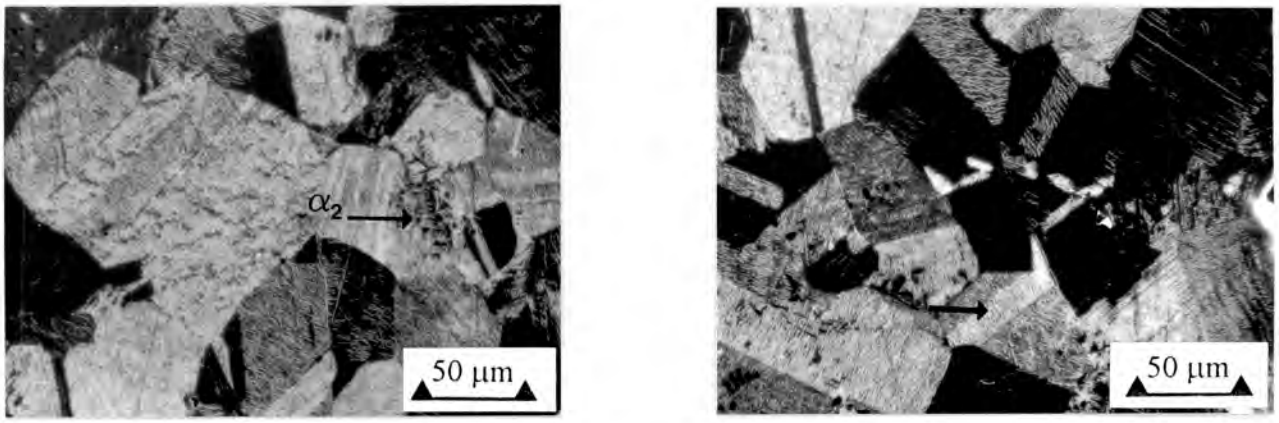

(a) (b)

Figure 47. S.E.M. images of the microstructure of near-γ Ti-48Al-2Mn-2Nb (at.%) in the longitudinal orientation and near the edge of the ingot. (a) The microstructure consists mainly of equiaxed γ grains and a small volume fraction of α_2 precipitates. (b) Twinned γ grains are indicated in this micrograph.

4.2. Particle Erosion

4.2.1. Test Results

The cumulative volume loss versus mass of erodent graphs are shown in Figures 48 and 49 for the titanium aluminide alloys, 304 stainless steel and aluminium 6261, at 90° impact and 30° impact respectively. The normalised steady state particle erosion rates are summarised in Table 19. The erosion rates for glass are two orders of magnitude larger than those of the other experimental materials as shown in Table 19. Greater erosion rates are obtained at 30° impact than at 90° impact for the titanium aluminide alloys, 304 stainless steel and annealed aluminium 6261, while glass exhibits a larger erosion rate at 90° impact than at 30° impact as shown in Table 19. Annealing does not significantly affect the particle erosion rate of Ti-25Al-10Nb-3V-1Mo (at.%) as shown in Table 19. This alloy exhibits superior particle erosion resistance to homogenized Ti-52Al (at.%) and homogenized Ti-48Al-2Mn-2Nb (at.%) at 90° impact.

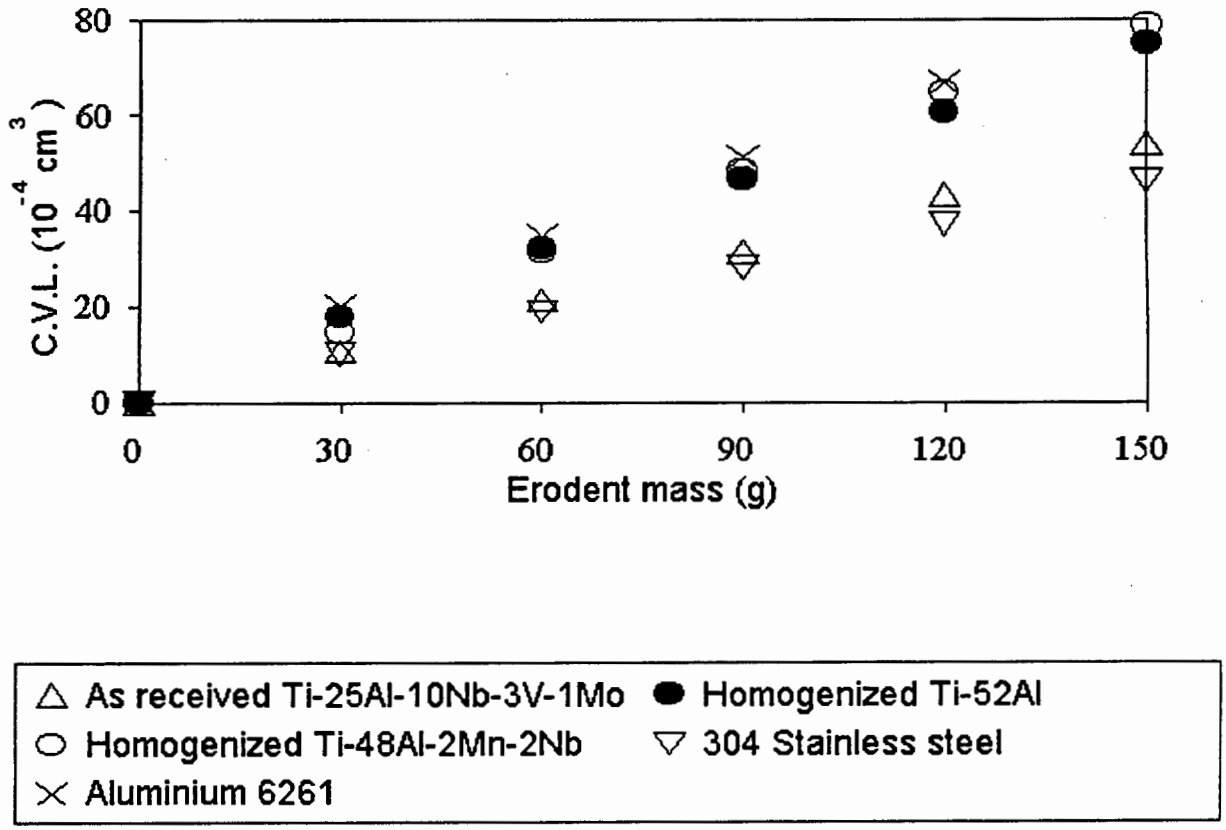

Figure 48. Graphs of cumulative volume loss (C.V.L.) versus mass of erodent at 90° impact for titanium aluminide alloys, 304 stainless steel and annealed aluminium 6261.

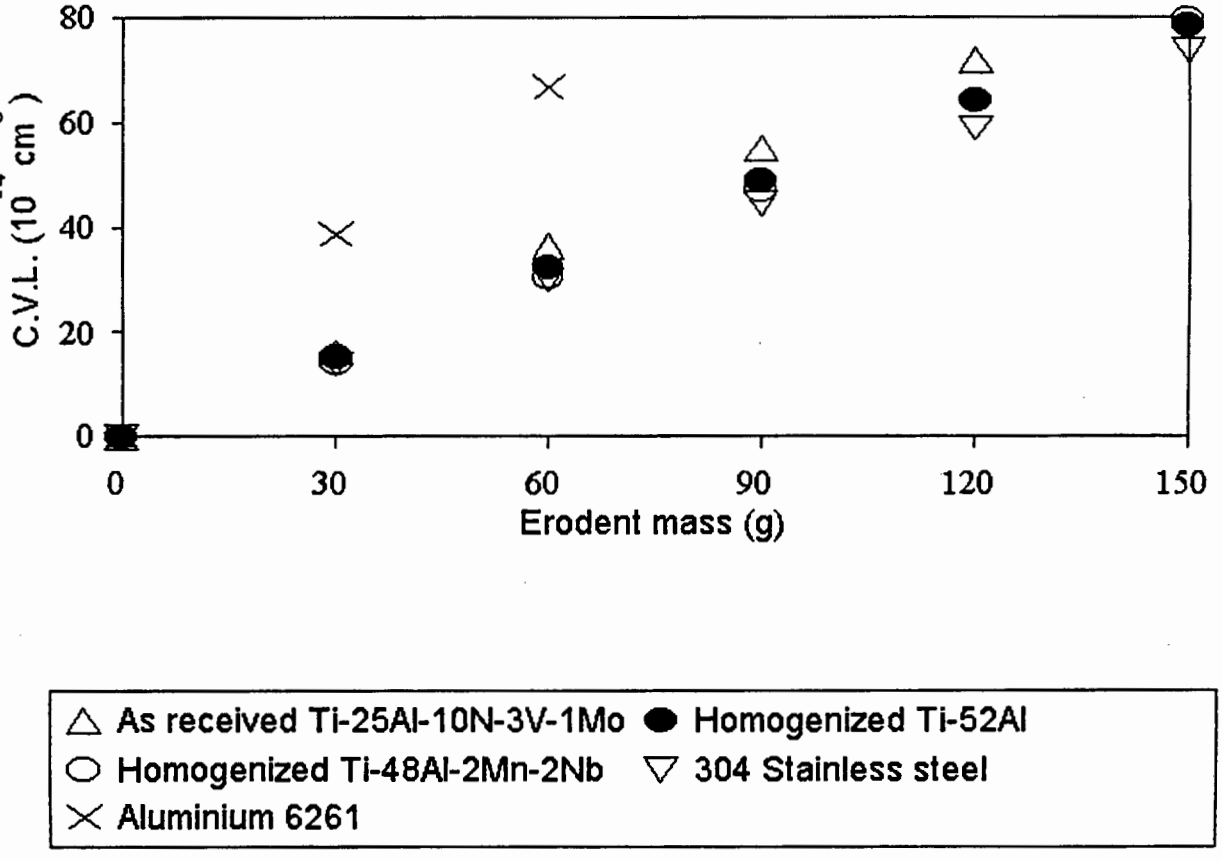

Figure 49. Graphs of cumulative volume loss (C.V.L.) versus mass of erodent at 30° impact for titanium aluminide alloys, 304 stainless steel and annealed aluminium 6261.

Table 19. Normalised steady state particle erosion rates obtained at room temperature with the room temperature apparatus .

Material	Erosion rate ($10^{-6}cm^3/g$)		Erosion rate ratio
	90°	30°	90°/30°
Ti-25Al-10Nb-3V-1Mo (at.%)			
As received	36	59	0.61
Annealed @ temperature for 24 hours, water quenched.			
700°C	36	-	-
800°C	35	-	-
900°C	36	-	-
950°C	36	-	-
1000°C	35	-	-
Homogenized Ti-52Al (at.%)	47	53	0.89
Homogenized Ti-48Al-2Mn-2Nb (at.%)	50	58	0.86
304 Stainless steel	30	49	0.61
Aluminium 6261	53	88	0.60
Glass	4400	1131	3.89

4.2.2. Examination of Particle Eroded surfaces

4.2.2.1. *As received Ti-25Al-10Nb-3V-1Mo (at.%)*

4.2.2.1.1. Single Impact Site Examination

At 90° impact, material is raised above the surface by the erodent particle, both α_2 grains and B2 matrix are plastically deformed and slip lines are produced within α_2 grains adjacent to the impact craters as shown in Figure 50(a). At 30° impact, material is ploughed into a lip on the edge of the crater as shown in Figure 50(b). The distribution of silicon in and around a single impact site are shown in Figure 51. The area in light contrast, i.e. with intense silicon x-ray detection is Si-rich, which identifies it as a SiC erodent particle. The single impact sites are much larger than the microstructural details of as received Ti-25Al-10Nb-3V-1Mo (at.%) as shown in Figure 27.

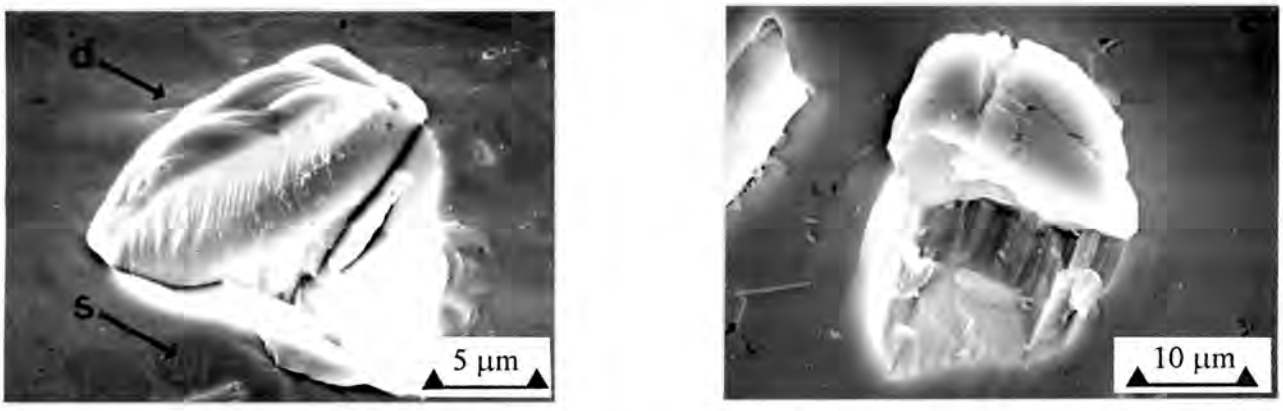

(a) (b)

Figure 50. S.E.M. images of single impact sites on the surface of as received Ti-25Al-10Nb-3V-1Mo (at.%). (a) At 90° impact, material is raised above the surface on more than one side of the crater. Deformed material beyond the lip is indicated by "d". The sets of slip lines adjacent to the impact site are contained within α_2 grains and are indicated by "s". (b) At 30° impact, a lip of material is produced on one side of the crater by cutting and ploughing.

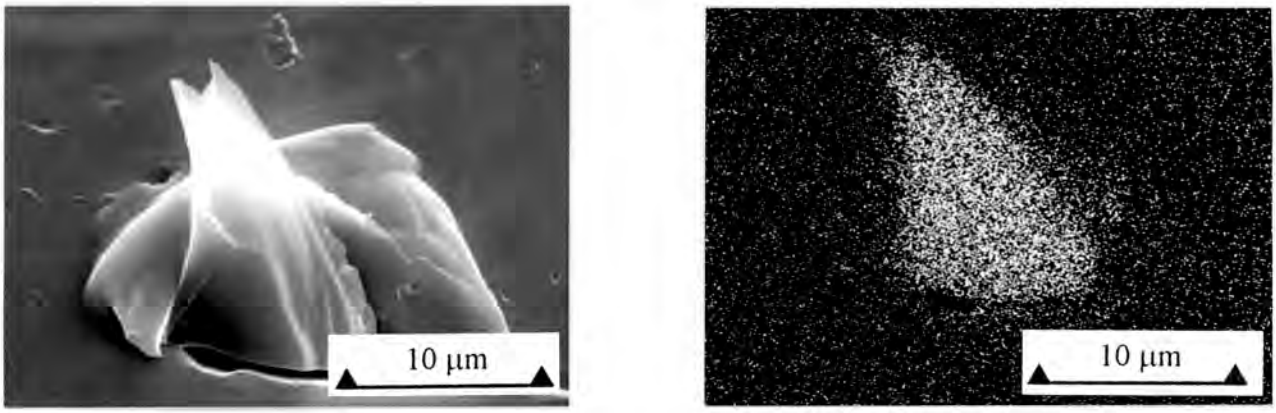

(a) (b)

Figure 51. S.E.M. images of single impact sites on Ti-25Al-10Nb-3V-1Mo (at.%) produced by (a) secondary electron detection and (b) Silicon x-ray detection showing a SiC erodent particle embedded in the surface.

4.2.2.1.2. Steady State Surface Examination

The steady state particle eroded surfaces of Ti-25Al-10Nb-3V-1Mo (at.%) are shown in Figure 52. At 90° impact, valleys in the surface are surrounded by flattened and fractures lips of plastically deformed as shown in Figure 52(a). At 30° impact, the lips produced by single particle impact are flattened against the surface by subsequent impacts and are fractured in places as shown in Figure 52(b).

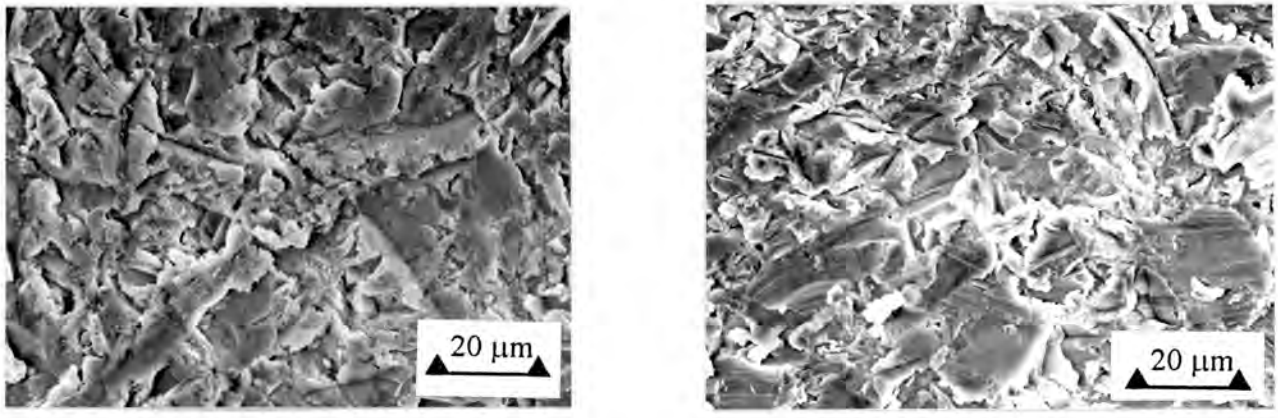

(a) (b)

Figure 52. S.E.M. images of the steady state particle eroded surface of as received Ti-25Al-10Nb-3V-1Mo (at.%). (a) At 90° impact, the eroded surface is characterised by grooves surrounded by deformed material. The deformed material is flattened against the surface by repeated impacts. (b) At 30° impact, the ploughed material is flattened and fractured in places.

4.2.2.1.3. Subsurface Hardening

The results of Knoop microhardness tests on a 5° tapered section of as received Ti-25Al-10Nb-3V-1Mo (at.%) after steady particle erosion at 90° impact shown in Figure 53. The Knoop microhardness of as received Ti-25Al-10Nb-3V-1Mo (at.%) is between 530 HK (15 gf) and 580 HK (15 gf) in the near-surface region (approximately 80 μm wide) and between 400 HK (15 gf) and 530 HK (15 gf) at depths greater than 80 μm from the eroded surface as shown in Figure 53.

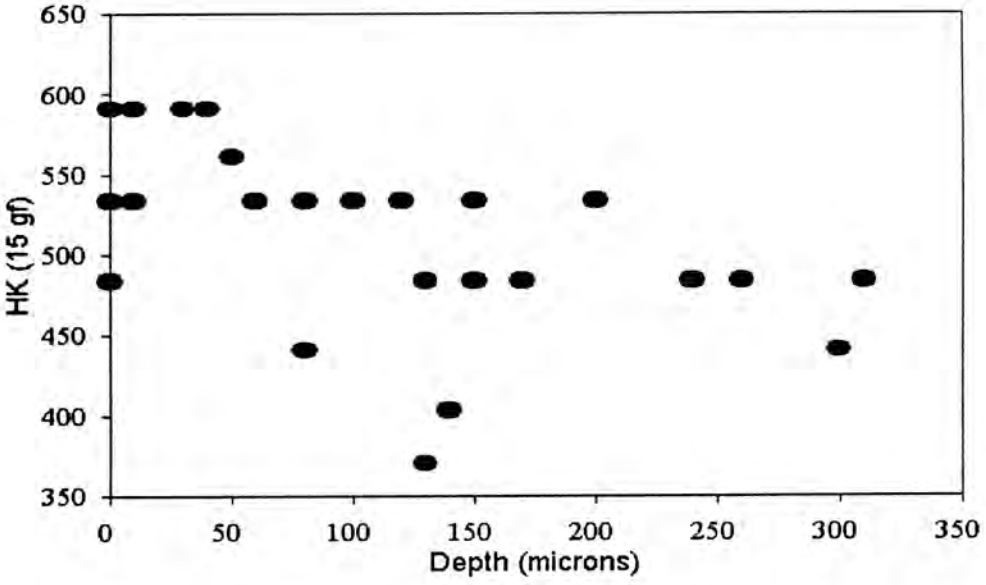

Figure 53. Graph of Knoop microhardness versus depth on a 5° tapered section of as received Ti-25Al-10Nb-3V-1Mo (at.%) after steady state particle erosion at 90° impact.

4.2.2.2. *Homogenized Ti-52Al (at.%)*

4.2.2.2.1. Single Impact Site Examination

Single impact sites on the surface of Ti-52Al (at.%) are shown in Figure 54. At 90° impact, a SiC particle is embedded in the impact crater and lines are produced in the surrounding material, while at 30° impact a lip is formed ahead of the impacting particle and greater deformation is evident at 30° impact than at 90° impact as shown in Figure 54.

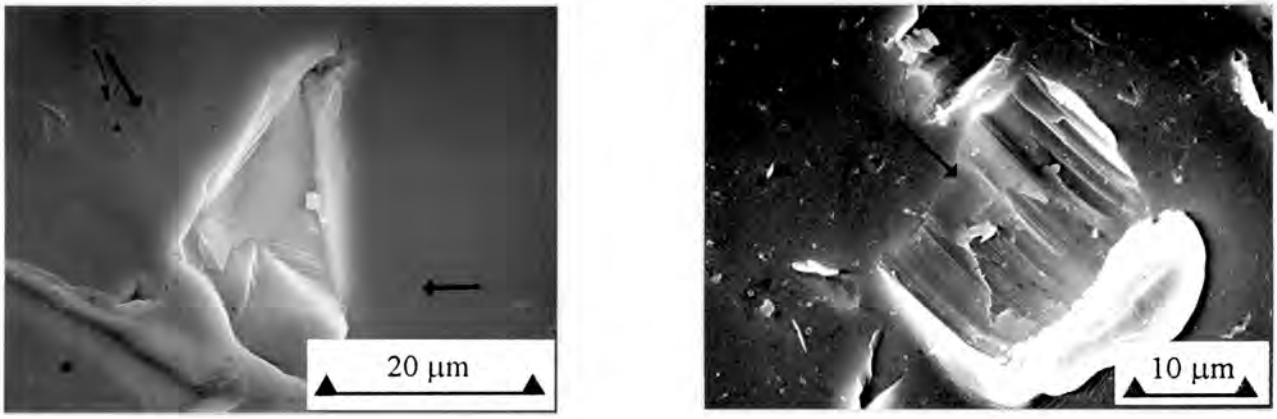

(a) (b)

Figure 54. S.E.M. images of single impact sites on the surface of homogenized Ti-52Al (at.%). (a) At 90° impact a SiC particle is embedded in the surface and slip lines are observed adjacent to the impact crater as indicated in the micrograph. (b) At 30° impact, ploughing and cutting produce a lip of material ahead of the impacting particle. The arrow indicates the direction of particle impact.

4.2.2.2.2. Steady State Surface Examination

The steady state particle eroded surface of homogenized Ti-52Al (at.%) is shown in Figure 55. At 90° impact, grooves are formed in the surface, raised material surrounding the impact crater is flattened against the surface and erodent particle fragments are embedded in some of these grooves as shown in Figure 55(a). At 30° impact, ploughing and cutting, lip formation and surface rupture are evident as shown in Figure 55(b).

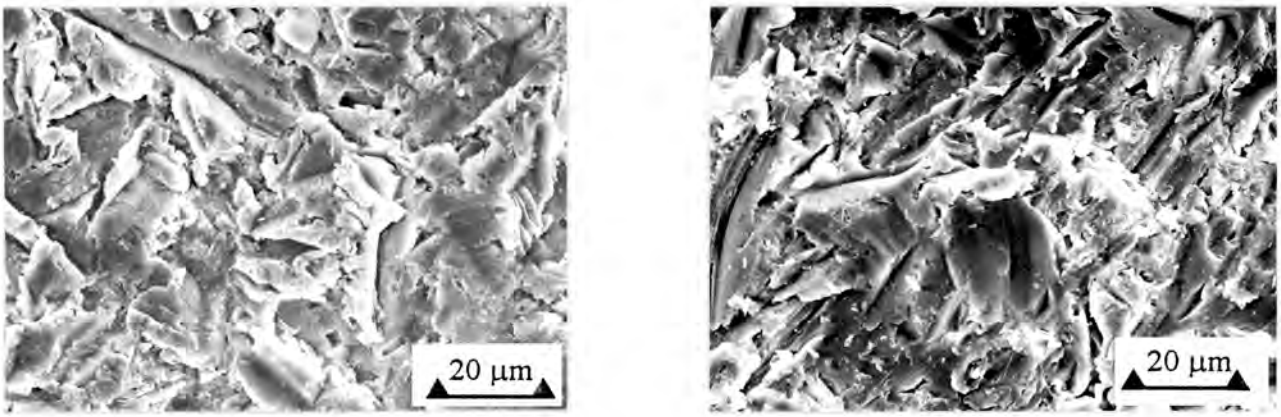

(a) (b)

Figure 55. S.E.M. images of the steady state particle eroded surface of homogenized Ti-52Al (at.%). (a) The surface of the specimen after 90° impact is characterised by grooves and fractured material and embedded SiC particles. (b) At 30° impact, ploughing and cutting, lip formation and fracture of lip material are evident.

4.2.2.3. *Homogenized Ti-48Al-2Mn-2Nb (at.%)*

4.2.2.3.1. Single Impact Site Examination

Single impacts sites on the surface of homogenized Ti-48Al-2Mn-2Nb (at.%) exhibit slip plastic deformation as shown in Figure 56. At 90° impact, material is raised above the surface adjacent to the impact site, while at 30° impact, material is ploughed ahead of the impacting particle and forms a lip of raised material as shown in Figures 56(a) and (b) respectively.

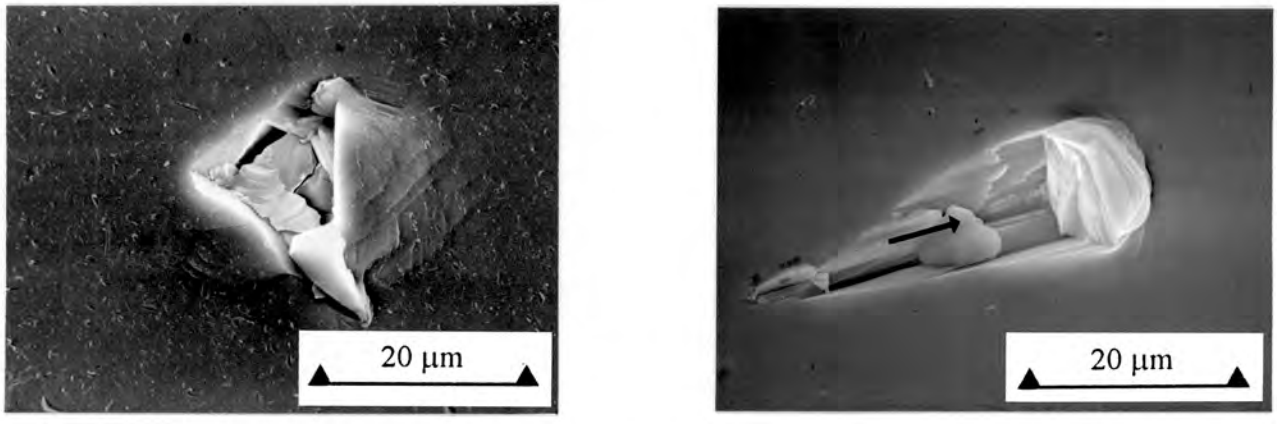

(a) (b)

Figure 56. S.E.M. images of single impact sites on the surface of homogenized Ti-48Al-2Mn-2Nb (at.%). (a) At 90° impact, erodent particles are embedded in the surface and material is raised around the crater. Slip lines are indicated adjacent to the impact crater. (b) At 30° impact, a lip of material is produced by ploughing and cutting.

4.2.2.3.2. Steady State Surface Examination

At 90° and 30° impact, raised lips are flattened against the surface and subsequently fracture as shown in Figures 57(a) and (b). The displacement of surface material is more pronounced during 30° impact due to the more efficient ploughing action at oblique angles as shown in Figure 57(b).

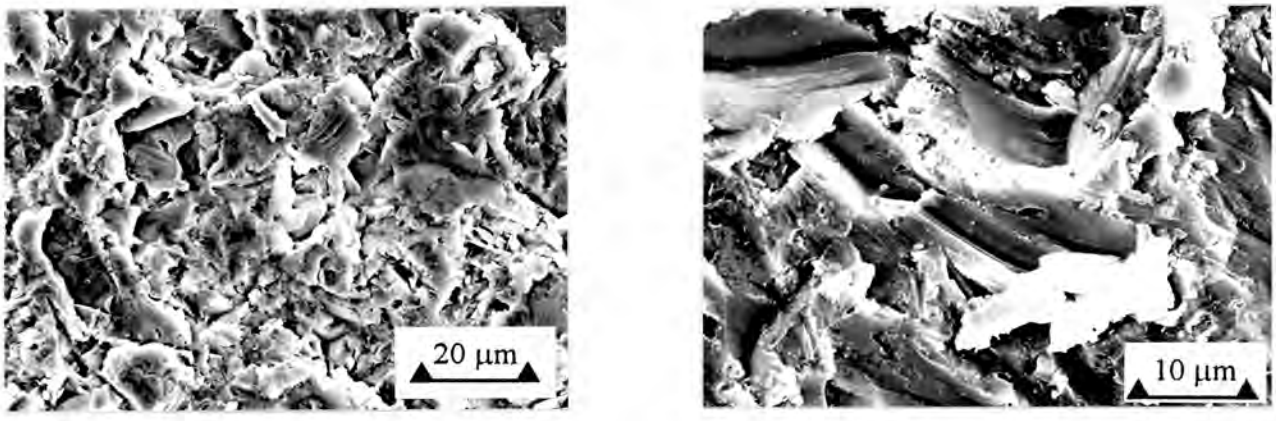

(a) (b)

Figure 57. S.E.M. images of the steady state particle eroded surface of Ti-48Al-2Mn-2Nb (at.%). (a) At 90° impact groove formation, flattening of lip material and micro cracking are observed. (b) At 30° impact groove formation by ploughing and cutting and rupture of heavily deformed material are evident.

4.2.2.4. *Stainless steel*

4.2.2.4.1. Single Impact Site Examination

Single impact sites on the surface of 304 stainless steel exhibit gross plastic deformation and slip lines adjacent to the crater as shown in Figure 58. At 30° impact, material is ploughed into a lip alongside and in front of the impacting particle and material within the crater is ruptured in places as shown in Figure 58(b).

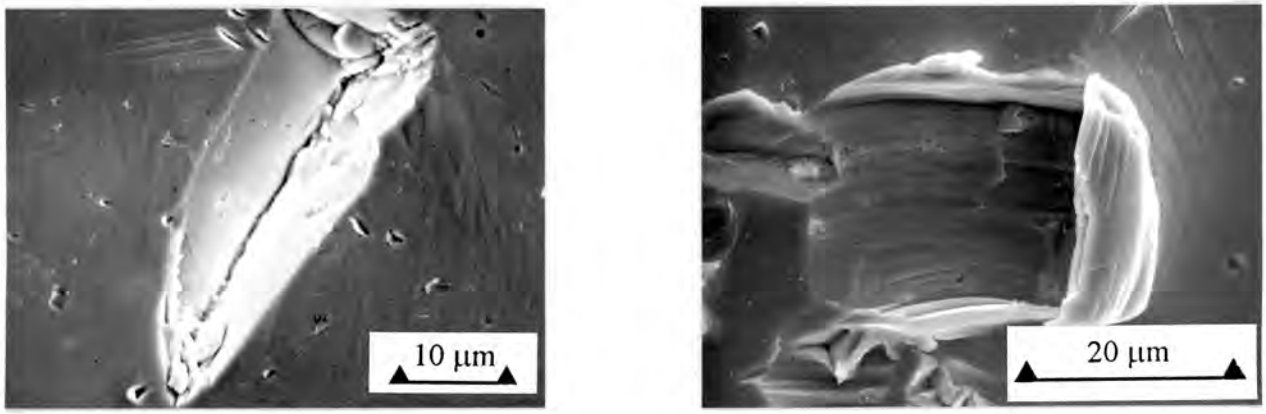

(a) (b)

Figure 58. S.E.M. images of single impact sites on the surface of 304 stainless steel. (a) At 90° impact, slip lines are observed adjacent to the impact site. (b) At 30° impact gross plastic deformation is observed in front and to the sides of the impacting particle.

4.2.2.4.2. Steady State Surface Examination

The steady state eroded surfaces of 304 stainless steel produced by 90° impact contains deep grooves, embedded particles and lips of material that are flattened by successive particle impacts as shown in Figure 59(a). At 30° impact, cutting and ploughing produce large lips which undergo substantial plastic deformation and are flattened against the surface by successive impacts and eventually fracture as shown in Figure 59(b).

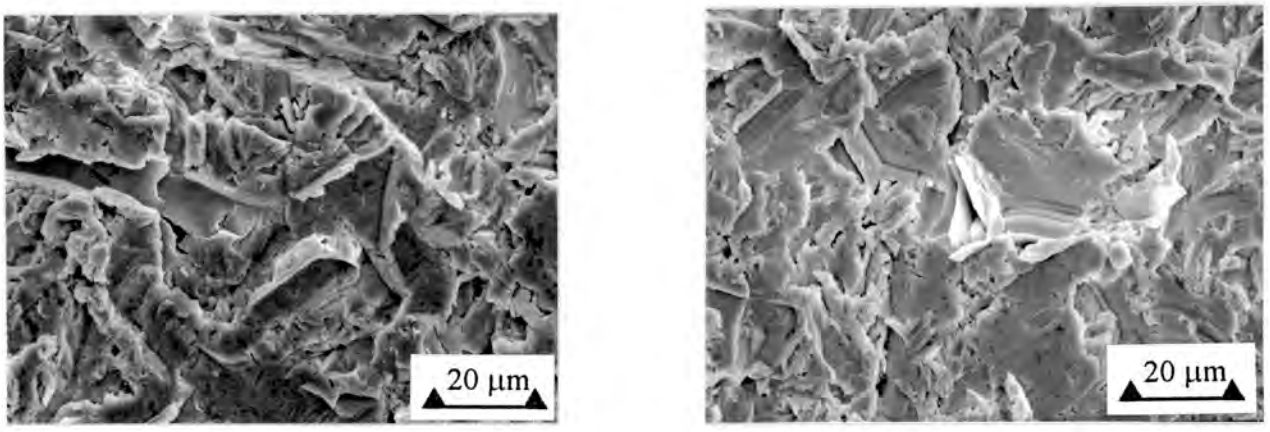

(a) (b)

Figure 59. S.E.M. images of the steady state particle eroded surfaces of 304 stainless steel. (a) At 90° impact, craters are surrounded by flattened and fractured lips . (b) At 30° impact, ploughing and cutting produce highly strained lips of material which are subsequently flattened and eventually fracture.

4.2.2.5. *Annealed Aluminium 6261*

4.2.2.5.1. Single Impact Site Examination

At 90° impact, narrow craters are produced by the impact of angular SiC particles on annealed aluminium 6261 as shown in Figure 60(a). Larger impact sites are produced at 30° impact by the ploughing action of the impacting particle as shown in Figure 60(b).

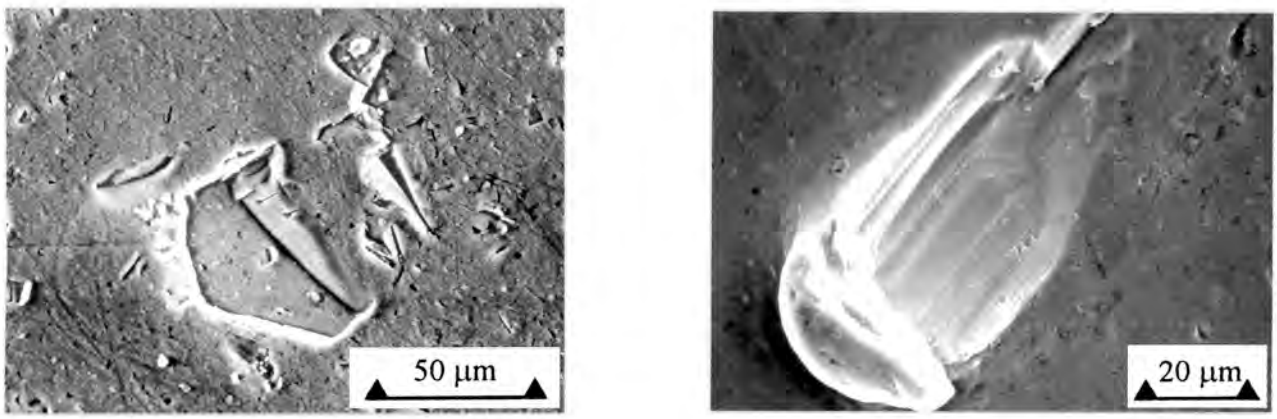

(a) (b)

Figure 60. S.E.M. images of single impact sites on annealed aluminium 6261. (a) At 90° impact, the impact crater are mostly narrow and material within the impact craters is pressed into the surface. (b) At 30° impact, material is ploughed into a lip ahead of the impacting particle.

4.2.2.5.2 Subsurface Hardening

Knoop microhardness indents on annealed aluminium alloy 6261 after steady state particle erosion are plotted as a function of depth below the eroded surface on a 5° tapered section and reveal hardening of the near-surface region as shown in Figure 61. The microhardness of aluminium 6261 decreases from 66 HK (15 gf) to 28 HK (15 gf) after annealing. During particle erosion the microhardness of the near surface region increases to approximately the pre-annealing value as shown in Figure 61.

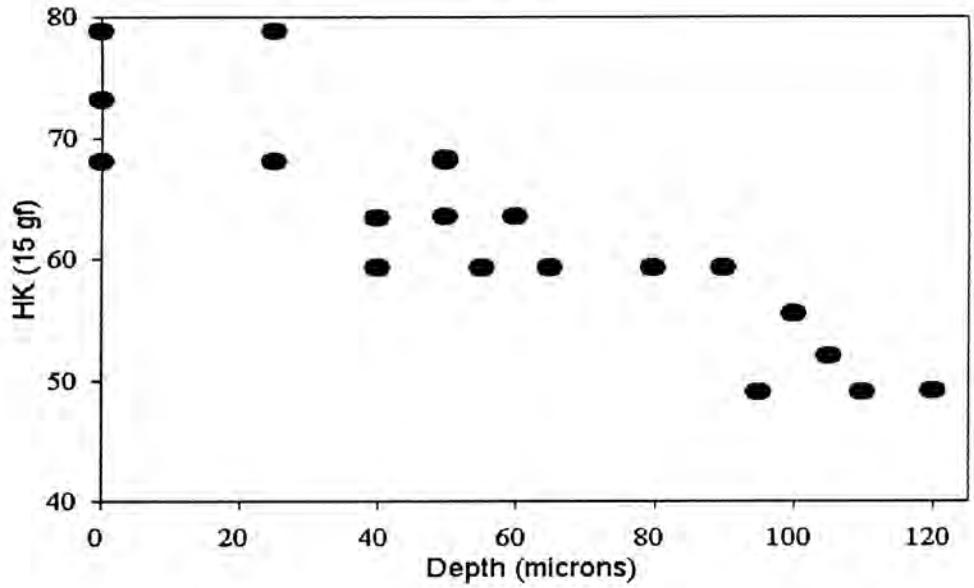

Figure 61. Graph of Knoop microhardness versus depth on a 5° tapered section of annealed aluminium alloy 6261 after steady state particle erosion shows the suburface hardening that is produced by particle erosion.

4.2.2.6. *Glass*

4.2.2.6.1. Single Impact Site Examination

Single impact sites produced by 90° impact on glass exhibit a crushed region in the centre of the impact site, saucer-shaped fracture surfaces with radial striations and concentric ripples and saucer-shaped discs which are barely attached to the surface as shown in Figures 62(a) and (b). Radial and lateral cracks which emanate from the centre of the impact site are shown in Figures 62(a) and (b).

The single impact sites shown in Figure 63 are produced by 30° impact and are similar in appearance to those produced by 90° impact. Radial cracks emanate from the centre of the impact site as shown in Figure 63(a). The centre of the impact site consists of crushed target material and adjacent to it are saucer-shaped fracture surfaces resulting from lateral cracking as shown in Figure 63(b).

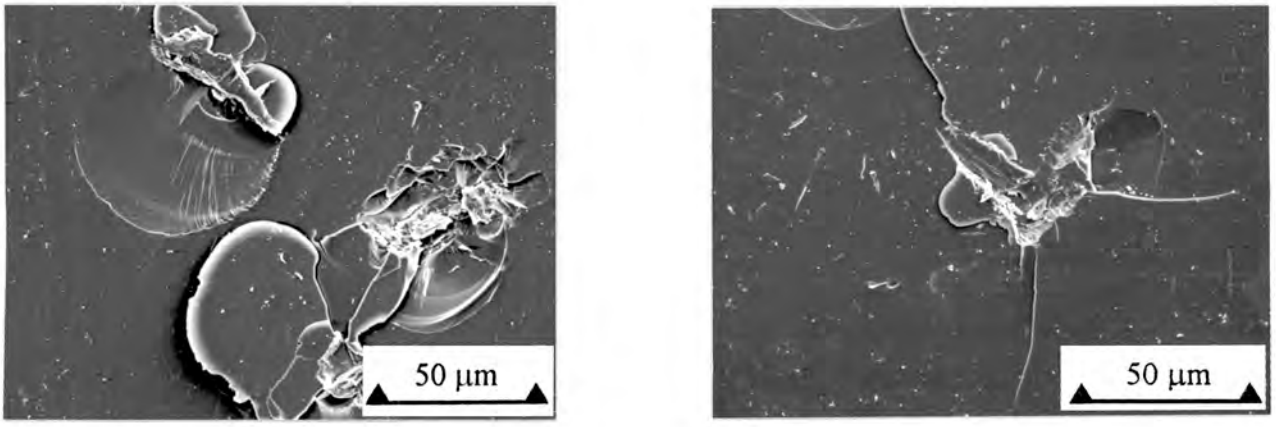

(a) (b)

Figure 62. S.E.M. images of single impact sites produced on glass at 90° impact. (a) Saucer-shaped fracture surfaces and discs of target material are observed on the surface. (b) Radial and lateral cracks emanate from the central crushed zone.

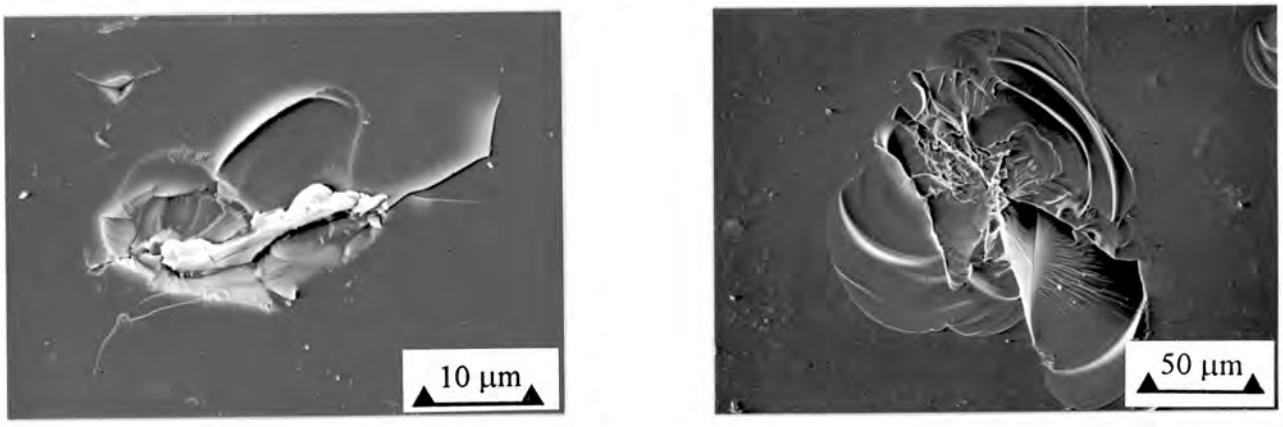

(a) (b)

Figure 63. S.E.M. images of single impact sites produced by 30° impact on glass. (a) Cracks emanate from the impact site. (b) Saucer-shaped fracture surfaces are produced by extensive lateral cracking and contain radial striations and concentric ripples.

4.2.3. The Effect of Temperature on Particle Erosion

The results of particle erosion tests performed with the high temperature apparatus are summarised in Figure 64. The particle erosion rates of the titanium aluminide alloys and 304 stainless steel increase with increasing test temperature. The 25°C particle erosion rates shown in Table 20 are not significantly different from one another, but at 500°C the erosion rates for the titanium aluminides are significantly larger than those for 304 stainless steel. At 300°C, the erosion rates of Ti-52Al (at.%) and Ti-48Al-2Mn-2Nb (at.%) are significantly larger than 304 stainless steel. The increase in the particle erosion rate per unit temperature for Ti-52Al (at.%) is greater between 25°C and 300°C than between 300°C and 500°C and vice versa for Ti-25Al-10Nb-3V-1Mo (at.%) and 304 stainless steel as shown in Figure 64.

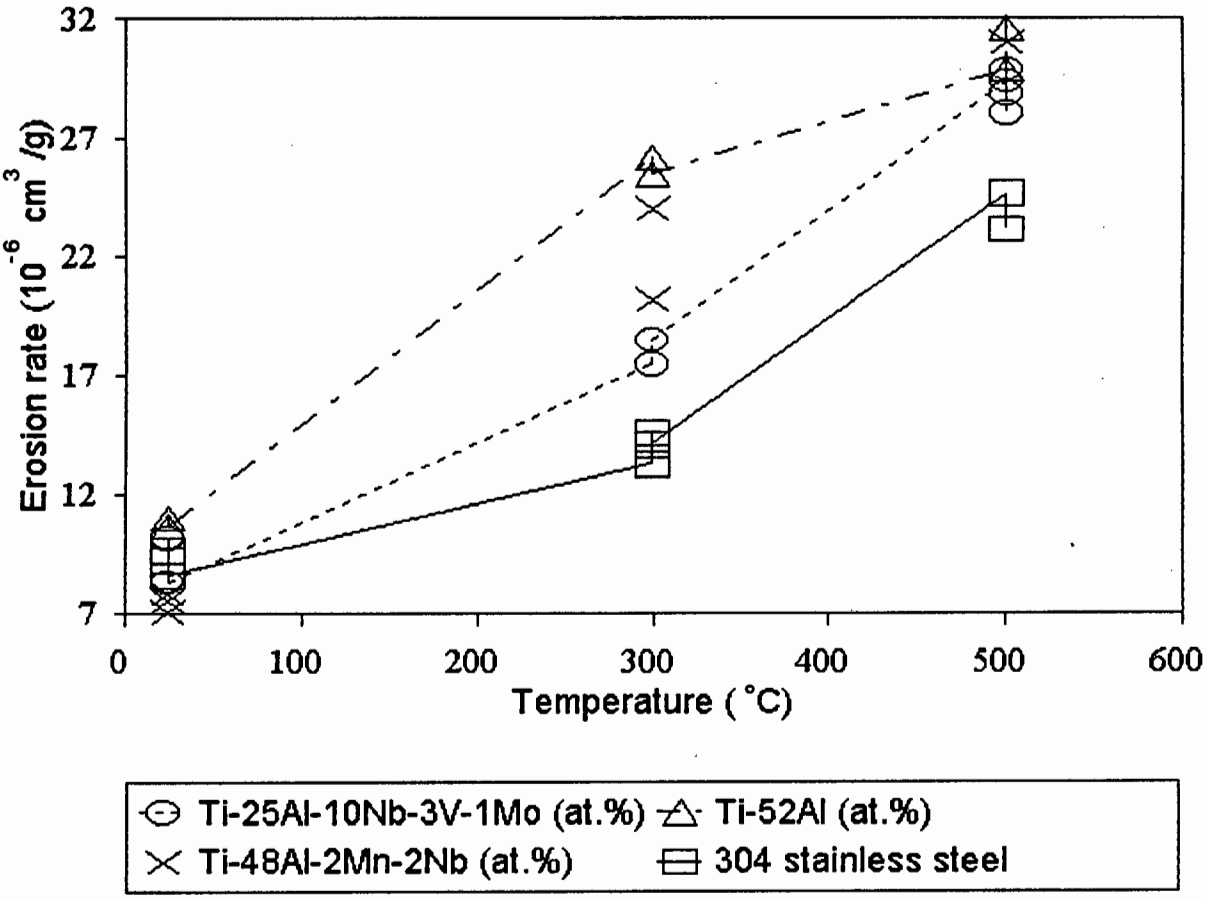

Figure 64. Graph of particle erosion rate as a function of test temperature for tests conducted with the high temperature apparatus. Erosion rate increases with an increase in temperature for the titanium aluminide alloys and 304 stainless steel.

Table 20. Normalised particle erosion rates from tests performed with the high temperature apparatus.

Test temperature (°C)	Particle erosion rate ($10^{-6}cm^3/g$)			
	Ti-25Al-10Nb-3V-1Mo (at.%)	Ti-52Al (at.%)	Ti-48Al-2Mn-2Nb (at.%)	304 stainless steel
25	10	11	8	9
25	10	11	8	10
25	8	-	7	9
300	17	26	24	13
300	18	25	20	15
300	-	-	-	14
500	29	30	31	25
500	29	32	33	23
500	30	-	-	-
500	28	-	-	-

4.2.4. Overview

4.2.4.1. *Single impact features*

Ductile single impact sites are observed on the titanium aluminide alloys, 304 stainless steel and annealed aluminium 6261. The impact craters are between 10 μm and 20 μm wide and material is displaced from the surface into a lip around the crater. Line features are produced within some impact craters by the features on the surface of the SiC erodent particles and SiC fragments are still firmly embedded in many of the craters after ultrasonic cleaning. Slip lines are observed adjacent to some of the single impact on the titanium aluminide alloys and 304 stainless steel. Greater plastic deformation is observed at the single impact sites on 304 stainless steel and aluminium 6261 than those on the titanium aluminide alloys. At 90° impact, grooves are formed in the target surface and material is piled up on the crater edges, and at 30° impact, material is ploughed into a lip by the obliquely impacting particle, mainly on one side of the crater.

Glass exhibits brittle single impact sites with radial and lateral cracks. Lateral cracking produces flakes which are either loosely attached to the surface or completely removed from the surface and accounts for the majority of material loss during particle erosion.

4.2.4.2. *Steady state features*

The particle erosion rates of the titanium aluminide alloys, 304 stainless steel and annealed aluminium 6261 are larger at 30° impact than 90° impact and the steady state particle eroded surfaces consist of highly strained and flattened material which is fractured in places. In contrast, glass exhibits a larger particle erosion rate at 30° impact than at 90° impact.

4.3. Cavitation Erosion

4.3.1. Test results

The incubation periods and steady state erosion rates of the experimental materials are shown in Table 21.

Table 21. Results of cavitation erosion tests, hardness measurements and % α_2 measurements.

Material and heat treatment condition	Hardness (HV30)	% α_2	Steady state erosion rate (10^{-5} cm^3/hour)	Incubation period (hours)
Ti-25Al-10Nb-3V-1Mo				
As received	420	48±4	8	7
Annealed for 24 hours				
700°C	370	54±3	12	7
800°C	342	52±4	14	7
900°C	350	62±4	13	6
950°C	350	54±3	-	-
1000°C	382	71±3	11	5
Aged @ 650°C	505	-	6	7
Ti-52Al (at.%) Homogenized	182	-	5	5
Ti-48Al-2Mn-2Nb Homogenized	230	-	5	6
Near-γ	225	-	3	7
304 stainless steel	177	-	78	3
WC-15Co (wt.%)	1050	-	11	5
Annealed Aluminium 6261	28	-	2962	0.2
Soda-lime-silica glass	540[97]	-	292	0.2

4.3.2. Ti-25Al-10Nb-3V-1Mo (at.%)

The cumulative volume loss of Ti-25Al-10Nb-3V-1Mo (at.%) versus time of erosion in the as received and annealed and aged conditions is shown in Figure 65. The cumulative volume loss versus time curves for as received and heat treated specimens of Ti-25Al-10Nb-3V-1Mo (at.%) exhibit an initial period of small material loss and an extended period of steady state material removal, as shown in Figure 65. The annealed specimens exhibit larger cavitation erosion rates than the as received and aged (650°) specimens as shown in Table 21.

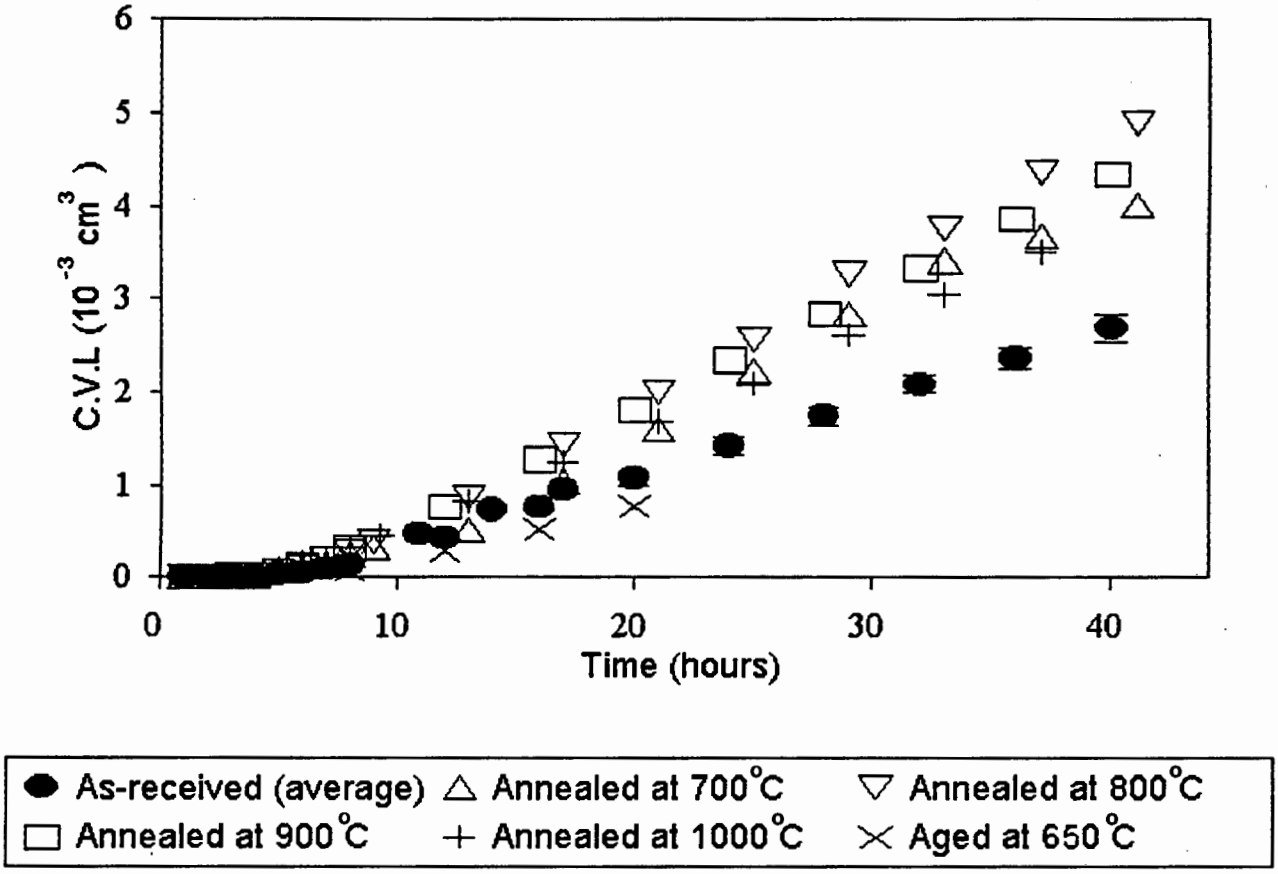

Figure 65. Graphs of cumulative volume loss (C.V.L.) versus time of exposure to cavitation erosion for Ti-25Al-10Nb-3V-1Mo (at.%). The results are shown for as received specimens (the average of four tests), specimens that were annealed for 24 hours at the temperatures shown and for a specimen that was aged for 2 hours at 650°C.

4.3.2.1. *Transition Region Examination*

The transition region, i.e. the region between the central steady state cavitation eroded region and the polished edge of the specimen, reveals light damage and provides information regarding the initiation of damage as shown in Figure 66. The primary α_2/B2 grain boundaries within the transition regions of as received and annealed (800°C) Ti-25Al-10Nb-3V-1Mo (at.%) appear to experience high local deformation as shown in Figure 66(a).

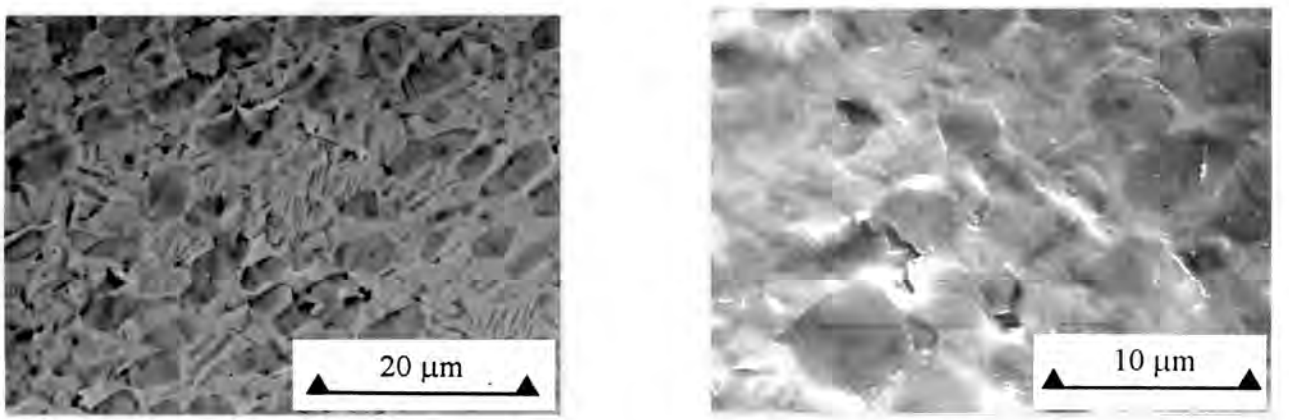

(a) (b)

Figure 66. S.E.M. images of the transition region of Ti-25Al-10Nb-3V-1Mo (at.%), i.e. at the edge of the area of severe cavitation. (a) The detection of a mixed secondary- and back-scattered electron signal reveals the microstructure and cavitation erosion damage on an as received specimen. Deformation at α_2/B2 grain boundaries is indicated. (b) Secondary electron image from an annealed (800°C) specimen showing faint phase contrast and deformation of the α_2 and B2 phases and pronounced strain at α_2 grain boundaries.

4.3.2.2. *Steady State Examination*

The steady state cavitation eroded specimens of as received and annealed Ti-25Al-10Nb-3V-1Mo (at.%) exhibit streaking in the direction of primary α_2 grain elongation such as shown in Figure 67(a). The steady state cavitation eroded surface of as received Ti-25Al-10Nb-3V-1Mo (at.%) after a 20 hour test reveals mainly brittle fracture and some smeared ductile areas as shown in Figure 67(b).

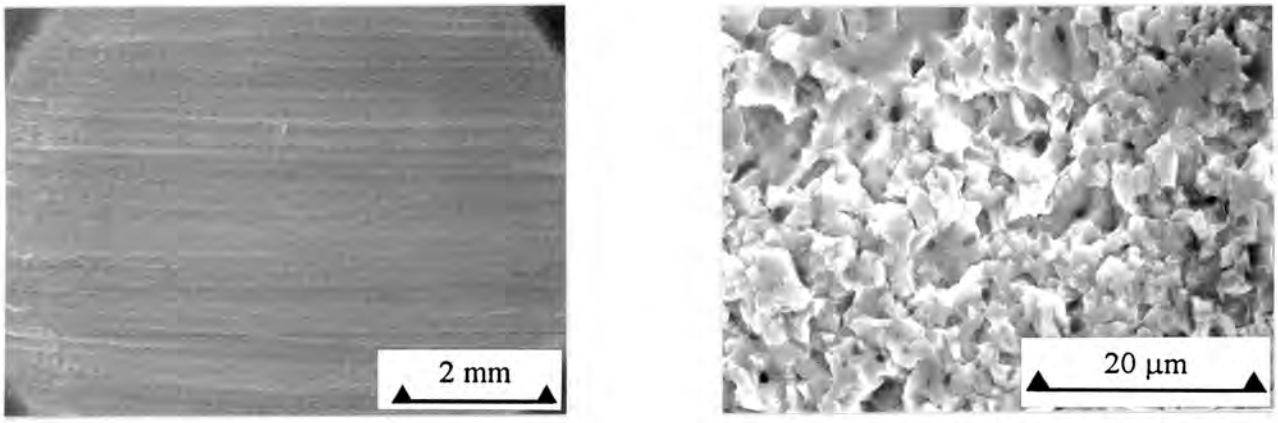

(a) (b)

Figure 67. S.E.M. images of the steady state cavitation eroded specimens of as received Ti-25Al-10Nb-3V-1Mo (at.%). (a) Streaks are evident on the surface when viewed at low magnification after exposure to cavitation erosion for 40 hours. (b) When viewed at high magnification after exposure to cavitation erosion for 20 hours the surface is smeared in places, but consists mainly of brittle fracture surfaces.

High magnification images of the cavitation eroded surface of as received Ti-25Al-10Nb-3V-1Mo (at.%) after exposure for 18 hours are shown in Figure 68 and reveal fractured surface material and lines on the side of a hole in the surface which is similar in size to the primary α_2 grains. It appears as if the primary α_2 grains are plucked out of the more ductile B2 matrix.

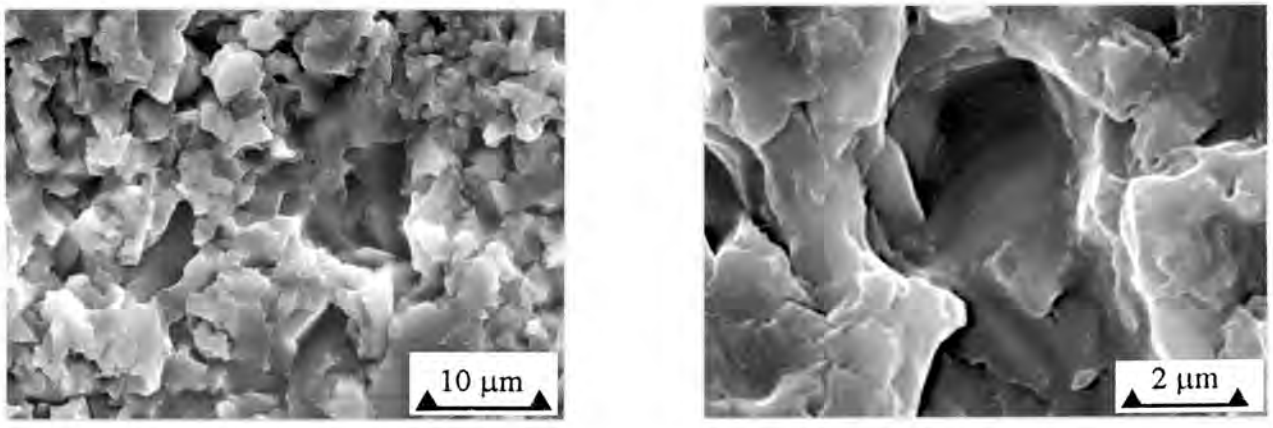

(a) (b)

Figure 68. S.E.M. images of the steady state cavitation eroded (18 hours) surface of as received Ti-25Al-10Nb-3V-1Mo (at.%) exhibits (a) fracture surfaces and (b) lines on the side of a hole in the surface.

The steady state cavitation erosion damage and subsurface microstructure of Ti-25Al-10Nb-3V-1Mo (at.%) are revealed by selective electropolishing, as described in section 3.9, and shown in the micrograph in Figure 69. The valleys in the cavitation eroded surface are similar in size to the primary α_2 grains as shown in Figure 69. This is consistent with the streaking parallel to the direction of α_2 grain elongation, since the preferential removal of the primary α_2 grains and the deformation of the surrounding B2 matrix produce elongated troughs and peaks on the cavitation eroded surface which have a streaked appearance when viewed at low magnification as shown in Figure 67.

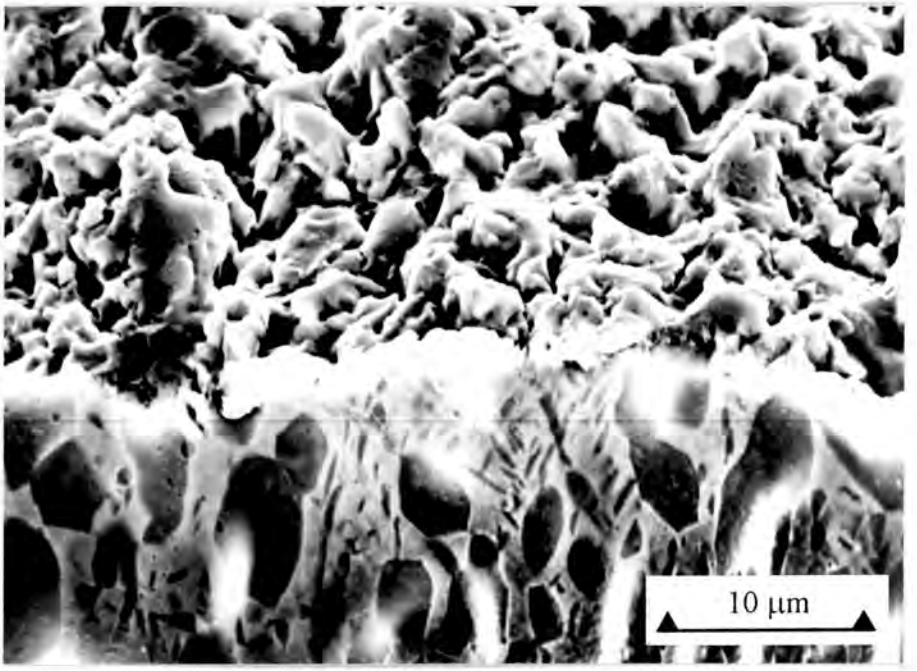

Figure 69. S.E.M. image of the groove formed by electropolishing the partially lacquered cavitation eroded surface of Ti-25Al-10Nb-3V-1Mo (at.%). The surface valleys are similar in size to the primary α_2 grains in dark contrast.

4.3.2.3. *X-ray diffraction*

X-ray diffraction spectra obtained from as received Ti-25Al-10Nb-3V-1Mo (at.%) before and after steady state cavitation erosion reveal that the intensity of x-rays diffracted by the α_2 (002) planes relative to the intensity of x-rays diffracted by the B2 (110) planes decreases after cavitation erosion as shown in Table 22. This suggests that the volume fraction of the α_2 phase relative to that of the B2 phase is reduced, i. e. that the phase is preferentially removed during cavitation erosion.

Table 22. X-ray diffraction integrated peak intensities for Ti-25Al-10Nb-3V-1Mo (at.%) before and after 40 hours of cavitation erosion.

2-Theta	phase and hkl plane	I x 100 / I (α_2(002))	
		Before	After
36.0	α_2 (200)	10	10
39.0	α_2 (002)	100	100
39.5	β (110)	117	201
41.0	α_2 (201)	23	20
54.0	α_2 (202)	3	5
57.0	β (200)	5	6
71.5	β (211)	24	34

4.3.2.4. *Subsurface Microhardness Tests*

Knoop microhardness profiles for as received and annealed (800°C) Ti-25Al-10Nb-3V-1Mo (at.%) which have been cavitation eroded for 40 hours are shown in Figure 70. Neither of these graphs show a clear increase of microhardness with decreasing distance from the cavitation eroded surface; most of the microhardness values are between 450 HK (15 gf) and 550 HK (15 gf) for both specimens as shown in Figure 70.

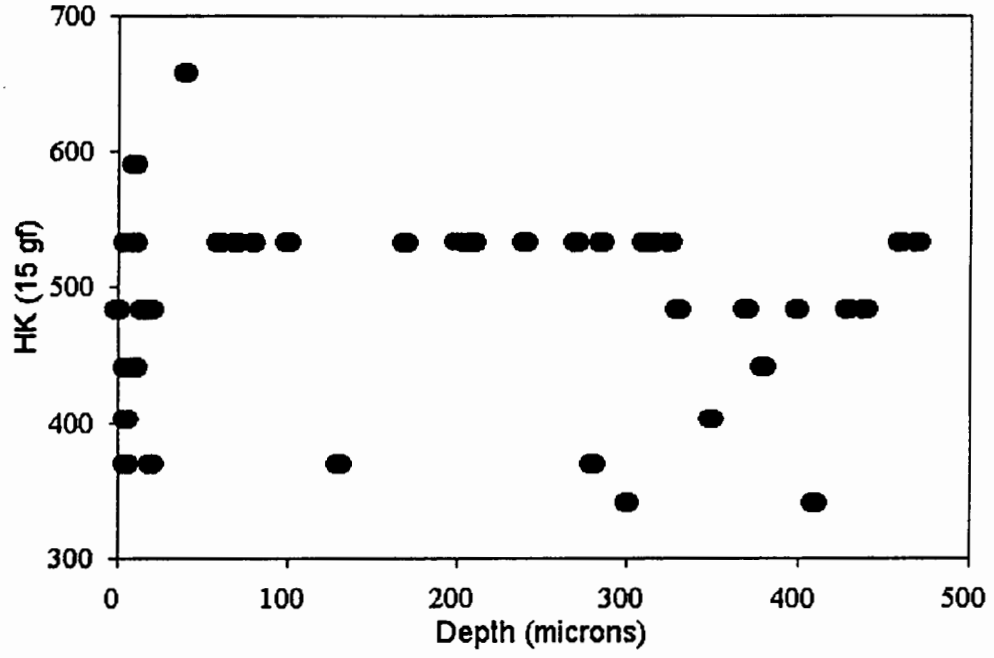

(a)

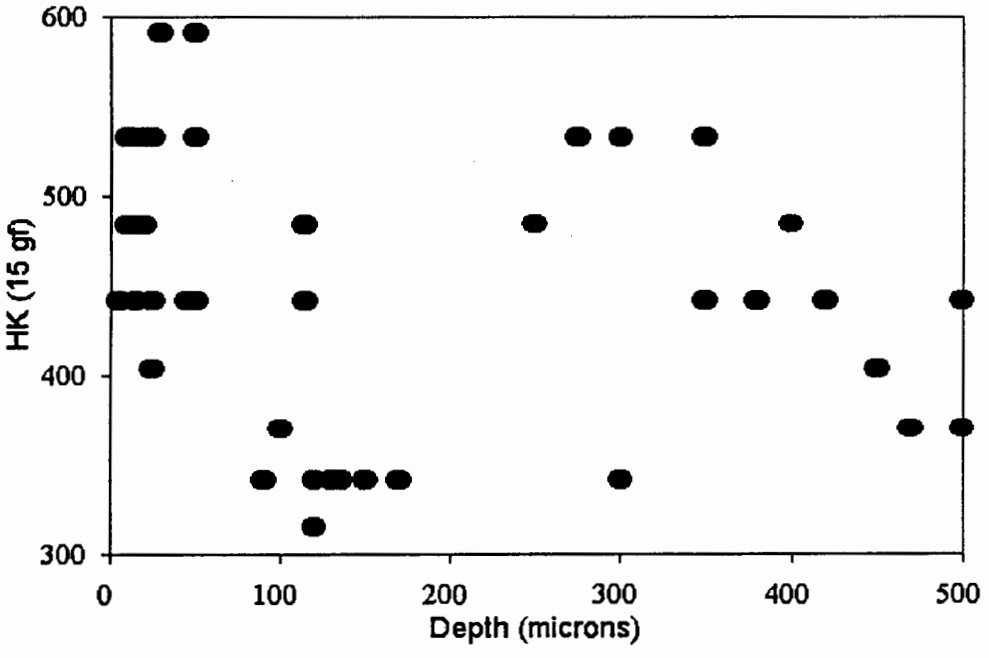

(b)

Figure 70. Knoop microhardness (HK 15 gf) versus depth profiles on 5° tapered sections of Ti-25Al-10Nb-3V-1Mo (at.%) after 40 hours of cavitation erosion. (a) As received Ti-25Al-10Nb-3V-1Mo (at.%). (b) Annealed (800 °C) Ti-25Al-10Nb-3V-1Mo (at.%).

4.3.3. Test results for Ti-52Al (at.%) and Ti-48Al-2Mn-2Nb (at.%).

The graphs of cumulative mass loss versus time of cavitation erosion are shown in Figure 71 for homogenized Ti-52Al (at.%) and homogenized and near-γ Ti-48Al-2Mn-2Nb (at.%).

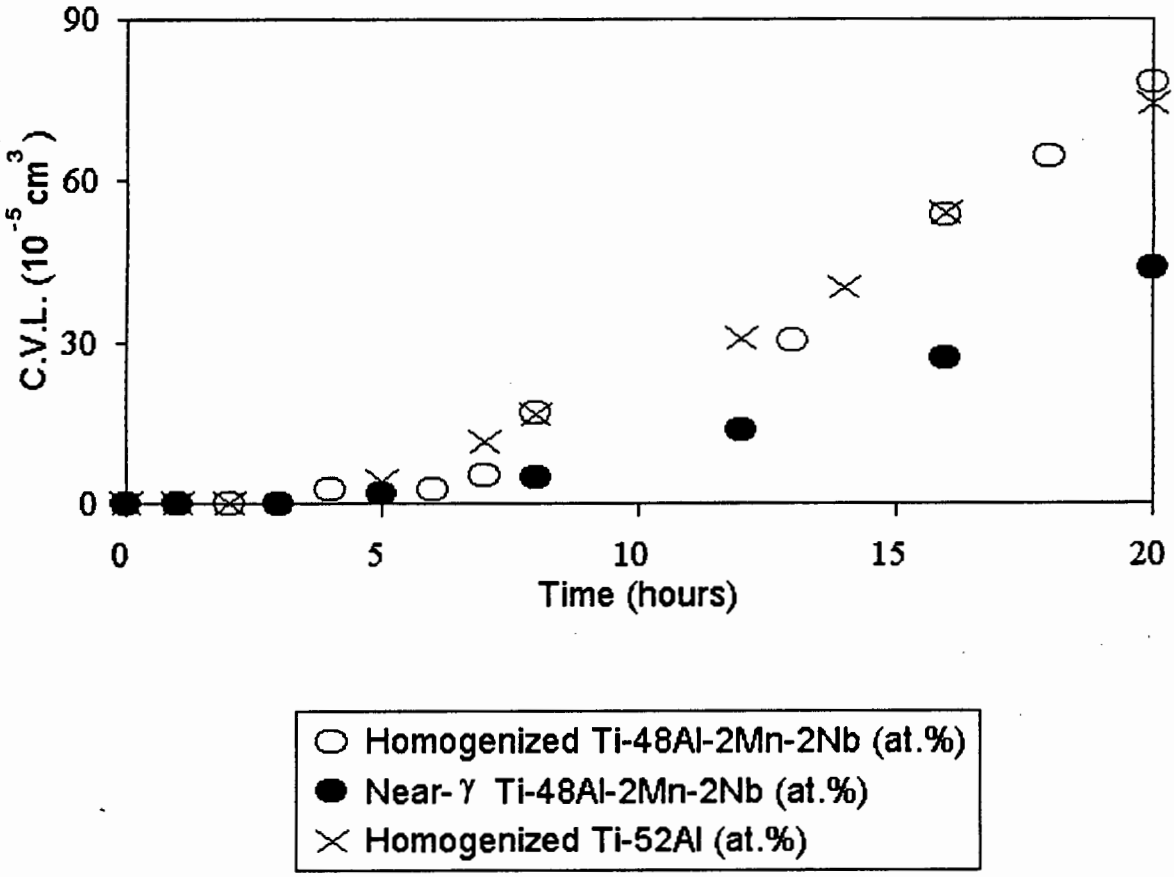

Figure 71. Graph of cumulative volume loss (C.V.L.) versus time of cavitation erosion for homogenized Ti-52Al (at.%), homogenized Ti-48Al-2Mn-2Nb (at.%) and near-γ Ti-48Al-2Mn-2Nb (at.%).

4.3.4. Homogenized Ti-52Al (at.%)

4.3.4.1. *Transition Region*

The transition region of homogenized Ti-52Al (at.%) exhibits mainly thick deformation lines and some fainter crossed lines, such as those shown in Figure 72. The thick lines are grouped in parallel sets, with each set comprising lines of a single orientation. Material is removed from the grain boundaries and along the deformation lines as shown in Figure 73.

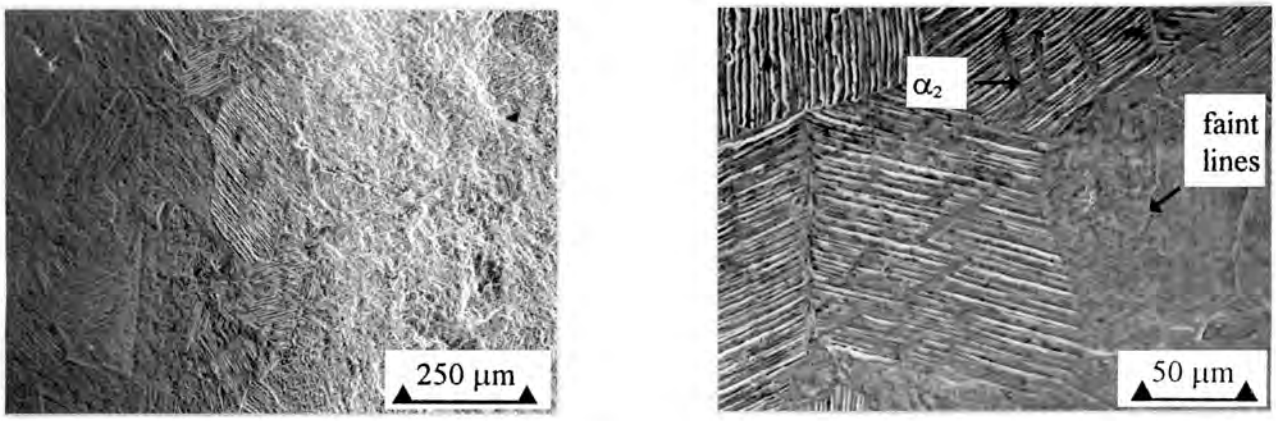

(a) (b)

Figure 72. S.E.M. images of the transition region of the steady state cavitation eroded surface of homogenized Ti-52Al (at.%). (a) Erosion damage increases towards the centre of the specimen, i.e. from left to right in the micrograph. Thick deformation lines are observed within the area of lighter erosion. The deformation lines in the area of heavier damage are unclear because of material removal. (b) Faint crossed lines and thick deformation lines are observed in the transition region as shown in this micrograph. Material is removed from the thick deformation lines as observed in the top left hand corner of the micrograph.

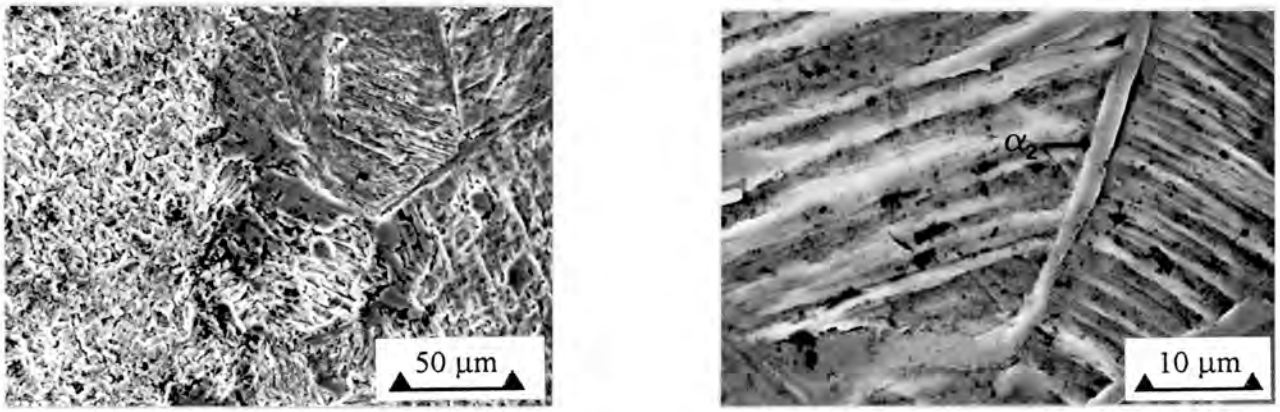

(a) (b)

Figure 73. S.E.M. images of the transition region of homogenized Ti-52Al (at.%). (a) Material loss occurs at the deformation lines which are evident in Figure 72. (b) Fracture at an equiaxed γ grain boundary is observed. A grain boundary α_2 precipitate is delineated by material removal from the interface with the matrix.

4.3.4.2. *Steady state cavitation erosion*

The steady state cavitation eroded surface of Ti-52Al (at.%) consists of sets of parallel troughs and flat areas in dark contrast such as those shown in Figure 74. Some of the troughs have cleavage-type fracture markings and the flat eroded areas contain surface cracks.

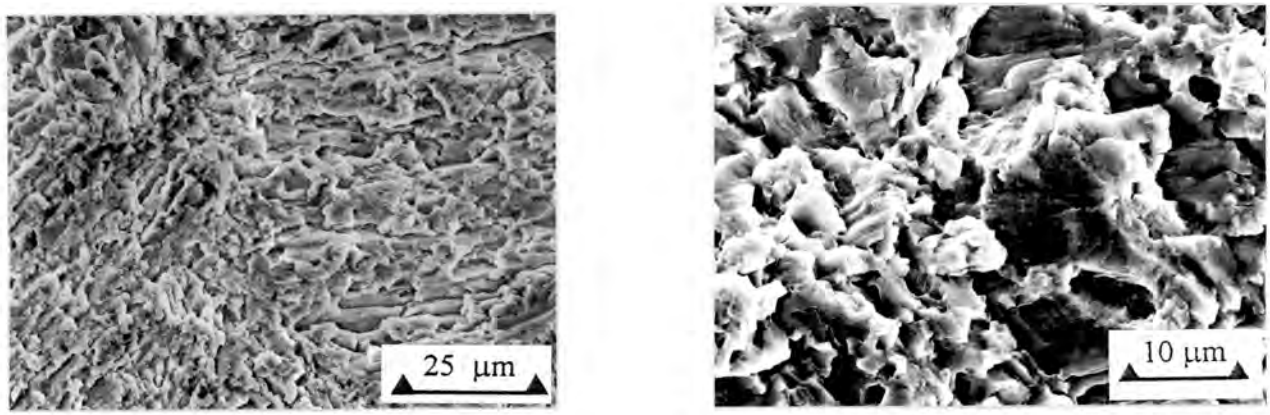

(a) (b)

Figure 74. S.E.M. images of the steady state cavitation eroded surface (20 hours) of Ti-52Al (at.%). (a) Parallel surface troughs. (b) The higher magnification image shows fracture markings in the troughs and surface cracks on the flatter areas.

4.3.5. Homogenized Ti-48Al-2Mn-2Nb (at.%)

4.3.5.1. *Transition Region*

The transition region of homogenized Ti-48Al-2Mn-2Nb (at.%) exhibits sets of thick parallel deformation lines, α_2 precipitates and faint lines crossing the thick lines as shown in Figure 75. α_2 precipitates intersect the thick lines and the flat areas are cracked. Surface fracture of homogenized Ti-48Al-2Mn-2Nb (at.%) is shown in Figure 76.

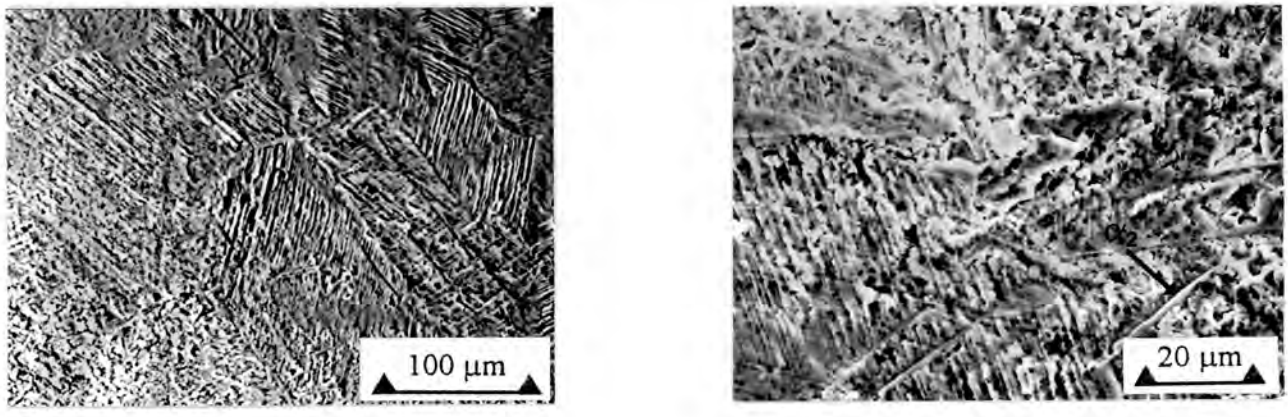

(a) (b)

Figure 75. S.E.M. images taken from the transition region of cavitation eroded Ti-48Al-2Mn-2Nb (at.%). (a) Sets of thick parallel lines from which material is removed are shown. (b) The needle-like α_2 precipitates and faint lines cross the thick lines.

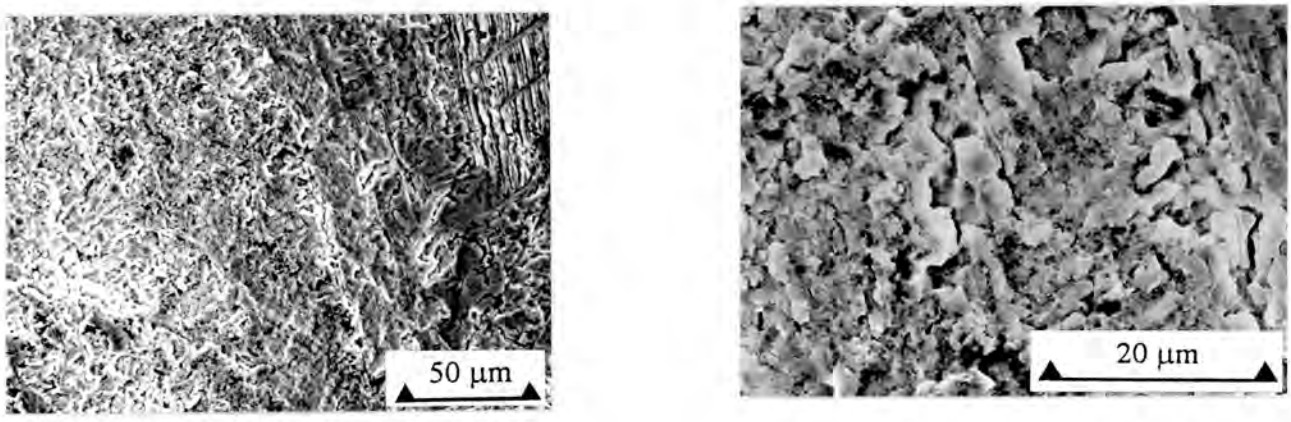

(a) (b)

Figure 76. S.E.M. images taken from the transition region of homogenized Ti-48Al-2Mn-2Nb (at.%). (a) Thick lines in the top right hand corner of the micrograph are intersected by α_2 precipitates, while flat eroded areas are observed to the left of these lines. (b) A higher magnification image shows surface fracture and material removal from the deformation lines.

4.3.5.2. *Steady state cavitation erosion*

The steady state cavitation eroded surface of homogenized Ti-48Al-2Mn-2Nb (at.%) after the completion of a 20 hour test exhibits mainly brittle fracture in the form of parallel elongated surface troughs which are confined to areas similar in size to the equiaxed γ grains as shown in Figure 77. Other areas on the steady state cavitation eroded surface do not contain elongated troughs, but exhibit more equiaxed and faceted fracture surfaces such as those shown in Figure 78.

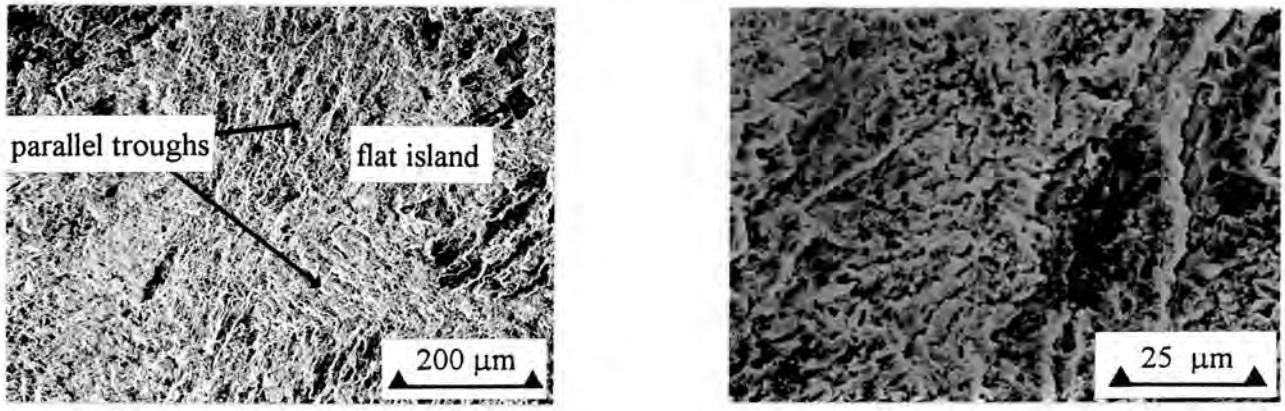

(a) (b)

Figure 77. S.E.M. images of the steady state cavitation eroded surface of homogenized Ti-48Al-2Mn-2Nb (at.%) after a 20 hour test. (a) Sets of parallel troughs and flat islands are indicated. (b) The flat area contains isolated cracks and the fractures on the adjacent region are aligned roughly parallel.

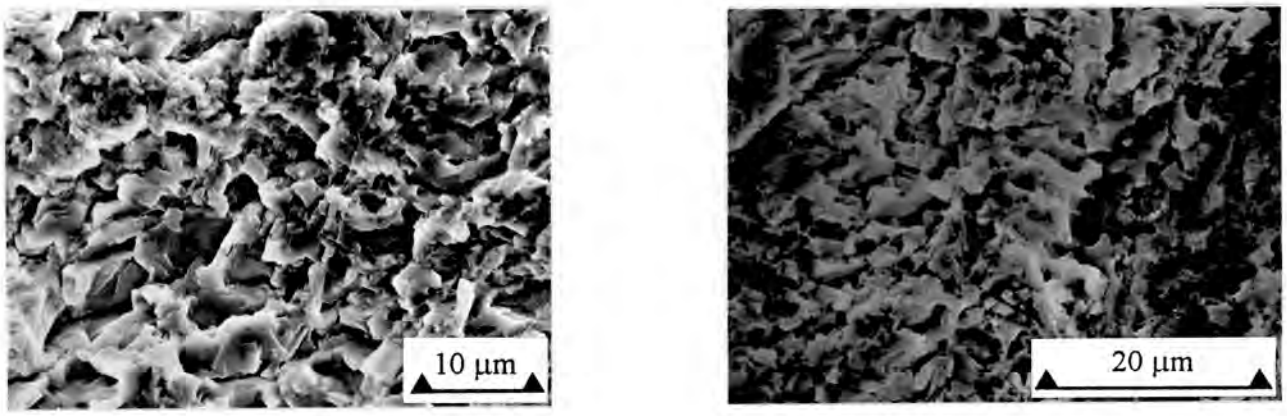

(a) (b)

Figure 78. High magnification S.E.M. images of the steady state cavitation eroded surface of homogenized Ti-48Al-2Mn-2Nb (at.%) after a 20 hour test. (a) Equiaxed fracture surfaces are brittle in appearance. (b) Material is removed from elongated regions to produce troughs on eroded surface

4.3.6. Cavitation Progression - Near-γ Ti-48Al-2Mn-2Nb (at.%)

Two series of micrographs were recorded with the S.E.M. from adjacent areas on the specimen of near-γ Ti-48Al-2Mn-2Nb (at.%) before cavitation erosion and after exposure to cavitation erosion for 15, 30, 45, 135 and 195 minutes. In both areas the starting microstructure consists mainly of equiaxed and twinned γ grains as shown in Figures 79(a) and 79 (b). Before the start of the first cavitation erosion exposure the effects of etching were removed by mechanical polishing.

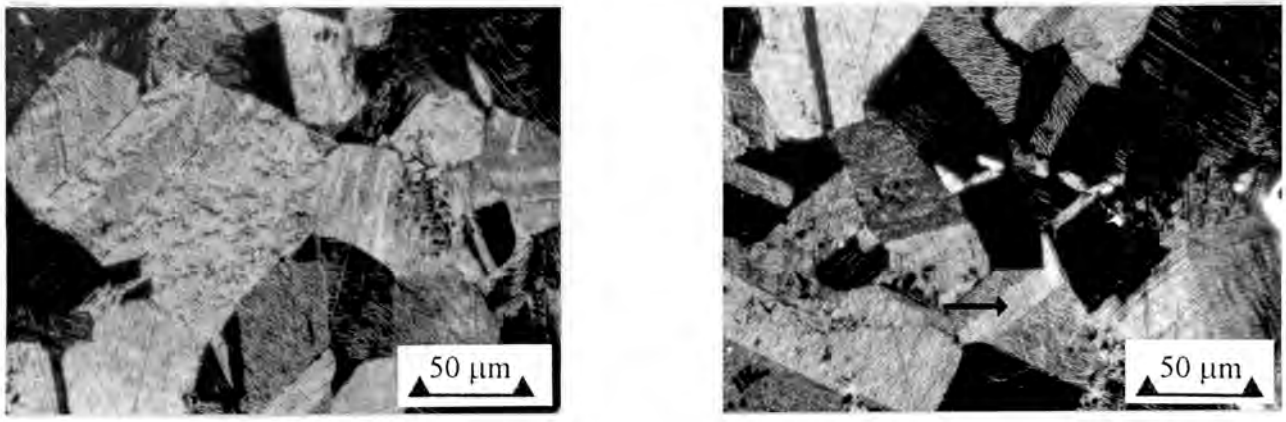

(a) (b)

Figure 79. S.E.M. images of the etched microstructure of near-γ Ti-48Al-2Mn-2Nb (at.%) taken from adjacent areas before cavitation erosion. (a) The microstructure consists mainly of equiaxed γ grains and a small volume fraction of α_2 precipitates. (b) Annealing twins are indicated in this micrograph.

Sets of parallel raised lines appear on the polished surface after 15 minutes of cavitation erosion and some grain boundaries are faintly delineated as shown in Figures 80(a) and 80(c). The parallel raised lines are not aligned parallel to the etched grooves, whereas the parallel grooves shown in Figure 80(c) are parallel to the widely-spaced grooves in Figure 79(b). The three sets of raised lines with the same orientation shown in Figure 80(b) are each within a γ grain which exhibits etched grooves of the same orientation. In addition to the parallel lines and grooves a set of faint crossed lines is observed in the top left hand corner of Figure 80(c).

After cavitation erosion for 30 minutes the sets of raised parallel lines and the grain boundaries are more prominently delineated than after 15 minutes and material is removed from the large flaw in the surface as shown in Figures 80(b) and (d).

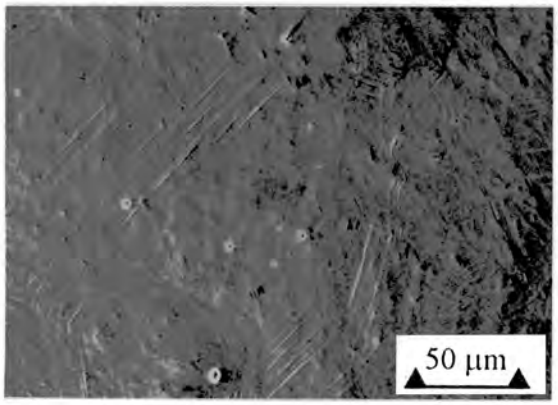

(a)

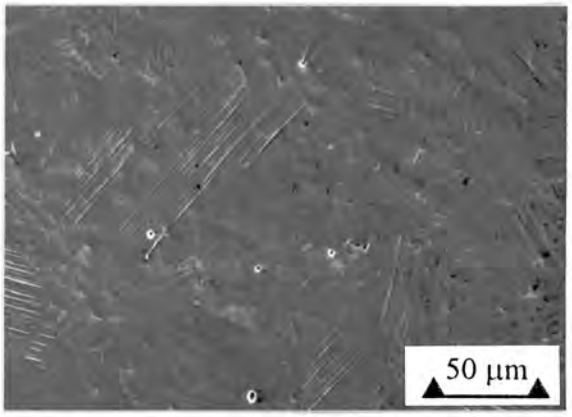

(b)

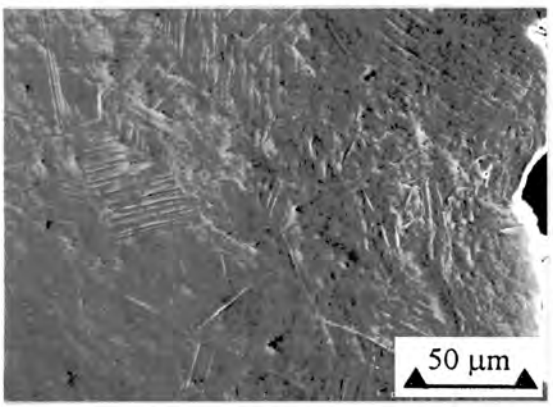

(c)

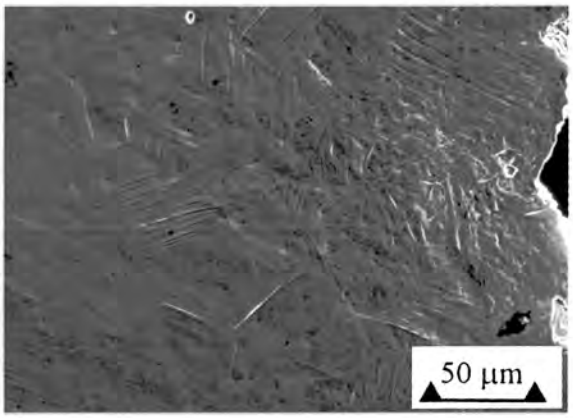

(d)

Figure 80. S.E.M. images of near-γ Ti-48Al-2Mn-2Nb (at.%) after exposure to cavitation erosion. (a) After 15 minutes sets of evenly-spaced parallel lines are raised above the surface. (b) After 30 minutes sets of parallel lines are more clearly delineated. (c) After 15 minutes a set of parallel grooves is observed in the top right hand corner of this micrograph and some grain and twin boundaries are faintly delineated. Faint crossed lines are observed in the top left hand corner. (d) After 30 minutes material is removed from the large flaw in the surface and the grain and twin boundaries are more clearly delineated.

After exposure to cavitation erosion for 45 minutes, material is removed from a small hole in the centre of the area shown in Figure 81(a) and from the large flaw shown in Figure 81(c). Further material loss occurs from these sites after 135 minutes as shown in Figures 81(c) and (d) respectively. Heavy deformation lines are observed in a grain in which only faint crossed lines were previously observed as shown in the top left hand corner of Figure 81(d). Material is removed from a twin boundary as shown in Figure 81(d).

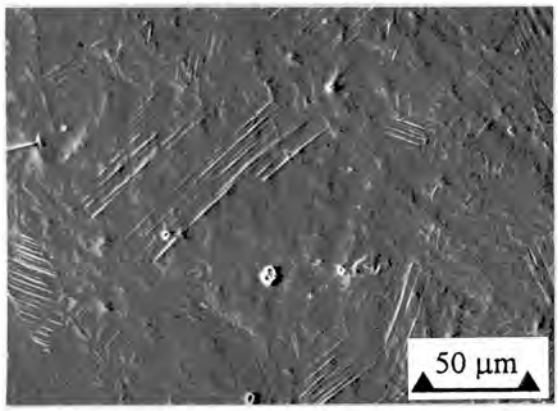

(a)

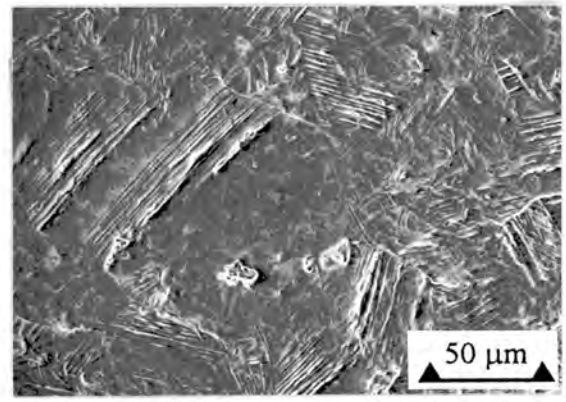

(b)

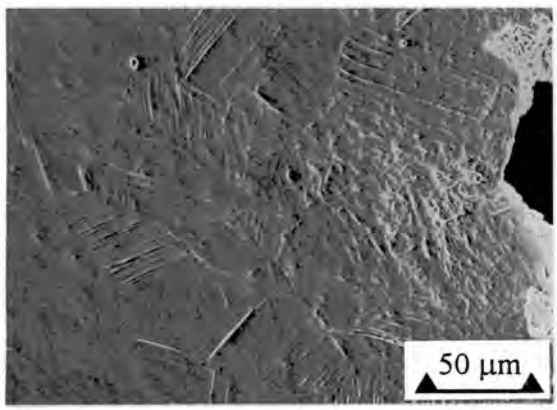

(c)

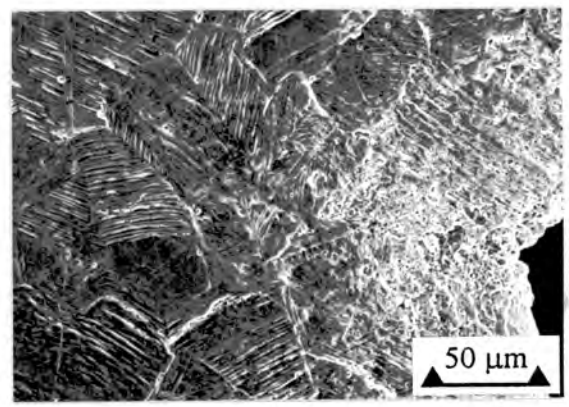

(d)

Figure 81. S.E.M. images of near-γ Ti-48Al-2Mn-2Nb (at.%) after exposure to cavitation erosion. (a) After 45 minutes material is removed from the small hole in the surface. (b) After 135 minutes further material is removed from the small pit in the surface. (c) After 45 minutes material is been removed from the large flaw and from the regions immediately adjacent to it. (d) After 135 minutes more material is removed from the large flaw and from a twin boundary.

After exposure to cavitation erosion for 195 minutes some areas on the surface are still without sets of parallel lines; grain boundaries are well defined and deformation lines are ragged because of material removal as shown in Figures 82(a) and (b). The most pronounced material removal occurs from the edge of the large flaw shown in Figure 82(b). Material is also removed from the edges of the parallel grooves, the raised deformation lines and to a lesser extent from the grain boundaries and the twin boundary as shown in Figure 82(b).

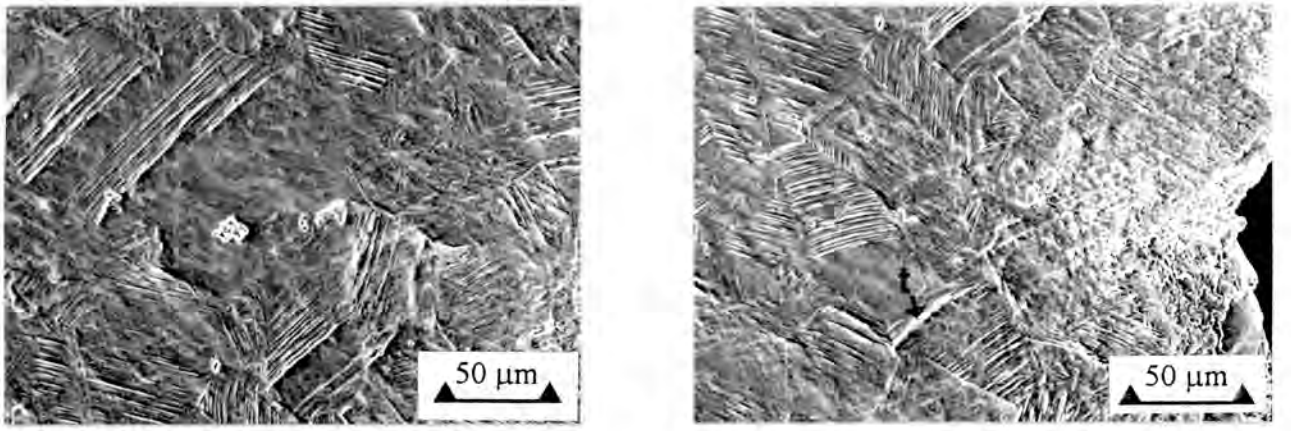

(a) (b)

Figure 82. S.E.M. images of near-γ Ti-48Al-2Mn-2Nb (at.%) after exposure to cavitation erosion for 195 minutes. (a) Material is removed from small pits, grain boundaries and thick deformation lines. (b) Material is removed from small pits and from the large surface flaw and from the grain boundaries and the annealing twin boundary in the bottom centre of the micrograph.

4.3.7. Subsurface hardening of Ti-52Al (at.%) and Ti-48Al-2Mn-2Nb (at.%)

Homogenized Ti-52Al (at.%) and Ti-48Al-2Mn-2Nb (at.%) exhibit a sharp increase in hardness at the cavitation eroded surface as shown by the Knoop microhardness profiles in Figure 83. The microhardness of the near-surface regions (approximately 80 μm wide) of homogenized Ti-52Al (at.%) and homogenized Ti-48Al-2Mn-2Nb (at.%) are between 600 HK (15 gf) and 750 HK (15 gf) and between 700 (15 gf) and 850 HK (15 gf) respectively. The bulk microhardness, i. e. at a distance greater than 500 μm from the surface is between 440 (15 gf) and 540 (15 gf) for Ti-52Al (at.%) and Ti-48Al-2Mn-2Nb (at.%). It is not possible to distinguish the bulk microhardness values of these two materials because of the scatter in the results.

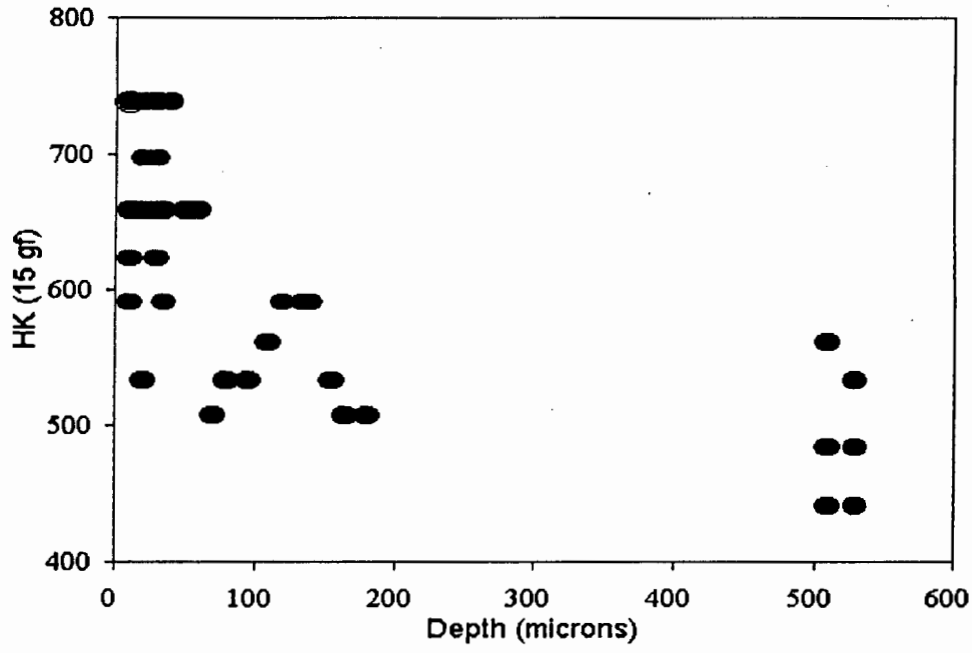

(a)

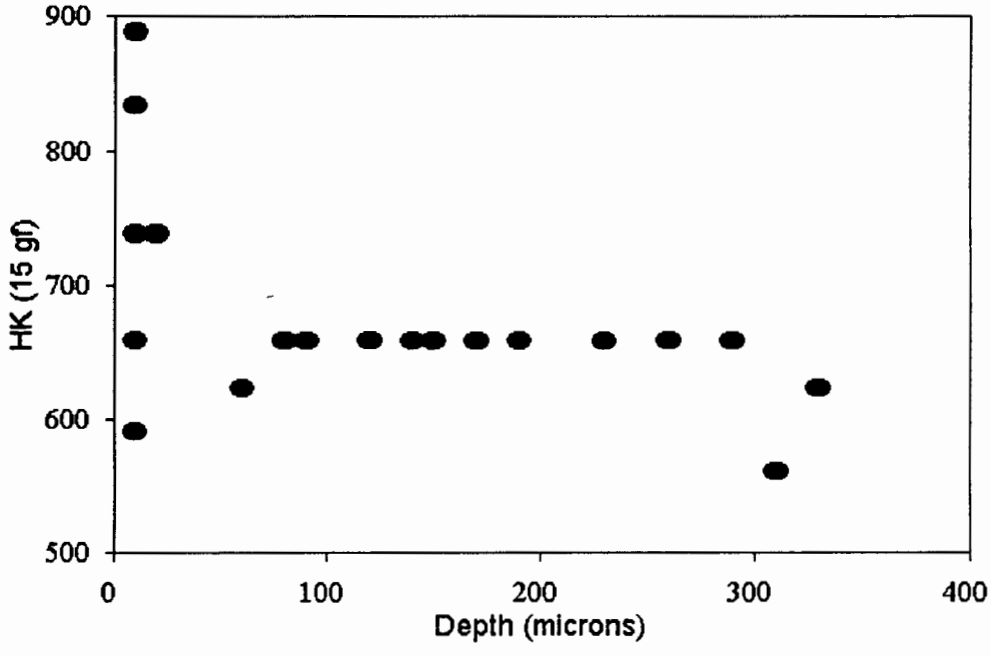

(b)

Figure 83. Knoop microhardness (HK 15 gf) versus depth profile measured on 5° tapered sections after exposure to cavitation erosion for 20 hours. (a) Microhardness profile for Ti-52Al (at.%). (b) Microhardness profile for Ti-48Al-2Mn-2Nb (at.%).

4.3.8. Annealed Aluminium 6261

Annealed aluminium 6261 and soda-lime-silica glass exhibit the same incubation period of 12 minutes, but the steady state cavitation erosion rate of the glass specimen is an order of magnitude less than that of the aluminium specimen. However, the glass fractures into two or three large pieces after exposure to cavitation varying from 20 minutes to an hour, while aluminium continues to erode at the steady rate as shown in Figure 84.

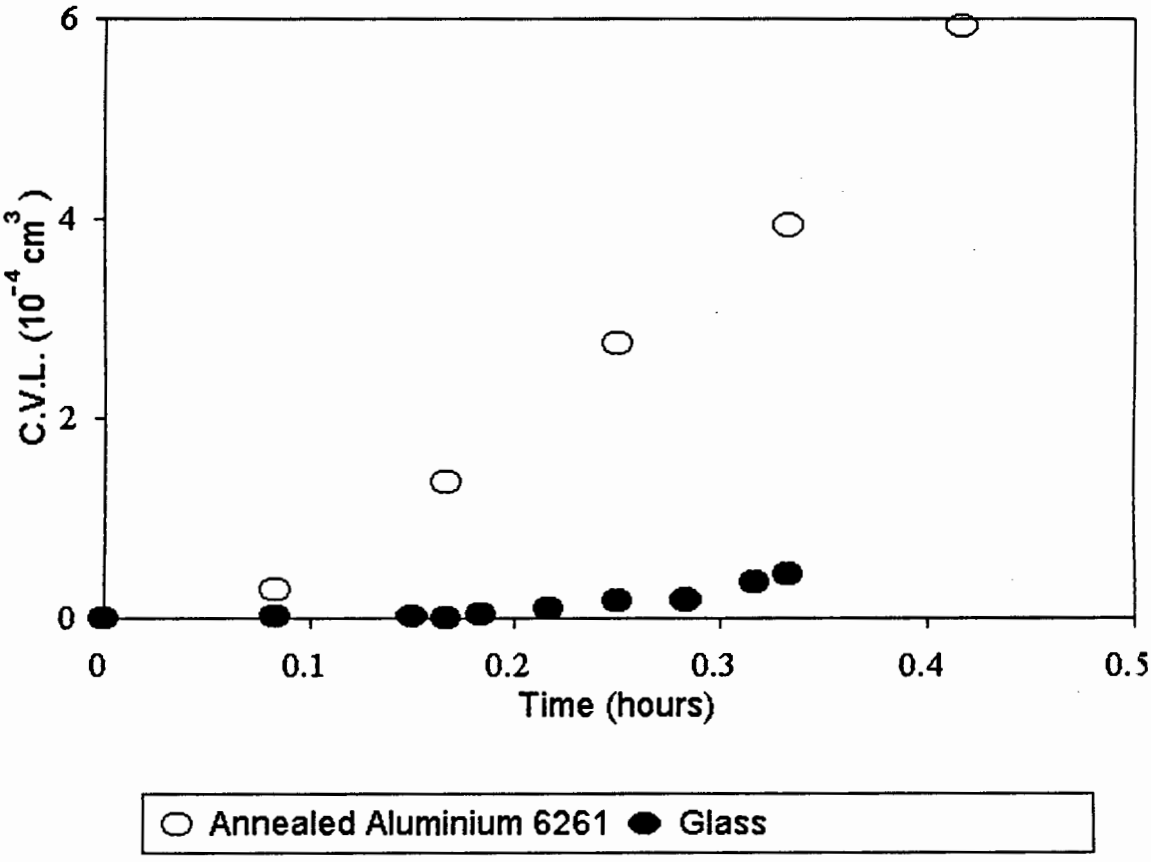

Figure 84. Graphs of cumulative volume loss (C.V.L.) versus time of exposure to cavitation erosion for annealed aluminium 6261 and soda-lime-silica glass.

Annealed aluminium 6261 attains a steady state of cavitation erosion at a rate of 2962 $x10^{-5}$ cm^3/hour after an incubation period 12 minutes, compared to the titanium aluminide alloys which exhibit cavitation erosion rates of between 3 $x10^{-5}$ cm^3/hour and 14 $x10^{-5}$ cm^3/hour after an incubation period of 5-8 hours. The transition region of a specimen of annealed aluminium 6261 eroded for 10 minutes exhibits shallow undulations and cracks in the surface as shown in Figure 85. Ductile peaks and troughs are prominent on the steady state cavitation eroded surface as shown in Figure 86. No brittle cleavage fracture is observed on the cavitation eroded surface, in contrast to the titanium aluminide alloys which exhibit brittle cleavage and ductile deformation.

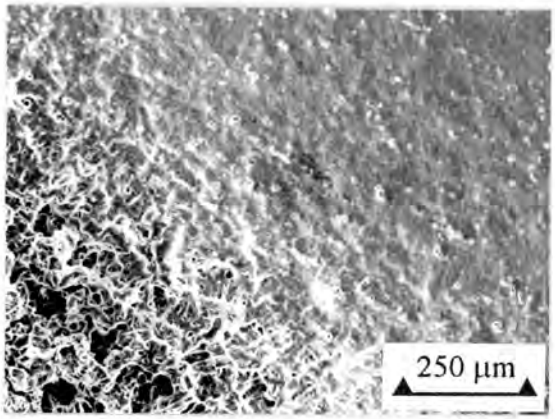

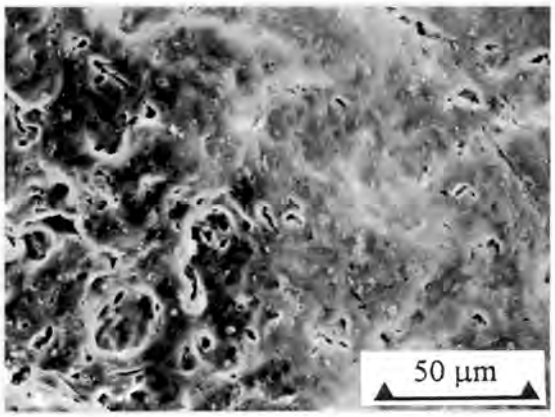

(a) (b)

Figure 85. S.E.M. images of the transition region of annealed aluminium alloy 6261 after 10 minutes of cavitation erosion. The surface is undulating and small cracks are observed.

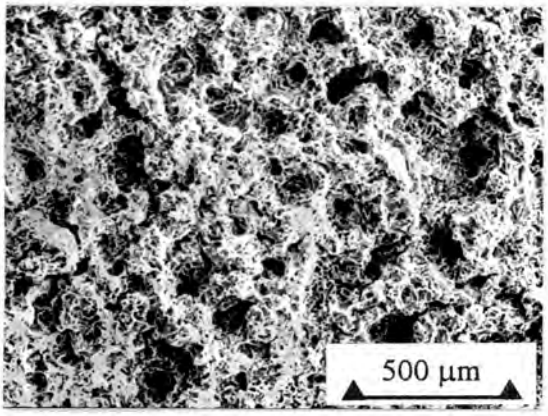

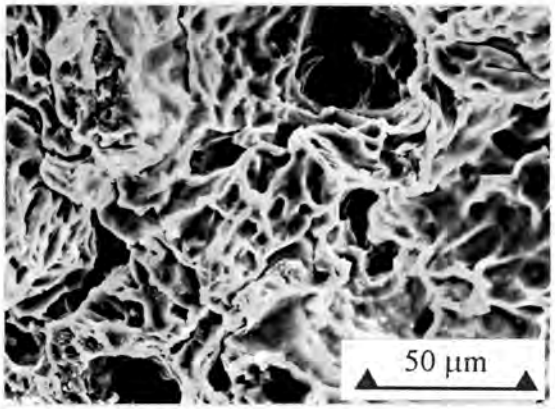

(a) (b)

Figure 86. S.E.M. images of the steady state cavitation eroded surface of annealed aluminium alloy 6261. (a) There are holes in the surface and the peaks are dimpled. (b) This higher magnification image shows the ductile dimples on the peaks and the holes with smooth ductile surfaces.

4.3.8.1. *Subsurface hardening*

The results of microhardness indents on a 5° tapered section of annealed aluminium after 30 minutes exposure to cavitation erosion reveal subsurface hardening as shown in Figure 87. The Knoop microhardness of the extruded material before annealing is approximately 66 HK (15 gf) and after annealing it is approximately 46.3 HK (15 gf). The microhardness of the near surface region increases to between 52 HK (15 gf) and 62 HK (15 gf) during cavitation erosion and restores some of the original hardness, i.e. the hardness before annealing as shown in Figure 87.

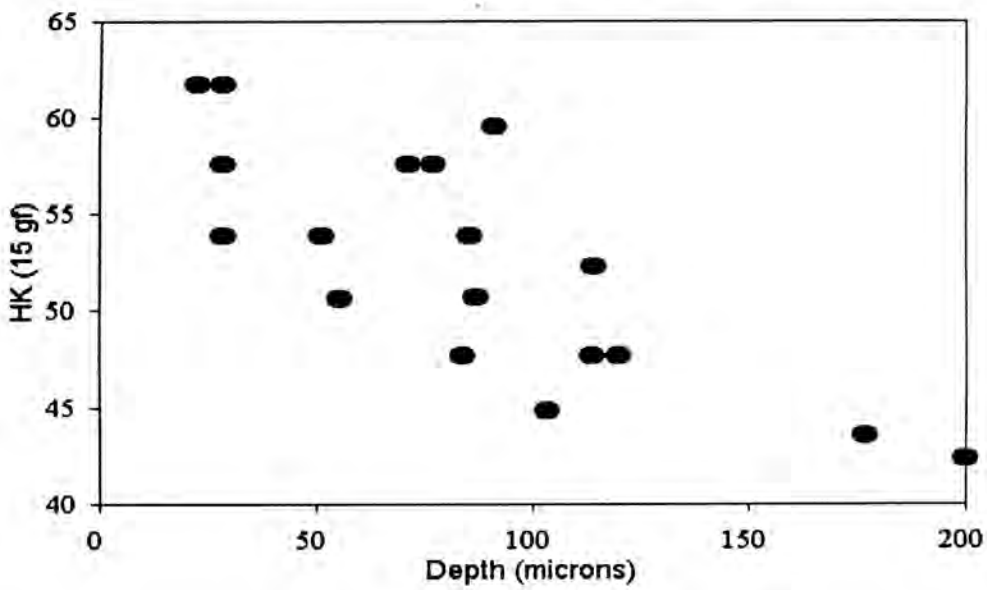

Figure 87. 5° tapered section of annealed aluminium alloy 6261 after 30 minutes (steady state) exposure to cavitation erosion.

4.3.9. Glass

The uneroded edge of a soda-lime-silica glass specimen contains isolated microscopic flaws as shown in Figure 88(a). After exposure to erosion for 10 minutes the steady state region of the specimen exhibits cracking between the pre-existing flaws and the flaws are enlarged as shown in Figures 88(a) and 88(b) respectively. Within the transition region of the glass specimen eroded for 40 minutes, i.e. in the early stages of cavitation, small pieces of material approximately 5μm wide are surrounded by cracks as shown in Figure 89(a). The holes in the transition region are larger nearer the centre of the specimen as shown in Figure 89(b). The fracture surfaces of the enlarged flaws (surface holes) are brittle and the enlarged flaws and cracks form a continuous network as shown in Figure 89.

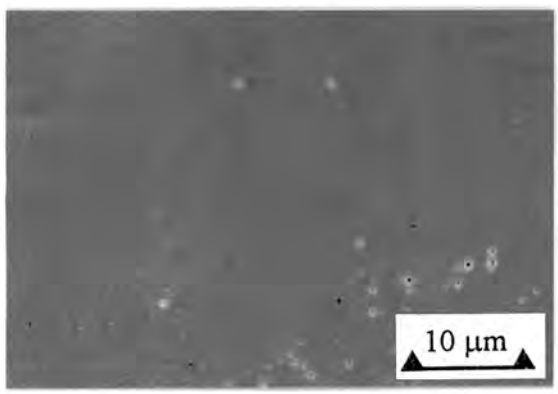

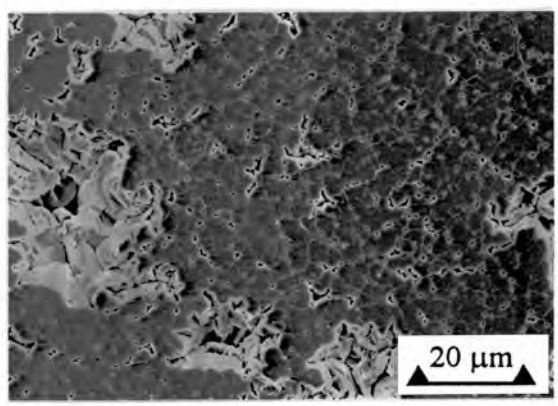

(a) (b)

Figure 88. S.E.M. images of a cavitation eroded glass specimen. (a) Uneroded glass contains isolated surface flaws. (b) The cavitation eroded surfaces contains cracks between the enlarged surface flaws after 10 minutes of erosion.

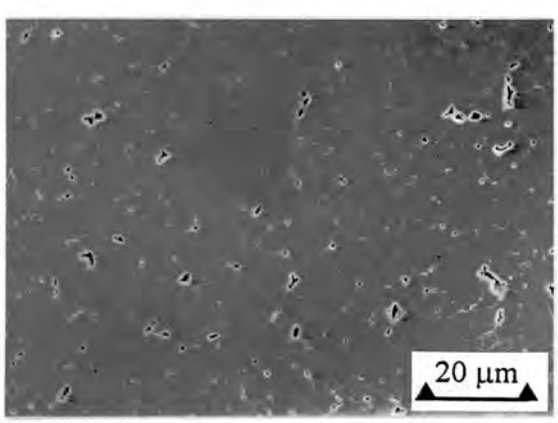

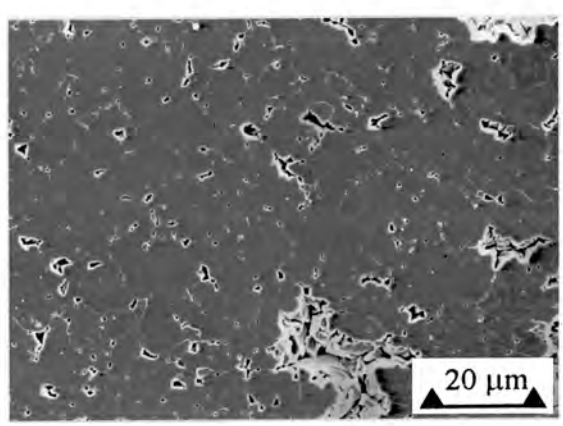

(a) (b)

Figure 89. S.E.M. images of the transition region of a glass specimen after 40 minutes of cavitation erosion. (a) Intersecting surface cracks surround small regions which are ready for removal from the surface. (b) The holes are larger nearer the more heavily eroded centre of the specimen and form a continuous network with the surface cracks.

The steady state cavitation eroded surface of glass after 40 minutes of erosion is shown in Figures 90(a) and (b). The surface exhibits completely brittle fracture and radial striations near the perimeter of the disc-shaped fracture surfaces are a common feature as shown in Figure 90(b).

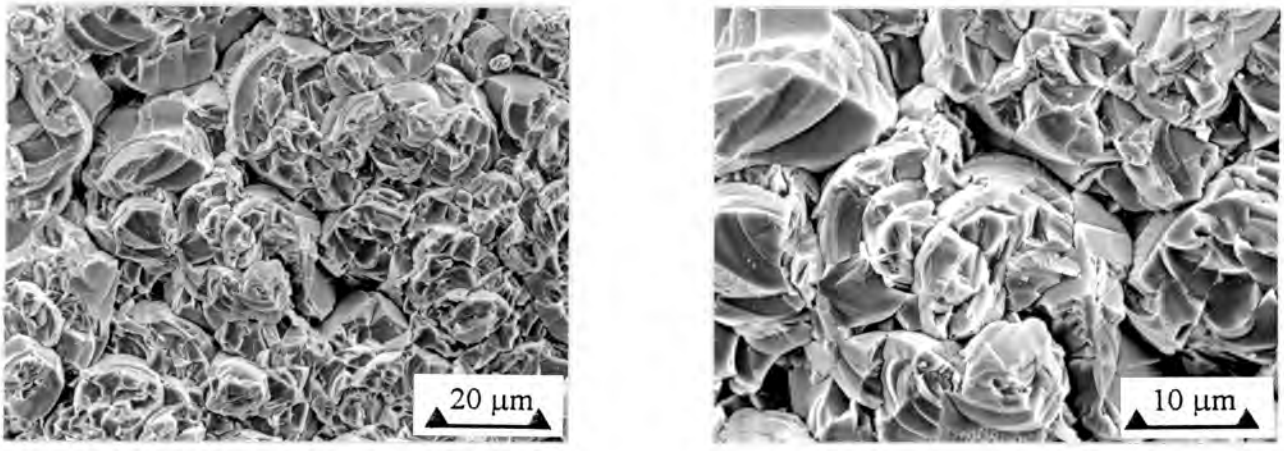

(a) (b)

Figure 90. S.E.M. images of the surface of glass after cavitation erosion for 40 minutes. (a) The fracture surfaces are brittle. (b) At higher magnification, radial striations are observed on the fracture surfaces.

4.3.10 Transmission Electron Microscope Examination

The results of transmission electron microscope (T.E.M.) examinations of foil specimens of homogenized Ti-52Al (at.%) after 10 minutes of cavitation erosion are shown in summary in Figures 91 and 92. A cavitation erosion specimen was thinned from the back surface, i.e. not the cavitation eroded surface and the deformation microstructure produced by cavitation erosion was examined. The lines produced by 10 minutes of cavitation erosion are typically 0.1 μm wide and are oriented in two directions, at 70° to each other within a grain, as shown in Figure 91 Two twin variants on {111} type planes and the γ matrix reflections are identified as shown schematically in Figure 92(b). A reflection from each twin variant is used to produce the dark field images shown in Figure 92(c) and 92(d).

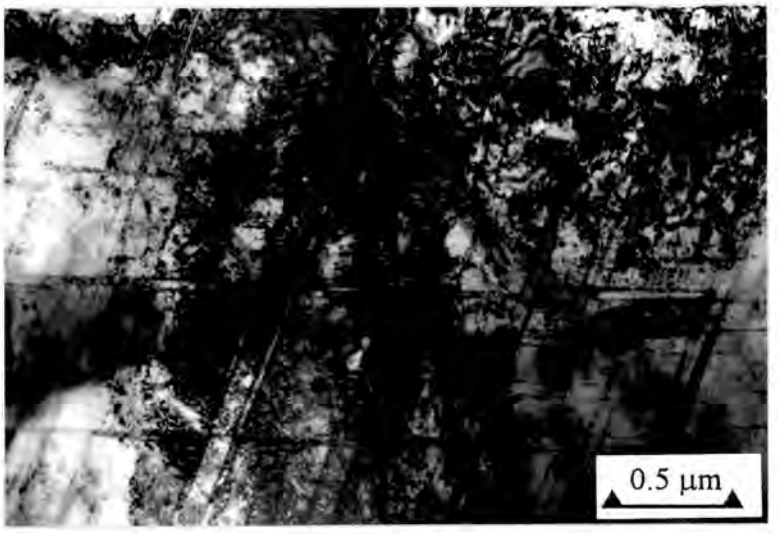

Figure 91. Bright field T.E.M. image of homogenized Ti-52Al (at.%) after 10 minutes of cavitation erosion. Twins are approximately 0.1 μm wide and are oriented in two directions with the γ grain.

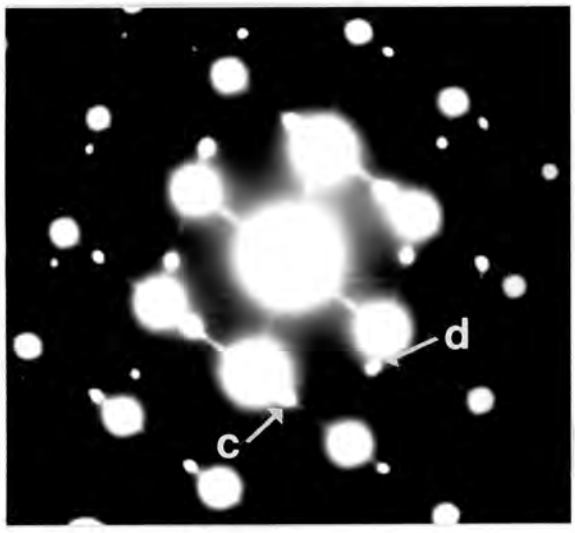

(a)

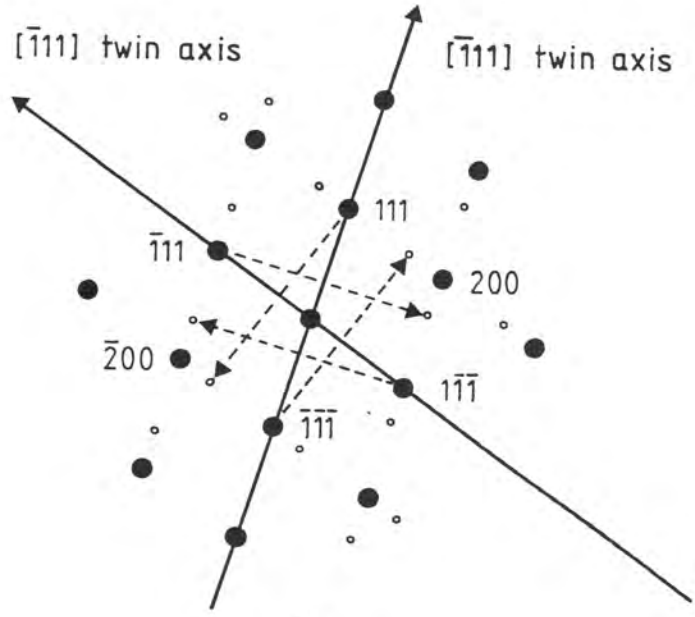

(b)

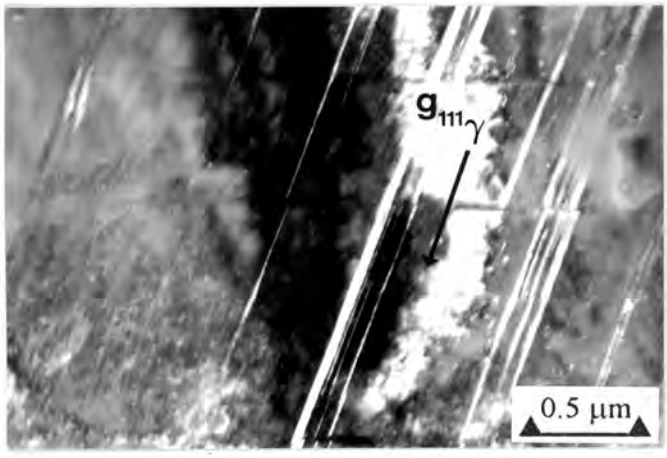

(c)

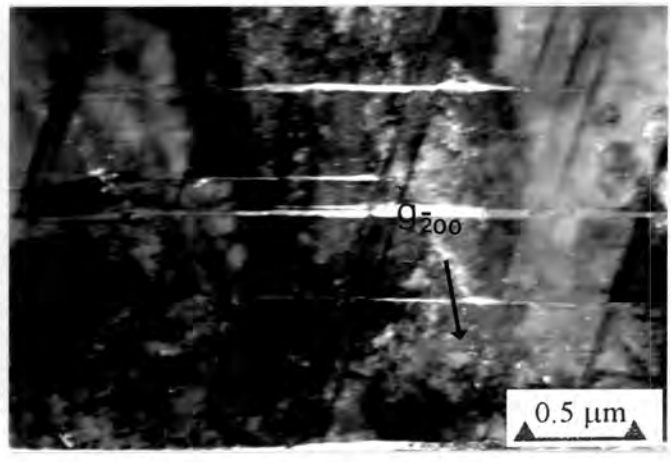

(d)

Figure 92. T.E.M. results for homogenized Ti-52Al (at.%) after 10 minutes of cavitation erosion. (a) γ [011] zone axis S.A.D.P. The twinning reflections which produce the dark field images are indicated by "c" and "d". (b) Schematic representation of the [011] zone axis diffraction pattern for the γ matrix and two twin variants. The matrix reflections are indicated by "•" and the twinning reflections are indicated by "o". (c) Dark field image produced with the twinning reflection indicated by "c" in the S.A.D.P (d) Dark field image produced with the twinning reflection indicated by "d" in the S.A.D.P.

5. DISCUSSION

5.1. Materials Characterisation

5.1.1. Ti-25Al-10Nb-3V-1Mo (at.%)

5.1.1.1. *Microstructure*

The α_2/O and B2 phases are the main constituents of the microstructure of as received Ti-25Al-10Nb-3V-1Mo (at.%). X.R.D. spectra do not show the (100) superlattice peak for the B2 phase, but both fundamental b.c.c. reflections and B2 superlattice reflections are present in the selected area diffraction patterns obtained from the β(B2) phase with the transmission electron microscope.

The S.A.D.P. produced by the matrix and precipitates shown in Figure 29(b) matches that produced by Bendersky, Boettinger and Royturd[98] from a region of the microstructure of an Ti-12.2Al-37.2Nb (at.%) alloy consisting of a B2 matrix and needle-like ordered orthorhombic (O) precipitates. Superlattice reflections were indexed by Bendersky et al.[98] for two variants of the O phase with the same orientation relationship with the B2 matrix as the Burgers relationship between b.c.c. and h.c.p structures[99], i. e. $[011]_c$ // $[001]_O$; $(\bar{2}\bar{1}1)_c$ // $(110)_O$ for the first variant and $[011]_c$ // $[001]_O$; $(\bar{2}1\bar{1})_c$ // $(1\bar{1}0)_O$ for the second variant. Microdiffraction was used to identify the O precipitates[98] since the selected area diffraction patterns from the α_2 and O phases are difficult to distinguish.

In the present study, the needle-like precipitates are not unambiguously identified and could be either orthorhombic (O) phase or α_2 phase; however the size and distribution of the needle-like precipitates of either the α_2 or the O phase within the transformed B2 matrix is more important than the identity of the phase because of their similar structure and response to heat treatment[17].

5.1.1.2. *Mechanical Properties*

The superior hardness of Ti-25Al-10Nb-3V-1Mo (at.%) after ageing at 650°C for 2 hours could be due to O laths in the B2 matrix which are too fine to be resolved with scanning electron microscopy[30]. The time-temperature-transformation (T.T.T.) diagram[30] shown in Figure 5, section 2.2.1, shows that ageing Ti-25Al-10Nb-3V-1Mo (at.%) between 650°C and 850°C for 2 hours results in the transformation of the high temperature β phase to fine laths of the O phase, while ageing at 950°C produces secondary α_2 laths. The greater hardness of as received Ti-25Al-10Nb-3V-1Mo (at.%) compared to the sample aged at 950°C for 2 hours could be due to the longer time (2 hours compared to 1 hour) at temperature[30].

Ti-25Al-10Nb-3V-1Mo (at.%) exhibits a higher yield strength and a considerably higher work hardening rate than that of 304 stainless steel, but 304 stainless steel exhibits greater ductility and work to fracture than Ti-25Al-10Nb-3V-1Mo (at.%). Court et al.[19] showed that Ti_3Al-based alloys undergo plastic deformation by the movement of super-partial pairs of dislocations, which contributes to the high work hardening rates of intermetallics which deform in this way since the super-partial dislocations must associate before cross slip can occur and this requires a large increase in stress per unit strain[13]. 304 austenitic stainless steel has a higher work hardening rate than many other metallic materials because of its low stacking fault energy, and hence large stress required for cross slip, but the additional influence of the ordered crystal structure of Ti-25Al-10Nb-3V-1Mo (at.%) increases the stress required for cross slip and contributes to its higher work hardening rate.

The tensile fracture surface of as received Ti-25Al-10Nb-3V-1Mo (at.%) exhibits transgranular cleavage fracture and ductile dimples as shown in Figure 39. The dimples are produced by ductile tearing of the B2 matrix normal to the surface as shown schematically in Figure 93. The cleavage markings are confined to areas similar in size to the primary α_2 grains, which is consistent with the greater ductility and toughness of the B2 phase. The observation of cleavage fracture and ductile tearing is consistent with the findings of Chen et al.[30]. A specimen aged at 950°C, with a similar microstructure to that of as received Ti-25Al-10Nb-3V-1Mo (at.%), exhibited ductile tearing of the B2 phase. Chan[26] showed that the B2 phase can accommodate greater strain prior to fracture than the α_2 phase; the local strain near the tip of a micro crack in Ti-24Al-11Nb (at.%) was measured as 5 per cent in the α_2 phase and as 40 per cent in the β phase. The influence of the B2 phase in Ti_3Al-based alloys is to delay cleavage fracture of the α_2 phase to larger strains, thereby increasing the fracture toughness and tensile ductility[18].

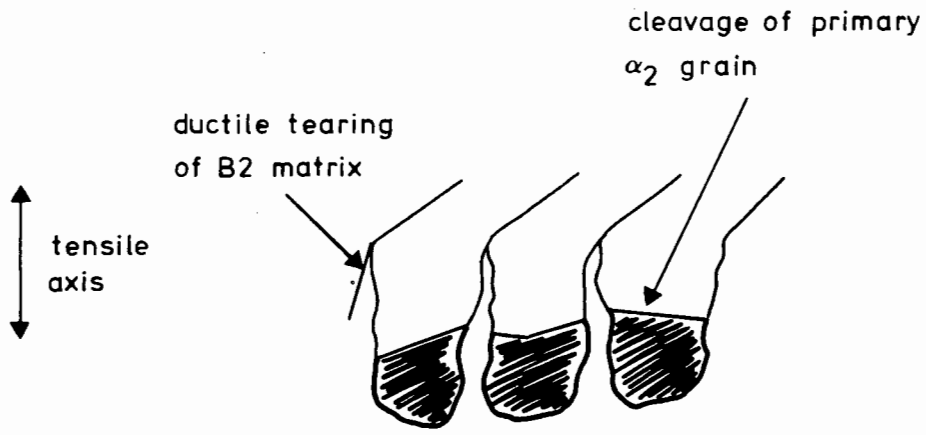

Figure 93. Schematic representation of tensile failure of as received Ti-25Al-10Nb-3V-1Mo (at.%). The B2 matrix exhibits ductile tearing and the primary α_2 grains undergo cleavage, resulting in a dimpled fracture surface.

The slip lines which are observed within primary α_2 grains on the gauge length of the compression specimen of as received Ti-25Al-10Nb-3V-1Mo (at.%) after approximately 3% strain are evidence of the plastic deformation of this phase. The slip lines are widely-spaced and are oriented in a single orientation within each primary α_2 grain, which is indicative of the limited number of slip systems and the difficulty of cross-slip in the ordered structure. The dimples on the compression fracture surface are formed by shear stresses at 45° to the compression axis, in contrast to those on the tensile fracture surface which are formed in tension, parallel to the tensile axis. The larger dimples and absence of cleavage fracture on the compression fracture surface compared to the tensile fracture surface are consistent with the compressive strain to fracture of 20 per cent for Ti-24.5Al-10.5Nb-1.5Mo (at.%)[33] compared with 1.5 per cent measured in tension for Ti-25Al-10Nb-3V-1Mo (at.%)[30].

5.1.2. Ti-52Al (at.%) and Ti-48Al-2Mn-2Nb (at.%)

5.1.2.1. *Microstructure*

Ti-52Al (at.%) and Ti-48Al-2Mn-2Nb (at.%) have typical cast structures; columnar grains grow from the side of the ingot and the central region consists of more equiaxed grains. Solidification along the longitudinal direction, from the bottom of the ingot, produces the dendritic structure reported in as cast Ti-52Al (at.%)[100] and a smaller columnar region than as cast Ti-48Al-2Mn-2Nb (at.%), which suggests that the Ti-48Al-2Mn-2Nb (at.%) disc was cut from closer to the top of the ingot than Ti-52Al (at.%). X-ray diffraction (X.R.D.) confirms that both TiAl-based alloys

consist of the γ phase and the α_2 phase. Numerous γ peaks are identified in the X.R.D. spectra for homogenized Ti-52Al (at.%) and homogenized Ti-48Al-2Mn-2Nb (at.%) and near-γ Ti-48Al-2Mn-2Nb (at.%). The identification of both the $\alpha_2(002)$ and γ(111) peaks at $2\theta = 38.9°$ and the identification of both the α_2 (110) and γ (110) peaks at $2\theta = 32°$ is consistent with the orientation relationship between the α_2 and γ phases, i. e. $\{002\}\alpha_2 // \{111\}\gamma$, $<110>\alpha_2 // <110>\gamma$[101].

The homogenizing temperature of 1380°C is close to the $\alpha/(\alpha+\gamma)$ transformation temperature of 1383°C determined by Takeyama for Ti-48Al (at.%)[40] and produces microstructures consisting of equiaxed γ grains and α_2 precipitates. Ti-52Al (at.%) has a near-stoichiometric composition and the homogenized microstructure consists mainly of the γ phase as shown in Figure 42. Annealing twins are observed in homogenized Ti-52Al (at.%) and homogenized Ti-48Al-2Mn-2Nb (at.%) and in near-γ Ti-48Al-2Mn-2Nb (at.%). Ti-48Al-2Mn-2Nb (at.%) contains a larger volume fraction of α_2 precipitates than Ti-52Al (at.%) after homogenization because of the α- stabilizing effect of niobium and manganese as shown in Figure 46.

The near-γ heat treatment of Ti-48Al-2Mn-2Nb (at.%) in the lower part of the α+γ phase field (Figure 2) produces a greater volume fraction of the γ phase compared to the homogenizing treatment of the same material higher up in the phase field (1380°C) and nearer to the α phase boundary.

5.1.2.2. *Mechanical Properties*

The greater hardness of homogenized Ti-48Al-2Mn-2Nb (at.%) than homogenized Ti-52Al (at.%) is consistent with the larger volume fraction of the harder α_2 phase[43] and the solid solution strengthening effects of manganese and niobium[38]. The hardness of homogenized Ti-48Al-2Mn-2Nb (at.%) is not significantly different to that of near-γ Ti-48Al-2Mn-2Nb (at.%). This is consistent with the results of Zhang and Chaturverdi[41] who found that α_2 precipitates did not significantly affect the room temperature strength or ductility of a Widmanstatten-type Ti-50Al-2Mn-1Nb (at.%) specimen and produced only a small increase in the work hardening rate compared to that of a near-γ specimen.

It appears from the results of previous workers[34,48] that higher work hardening rates are expected for the TiAl-based alloys, Ti-52Al (at.%) and Ti-48Al-2Mn-2Nb (at.%) than the Ti_3Al-based, Ti-25Al-10Nb-3V-1Mo (at.%) alloy. The work hardening rate of TiAl-based Ti-48Al-1V (at.%)[48] was measured as 3790 MPa per unit strain at a strain rate of 10^{-3} s^{-1} and as 4640 MPa per unit strain at a strain rate of $4.5x10^3$ s^{-1}, while the work hardening rate of Ti_3Al-based Ti-24.5Al-10.5Nb-1Mo (at.%)[34] was measured as 3300 MPa per unit strain at a strain rate of 10^{-3} s^{-1} and 4200 MPa per unit strain at a strain rate of $6x10^3$ s^{-1}. The microstructure of Ti-48Al-1V (at.%)[48] consisted mainly of equiaxed γ grains and approximately 10 % lamellar α_2 grains and the

microstructure of Ti-24.5Al-10.5Nb-1Mo (at.%)[34] consisted of primary α_2 grains and fine secondary α_2 plates within the B2 matrix; which are similar microstructures to those of Ti-25Al-10Nb-3V-1Mo (at.%) and the TiAl-based alloys in the present study.

5.2. Particle erosion at Room Temperature

5.2.1. Test Results

The particle erosion rates of all the materials tested, except for soda-lime-silica glass, are greater at 30° impact than at 90° impact, which is typical of a ductile mode of erosion[102] and has been observed for Ni_3Al-based nickel aluminide intermetallic alloys[103]. The ratio of 90° erosion rate to 30° erosion rate is the same for Ti-25Al-10Nb-3V-1Mo (at.%), 304 stainless steel and annealed aluminium 6261, and lower than those for the two γ alloys, which suggests that the modes of erosion for Ti-25Al-10Nb-3V-1Mo (at.%), 304 stainless steel and annealed aluminium 6261 are more ductile than the two γ alloys as shown in figure 94.

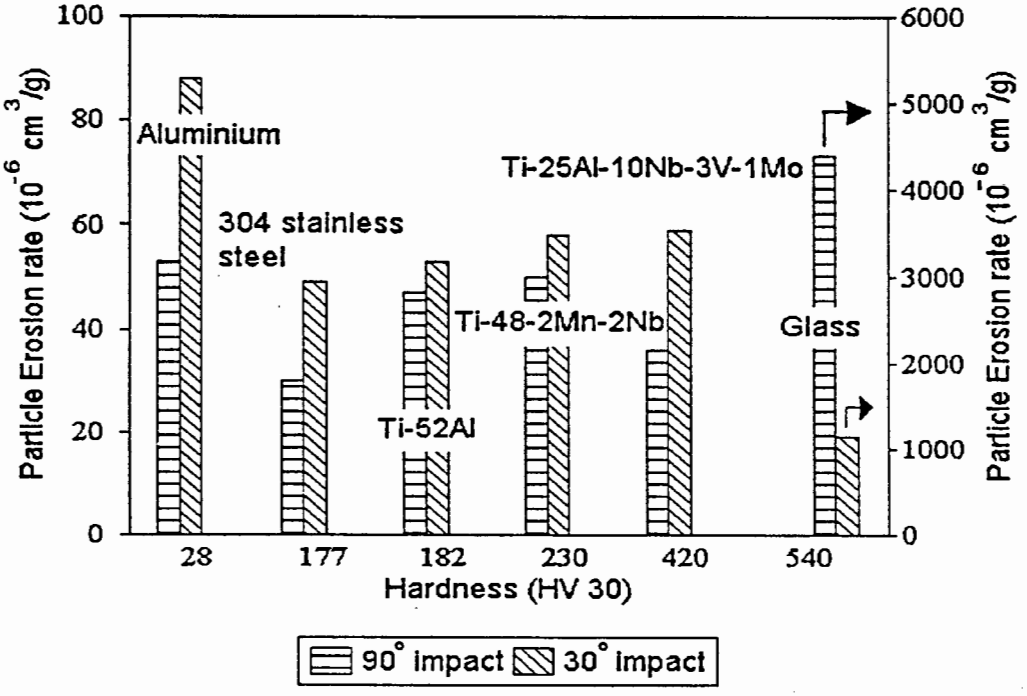

Figure 94. Graph of bulk hardness versus the particle erosion rates at 90° impact and at 30° impact for the titanium aluminide alloys, 304 stainless steel, annealed aluminium 6261 and soda-lime-silica glass. The ratio of the particle erosion rate at 90° impact to the particle erosion rate at 30° impact is greater than one for glass and less than one for the other materials which exhibit a ductile mode of erosion.

At 90° impact, the harder Ti-25Al-10Nb-3V-1Mo (at.%) specimens exhibit lower particle erosion rates than the homogenized Ti-52Al (at.%) and homogenized Ti-48Al-2Mn-2Nb (at.%) specimens. The harder γ alloy, homogenized Ti-48Al-2Mn-2Nb (at.%), exhibits a larger particle erosion rate than homogenized Ti-52Al (at.%). Specimens of Ti-25Al-10Nb-3V-1Mo (at.%) with different hardnesses do not exhibit significantly different particle erosion rates as shown in Figure 95. At 30° impact, the erosion rates of the softer γ alloys are lower than that of as received Ti-25Al-10Nb-3V-1Mo (at.%) as shown in figure 94. It appears from these results that no simple correlation exists between the hardness and particle erosion rates of the titanium aluminide alloys. This is consistent with the results of other workers[104,105]. Ninham[104] observed only small differences in the particle erosion rates of a variety of metallic materials which were heat treated to different starting hardnesses. Ball, Willmott and Resente[105] showed that hardening and tempering a medium carbon steel to quite different levels of hardness produced no effect on the particle erosion performance.

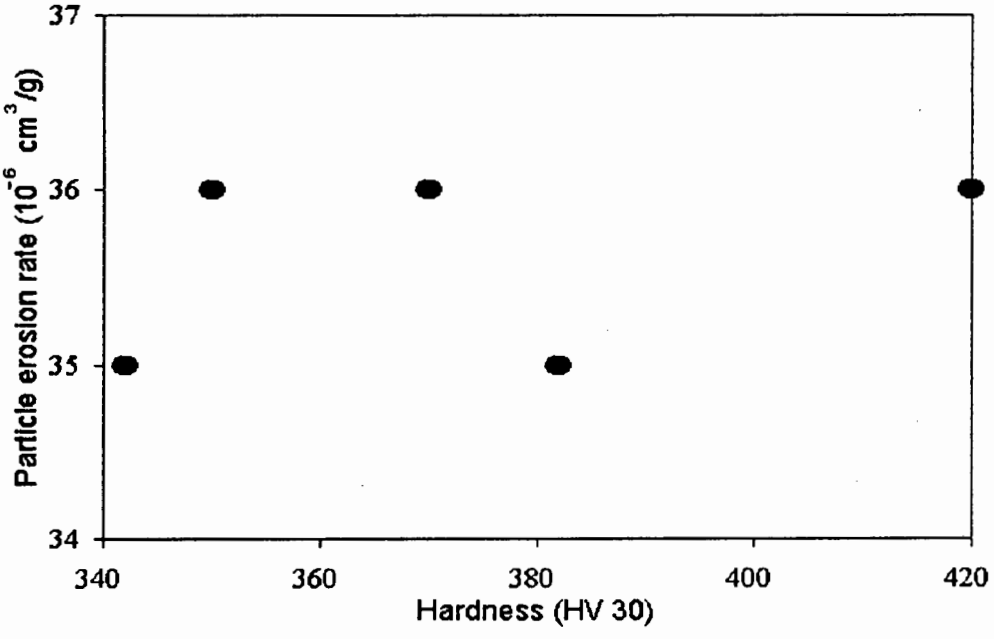

Figure 95. Graph of bulk hardness versus steady state particle erosion rate at 90° impact for Ti-25Al-10Nb-3V-1Mo (at.%) specimens.

The competing effects of yield strength, strain to fracture and work hardening rate on the particle erosion performance of Ti-25Al-10Nb-3V-1Mo (at.%), 304 stainless steel, annealed aluminium 6261 and glass may be discussed with the aid of the schematic stress-strain curves shown in Figure 96. The fracture strength of glass is exceeded by single particle impact as evidenced by the lateral and radial fracture at single impact sites shown in Figures 62 and 63. The plastic deformation at the single impact sites of the titanium aluminide alloys, 304 stainless steel and annealed aluminium 6261 indicate that the yield strength of each material is exceeded by a single particle strike and that

the post yield stress regions of the stress-strain curves shown in Figure 96 are of greater importance than the elastic regions and the yield stress when considering the effects of mechanical properties on the steady state particle erosion rate. Annealed aluminium 6261 has an exceptionally low yield strength and a low work hardening rate which may result in the attainment of the fracture stress and material loss after only a few particle strikes. The high work hardening rate of Ti-25Al-10Nb-3V-1Mo (at.%) will result in a rapid rise in flow stress during particle impact, but the surface can accommodate a smaller strain to fracture than 304 stainless steel and annealed aluminium 6261 as shown in Figure 96.

The lower particle erosion rate of 304 stainless steel than the titanium aluminide alloys is consistent with the greater strain to fracture of 304 stainless than Ti-25Al-10Nb-3V-1Mo (at.%) in a conventional tensile test as shown in Table 14 and illustrated in Figure 96. 304 stainless steel has a greater ability to absorb the kinetic energy of impacting erodent particles by undergoing plastic deformation. This is consistent with Levy's[57] observation that ductility contributes to the particle erosion resistance of ductile metals.

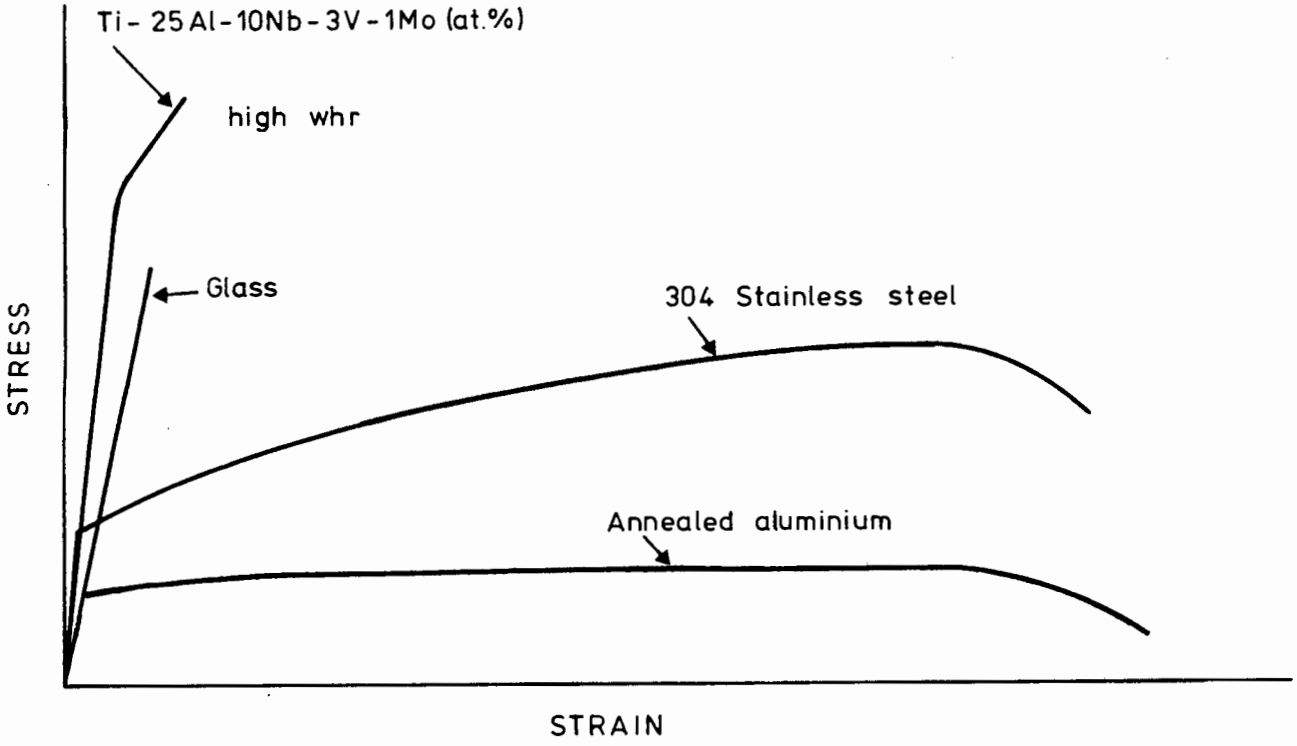

Figure 96. A schematic representation of the stress-strain curves for Ti-25Al-10Nb-3V-1Mo (at.%), 304 stainless steel, annealed aluminium 6261 and glass.

While particle erosion of the titanium aluminide alloys, 304 stainless steel and annealed aluminium 6261 is a ductile shear process and is influenced by the strain to fracture, the particle erosion performance of brittle materials such as glass, alumina and polycrystalline diamond are influenced by fracture processes which are quantified by material properties such as fracture toughness and hardness relative to the hardness of the erodent[62]. The superior resistance of polycrystalline diamond compared to glass and alumina, shown in Figure 97, is due to its greater hardness than the SiC erodent, i.e. 5000 VHN (20 kg) for polycrystalline diamond[62] compared to 2500 VHN (30 kg) for SiC, and its greater toughness than alumina and glass[106]. Alumina and soda-lime-silica glass, with hardnesses of 1892 VHN (20 kg)[62] and 540 VHN (30 kg)[97] respectively, are softer than SiC, but alumina has a greater toughness than glass by virtue of its polycrstalline structure[107] and is therefore more resistant to material removal during particle erosion.

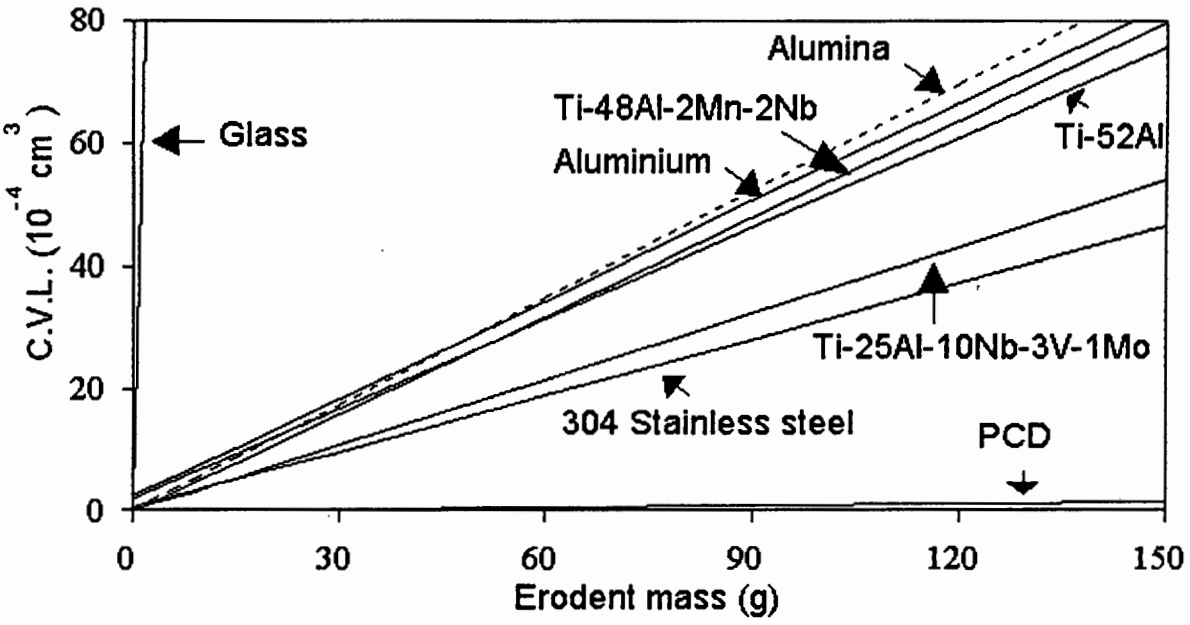

Figure 97. Graphs of cumulative volume loss (C.V.L.) versus mass of erodent at 90° impact for the titanium aluminide alloys and comparative materials. The results for alumina and polycrystalline diamond (PCD) were obtained by Doyle[108].

5.2.2. Examination of Particle Eroded Specimens

Examination of the single impact sites on the titanium aluminide alloys reveals that particle impact is accompanied by plastic deformation. At 90° impact, the material adjacent to the impact craters is raised above the surface in order to accommodate the material which is deformed below the impacting particle, while at 30° impact, ploughing and cutting produce a lip of material ahead of the erodent particle.

Plastic deformation of titanium aluminides during particle erosion is also evidenced by slip lines adjacent to single impact sites. These lie within primary α_2 grains on the surface of as received Ti-25Al-10Nb-3V-1Mo (at.%) and have the same appearance as the lines on the gauge length of the compression specimen of this material after 3% strain and after strain to fracture. In particle erosion and compression the B2 matrix is heavily deformed, although slip lines are not observed in the B2 phase. More extensive slip and greater bulk deformation at the single impact sites on 304 stainless steel than on the titanium aluminide alloys are consistent with the greater tensile ductility of 304 stainless steel.

The ductility exhibited by the usually brittle titanium aluminides during particle erosion is indicative of the constrained conditions which prevail during particle erosion and which inhibit fracture which limits ductility in a conventional tensile test. The ability of the α_2 and γ alloys to plastically deform during particle erosion is consistent with the achievement of true strains in compression of 11% for Ti-24.5Al-10.5Nb-1.5Mo (at.%) (strain rate of $3x10^3s^{-1}$)[34] and 15% for Ti-48Al-1V (at.%)[48] (strain rate of $4x10^3s^{-1}$). In contrast, the true strain to fracture of as received Ti-25Al-10Nb-3V-1Mo (at.%) is approximately 2% in unconstrained uni-axial tension.

The steady state particle eroded surfaces of the titanium aluminide alloys and 304 stainless steel consist mainly of highly strained and flattened material which is fractured in places. These observations are consistent with the platelet mechanism of erosion of ductile materials which was proposed by Levy[57]. According to this mechanism, thin platelets are formed on the edge of impact craters and are forged against the hardened surface by subsequent impacts. Material loss occurs when the platelets reach their fracture strain. This mechanism accounts for the lower particle erosion rate of 304 stainless steel compared to the titanium aluminide alloys, since the higher work hardening rates and lower ductility of the titanium aluminide alloys lead to the formation of the hardened subsurface anvil at a lower strain than for 304 stainless steel and result in higher rates of material loss.

In contrast to the plastic deformation observed at single impact sites on the titanium aluminide alloys, 304 stainless steel and annealed aluminium 6261, glass exhibits saucer-shaped fracture

surfaces which are produced by the intersection of lateral cracks with the target surface during the unloading cycle[55] as shown schematically in Figure 9. The saucer-shaped fracture surfaces exhibit concentric ripples which are produced by a simultaneous change in the plane of crack propagation for the whole crack front[109]. The steps or striations that are oriented radially (parallel to the direction of lateral crack propagation) on the saucer-shaped fracture surfaces are produced when adjacent sections of the lateral crack front follow paths at slightly different levels[109]. Radial cracks are produced on median planes during the loading cycle of each single impact event. Lateral cracks lead to the removal of saucer-shaped flakes of material and in this way are responsible for greater material loss than the radial cracks.

The Knoop microhardness profiles obtained from Ti-25Al-10Nb-3V-1Mo (at.%) and annealed aluminium 6261 show a small amount of subsurface hardening in the near-surface region of Ti-25Al-10Nb-3V-1Mo (at.%) and appreciable hardening of the annealed aluminium 6261. The microhardness of Ti-25Al-10Nb-3V-1Mo (at.%) is between 530 HK (15 gf) and 580 HK (15 gf) in the near surface region (approximately 80 μm wide) and between 400 HK (15 gf) and 530 HK (15 gf) at depths greater than 80 μm below the surface. The Knoop microhardness of annealed aluminium 6261 increases from 46 HK (15 gf) in the bulk material to approximately 70 HK (15 gf) in the near surface-region. The increase in the mean microhardness due to particle erosion, i.e. the difference between the mean value of the range of microhardness values in the near-surface region and in the bulk material, is approximately 20 percent for as received Ti-25Al-10Nb-3V (at.%) and approximately 52 percent for annealed aluminium 6261. This is a result of the work-hardened condition of as received Ti-25Al-10N-3V-1Mo (at.%) compared to the annealed condition of the aluminium specimen. The microhardness of annealed aluminium 6261 after particle erosion is 70 HK (15 gf) compared to the microhardness before annealing of approximately 66 HK (15 gf).

5.2.3. Thermal Effects

Heating of the surface by the kinetic energy of the impacting particle should be considered because of the potential effect on material properties and consequently on particle erosion performance. The possibility of local heating during particle impact was considered by Hutchings and Levy[60] for both single impact and multiple particle impact. The expression for the temperature rise at a single impact site under adiabatic conditions and the ratios of the root mean square (r.m.s.) diffusion distance to the depth of the plastic zone for single and for multiple particle impact are summarised in section 2.4.2.

The calculations for heating of the particle eroded surface were performed for as received Ti-25Al-10Nb-3V-1Mo (at.%). The thermal conductivity could not be obtained for TiAl, but the results for Ti-25Al-10Nb-3V-1Mo (at.%) provide a useful approximation of the thermal conditions during particle impact of the TiAl alloys since the hardness is the same order of

5.2.4 The Effect of Particle Velocity on Particle Erosion

At room temperature, the particle erosion rates of the titanium aluminide alloys and 304 stainless steel increase approximately five fold with a two fold increase in particle velocity from 20 $m.s^{-1}$ to 40 $m.s^{-1}$. These observations are reminiscent of the increase in the kinetic energy of the particles striking the surface with the square of the particle velocity, i.e. kinetic energy, $E_k = 0.5mv^2$, where m is the mass of the erodent particle and v is the particle velocity and are consistent with observations of an increase in particle erosion rate proportional to between v^2 and v^3, where v is the particle velocity[50].

In addition to the increased kinetic energy dissipated against the target at a higher velocity, the response of the target material will be different at the higher strain rate accompanying the greater particle velocity. According to Hutching's analysis for spherical quartz particles, the strain rate increases in proportion to the square root of the particle velocity[63]. An increase in particle velocity from 20 $m.s^{-1}$ to 40 $m.s^{-1}$ for a spherical particle of 100 μm diameter will result in an increase in strain rate from approximately 8×10^5 s^{-1} to 10^6 s^{-1} with a possible decrease in the strain to fracture with the increase in the rate of deformation.

5.2.5 The Effect of Temperature on Particle Erosion

No appreciable mass gain is measured after blasting the titanium aluminide alloys and 304 stainless steel with hot air at 300°C and 500°C for the duration of a normal erosion test, which is consistent with the mass gain measured for Ti-25Al-10Nb-3V-1Mo (at.%) of only 0.101 mg/cm^3 after 100 hours at 650°C in high purity air at a low flow rate of 1 $cm^3.s^{-1}$ [112]. The ability of the experimental materials to dissipate the heat produced by the impacting particles does not change significantly between 25°C and 500°C as shown in section 5.2.3., which means that changes in mechanical properties are responsible for the observed increase in particle erosion rate with increasing temperature.

The melting point of Ti-50Al (at.%) is 1460°C and the melting point of Ti-25Al (at.%) is 1600° C[25]. The melting point of 304 stainless steel is in the range 1400°C to 1450°C[113]. The phase diagram in section 2.3.1 shows that the melting point of Ti-52Al (at.%) is within 10°C of that of Ti-50Al (at.%) and the melting point of Ti-48Al-2Mn-2Nb (at.%) may be 10°C higher due to the addition of niobium and manganese. There is not much difference between the melting points of these materials and therefore not much difference between their homologous temperatures (H.T.), which are approximately equal to 0.02 at 25°C, 0.2 at 300°C and 0.4 at 500°C. Gat and Tabakoff[65] found that the particle erosion rates of a variety of metals decrease as temperature is increased in the temperature range where H.T. < 0.2 and increase with increasing temperature in

it is conceivable that the decrease in yield strength between 25°C and 500°C is sufficient to result in the displacement and removal of material from the surface after one or a few particle strikes at 500°C as opposed to the repeated impact that is required to remove material at 25°C. Such a change in particle erosion mechanism would contribute to an increase in the particle erosion rate of Ti-25Al-10Nb-3V-1Mo (at.%) between 25°C and 500°C. A similar change in the mechanism of particle erosion could be responsible for the increase in particle erosion rate with increasing temperature which is observed for the TiAl-based alloys and 304 stainless steel.

The rate of increase in the particle erosion rate with increasing temperature is significantly different for Ti-52Al (at.%) on the one hand and Ti-25Al-10Nb-3V-1Mo (at.%) and 304 stainless steel on the other as shown in Figure 64. This may be due to a change in the mechanism of particle erosion between 25°C and 300°C for Ti-52Al (at.%) and between 300°C and 500°C for Ti-25Al-10Nb-3V-1Mo (at.%) and 304 stainless steel, which in turn would be due to differences in the rates of change of the mechanical properties which influence particle erosion.

5.3. Cavitation erosion

5.3.1. Test Results

5.3.1.1. *Ti-25Al-10Nb-3V-1Mo (at.%)*

In this section the cavitation erosion behaviour of Ti-25Al-10Nb-3V-1Mo (at.%) is discussed in terms of microstructure and mechanical properties. The cavitation erosion rate of Ti-25Al-10Nb-3V-1Mo (at.%) is inversely proportional to the hardness of the material as shown in Figure 98.

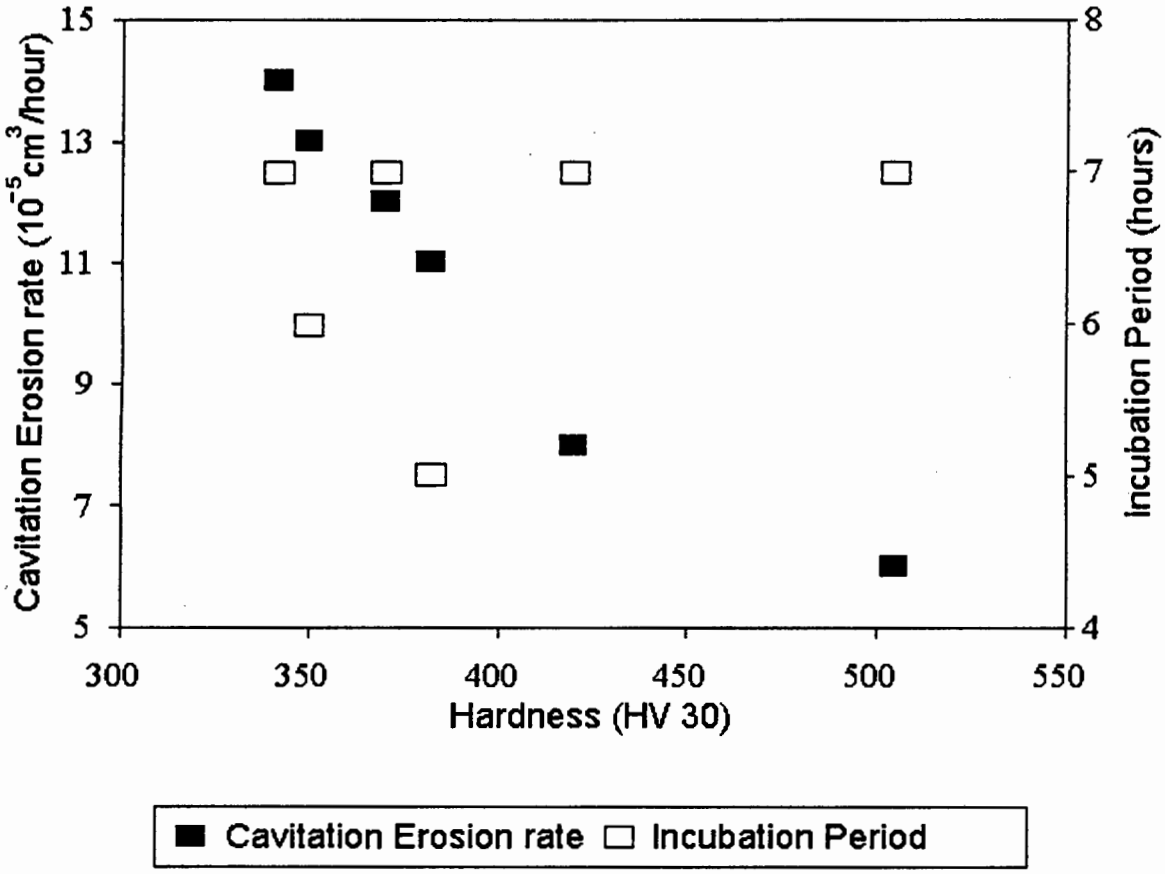

Figure 98. Graphs of steady state cavitation erosion rate and incubation period versus starting hardness (30 kg Vickers) for specimens of Ti-25Al-10Nb-3V-1Mo (at.%).

The close inverse correlation that exists between the Vickers hardness and the cavitation erosion rate of Ti-25Al-10Nb-3V-1Mo (at.%) arises from its high work hardening rate as discussed below. It can be shown from the geometry of the indentation that the Vickers hardness is equal to three times the yield strength if the yield strength remains constant during indentation, i.e. if the material does not work harden[116]. However, this relationship does not hold for materials such as Ti-25Al-10Nb-3V-1Mo (at.%) which work harden appreciably. The deformation in a Vickers indentation is equivalent to a tensile strain of approximately 8 per cent[117], so that for a material with a high work hardening rate such as Ti-25Al-10Nb-3V-1Mo (at.%), the flow stress at 8 per cent strain, i.e. the indentation hardness, is considerably larger than the yield strength. Therefore, the hardness of Ti-25Al-10Nb-3V-1Mo (at.%) is a measure of the flow stress at approximately 8 per cent strain, which is controlled by the yield strength and the work hardening rate.

The cavitation erosion rates of the titanium aluminide alloys are lower than those for 304 stainless steel and annealed aluminium 6261. The titanium aluminide alloys are slightly harder than 304 stainless steel and the work hardening rate of Ti-25Al-10Nb-3V-1Mo (at.%) is an order of magnitude higher than that for 304 stainless steel, which may contribute to its superior cavitation

erosion resistance. The contribution of work hardening rate to improving cavitation erosion performance has been reported by other workers[69,70,81]. The lower ductility and work to break for Ti-25Al-10Nb-3V-1Mo (at.%) compared to 304 stainless steel appears to have less of an effect on the cavitation erosion performance than the hardness and work hardening rate.

The observed increase in the cavitation erosion resistance of Ti-25Al-10Nb-3V-1Mo (at.%) with increasing hardness as discussed in the preceding paragraph is in general agreement with Ball's[70] reasoning that a high work hardening rate provides wear resistance. He argued that during erosive or abrasive wear the surface can be assumed to have reached the fracture strain and that material below the surface is plastically deformed and work hardened but has not yet achieved the fracture strain, as shown schematically in Figure 99. The benefit of a high work hardening rate is that the flow stress increases with increasing strain, thereby prolonging the attainment of the fracture strain to a higher stress. In contrast, a high yield strength is not beneficial to wear resistance unless there is an accompanying increase in the work hardening rate and ultimate strength and therefore in the stress at which the fracture strain is attained and at which material loss occurs.

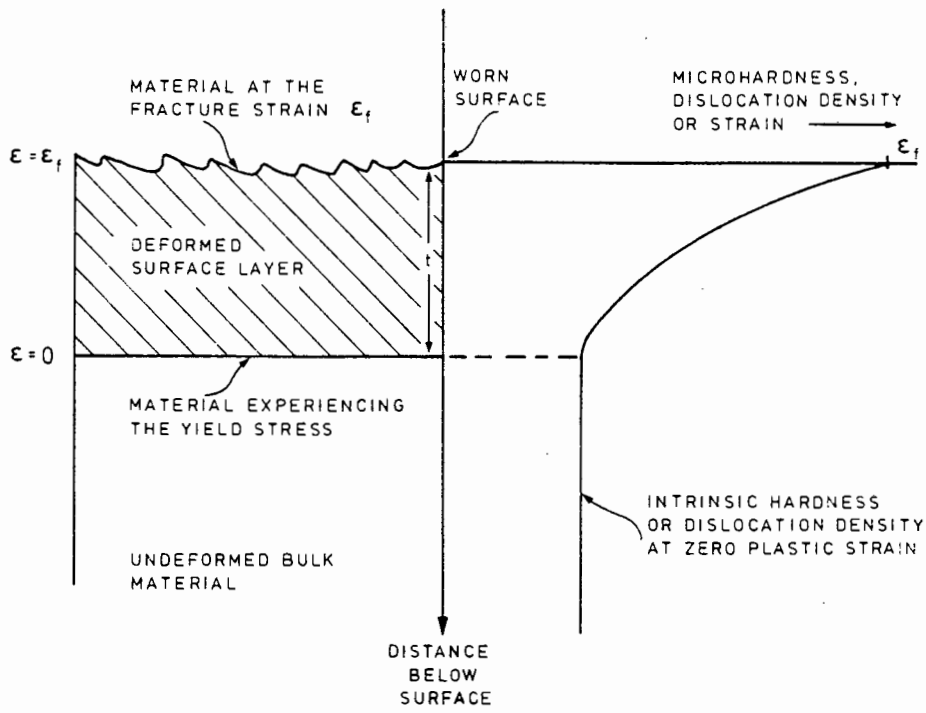

Figure 99. Schematic representation of the deformed surface layer of an eroded material. Strain decreases away from the worn surface. The strain (ε) at the worn surface is equal to the fracture strain, ε_f. The thickness, t, of the deformed layer increases with decreasing yield strength (after Ball[70]).

Incubation period is not proportional to bulk hardness and no simple correlation exists between starting hardness and the length of incubation period for specimens of Ti-25Al-10Nb-3V-1Mo (at.%) heat treated to different values of starting hardness as shown in Figure 98. The annealed

(800°C) specimen with the lowest hardness exhibits the same incubation period of 7 hours as the hardest, as received specimen, while the annealed (1000°C) material with an intermediate hardness exhibits an incubation period of 5 hours, the shortest incubation period of all the Ti-25Al-10Nb-3V-1Mo (at.%) specimens. The changes in hardness are accompanied by microstructural changes which also have an effect on the incubation period.

The shorter incubation period of annealed (1000°C) Ti-25Al-10Nb-3V-1Mo (at.%) compared to the other Ti-25Al-10Nb-3V-1Mo (at.%) specimens can be explained in terms of its microstructure as shown in Figure 30(f). Material loss during cavitation erosion is usually initiated at surface asperities since they have smaller cross-sectional areas than the surrounding unraised material and therefore provide less resistance to the cavitation stresses. The annealed (1000°C) specimen is distinguished from the other Ti-25Al-10Nb-3V-1Mo (at.%) specimens by a larger volume fraction of the α_2 phase, i.e. 70 ± 3% compared to between 45 % and 60 % and by a more continuous network of the α_2 phase (greater α_2/α_2 grain contact) than the other Ti-25Al-10Nb-3V-1Mo (at.%) specimens. Since greater strain incompatibility exists at interfaces between primary α_2 grains than between primary α_2 grains and the B2 matrix[18], a larger amount of strain accumulates at the α_2/α_2 interfaces after a given time of exposure to cavitation. Therefore material loss is initiated at the α_2/α_2 grain boundaries after a shorter exposure to cavitation than the α_2/B2 grain boundaries, which results in a shorter incubation period for annealed (1000°C) Ti-25Al-10Nb-3V-1Mo (at.%).

Figure 100 shows the cavitation erosion rate as a function of annealing temperature, as well as the increase in contiguity and grain size of the α_2 phase. The percentage of the α_2 phase after each heat treatment is also displayed and it is clear that the cavitation erosion rate exhibits a maximum at 52% α_2, which is the softest microstructural condition. The relationship between the annealing temperature and cavitation erosion rate shown in Figure 100 is the inverse of the relationship between the annealing temperature and the bulk hardness as shown in Figure 31. The cavitation erosion rate of the specimen of Ti-25Al-10Nb-3V-1Mo (at.%) which was aged at 650°C for 2 hours exhibits the lowest cavitation erosion rate of the Ti-25Al-10Nb-3V-1Mo (at.%) specimens. The matrix phase of the aged (650°C) specimen, shown in Figure 32, is thought to consist of fine precipitates which are not resolved with the scanning electron microscope and gives rise to the greater hardness of the aged (650°C) specimen compared to the other Ti-25Al-10Nb-3V-1Mo (at.%) specimens.

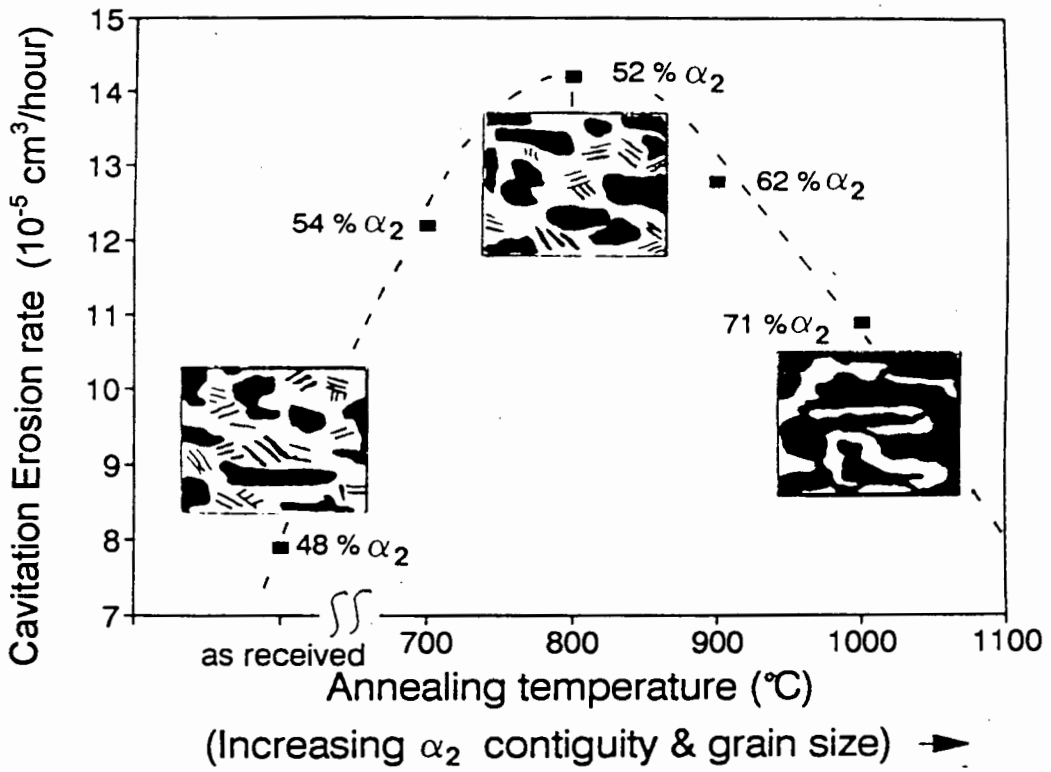

Figure 100. Steady state cavitation erosion rate as a function of annealing temperature for Ti-25Al-10Nb-3V-1Mo (at.%). The volume percent α_2 phase and the increase in contiguity and grain size of the α_2 phase with increasing heat treatment temperature are indicated. Sketches of three representative microstructures are shown for the as received and heat treated (800°C and 1000°C) conditions, with the α_2 phase shown in dark contrast and the B2 phase in bright contrast.

5.3.1.2. *Ti-52Al (at.%) and Ti-48Al-2Mn-2Nb (at.%)*

The steady state cavitation erosion rates of homogenized Ti-52Al (at.%) and homogenized Ti-48Al-2Mn-2Nb (at.%) are the same and lower than that of as received Ti-25Al-10Nb-3V-1Mo (at.%) as shown in Figure 101. The reasons for this are discussed in the following paragraphs.

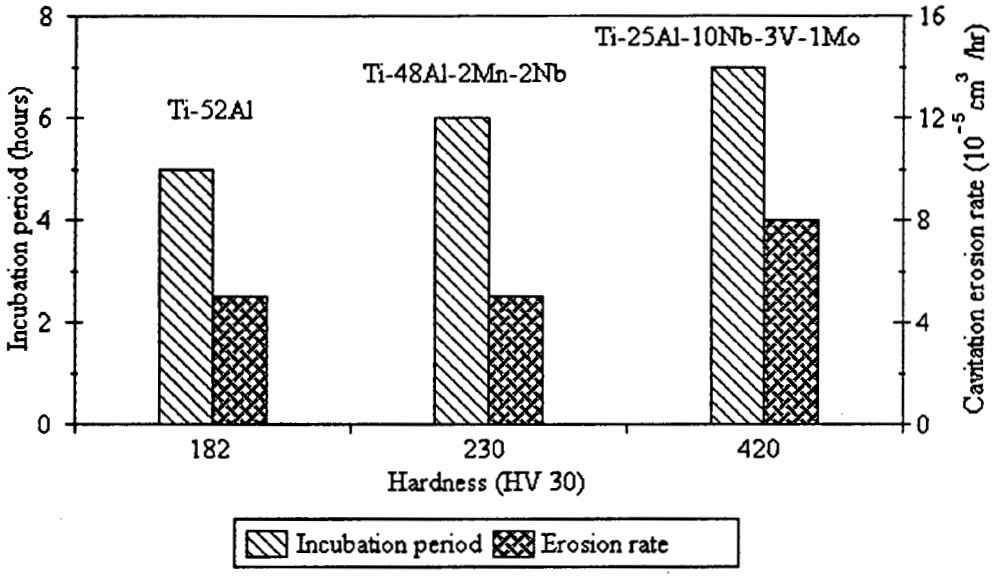

Figure 101. Cavitation erosion results for homogenized Ti-52Al (at.%), homogenized Ti-48Al-2Mn-2Nb (at.%) and as received Ti-25Al-10Nb-3V-1Mo (at.%) as a function of bulk hardness. Incubation period is extended by the increase in bulk hardness and the erosion rate increases with increasing bulk hardness.

Hardening of the near-surface region after exposure to cavitation erosion for 20 hours is measurable for homogenized Ti-52Al (at.%) and homogenized Ti-48Al-2Mn-2Nb (at.%), but not for as received Ti-25Al-10Nb-3V-1Mo (at.%) as shown in Figures 83 and 70(a) respectively. The microhardness of homogenized Ti-52Al (at.%) and homogenized Ti-48Al-2Mn-2Nb (at.%) increase by approximately 40 percent and 50 percent respectively from the bulk material to the near-surface region as shown in Figure 83. The lower steady state cavitation erosion rate of homogenized Ti-52Al (at.%) and homogenized Ti-48Al-2Mn-2Nb (at.%) compared to as received Ti-25Al-10Nb-3V-1Mo (at.%) can be ascribed to the greater increase in microhardness with decreasing distance from the eroded surface, i.e. with increasing strain, for homogenized Ti-52Al (at.%) and homogenized Ti-48Al-2Mn-2Nb (at.%) than for Ti-25Al-10Nb-3V-1Mo (at.%). The benefit to cavitation erosion resistance of a high work hardening rate, i.e. the increase in flow

stress with increasing strain is discussed in the previous section for specimens of Ti-25Al-10Nb-3V-1Mo (at.%). The observation of slightly greater work hardening for the TiAl-based alloys during cavitation erosion is consistent with the work hardening rates measured at high strain rates for Ti-24.5Al-10.5Nb-1.5Mo (at.%) and Ti-48Al-1V (at.%). Gray et al.[34] measured a work hardening rate of 4200 MPa per unit strain at a strain rate of 6000 s^{-1} for Ti-24.5Al-10.5Nb-1.5Mo (at.%) and Gray[48] recorded a work hardening rate of 4640 MPa per unit strain at a strain rate of 4500 s^{-1} for Ti-48Al-1V (at.%).

The competing effects of hardness and microstructure contribute to the equal cavitation erosion rates of homogenized Ti-52Al (at.%) and homogenized Ti-48Al-2Mn-2Nb (at.%) as follows. The greater hardness of homogenized Ti-48Al-2Mn-2Nb (at.%) provides greater cavitation erosion resistance as discussed above for specimens of Ti-25Al-10Nb-3V-1Mo (at.%) and the smaller volume fraction of α_2 precipitates in homogenized Ti-52Al (at.%) than in homogenized Ti-48Al-2Mn-2Nb (at.%) is beneficial to cavitation erosion resistance as discussed in section 5.3.2.

The longer incubation period of the harder homogenized Ti-48Al-2Mn-2Nb (at.%) material compared to that of homogenized Ti-52Al (at.%) suggests that the starting hardness, as a measure of the yield strength, contributes to cavitation erosion by increasing the stress required for the formation of surface asperities from which material loss is initiated as shown in Figure 101. The formation of twins will also affect the onset of steady state material loss as discussed below.

The incubation periods for Ti-25Al-10Nb-3V-1Mo (at.%) and Ti-52Al (at.%) are 6.6 hours (rounded to 7 hours) and 5 hours respectively as shown in Figure 102. The rate of material loss for Ti-25Al-10Nb-3V-1Mo (at.%) between 5 and 8 hours is greater than the low initial rate but smaller than the steady state erosion rate given by the regression line, while the rate of material loss for Ti-52Al (at.%) increases from the initial low rate to the steady state erosion rate in a more abrupt fashion after approximately 5 hours as shown in Figure 102. In this regard an alternative definition for the incubation period has been defined by previous workers[118], i.e. as the time at which the rate of material loss deviates from the initial low rate. Precise values for the incubation period using this definition are difficult to obtain in the present study; they are between 4 and 7 hours for Ti-25Al-10Nb-3V-1Mo (at.%) and between 6 and 8 hours for Ti-52Al (at.%) and Ti-48Al-2Mn-2Nb (at.%).

The heavy deformation lines which appear on Ti-52Al (at.%) and Ti-48Al-2Mn-2Nb (at.%) after 15 minutes of cavitation erosion are sites of easy material removal since they are raised above the surrounding surface and have smaller cross-sectional areas and therefore offer less resistance to cavitation stresses. The more homogeneously deformed surface of Ti-25Al-10Nb-3V-1Mo (at.%) does not provide as many sites for easy material removal during the same time period which may

contribute to the longer incubation period and more gradual onset of steady state material loss for Ti-25Al-10Nb-3V-1Mo (at.%) as shown in Figure 102.

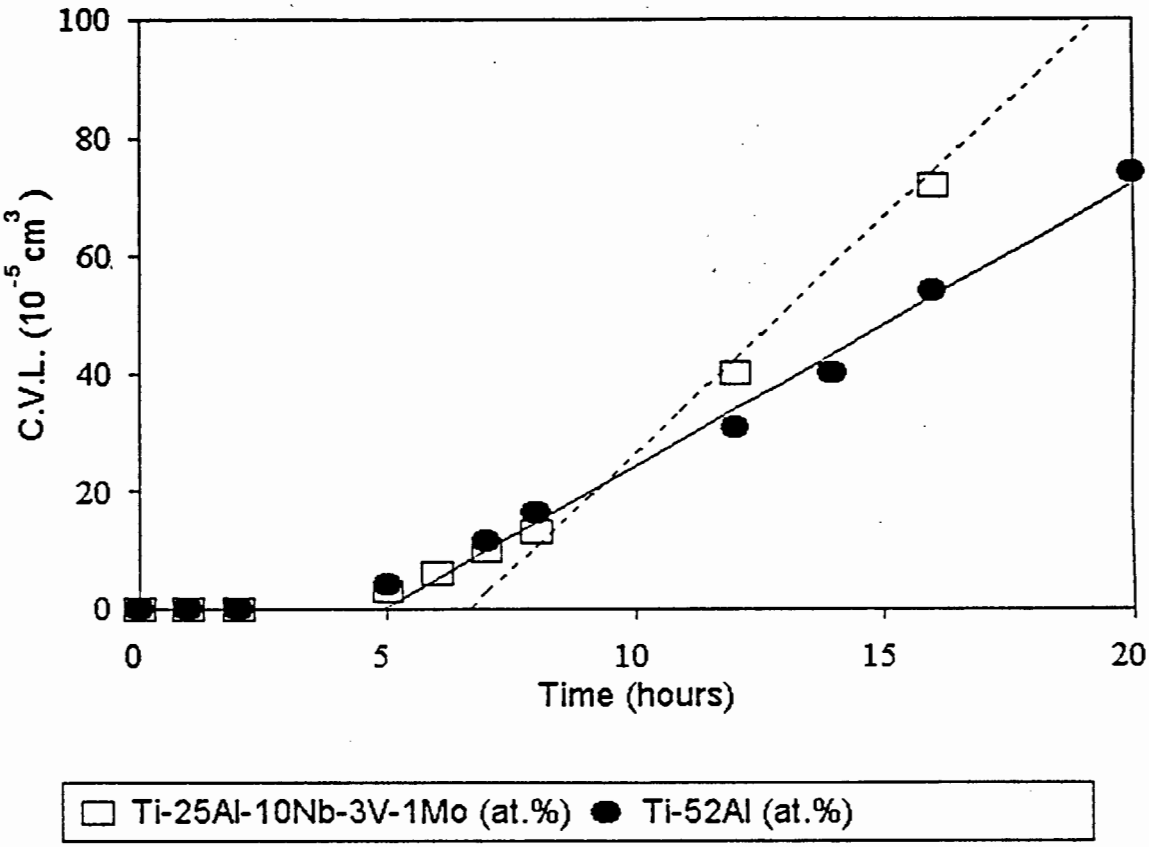

Figure 102. Cavitation erosion graphs of cumulative volume loss (C.V.L.) versus time of erosion for as received Ti-25Al-10Nb-3V-1Mo (at.%) and homogenized Ti-52Al (at.%). The longer incubation period of as received Ti-25Al-10Nb-3V-1Mo (at.%) is due to the more gradual onset of steady state cavitation erosion compared to Ti-52Al (at.%).

The cavitation erosion resistance of the Ti_3Al-based and TiAl-based titanium aluminide alloys compares favourably with those of a large number of materials which Heathcock[118] evaluated. The materials which exhibited the lowest cavitation erosion rates were Stellites, the Ni-51Ti (at.%) shape memory intermetallic alloy and hardmetals consisting of sintered carbides with a cobalt-based or nickel-based binder phase. These results are shown in Figure 103 with the results for the titanium aluminide alloys and the WC-15Co (wt.%) hardmetal which were obtained in the present study. It can be seen from Figure 103 that a high starting hardness is not a prerequisite for cavitation erosion resistance. The alloys based on Ti_3Al, TiAl and NiTi intermetallic compounds have relatively low starting hardness and high work hardening rates and exhibit lower cavitation erosion rates than the erosion resistant WC-15Co (wt.%) hardmetal. In contrast, 430 ferritic stainless steel, with approximately the same starting hardness as the TiAl-based titanium aluminide alloys and Ni-51Ti (at.%), but with a much lower work hardening rate, exhibits a cavitation

erosion rate which is two orders of magnitude larger than that of the TiAl-based alloys and Ni-51Ti (at.%).

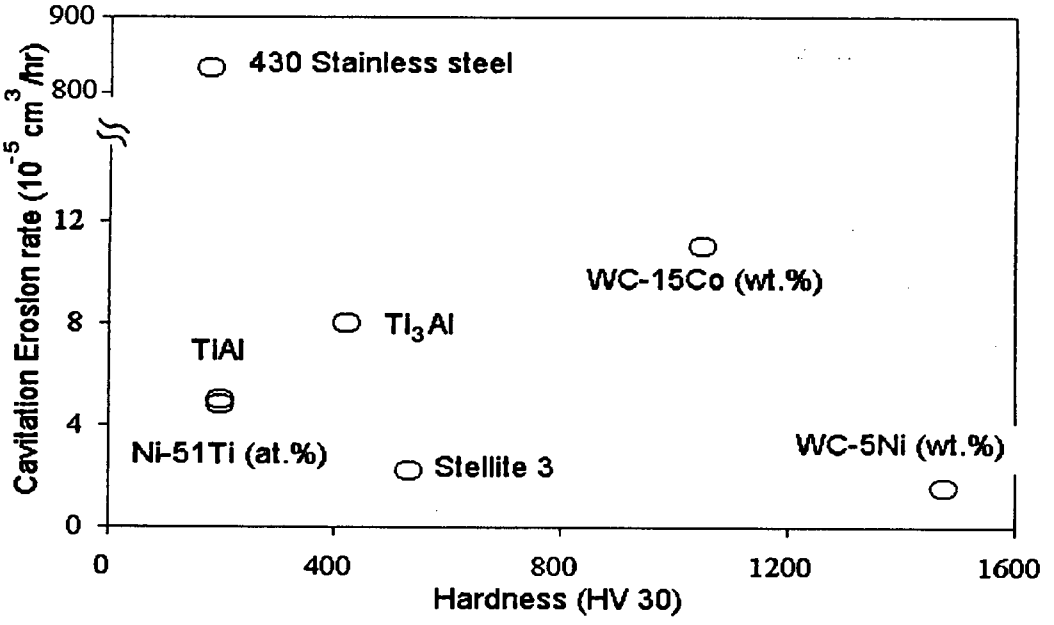

Figure 103. Graph of steady state cavitation erosion rates as a function of bulk hardness for Stellite 3, Ni-51Ti (at.%), WC-5Ni (wt.%) and 430 stainless steel reported by Heathcock[118] and the Ti_3Al-based and TiAl-based titanium aluminide alloys and WC-15Co (wt.%) tested in the present study.

5.3.2. Surface Examination - Ti-25Al-10Nb-3V-1Mo (at.%)

Light cavitation erosion damage on as received and annealed Ti-25Al-10Nb-3V-1Mo (at.%) specimens is pronounced at primary α_2 grain boundaries as shown in Figure 66. Brittle fracture surfaces and ductile smeared areas are observed on the steady state eroded surfaces. The valleys or voids in the steady state cavitation eroded surfaces correspond in size and shape to the primary α_2 grains as shown in Figure 69. The line features that are observed on the cavitation eroded surfaces of Ti-52Al (at.%) and Ti-48Al-2Mn-2Nb (at.%) are not detected on the surface of lightly damaged Ti-25Al-10Nb-3V-1Mo (at.%). Twinning is not commonly observed in α_2 titanium aluminides even in high strain rate conditions[23] and neither is it observed in the high strain rate conditions of cavitation erosion.

The mechanism of material removal appears to involve the accumulation of strain preferentially at the phase boundary regions, followed by fracture and subsequent fall-out of the primary α_2 grains as shown schematically in Figure 104. This is similar to the pronounced grain boundary deformation and preferential β phase removal observed by Karimi and Avellan for α + β brass[72] and is consistent with the mechanism of tensile failure of Ti-25Al-10Nb-3V-1Mo (at.%) which involves cleavage fracture of the less ductile α_2 phase and ductile tearing of the B2 matrix. The tensile fracture surface exhibits brittle cleavage fracture on areas similar in size to the primary α_2 grains, but exhibits more pronounced deformation than the steady state cavitation eroded surfaces as shown in the micrographs in Figures 39 and 67 and illustrated schematically in Figures 93 and 104. This may be indicative of the higher strain rate which prevails during cavitation erosion compared to that of the tensile test.

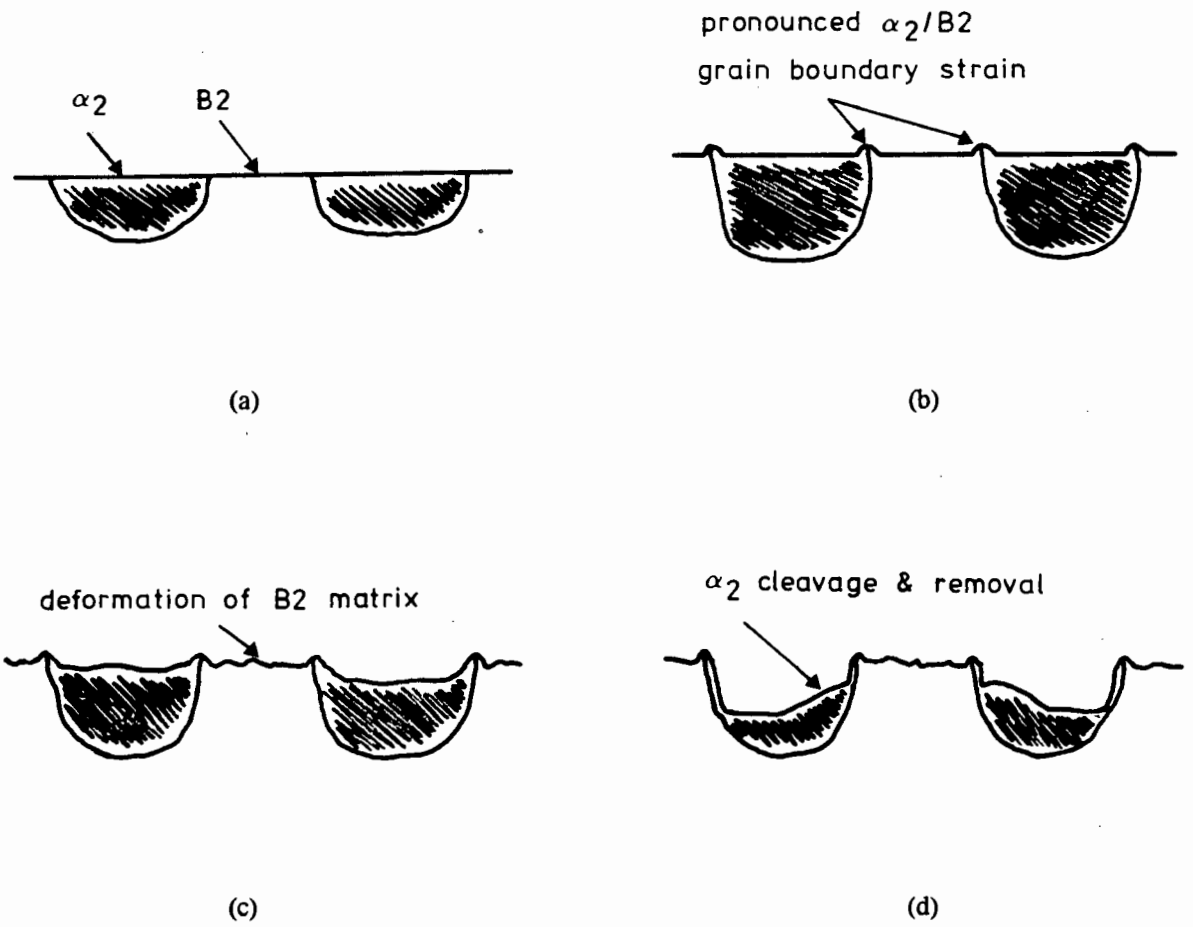

Figure 104. Schematic diagram of the mechanism of cavitation erosion of as received Ti-25Al-10Nb-3V-1Mo (at.%). (a) The starting microstructure consists of the B2 matrix, primary α_2 grains and secondary α_2/O precipitates (not shown). (b) Light cavitation produces pronounced deformation at the primary α_2/B2 grain boundary regions. Material removal is initiated at these asperities. (c) Further cavitation results in deformation of the bulk of the B2 matrix, i.e. away from the phase boundaries. (d) Steady state cavitation erosion involves the cleavage and preferential removal of primary α_2 grains.

5.3.3. Surface Examination - Ti-52Al (at.%) and Ti-48Al-2Mn-2Nb (at.%)

The identification of deformation twins on γ{111} planes in Ti-52Al (at.%) by transmission electron microscopy is consistent with the observations of other workers in TiAl-based alloys[41,48,119,120]. Twins form more readily as the rate of deformation is increased since thermally activated dislocation movement is inhibited. Gray[48] observed an increase the propensity for twinning in Ti-48Al-1V (at.%) with an increase in strain rate from 10^{-3} s^{-1} to 7500 s^{-1}. The deformation twins observed with the T.E.M. correspond to the faint crossed lines observed with the S.E.M. in the transition regions of the cavitation eroded TiAl-based alloy specimens as shown in section 4.3. The twins and faint crossed lines are approximately 0.1μm wide and each appear as two sets of parallel lines with an angle of 70° between the two sets. The 70° angle between the sets of parallel twins, i.e. between the two twin variants and between the sets of faint lines is consistent with the angle between the γ{111} planes as shown in the S.A.D.P. in Figure 92.

Sets of faint lines, now identified as twins, are observed on near-γ Ti-48Al-2Mn-2Nb (at.%) after 15 minutes of cavitation erosion as shown in Figure 80. One twin variant increases in width from approximately 0.1 μm to approximately 4 μm after exposure to cavitation erosion for between 45 minutes and 135 minutes, while the other does not increase with increasing time of cavitation erosion for up to 195 minutes as shown in Figures 81 and 82. These thicker twins are the same width as the thicker lines which form within the first 15 minutes of cavitation erosion on near-γ Ti-48Al-2Mn-2Nb (at.%) and are a prominent feature of the transition regions of the TiAl-based cavitation eroded specimens.

Twin thickening was observed by Frommeyer, Wunderlich, Kremser and Liu[121] and by Shechtman, Blackburn and Lipsitt[119] in TiAl-based titanium aluminide alloys tested in tension and compression respectively. The mechanism of twin thickening in Ti-50Al (at.%) and Ti-54Al (at.%) was identified as the movement of partial dislocations at the twin interfaces[119]. It seems reasonable therefore that the thick deformation lines on the cavitation eroded surfaces of the TiAl-based alloys are twins which are favourably aligned for partial dislocation movement, while the fainter lines are unfavourably aligned for partial dislocation movement.

The parallel troughs on the steady state cavitation eroded surfaces of the TiAl-based alloys are evidence of preferential material removal from the twins and from the untwinned regions parallel to the twins as shown in Figures 74 and 77. Grain and annealing twin boundaries and the matrix/ α_2 precipitate interfaces are also sites of preferential material removal as shown in Figures 73 and 75.

The mechanism of cavitation erosion of the TiAl-based alloys is summarised schematically in Figure 105. During the incubation period, deformation twins are produced by cavitation and the surrounding material exhibits only light deformation as shown schematically in Figure 105(a). Further cavitation results in thickening of some twin variants and the initiation of material removal from the raised twins and the matrix areas adjacent to the twins as shown in Figures 105(b) and (c).

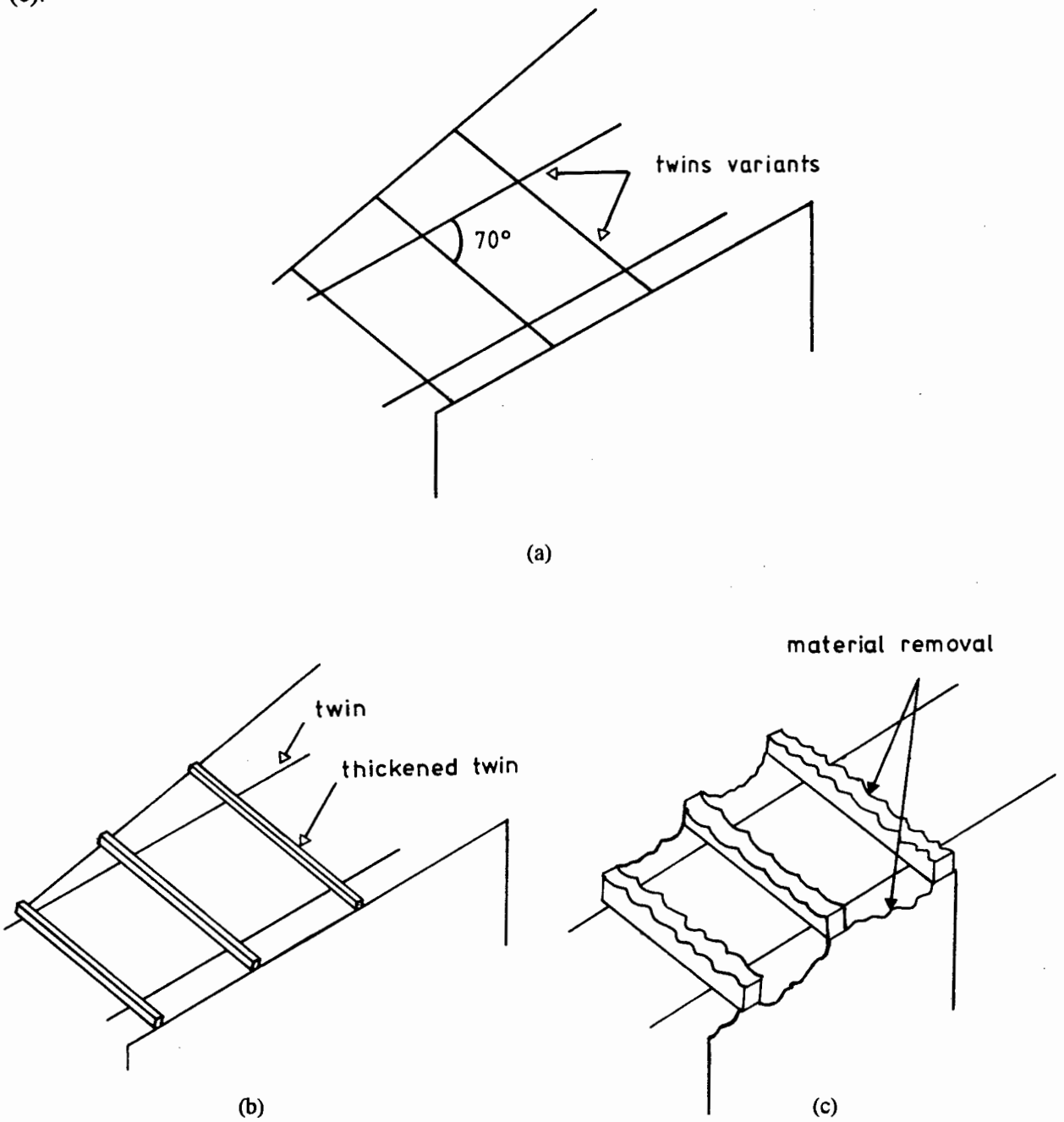

Figure 105. Schematic representation of the initiation and progression of cavitation erosion for TiAl-based alloys. (a) Initially, twins are produced within γ grains. (b) Some twin variants thicken, while others retain their original appearance. (c) Material is removed from the twins and from the untwinned regions adjacent to the twins.

Near-γ Ti-48Al-2Mn-2Nb (at.%) exhibits a lower cavitation erosion rate and a longer incubation period than homogenized Ti-48Al-2Mn-2Nb (at.%) although their hardnesses are not significantly different. The main difference between the microstructures of near-γ Ti-48Al-2Mn-2Nb (at.%) and homogenized Ti-48Al-2Mn-2Nb (at.%) is the larger volume fraction of α_2 precipitates in the homogenized material. Evidence for the α_2 precipitates having an effect on the cavitation erosion is found in the micrographs of the steady state regions of homogenized Ti-52Al (at.%) and homogenized Ti-48Al-2Mn-2Nb (at.%). The α_2 precipitates cross the twins and the twins appear not to penetrate the α_2 precipitates. The α_2 precipitates in homogenized Ti-52Al (at.%) and Ti-48Al-2Mn-2Nb (at.%) are generally greater than 1 μm wide. Shearing of α_2 precipitates by deformation twins was observed by Frommeyer et al.[121] in Ti-48Al (at.%) when the thickness of the α_2 precipitates was below 1 μm. The continuity of the thick twins across the γ matrix is interrupted by the α_2 precipitates and the precipitates are clearly delineated by material removal along the α_2 precipitate/matrix interface as shown in Figures 72 and 75. The greater cavitation erosion rate of homogenized Ti-48Al-2Mn-2Nb (at.%) with a higher volume fraction of α_2 precipitates can be attributed to the removal of material at the interfaces between the α_2 precipitates and the γ matrix. This finding is consistent with the results of Wilson and Ball[122]. They attributed the increase in cavitation erosion rate of 6061 and 2014 aluminium alloys with the introduction of alumina reinforcement particles to matrix/particulate interfacial degradation.

Deformation twinning is advantageous to cavitation erosion resistance since it absorbs cavitation-induced strain without the accumulation of dislocations. The measurement of hardening in the near-surface region of homogenized Ti-52Al (at.%) and homogenized Ti-48Al-2Mn-2Nb (at.%) is evidence of significant dislocation activity and is consistent with the high work hardening rate of TiAl-based intermetallic alloys. TiAl-based titanium aluminide alloys exhibit a similar sequence of events in response to cavitation erosion as NiTi alloys. In TiAl-based titanium aluminide alloys, twinning initially absorbs strain without increasing the dislocation density and subsequent deformation produces a hardened near-surface region. NiTi alloys exhibit either a stress-induced phase transformation to martensite or the reorientation or growth of existing martensite in the initial stages of cavitation[76], followed by extreme work hardening[78].

5.3.4. Aluminium

Annealed aluminium 6261 reaches a steady state of cavitation erosion after only 12 minutes. The surface exhibits ductile rumpling and material is removed by ductile fracture. There is no evidence of brittle fracture as there is for the titanium aluminide alloys and for glass.

The Knoop microhardness of the subsurface region of the steady state cavitation eroded specimen of aluminium is approximately 58 HK (15 gf) compared to approximately 46 HK (15 gf) in the

bulk material. Work hardening during cavitation erosion appears to restore some of the hardness which is reduced by annealing, however the hardness and work hardening rate are still much lower than the titanium aluminide alloys and 304 stainless steel and results in the inferior cavitation erosion resistance compared to these materials.

5.3.5. Glass

During the cavitation erosion of glass, fracture is initiated at pre-existing microscopic surface flaws, which are enlarged by the removal of material as shown in Figures 88 and 89. Subsequently, a continuous network of flaws and cracks is produced which leads to a steady state of material removal; flakes are removed from the original surface and from the enlarged flaws. The fracture surfaces of the enlarged flaws are entirely brittle as shown in Figure 90. Some of the fracture surfaces are smooth and others exhibit radial striations which indicate that adjacent sections of the crack front follow paths at slightly different levels[109].

The appearance of the fracture which accompanies cavitation erosion is very different to the lateral and radial fractures produced by particle impact as shown in Figures 84, 62 and 63. The particle impact is very localized whereas the biaxial stress imposed by cavitation is experienced over the entire exposed surface and fracture is initiated at flaws.

The initial stages of the cavitation erosion of glass involves the formation of cracks, in contrast to that of the titanium aluminides, 304 stainless steel and aluminium which involves the accumulation of strain. Although the steady cavitation erosion rate of glass is an order of magnitude less than that of annealed aluminium 6261 as shown in Table 21, macroscopic cracks are produced after approximately 30 minutes of exposure to cavitation and the glass breaks into two or more large pieces.

6. CONCLUSIONS

The microstructure of the Ti_3Al-based alloy consists of primary α_2 phase and needle-like precipitates of either the α_2 phase or the orthorhombic phase within the ordered B2 matrix. Heat treatment which reduces the volume fraction of α_2/O precipitates results in a decrease in bulk hardness.

The microstructure of the TiAl-based alloys consist of equiaxed γ grains and lamellar α_2/γ colonies in the as cast condition and after an homogenizing heat treatment, the microstructure consists mainly of equiaxed grains of the γ phase and needle-like α_2 precipitates.

The Ti_3Al-based alloy exhibits a higher work hardening rate and greater strength, but lower ductility than that of 304 stainless steel in tensile tests. The tensile fracture surface of the Ti_3Al-based alloy exhibits cleavage fracture of the primary α_2 grains and ductile tearing of the B2 matrix, while compression specimens of the Ti_3Al-based alloy exhibit extensive ductile dimples on the fracture surface and slip lines on the gauge length after testing, but do not exhibit cleavage fracture.

All of the titanium aluminide intermetallic alloys tested exhibit ductile particle erosion behaviour, with more efficient material removal occurring at oblique impact by the ploughing and cutting action of the erodent particles than at 90° impact. The heat that is produced on the target surface by particle impact is dissipated from the surface and does not influence the mechanical response of the material to particle impact. Similar eroded surface topography was observed on the titanium aluminide alloys as on 304 stainless steel, but greater ductility and more extensive slip were observed on 304 stainless steel. The lower strain to fracture of the titanium aluminide alloys than 304 stainless steel appears to be responsible for the greater particle erosion rates exhibited by the titanium aluminide alloys. The ductile mode of particle erosion exhibited by the titanium aluminide alloys is in contrast to the brittle mode exhibited by glass. The particle erosion rates of the titanium aluminide alloys and 304 stainless steel at 30° impact increase with increasing test temperature between 25°C and 500°C.

In cavitation erosion, the titanium aluminide alloys exhibit erosion rates which are comparable to those of an erosion resistant WC-15Co (wt.%) hardmetal and considerably lower than that for 304 stainless steel because of their higher work hardening ability. The lower steady state cavitation erosion rates of the TiAl-based alloys compared to the Ti_3Al-based alloy are due to deformation twinning and greater work hardening during erosion. The cavitation erosion rate of the Ti_3Al-based alloy is inversely proportional to the starting hardness of the alloy since the hardness is a measure of the work hardening rate for the titanium aluminide alloys.

The mechanism of cavitation erosion for the Ti_3Al-based alloy involves strain accumulation in the phase boundary regions followed by ductile tearing of the B2 matrix and preferential removal of the primary α_2 grains. The TiAl-based alloys exhibit twinning followed by material removal from the twins and the boundaries between the α_2 precipitates and the γ grains. The twins are raised above the surface and as such are sites for easy material removal during the early stages of cavitation, leading to a shorter incubation period than for the Ti_3Al-based alloy.

The present study is one of the first to characterise the particle erosion and cavitation erosion behaviour of titanium aluminide alloys and to explain the excellent cavitation erosion resistance in terms of microstructure and mechanical properties. Titanium aluminide alloys are finding increasing application in areas other than aircraft engines and their superior resistance to cavitation erosion means that they are suitable for components in hydrodynamic systems such as valves and impeller vanes.

Appendix - A - X-Ray Diffraction

The Powder Diffraction File (P.D.F.) Cards which were used to index the x-ray diffraction spectra of the Ti_3Al-based alloy and the TiAl-based alloys are shown below.

(a) P.D.F. card for the Ti_3Al intermetallic compound.

14-451

d	2.19	1.31	1.23	3.38	$(Ti_3Al)8H$
I/I_1	100	30	30	4	ALUMINUM TITANIUM

Rad. CuKα λ 1.5418 Filter Ni Dia.
Cut off I/I_1 COUNTER DIFFRACTOMETER
Ref. GOLDAK AND PARR, TRANS. A.I.M.E. 221 639 (1961)

Sys. HEXAGONAL S.G. $P6_3/mmc$ (194)
a_o 5.77 b_o c_o 4.62 A C 0.801
α β γ Z 2 Dx
Ref. IBID.

ε α nωβ ε γ Sign
2V D mp Color
Ref.

d Å	I/I_1	hkl	d Å	I/I_1	hkl
3.38	4	101	0.806	40	423
2.88	2	110	0.783	18	602
2.498	20	200			
2.307	25	002			
2.191	100	201			
1.699	18	202			
1.440	18	220			
1.310	30	203			
1.249	2	400			
1.225	30	222			
1.204	18	401			
1.156	4	004			
1.099	4	402			
1.049	4	204			
0.970	10	403			
0.925	18	421			
0.903	18	224			
0.874	4	422			
0.868	10	205			
0.832	25	600,215			

(b) P.D.F. card for the Ti-55Al (at.%) intermetallic compound

5-0678

d	2.31	1.99	1.424	4.07	ALTI(55 AT. % AL)
I/I_1	100	60	60	20	ALUMINUM TITANIUM

Rad. CuKα λ 1.54 Filter Ni
Dia. 14.32CM Cut off Coll.
I/I_1 d corr. abs.?
Ref. DUWEZ AND TAYLOR, J.METALS 4, TRANS. 70-1 (1952)

Sys. TETRAGONAL S.G. D_{4H}^1 - $P4/mmm$
a_o 2.82 b_o c_o 4.08 A C 1.448
α β γ Z 2
Ref. IBID.

ε α nωβ ε γ Sign
2V D mp Color
Ref.

PATTERN INDEXED AS CELL TYPE LI_0(AuCu ORDERED)

d Å	I/I_1	hkl	d Å	I/I_1	hkl
4.07	20	001	.915	10	331
2.81	20	110	.908	10	204
2.31	100	111	.895	10	402
2.04	20	002	.891	10	420
1.99	60	200	.872	5	421
1.79	10	201	.826	20	224
1.65	10	112	.817	60	422
1.424	60	202	.805	5	403
1.407	20	220	.793	10	314
1.353	5	003	.784	60	115
1.331	5	221	.773	60	333
1.263	5	130			
1.224	20	113			
1.203	60	131			
1.159	20	222			
1.071	5	132			
1.020	10	004			
0.996	10	400			
.925	20	313			

Appendix B - Cavitation Erosion

The results of four cavitation erosion tests on as received Ti-25Al-10Nb-3V-1Mo (at.%) are shown in figure 106. In the steady state regime the standard deviation is less than 9% of the cumulative volume loss average for each measurement interval.

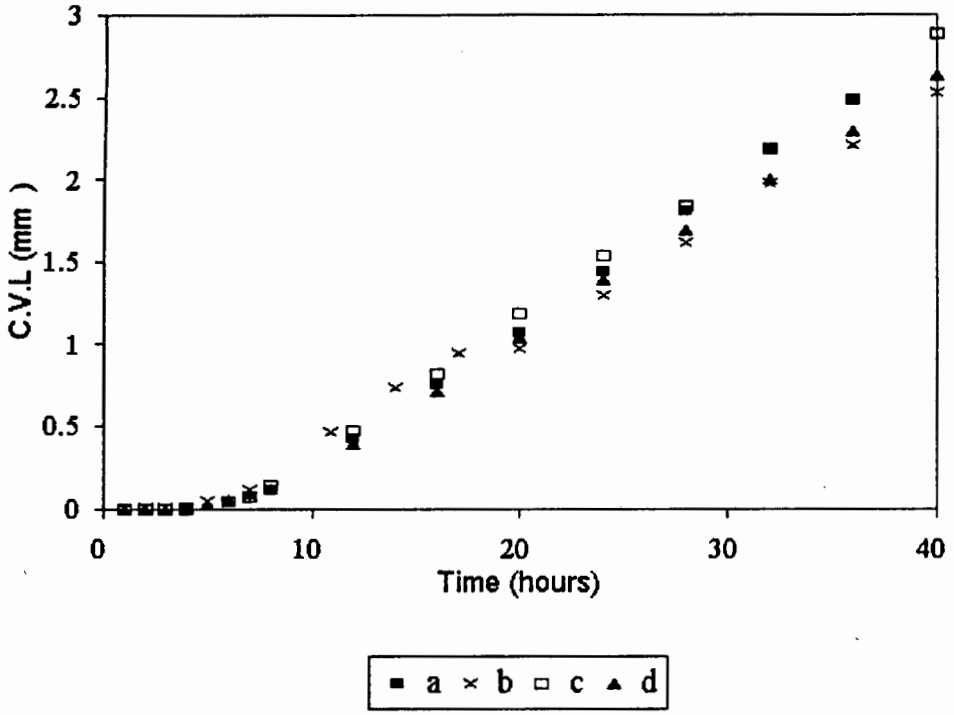

Figure 106. Cavitation erosion cumulative volume loss (C.V.L.) versus time of erosion for four tests (labelled a, b, c and d) on as received Ti-25Al-10Nb-3V-1Mo (at.%).

Table 23. Cavitation erosion results for four tests on as received Ti-25Al-10Nb-3V-1Mo (at.%) in the as received condition.

Test number	Steady state erosion rate (10^{-5} cm/hour)	Incubation period (hour)	Correlation coefficient (R^2)
a	8.7	7.3	0.999
b	8.0	6	0.998
c	8.0	6.6	0.998
d	8.5	6.3	0.999
average	8.3	6.6	-

Appendix C - Solid Particle Erosion with the Room Temperature Apparatus

A specimen of as received Ti-25Al-10Nb-3V-1Mo (at.%) was tested in three separate tests at 90° impact under standard test conditions and the cumulative mass losses and steady state erosion rates are recorded in table 24. The maximum variation between the cumulative mass loss measurements was 26 percent after 30g of erodent. Otherwise, a variation of less than 15 percent was measured for the cumulative mass loss measurements and a variation of 3 percent was obtained for the particle erosion rates as shown in table 24. Correlation coefficients of 0.998, 0.999 and 0.999 between the mass of erodent and the cumulative mass loss were obtained for tests a, b and c respectively.

Table 24. Results of three solid particle erosion tests with the room temperature apparatus on as received Ti-25Al-10Nb-3V-1Mo (at.%).

Erodent mass (g)	Cumulative mass loss (mg)			Maximum variation (%)
	(a)	(b)	(c)	
30	2.4	1.9	2.2	26
60	4.8	4.3	4.6	12
90	7.0	6.6	6.9	6
120	9.6	9.0	9.2	7
Erosion rate (mg/g)	0.0798	0.0785	0.0776	3

Appendix D - Thermal Effects in Particle Erosion

The thermal properties used to calculate the temperature rise and heat dissipation away from impact sites on Ti-25Al-10Nb-3V-1Mo (at.%) during particle erosion are summarised in table 25.

Table 25. Thermal properties used for the calculation of heating during particle erosion.

Material	Specific heat ($J.kg^{-1}.K^{-1}$)	Thermal conductivity ($W.m^{-1}.K^{-1}$)	
	Room temperature	Room temperature	500°C
Ti_3Al[123]	-	10	15
Ti[124]	528	-	-

7. REFERENCES

1. Froes, F. H., Suryanarayana, C. and Eliezer, D., J. Mater. Sci., **27**, 1992, 5113-5140.
2. Dahms, M., Advanced Performance Materials, **1**, 1994, 157-183.
3. Christodoulou, L., Titanium Aluminides, in Cahn, R. W. (ed.), Encyclopaedia of Materials Science and Engineering, Suppl. **2**, Pergamon, Exeter, 1990, 1346-1354.
4. Fleischer, R. L., Dimiduk, D. M. and Lipsitt, H. A., Annu. Rev. Mater. Sci. 1989, **19**, 231-263.
5. Kim, Y-W., JOM, **46**, 7, 1994, 30-39.
6. Chesnutt, J. C. and Williams, J. C., Defence and Aerospace, August 1990, 509-511.
7. Austin, C. M. and Kelly, T. J., in Darolia, R., Lewandowski J. J., Liu, C. T., Martin, P. L., Miracle, D. B. and Nachal, M. V. (eds.), Proc. Int. Symp. on Structural Intermetallics, TMS, Warrendale, 1993, 143.
8. Schell, J. D. and Taylor, K. P., Wear of Jet Engine Components, in Henry, S. D (ed.), Friction, Lubrication and Wear Technology, *ASM International Handbook,* **18**, 1992, 588-592.
9. Baker, I. and Munroe, P. R., JOM, 1988, **40**, 2, 28-31.
10. Cahn, R. W., Metals, Materials and Processes, **1**, 1, 1989, 1-19.
11. Yamaguchi, M. and Umakoshi, Y., Prog. Mater. Sci., **34**, 1990, 1-148.
12. Khan, T., Naka, S., Veyssiere, P. and Costa, P., Intermetallics for Structural Applications, in Bachelet, E., Brunetaud, R., Coutsouradis, D., Esslinger, P., Ewald, J., Kvernes, I., Lindblom, Y., Mendewerft, D. B., Regis, V., Scarlin, R. B., Schneider, K. and Singer, R. (eds.), Proc. Conf. on High Temperature Materials for Power Engineering, 1990, **1**, 1533-1588.
13. Smallman, R. E., Modern Physical Metallurgy, 4th ed., Butterworths, Essex, 1985, 227-229.
14. Honeycombe, R. W. K., The Plastic Deformation of Metals, Edward Arnold, London, 1968, 171-172.
15. Ball, A. and Smallman, R. E., Acta Metall., **14**, 10, 1966, 1349-1355.
16. Ball, A. and Smallman, R. E., Acta Metall., **14**, 11, 1966, 1517-1526.
17. Ward, C. H., Int. Mater. Rev., **38**, 2, 1993, 79-101.
18. Banerjee, D., Ti_3Al and its Alloys, in Westbrooke, J. H. and Fleischer, R. L. (eds) Intermetallic Compounds-Principles and Practice, **2**, Wiley , Chichester, 1995, 91-131.
19. Court, S. A., Lofvander, J. P. A., Loretto, M. H. and Fraser, H. L., Phil. Mag. A, **61**. 1, 1990, 109-139.
20. Banerjee, D., Gogia, A. K. and Nandy, T. K., Metall. Trans. A, **21**, 1990, 627-639.
21. Mozer, B., Bendersky, L. A., Boettinger, W. J. and Rowe, R. G., Scripta Metall. et Mater., **24**, 1990, 2363-2368.

22. Banerjee, D., Gogia, A. K., Nandi, T.K. and Joshi, V. A., Acta. Metall., **36**, 1988, 871-882.
23. Gray, G. T. III, Deformation twinning: Influence of Strain Rate, in Yoo, M. H. and Wuttig, M. (eds.), Twinning in Advanced Materials", The Minerals, Metals and Materials Society, 1994, 338-349.
24. Morris, M. A. and Morris, D. G., Phil. Mag. A, **63**, 6, 1991, 1175-1194.
25. Rowe, R. G. and Huang, S. C., Israel J. Tech., 24, 1988, **255** - cited in Froes, F. H., Suryanarayana, D. and Eliezer, D., J. Mater. Sci., **27**, 1992, 5113-5140.
26. Chan, K. S., Metall. Trans. A, **21**, 10, 1990, 2687-2699.
27. Chan, K. S., Metall. Trans. A, **24**, 3, 1993, 569-583.
28. Haddad, J., Zevin, L. and Eliezer, D., J. Mater. Sci., **29**, 1994, 373-375.
29. Dickson, M. J., J. Appl. Cryst., **2**, 1969, 176-180.
30. Chen, Z., Simca, F. and Cope, M. T., Mat. Sci. and Tech., **8**, 8, 1992, 729-738.
31. Proske, G., Lutjering, G., Albrecht, J., Helm, D. and Daenbler, M., Mater. Sci. Eng., **A152**, 1992, 310-316.
32. Kim, Y-W. and Froes, F. H., Physical Metallurgy of Titanium Aluminides, in Whang, S. H., Liu, C. T. and Pope, D. (eds.), High Temperature Aluminides and Intermetallics, TMS, Warrendale, PA, 1990.
33. Gray, G. T. III and Embury, J. D., The Behaviour of Intermetallic Compounds at Large Plastic Strains, Mat. Res. Soc. Symp. Proc., **288**, 1993, MRS, 585-590.
34. Gray, G. T. III, Hong, S. I. and Marquardt, B. J., Influence of Strain Rate on the Structure/Property Behaviour of the Alpha-2 Alloy Ti-24.5Al-10.5Nb-1.5Mo, in Froes, F. H. and Caplan, I. L. (eds.), Proc. Seventh World Conf. on Titanium, **2**, 1992, 1163-1170.
35. Ward, C. H., Thompson, J. C. and Williams, J. C., Metall. Mater. Trans., **26A**, 3, 703-720.
36. Ward, C. H. and Balsone, S. J., The Effect of the Salient Microstructural Constituents on Tensile and Creep Deformation of Ti-25Al-10Nb-3V-1Mo, in Kim, Y-W. and Boyer, R. R.(eds.), Microstructure/Property Relationships in Titanium Aluminides and Alloys". The Minerals, Metals and Materials Society, 1991, 373-386.
37. Kim, Y-W., JOM, **41**, 7, 1989, 24-30.
38. Kim, Y-W., JOM, **46**, 7, 1994, 30-39.
39. Zhang, X. D., Ramanujan, R. V., Dean, T. A. and Loretto, M. H., Mater. Sci. Eng., **A185**, 1994, 17-24.
40. Takeyama, M., Mater. Sci. Eng., **A152**, 1992, 269-276.
41. Zhang, Y. G. and Chaturverdi, M. C., Mater. Sci. Eng., **A174**, 1994, 45-57.
42. Hug, G., Loiseau, A. and Veyssiere, P., Phil. Mag. A, **57**, 3, 1988, 499-523.
43. Prasad Rao, P. and Tangri, K., Mater. Sci. Tech., **8**, 1992, 1117-1124.
44. Rogers, N. J. and Bowen, P., Proc. Euromat '91, July 1991, 410-417.
45. Chan, K. S., JOM, **44**, 4, 1992, 30-38.

46. Chan, K.S. and Kim, Y.W., Metall. Trans. A, **23**, 6, 1992, 1663-1677.
47. Kim,Y-W. and Dimiduk, D. M., Mat. Res. Soc. Symp. Proc., **288**, 1993, 671-677.
48. Gray, G. T. III, The Influence of Strain Rate on the Structure/Property Behaviour of Ti-48Al-1V, in Kim, Y-W. and Boyer, R. R. (eds.), Microstructure/Property Relationships in Titanium Aluminide and Alloys, Minerals, Metals and Materials Society, 1991, 263-274.
49. Kimura, A., Koya, A., Morimura, T. and Misawa, T., Mater. Sci. Eng., **A176**, 1994, 425-430.
50. Ruff, A. W. and Wiederhorn, S. M., Erosion by Solid Particle Impact, in Treatise on Materials Science and Technology, **16**, 1979, 69-126.
51. Sundararajan, G, Wear, (in press).
52. Field, J. E. and Hutchings, I. M., Impact Erosion Processes in Harding, J. (ed.), Mechanical Properties at High Rates of Strain, Inst. of Physics Conf. Series, **70**, 1984, 349-111.
53. Hutchings, I. M., Tribology - Friction and Wear of Engineering Materials, Edward Arnold, Sevenoaks, 1992, 182.
54. Finnie, I., Wear, **3**, 1960, 87-103.
55. Lawn, B., Fracture of Brittle Solids, 2nd ed., Cambridge University Press, Cambridge, 1993, 257.
56. Ives L. K. and Ruff, A. W., Wear, **46**, 1978, 149-162.
57. Levy, A. V., Wear, **108**, 1986, 1-21.
58. Sundararajan, G., Wear, **149**, 1991, 111-127.
59. Sundararajan, G. and Shewmon, P. G., Wear, **84**, 1983, 237-258.
60. Hutchings, I. M. and Levy, A. V., Wear, **131**, 1989, 105-121.
61. Tabor, D., The Hardness of Metals, Clarendon Press, Oxford, 1951.
62. Doyle, R.A. and Ball, A. Wear, **151**, 1991, 87-95.
63. Hutchings, I. M., Physical and Metallurgical Aspects of the Erosion of Metals, Proc. Conf. on Corrosion/Erosion of Coal Conversion System Materials, N.A.C.E., Houston, January 1979, 393-428.
64. Marquardt, B. J., Baker, D. M. and Wert, J. J., Erosive Wear of Ductile Ordered Alloys in Ludema, K. C. (ed.), Proc. Int. Conf. on Wear of Materials, ASME, April 1985, 693-698.
65. Gat, N. and Tabakoff, W., Wear, **50**, 1978, 85-94.
66. Zhou, J. and Bahadur, S., Wear, (in press).
67. Karimi, A. and Martin, J. L., Int. Met. Rev., **31**, 1, 1986, 1-26.
68. Woodford, D. A., Metall. Trans., **3**, 5, 1972, 1137-1145.
69. Heathcock, C. J., Protheroe, B. E. and Ball, A., The Influence of Microstructure on the Cavitation Erosion of Materials, in Haasen, P., Gerold, V. and Kostorz, G. (eds.), Proc. 5th Int. Conf. on Strength of Metals and Alloys, August 1979, Pergamon, Oxford, 219-224.
70. Ball, A., Wear, **91**, 1983, 201-207.

71. Richman, R. H. and McNaughton, W. P., Wear, **140**, 1990, 63-82.
72. Karimi, A. and Avellan, F., Wear, **113**, 1986, 305-322.
73. Richman, R. H. and Rao, A. S., Microstructural Sci., **19**, 1992, 445-457.
74. Preece, C.M, "Erosion of Metals and Alloys", in Latanision, R. M. and Fourie, J. T. (eds.), Proc. NATO Advanced Study Institute on Surface Effects in Crystal Plasticity, Hohegeiss, Germany, 5-14 September 1975, 889-909.
75. Vyas, B. and Preece, C. M., ASTM STP: Erosion, Wear and Interfaces with Corrosion, 1974, 77-101.
76. Richman, R. H., Rao, A. S. and Hodgson, R. H., Wear, **157**, 1992, 401-407.
77. Otsuka, K. and Shimizu, K., Int. Metall. Rev., **31**, 3, 1986, 93-114.
78. Ball, A., Bergersen, S. G. and Hutchison, M. M., The Effect of Room Temperature Prestrain on the Tensile Properties of the Intermetallic Compound NiTi in the Temperature Range 150° - 370°. Suppl. Trans. Japan Inst. Metals, **9**, 1968, 291-295.
79. Wright, R. N. and Mikkola, D. E., Mater. Sci. Eng., **26**, 1976, 263-268.
80. Johnson, M., Mikkola, D. E., March, P. A. and Wright, R. N., Wear, **140**, 1990. 279-289.
81. Okada, T. and Hattori, S., Cavitation-Erosion Resistance of Titanium Aluminide Intermetallic Alloys, in Proc. 41st Annual Meeting of the Society of Materials Science-Japan, May 1992, 179-181.
82. Edelson, L. H. and Ritchie, R. O., Mater. Sci. Eng., **A130**, 1990, 193-203.
83. Baeslack, W. A., McQuay, P. A., Lee, D. S. and Fletcher, E. D., Mater. Char., **31**, 1993, 197-207.
84. Cass, T., Statistical Methods in Management, Cassell, London, 1974, 120-127.
85. Ruff, A. W. and Ives, L. K., Wear, **37**, 1975, 195-199.
86. Suckling, M. B. and Allen, C., Wear, (in press).
87. Annual book of A.S.T.M. Standards, 03.02, G32, 1993, 115-127.
88. Shechtman, D., Metall. Trans., **7A**, 1976, 151-152.
89. Cullity, B. D., Elements of X-Ray Diffraction, Addison-Wesley Inc., Reading, Massachusetts, 1956, 269.
90. ibid, 82.
91. ibid, 312.
92. Barrett, C. and Massalski, T. B., Structure of Metals, 3rd ed., Pergamon Press, Oxford, 1980, 277.
93. Cullity, B. D., Elements of X-Ray Diffraction, Addison-Wesley Inc., Reading, Massachusetts, 1956, 301.
94. ibid, 311
95. Muraleedharan, K., Nagender Naidu, S. V. and Banerjee, D., Scripta Metall. et Mater., **24**, 1990, 27-32.
96. Morris, M. A. and Morris, D. G., Phil. Mag. A, **63**, 6, 1991, 1175-1194.

97. Holloway, D. G., The Physical Properties of Glass, Wykeham Publications Ltd., London, 1973, 144.
98. Bendersky, L. A., Boettinger, W. J. and Royturd, A., Acta. Metall. Mater., **39**, 8, 1991, 1959-1969.
99. Barrett, C. and Massalski, T. B., Structure of Metals, 3rd ed., Pergamon Press, Oxford, 1980, 492.
100. Ramanujan, R. V., Zhang, X. D., Jones, I. P., Young, J. M. and Sears, J. W., The Chemistry and Structure of Plasma-Melted γ-Based Titanium Aluminides, Proc. 7th World Conf. on Titanium, June 1992,
101. Zhang, X. D., Ramanujan, R. V., Dean, T. A. and Loretto, M. H., Mater. Sci. Eng., **A185**, 1994, 17-24.
102. Hutchings, I.M., Tribology - Friction and Wear of Engineering Materials, Edward Arnold, Sevenoaks, 1992, 175
103. Blau, P. J., Friction and Wear of Ordered Intermetallic Alloys of Ni3Al, in S.D. Henry (ed.) "Friction, Lubrication and Wear Technology", ASM Handbook , **18**, 1992, 772-777.
104. Ninham, A., Wear, **121**, 1988, 307-324.
105. Ball, A., Willmott, S. and Resente, A., Wear, **123**, 2 1988, 225-239.
106. Vaughan, R. A. and Ball, A., J. Hard Mater., **2**, 3/4, 1991, 257-269.
107. Lawn, B., Fracture of Brittle Solids, 2nd ed., Cambridge University Press, Cambridge, 1993, 100.
108. Doyle, R. A., MSc Thesis, University of Cape Town, 1989.
109. Holloway, D. G., The Physical Properties of Glass, Wykeham Publications Ltd., London, 1973, 177-182.
110. Shashikala, H. D., Suryanarayana, S. V. and Nagender Naidu, S. V., J. Appl. Cryst., **26**, 1993, 602 - 605.
111. Gray, E. D. (ed.), American Institute of Physics Handbook, 3rd ed., Mc Graw-Hill, New York, 1972, 4-116.
112. Wallace, T. A., Clark, R. K., Wiedemann, K. E. and Sankaran, S. N., Oxid. Metal., **36**, 3-4, 1992, 111-124.
113. Peckner, D. and Bernstein, I. M., Handbook of Stainless Steels, McGraw-Hill, New York, 1977, 19-20.
114. Foley T. and Levy, A., Wear, **91**, 1983, 45-64.
115. Chinnadurai, S. and Bahadur, S., Wear, 1995, (in press).
116. Ashby, M. F. and Jones, D. R. H., Engineering Materials-An Introduction to their Properties and Applications, Pergamon, 1980, Exeter, 105-106.
117. Cottrell, A. H., The Mechanical Properties of Matter, Wiley, Taunton, 1964, 330.
118. Heathcock, J. C., PhD thesis, University of Cape Town, 1980.

119. Shechtman, D., Blackburn, M. J. and Lipsitt, H. A., Metall. Trans. A, **5**, 6, 1974, 1373-1381.
120. Yamaguchi, M. and Umakoshi, Y., Prog. Mater. Sci., **34**, 1990, 1-148.
121. Frommeyer, G., Wunderlich,W., Kremser, Th. and Liu, Z. G., Mater. Sci. Eng., **A152**, 1992, 166-172.
122. Wilson, S. and Ball, A., Modes and Mechanisms of Wear in Metal Matrix Composites, Proc. 6th Int. Congress on Tribology-"EuroTrib '93", Budapest, Hungary, September 1993.
123. Nartova, T. T., Soviet J. Powder Metall. and Met. Ceramics, **5**, 1966, 630-633.
124. Ross, R. B., Metallic Materials Specification Handbook, 4th ed., Chapman and Hall, Hitchin, 1980, 594.